Metal doped MIL-101(Cr) for hydrogen storage

Abdelmalek Malouche

ÉCOLE DOCTORALE UNIVERSITÉ PARIS-EST
Sciences, Ingénierie et Environnement

Thesis to obtain Ph.D. degree

from the University Paris Est, Specialty in Materials Science

Institut de Chimie de Matériaux de Paris-Est, CNRS UMR 7182

Team : Chimie Métallurgique des Terres Rares

Metal doped MIL-101(Cr) for hydrogen storage

Submitted by Abdelmalek MALOUCHE

Thesis defended on November 25th, 2019

Jury

Dr. Vanessa FIERRO	Institut Jean Lamour, CNRS, France	Reviewer
Dr. Laetitia LAVERSENNE	Institut Néel, CNRS, France	Reviewer
Dr. Jean-Louis BOBET	Université de Bordeaux, CNRS, France	Examiner
Dr. Fermin CUEVAS	ICMPE, CNRS, France	Examiner
Dr. Gabriela BLANITA	INCDTIM, Romania	Invited
Dr. Claudia ZLOTEA	ICMPE, CNRS, France	Ph.D. supervisor

List of figures

List of tables

Nowadays, energy needs are mainly covered by fossil fuels that emit pollutants responsible for climate change. Among the various possible solutions to reduce the greenhouse effect, hydrogen has been proposed as a fuel and should play an important role in the future. Indeed, this gas is considered as an efficient energy vector because of its zero-emission behavior and very high gravimetric energy density (33 $kWhkg^{-1}$) compared to other forms of energy (*figure 1.1*). However, dihydrogen is the lightest gas having a molar mass of 2 $gmol^{-1}$. Thus, one kilogram of hydrogen fills 12.2 m^3 under normal conditions[1] which gives a very low volumetric energy density (3 $kWhm^{-3}$).

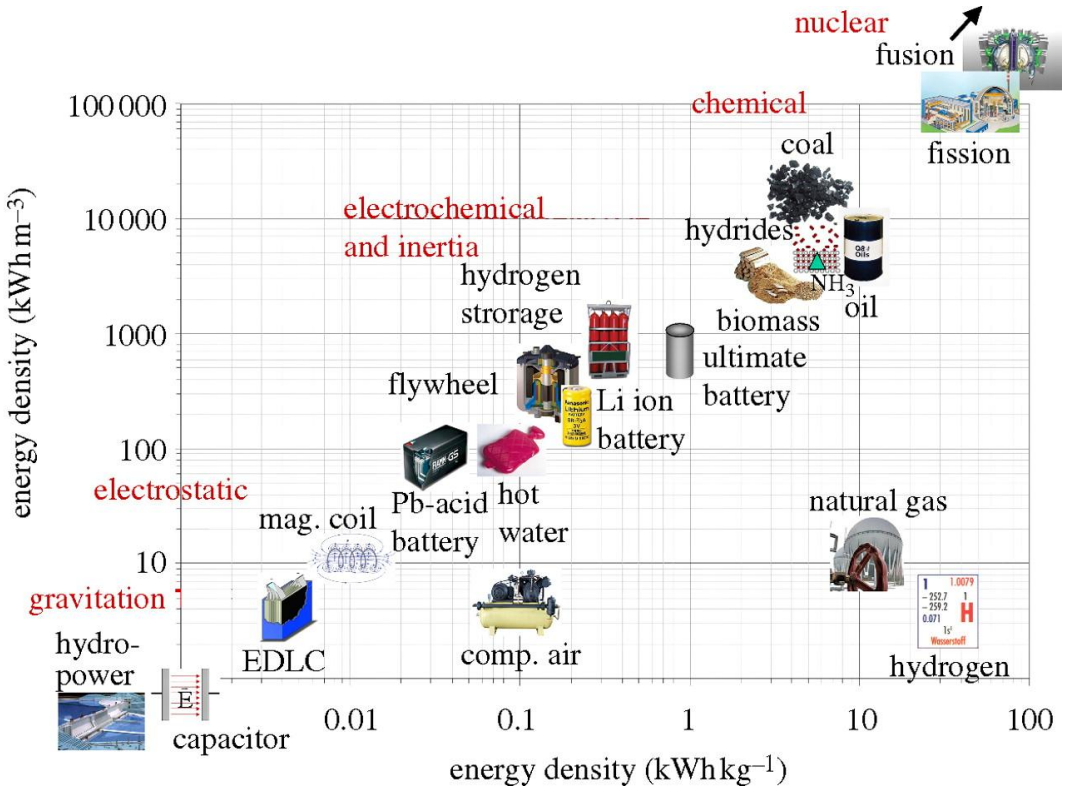

Figure 1.1: Volumetric vs. gravimetric density of the most important energy carriers. [2]

As a result, considerable research efforts are being made worldwide to develop high-density, safe, compact and efficient storage and transport devices for hydrogen[3]. Many systems have been tested and are still in competition for practical applications: compressed gas up to 700 bar in high-pressure tanks, cryogenic storage in the liquid state at 21 K, solid-state storage in hydride-forming metal materials and cryo-adsorption in highly porous adsorbent materials [2–4].

To minimize pressure and safety constraints, solid-state storage has been under consideration for several decades. This solid-state storage relays on two different phenomena: absorption and adsorption of hydrogen in/on solids.

The downsizing of metals/alloys has represented in the last decade an important strategy to control the kinetics, the reversibility and the equilibrium pressure for the storage of hydrogen in metal hydrides[5]. Indeed, reducing the size of the metal nanoparticles allows rapid kinetics for both the release and the absorption of hydrogen.

In this context, the National Research Agency (ANR) is financing the MEMOS project, based on an international collaboration between the Institut de Chimie et des Matériaux de Paris-Est (ICMPE) and the National Institute for Research & Development of Isotopic and Molecular Technologies (NIRDIMT, Cluj-Napoca, Romania) in coordination with Dan LUPU and Gabriela BLANITA, as Romanian partners. The main idea consists in combining absorption and adsorption by confining mono and bi-metallic nanoparticles into mesoporous Metal-Organic Frameworks (MOFs) for solid storage applications. The main challenge from material sciences point of view is to control the size, distribution, and dispersion of the nanoparticles within the pores of the MOF. This latter aspect is the core of this PhD thesis together with the study of hydrogen interaction with metal-doped MOFs.

This manuscript is divided into 5 chapters. A **first** chapter includes a bibliographic study on the importance of hydrogen as an energy carrier, its production, transport and storage in different forms and in different materials and highlighting the nanosize effect in hydrogen interaction with metals.

The **second** chapter will deal with experimental methods for the synthesis and the physicochemical characterization techniques of synthesized materials used throughout the thesis.

The **third** and the **fourth** chapters will describe the processes for the preparation of the MIL-101(Cr) doped Pd and Rh clusters, respectively, up to 20 wt.%, the physicochemical characterization and the hydrogen sorption properties of the different synthesized composites.

A **final** chapter will present the results obtained for MIL-101(Cr) doped with bimetallic (Pd-Rh, Pd-Pt, Rh-Ir) nanoparticles. The formation of these alloys will be discussed.

This manuscript ends with a general conclusion of the most significant results obtained during this thesis work and we propose some research perspectives.

CHAPTER I

GENERAL INTRODUCTION

1.1 Hydrogen aspects

1.1.1 Hydrogen: energy vector

Hydrogen is the smallest and the most abundant element of the universe, the 9th on the Earth and the 2nd in the oceans [6]. His name was proposed in 1787 among others by Lavoisier [7] and originates from Greek, meaning who generates the water. Thus, hydrogen reacts with oxygen to form water:

$$H_2\,(g) + \frac{1}{2}\,O_2\,(g) \rightleftarrows H_2O\,(g) + Energy\ (Lower\ Heating\ Value). \qquad \textbf{(Equation 1.1)}$$

$$H_2\,(g) + \frac{1}{2}\,O_2\,(g) \rightleftarrows H_2O\,(l) + Energy\ (Higher\ Heating\ Value). \qquad \textbf{(Equation 1.2)}$$

The amount of energy produced by the combustion of hydrogen is higher than for any other fuel. Comparing the calorific values, that of hydrogen is respectively 2.4, 2.8 and 4 times higher than that of methane, gasoline, and coal [8]. Consuming hydrogen thus has the advantage of not releasing CO_2. However, 98% of hydrogen is produced today by reforming oil or natural gas, which then releases a large amount of CO_2. We will see later that methods exist to solve this problem.

1.1.2 Hydrogen production

Hydrogen is today mainly produced by reforming fossil fuels. In order to develop hydrogen as a clean energy vector, other modes of industrial production must be developed. *Figure 1.2* shows different modes of production of hydrogen [9].

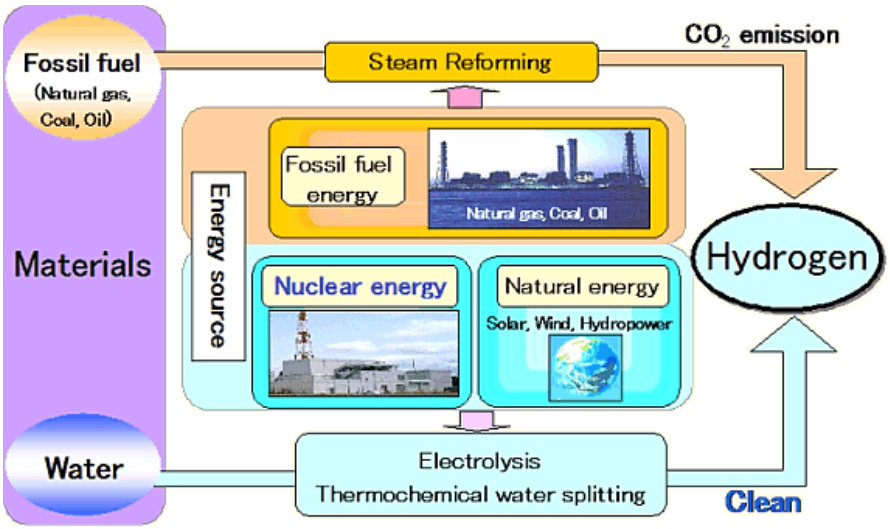

Figure 1.2: Different modes of hydrogen production. [10]

1.1.2.1 Fossil energy transformation

Oil and coal release large amounts of CO_2 to produce hydrogen. The trapping of carbon dioxide is possible in refineries unlike the case of mobile applications with embedded reforming. However, the possible capture of CO_2 does not solve the geopolitical problem of energy dependence on oil-producing countries and the end of fossil fuels [11].

1.1.2.2 Water electrolysis

Hydrogen could be also produced from water electrolysis by different ways.

1.1.2.2.1 Wind, solar

In isolated environments (especially islands), wind and solar renewable energies suffer from the problem of intermittency of their production (day/night phases, the absence of wind ...) [12]. To overcome this problem, hydrogen is a solution. In fact, when the consumption is lower than the production, the additional energy created is used to produce hydrogen. In the opposite case, the hydrogen is consumed. The production/energy demand curves are then smoothed.

1.1.2.2.2 Hydraulics

Hydraulics suffer less from the previous problem of fluctuating production because of the use of the produced energy excess to raise water upstream of the dam. Hydropower can also be considered to produce hydrogen in hard-to-reach areas (high-mountain chalet at the edge of a stream ...).

1.1.2.2.3 Nuclear

The electrical network of nuclear energy (80%) can provide hydrogen by electrolysis of water at low-temperature [13]. At 1123 K, 4th generation nuclear power will make it possible to obtain hydrogen by thermochemistry or electrolysis at high temperature.

1.1.2.3 Biomass

The recent controversy over biofuels raises the problem of land use for energy production to the detriment of food [14]. However, it is possible to use the non-edible parts of plants to transform them into energy. In addition, progress is being made to improve yields.

The recovery of household waste allows the manufacture of methane. Its reforming, coupled with the trapping of CO_2, allows a clean production of hydrogen.

It should also be noted that hydrogen can be produced from green algae, which consumes a lot of CO_2 [15].

1.1.3 Hydrogen transformation to energy

For mobile applications, there are two main paths for the use of hydrogen as an energy vector: internal combustion engine and fuel cell (*figure 1.3*).

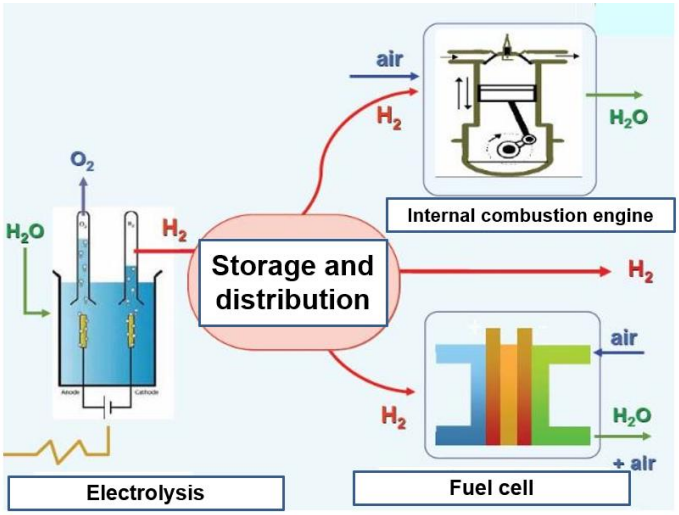

Figure 1.3: Hydrogen circuit (water electrolysis, storage and distribution to internal combustion engine and fuel cell. [16]

1.1.3.1 Internal Combustion Engine

BMW offers a sedan with an internal combustion engine of hydrogen (*figure 1.4*), coupled with cryogenic storage. Being able to "burn" hydrogen in combustion engines makes it possible to offer hybrid vehicles. The disadvantages of the internal combustion are the limited yield, the Carnot cycle (30 - 35%) and the formation of undesirable nitrogen oxides.

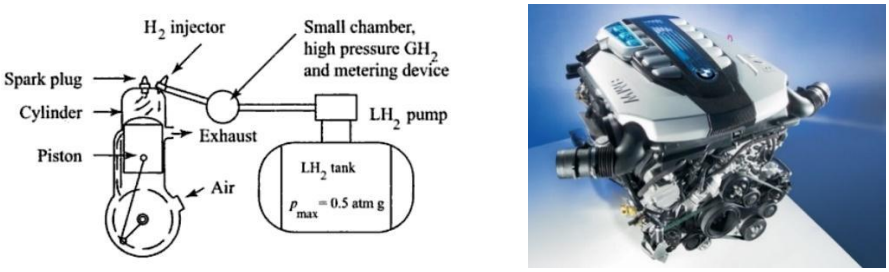

Figure 1.4: Internal combustion engine with liquid hydrogen tank (Left) and BMW internal combustion engine (Right). [17]

1.1.3.2 Fuel Cell

The fuel cell uses hydrogen and oxygen as the redox electrochemical couple as shown in *figure 1.5*. The reaction occurs within a structure composed of the anode (which receives hydrogen), the cathode (receiving oxygen from the air) which are separated by an electrolyte (material that allows the passage of ions). The efficiency is between 50-60% considering only the electrical energy released.

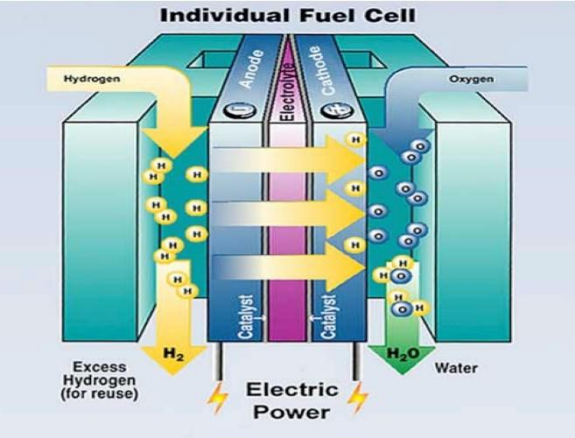

Figure 1.5: Schematic fuel cell. [18]

However, much of the energy is released as heat that can be reused to release hydrogen from the reservoir or to participate in a co-generation phenomenon: joint electricity and heat production bringing the overall efficiency of installation to 80-90%.

1.2 Hydrogen storage

Three major families stand out for hydrogen storage: the solid, liquid and gaseous pathways.

1.2.1 Gaseous storage

1.1.2.2 Hydrogen storage by compression

It is the most common storage mode today for mobile and transportable equipment. The tanks are designed to have the best possible ratio between the mass of hydrogen stored and the mass of the cylinder. They must also be able to answer two essential problems: sealing and mechanical resistance.

Two types of compression technologies can be used:

- Conventional technology: steel cylinders (*figure 1.6*) with a storage pressure between 150 and 300 bar (14 kg/m^3 at 200 bar and 294 K). These cylinders have a high weight and there are problems of embrittlement of the steel by hydrogen.

Figure 1.6: Hydrogen gas storage tanks up to 300 bar. [19]

- High pressure: rolled fiber cylinder (*figure 1.7*) whose storage pressures are much higher (standard 350 bar and up to 700 bar). These tanks consist of three layers: a sealed envelope that allows impermeability of hydrogen (stainless steel, aluminum, high-density polymer), a working structure that withstands pressure stresses (carbon fiber and resin helical winding) and an outer layer for protection against external aggressions (protective resin or fiberglass).

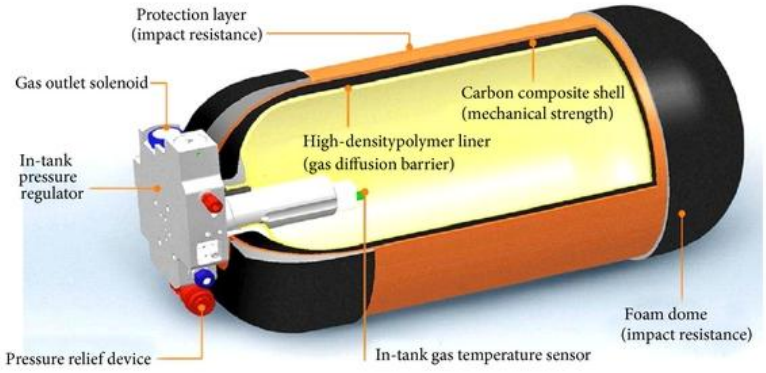

Figure 1.7: Hydrogen tank manufactured by Quantum Fuel Systems with a storage capacity of up to 5 kg of H_2 at 700 bar. [20]

Although this mode of storage has advantages like the control of the technology and the speed of the filling; it is limited by the low volumetric density, the development of tanks resistant to shocks and the adaptation of all auxiliaries (for automotive applications) [3,9].

1.2.2 Liquid storage

1.2.2.1 Hydrogen storage by liquefaction

The storage of hydrogen in liquid form at a very low temperature makes it possible to reach mass densities (70 kg of H_2 per cubic meter) and volume densities higher than the gas storage such as the liquid H_2 tank manufactured by Linde (*figure 1.8*). At 1 bar, the hydrogen is liquid below 20 K (liquefaction temperature) [9]. Tanks of 150 L and 145 kg can store 9.5 kg of H_2. From a technical point of view, the hydrogen is first cooled with liquid nitrogen down to 80 K. The Claude cycle is the thermodynamic pathway used to liquefy hydrogen. The latter undergoes compression-relaxation cycles further lowering its temperature and relaxation of Joule-Thomson leads to its liquefaction. However, this requires relatively heavy installations. The energy required for liquefaction represents one-third of the energy contained in the form of liquid hydrogen. On the other hand, about 1% of the stored hydrogen is lost daily by evaporation (boil-off phenomenon). Tanks with high thermal insulation can minimize this evaporation. The risks associated with this evaporation pose security problems in confined environments. The total energy cost of this storage channel can be up to 40% of the calorific value of hydrogen, which is a deterrent for prolonged storage. Overall, liquid storage appears to be more complex, more expensive and less energy efficient than gas storage. It is only preferred for long-distance transport and for aerospace applications.

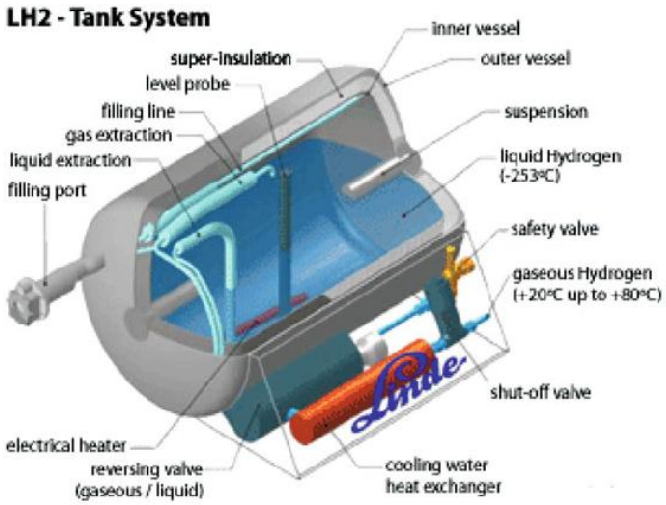

Figure 1.8: Liquid hydrogen tank manufactured by Linde with a volumetric capacity of 0.070 kg/L compared to 0.030 kg/L for 700 bar gas tanks. [21]

1.2.3 Solid storage

Solid-state storage of H_2 is possible through two phenomena between gas and solid materials. The most easily understood phenomenon is that of absorption, which reflects a fixation of gas molecules in the volume of the material and within its lattice itself. In a complementary manner, the adsorption is defined by an attraction between the gas molecules and the surface of the solid and therefore a fixation of the hydrogen on the surface of the material exclusively by the Van der Waals forces. *Figure 1.9* schematizes both phenomena. It should be noted, however, that absorption is always preceded by an adsorption step. The use of the term sorption displays a desire not to differentiate phenomena. The solid on which the sorption takes place is called substrate. In the case of adsorption, the adsorbing gas molecule is called adsorbate.

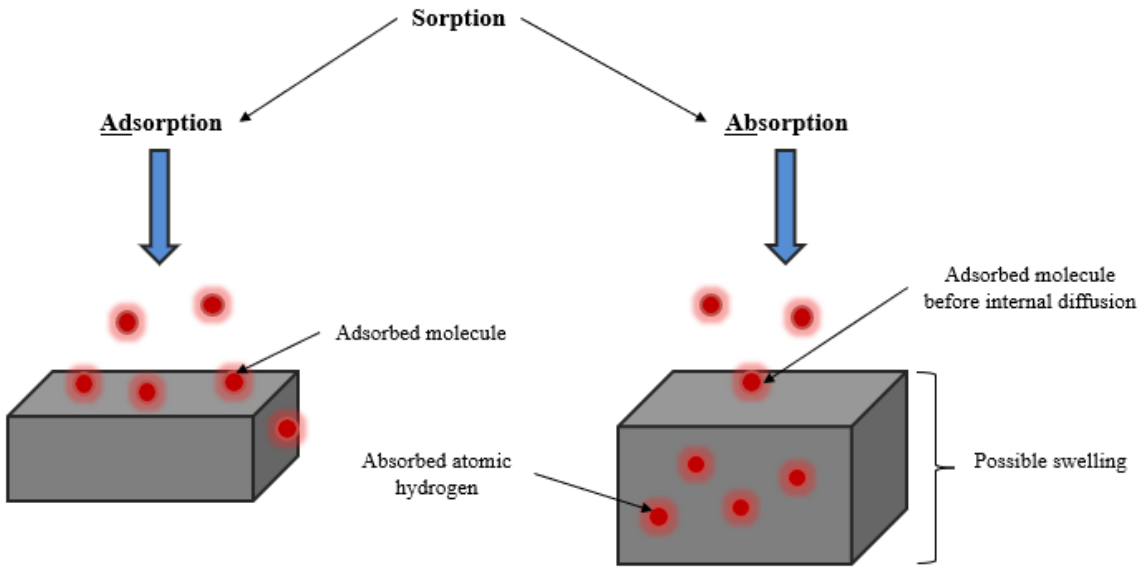

Figure 1.9: Schematization of the difference between adsorption and absorption.

At equilibrium, the amount of absorbed or adsorbed gas on the substrate is fixed. Nevertheless, this equilibrium is statistical, and, under the effect of a local perturbation, an adsorbed molecule can leave the substrate and be replaced by another initially present in the gas. The fact that a molecule leaves the substrate, whether it is an adsorbed or absorbed molecule, is called desorption. In some cases, absorption may result in swelling of the substrate. Adsorption and absorption on virgin substrates are generally thermodynamically favored phenomena and, as such, are spontaneous and exothermic.

1.2.3.1 Chemical storage

The process of chemical storage of hydrogen in metallic materials begins with the dissociation of the adsorbed hydrogen molecule on the surface of the metal. Then, the hydrogen is inserted into the crystal lattice of the metal and diffuses from a surface site to an interstitial site. The absorption of hydrogen is characterized by an expansion of the crystal lattice, proportional to the concentration of hydrogen, of about 2-3 $Å^3$ per hydrogen atom[2,4]. The process of forming a hydride from a metal is summarized by the reaction:

$$M_{solid} + \frac{x}{2} H_2 \leftrightarrow MH_x + Heat. \qquad \textbf{(Equation 1.3)}$$

The thermodynamic properties of hydride formation are determined by Van't Hoff equation starting from the solid-gas pressure-composition isotherms (PCI) as shown in *figure 1.10*.

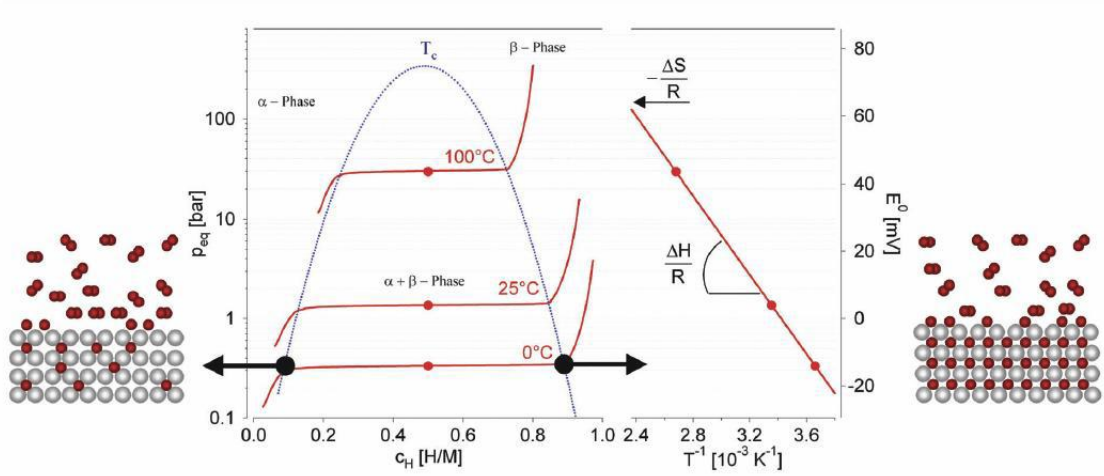

Figure 1.10: Isotherms pressure-composition of the hydrogen absorption by a metal (left) and the representation of the equation of Van't Hoff (right).[4]

At low pressure, the occupation of the interstitial sites of the metallic network by hydrogen is done randomly (the α phase) until reaching a ratio H / M of 0.1. For H / M values higher than 0.1, the hydrogen-hydrogen interactions are more and more important. The occupation of the sites then becomes ordered and the metal hydride (the β phase) is formed at higher pressures[2,22]. The simultaneous presence of both α and β phases leads to the appearance of an equilibrium pressure plateau on the pressure-composition isotherms (the Gibbs phase rule). The amount of hydrogen stored, reversibly, is determined by the length of the pressure plateau[4,5]. The increase in the hydrogenation temperature is accompanied by a shift of the equilibrium plateau to higher pressures and smaller amounts of hydrogen stored up

to a critical temperature T_C beyond which the transition phase α → β is continuous. The equilibrium pressure, P_{eq}, of the plateau is related to the temperature T by the law of Van't Hoff:

$$Ln(P_{eq}) = \frac{\Delta H}{RT} - \frac{\Delta S}{R} \qquad \textbf{(Equation 1.4)}$$

with $\boldsymbol{R}$: the perfect gas constant (8.314 $JK^{-1}.mol^{-1}$), $\boldsymbol{\Delta H}$: enthalpy of hydride formation (kJ/mol^{-1}), $\boldsymbol{\Delta S}$: entropy of the reaction ($JK^{-1}.mol^{-1}$) and $\boldsymbol{T}$: the temperature (K).

As mentioned above, the thermodynamic properties of hydride formation are determined from this equation. Indeed, the variation of entropy corresponds mainly to the passage of hydrogen from the gaseous state to the inserted state and the variation of the enthalpy characterizes the stability of the metal-hydrogen bond of the hydride.

The metal hydrides are classified according to the chemical bond formed between the metal and the hydrogen. The reversibility of the hydride formation reaction strongly depends on the type of bond and follows the increasing order: metal < ionic < covalent [23]. The different types of hydrides are compared in *figure 1.11* and listed below. For transportation applications, the US Department of Energy (DOE) has set an ultimate target of ≥ 7.5 wt.% as hydrogen storage capacity in fuel cell applications in vehicles under ambient temperature and a maximum pressure of 12 bar.[24,25]

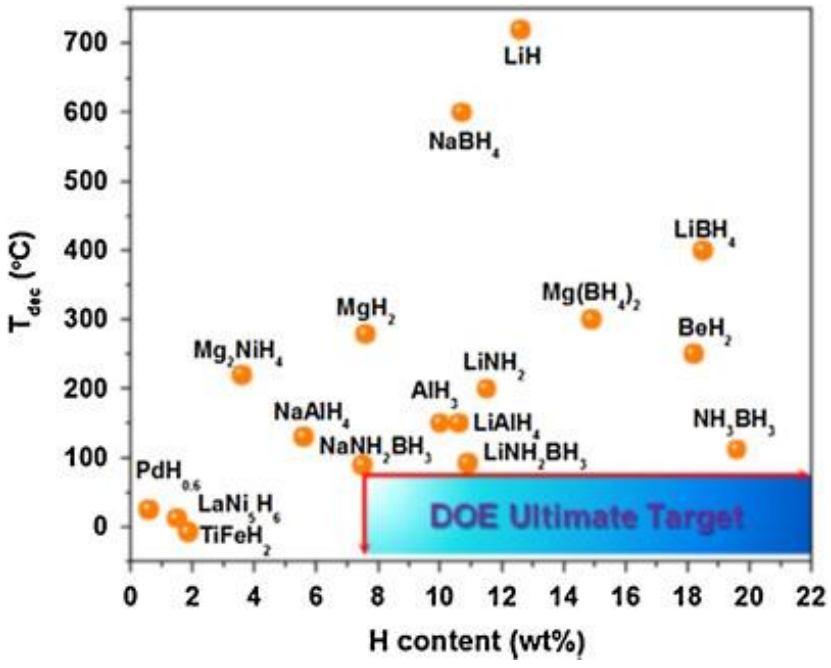

Figure 1.11: Thermal decomposition temperature of different hydrides as a function of hydrogen amount released. [24]

1.2.3.1.1 Complex hydrides

These hydrides are called complexes because they are formed by covalent bonds between hydrogen and a metal or nonmetallic atom to form a complex anion. The charge of the anion is compensated by a cation belonging to the alkaline or alkaline earth family. Their hydrogen storage capacity can reach 13.8 wt% (percentage of hydrogen per mass of adsorbent) for certain hydrides such as $LiBH_4$ ($LiBH_4 \rightarrow LiH + B + 1.5\ H_2$), but the adsorption/desorption process is reversible under hard conditions [3].

1.2.3.1.2 Ionic hydrides

These hydrides are formed by alkali or alkaline earth metals and hydrogen as an H^- anion. With a hydrogen storage capacity of 7.7 wt%, MgH_2 is an interesting candidate for hydrogen storage thanks to its low cost and the reversibility of the process. However, the thermodynamic properties of the material represent an obstacle to its use in atmospheric conditions. Indeed, MgH_2 is a typical example of high-temperature metal hydride with an equilibrium pressure of 0.1 MPa at temperatures of about 573 K [3].

1.2.3.1.3 Interstitial hydrides

As their name suggests, the interstitial hydrides are formed by the hydrogen occupation of the tetrahedral or octahedral interstitial sites of the metal structure forming a metal bond M-H[2]. Generally, the reaction between hydrogen and metal is reversible. Absorption and desorption of hydrogen depend on temperature and pressure. Absorption is an exothermic reaction while desorption is endothermic. The quantity of hydrogen that can be stored in this type of hydride is limited to 2 wt. % of H_2 (Laves phases compounds, $FeTiH_x$, $LaNi_5H_x$)[26].

1.2.3.2 Physical storage

This mode of storage is operating by adsorption phenomenon using the Van der Waals forces. In fact, the term adsorption was proposed at the beginning of the 20th century to designate the attraction between the gas molecules and the surface of the solid, *i.e.* without penetration. It occurs without modification of the molecular structure of gas and is perfectly reversible. Adsorption phenomenon is the result of non-specific physical interactions. The importance of the different types of interactions depends on the adsorbate (adsorbing molecule) / adsorbent (adsorption surface) pair.

From a thermodynamic point of view, physical adsorption is a spontaneous process that leads the system (adsorbate + adsorbent) to change to a more stable state: the free enthalpy variation of the system is negative. Overall, the adsorbent is not fundamentally modified by the adsorption and its entropy variation is negligible while the adsorbate is structured on the surface of the solid and its entropy variation is negative. In addition, the adsorption is an exothermic phenomenon: the enthalpy variation of the system is negative.

The adsorption processes are classified into two categories which are physical adsorption or physisorption, and chemical adsorption or chemisorption. These different processes are characterized by the binding energies involved in the adsorption process as well as by the nature of the bonds formed between the substrate and the adsorbate. Van der Waals forces govern the physisorption process.[27] These are made up of three components. The first, called the Keesom forces, results from permanent dipole / permanent dipole interaction (non-existent for H_2 which is not polar). The second, called the Debye forces, results from the interaction between a permanent dipole and an induced dipole. Finally, the London forces resulting from the intermolecular interaction between two induced dipoles. In the case of conventional and unpolarized physisorption, the forces governing the adsorption process are London type forces.

Chemisorption is a different process during which covalent bonds are established between the substrate and the adsorbate. The binding energies involved are of a few tens kJ.mol^{-1}. In the case of H_2, chemisorption can occur on the surface of metals. Prior to establishing covalent bonds between the substrate and H_2, dissociation of the H_2 molecule must occur. The chemisorption is then dissociative. This dissociation leads to a disruption of the H-H bond.

In general, the physical storage is a method with good mass capacities, low binding energies and can be applied to different porous materials with high surface area and porous volume such as, carbon (carbon nanotubes, activated carbons, carbon fibers), zeolites, silicate and Metal-Organic Framework (MOFs). Indeed, these materials tailored for hydrogen storage are an interesting route for storage and cryoadsorption might be a promising strategy for hydrogen storage system by increasing the volumetric density and avoiding the energy penalties by operating at low temperatures (77 K) and/or high pressure. One promising porous material for hydrogen storage are the MOFs due to their high specific area. Generally, the adsorbed capacities depend linearly to the pores volume and surface area. But, the capacities are important only at cryogenic temperature due to weak Van der Waals forces.

1.3 Hydrogen storage in Metal-Organic Frameworks

Metal-Organic Frameworks consist of inorganic subunits (secondary building units (SBU): transition materials, lanthanides, and oxygen.) connected to each other by organic ligands (carboxylates, imidazolates, etc.) thus forming ordered nanoporous crystalline hybrid networks (*figure 1.12*). The wide choice of metal centers and organic ligands allows the design of MOFs with adjustable crystalline properties and porosity. More than 60 000 MOFs have already been reported[28]. The most interesting MOFs for storage have very large surface areas and microporous volumes. Among the first hybrids studied for the storage of hydrogen, MOF-5 has a capacity of about 7 wt.% for a specific surface area of between 4000-5000 m^2/g. Very recently, hybrids with a specific surface area up to 6000 m^2/g have been synthesized. This is the case of NU-100 which contains micro and mesopores and can store about 9 wt.% of hydrogen at 77 K[29].

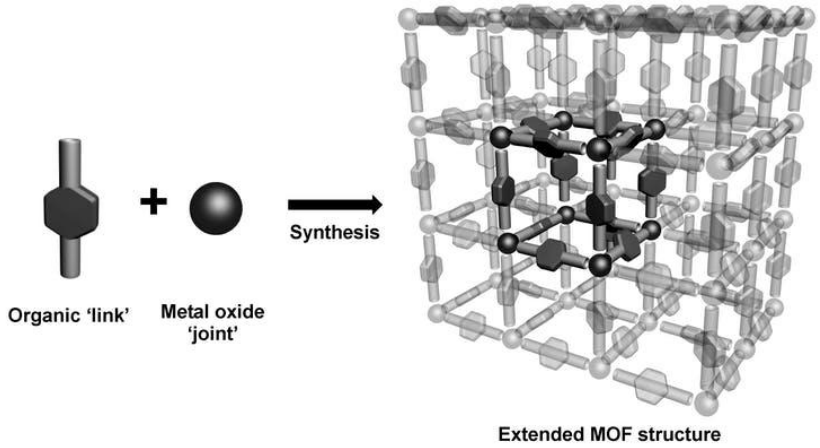

Figure 1.12: Representation of the MOF crystal structure. [30]

Despite enormous research efforts towards the development of their specific surfaces, MOFs suffer from low binding energies with H_2 molecules. For this reason, another part of the research effort is dedicated to increasing the adsorption energy. Among the various strategies envisaged, the insertion of metallic nanoparticles in the pores of MOFs is proposed to combine the adsorption properties of hydrogen at cryogenic temperature with the absorption properties of metals at room temperature. In fact, due to their ordered structure, the MOFs pores ensures the nanoconfinement and the monodispersion of the nanoparticles and, their stabilization against coalescence.

In this thesis project, one MOF was used as a confinement matrix for the nanoparticles. The MIL-101 ($(Cr_3O)X(H_2O)_2[O_2C\text{-}C_6H_4\text{-}CO_2]_3$, X = F^{-1}, Cl^{-1}, OH^{-1}), discovered by Férey and co-workers in 2005 [31], is a MOF with a very complex structure based on SBU of type μ_3-oxo-centered trimers of octahedral Cr(III) connected to six other connectors through doubly deprotonated terephthalic acid linkers [31] . The resulting tetrahedron is assembled into the so-called "super tetrahedrons" leading to two types of mesoporous cages with internal free diameters of about 2.9 and 3.4 nm and pore windows of 1.2-1.6 nm (*figure 1.13*). The MIL-101(Cr) was selected as a host matrix in this study not only for its large specific surface area (S_{BET} 3800 $m^2.g^{-1}$) and huge porosity (2.0 $cm^3.g^{-1}$) but also for its high thermal stability (up to 573 K) (*Annex 1*), and high chemical stability to water.

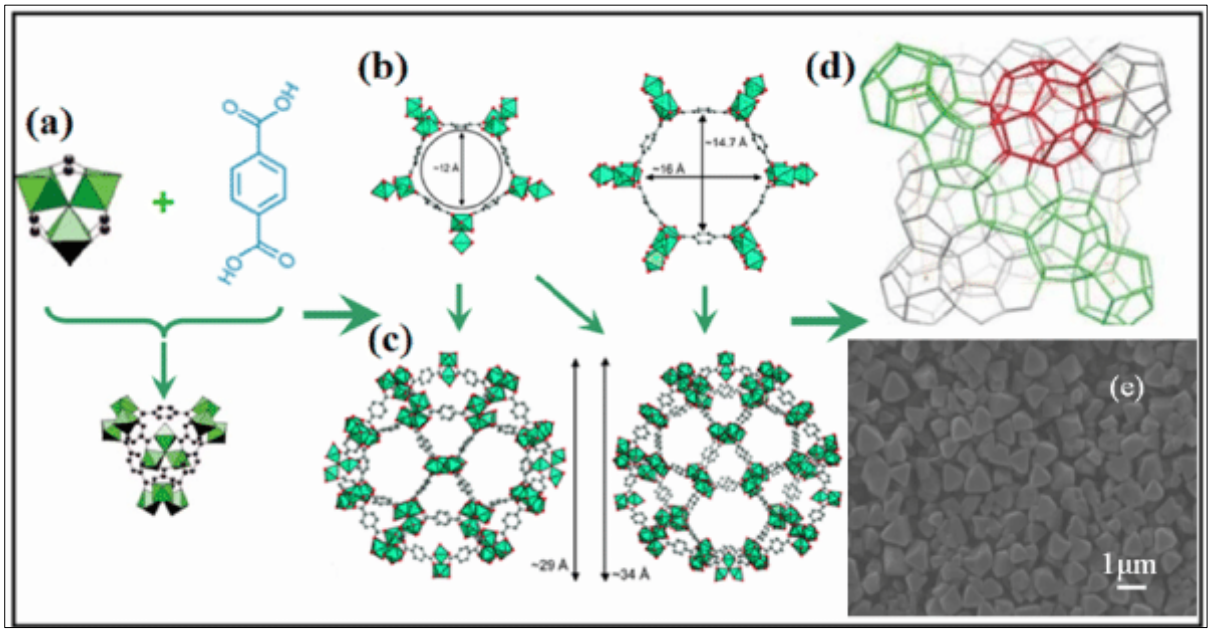

Figure 1.13: Structure of MIL-101(Cr) (a) cluster building unit (trimer of chromium octahedra) and the 1,4-benzendicarboxylate ligand, forming the hybrid supertetrahedron; (b) pentagonal (left) and larger hexagonal (right) windows and (c) the two types of mesoporous cages; (d) Schematic 3Drepresentation of the pores architecture (small cage is highlighted in green and large one is highlight in red); (e) a clear octahedral morphology with an average crystal size of ~1.0 µm. [32]

1.4 Nanosizing effect

Nanostructuration of solid materials may be carried out by two methods: *top-down* or *bottom-up*. *Top-down* approach is to miniaturize already existing objects of micro or macrometric size to approach the nanometric dimensions. On the other hand, *bottom-up* method consists in assembling elementary components (atoms, molecules, aggregates) to form more complex structures. Whatever approach is used, nanostructuration considerably changes the physicochemical properties, increases the specific surface and reduces the particle size. The thermodynamic properties during the reaction with hydrogen can be modified thanks to the non-negligible contribution of the surface energy term. The kinetics of reaction with hydrogen also increase due to two main factors: the enhancement of surface kinetics and the reduction of diffusion paths inside the particles.

1.4.1 Nanostructuration by mechanical milling

Mechanical milling is a technique of mechano-synthesis very widespread in research and industry despite its high energy cost. This *top-down* nanostructuration process makes it possible to obtain materials in the form of nanostructured powders under the effect of a succession of mechanical shocks on the particles inside a container. The process is called the co-milling method if it is carried out with additives (oxides, alloys, etc.) which remarkably increase the absorption/desorption kinetics[23]. Generally, after milling, a size reduction of the crystallites of the material around 10-20 nm is obtained as well as the formation of numerous defects and grain boundaries. The kinetics of the reaction of Mg/MgH_2 after milling are extremely fast (a few minutes) compared to the material before milling (few hours). However, the nanostructure is generally unstable during absorption/desorption cycling and progressive recrystallization is observed when exposed to high temperature. The thermodynamic properties of milled MgH_2 remain unchanged and require the use of rather high temperatures (around 573 K) to deliver 1 bar of H_2. The absorption reaction is very exothermic, and the heat must be evacuated very quickly to load a tank in a reasonable time. In order to increase the thermal conductivity and reduce the gradual recrystallization, a process for shaping the material with the addition of expanded natural graphite has recently been developed by the French company McPhy (www.mcphy.com). The company markets MgH_2-based tanks co-milled with additives and shaped with graphite for stationary hydrogen storage solutions.

1.4.2 Nanoparticles/nanowires formation

Other *top-down* methods such as spark discharge generation allow the synthesis of free Mg or MgH_2 particles with a size of 10-20 nm[33]. The reaction kinetics are very fast, and the desorption temperature is reduced compared to the bulk material. However, the synthesis is complex, and the quantities produced are limited. More original *top-down* methods (vapor deposition) have made it possible to develop one-dimensional nano-objects of Mg or MgH_2 with a controlled morphology (nanowires with diameter <50 nm)[34]. Again, downsizing increases the reaction kinetics and decreases the desorption temperature compared to the bulk material. Nevertheless, the disadvantage of these methods is the instability of the nanostructure. Progressive recrystallization (increase in crystallite size with slowing of kinetics) is observed during absorption/desorption cycling and exposure at a relatively high temperature.

1.4.3 Nanoconfinement: monodispersion

In order to reduce the size of nanoparticles (< 10 nm) and to stabilize them against coalescence, a promising strategy is the confinement of particles within a porous inert matrix[1]. Many porous matrices are available such as carbons, MOFs, polymers, and oxides. Both *top-down* (melted infiltration under controlled atmosphere) and *bottom-up* methods (liquid impregnation of precursors and decomposition/reduction under controlled atmosphere) can be applied to synthesize nanoparticles of controlled size of metals/ alloys/hydrides confined in different host matrices. In addition, the control of the pore size of the matrices allows, in principle, to develop limited size nanoparticles.

For example, MgH_2 nanoparticles confined in the pores of different carbons have been obtained with an extremely small size (1.3 nm)[35]. These nanoparticles show faster desorption kinetics than MgH_2 bulk, which is also dependent on size: the smaller the size, the faster the kinetics.

Another example that confirms the positive effects of nanoconfinement is the case of $NaAlH_4$ complex hydride (mass capacity of 7.4 wt%)[36]. In the massive state, this hydride decomposes in two stages with the help of catalyst additives:

$$NaAlH_4 \leftrightarrow \frac{1}{3} Na_3AlH_6 + \frac{2}{3} Al + H_2 \leftrightarrow NaH + Al + \frac{3}{2} H_2. \quad \textbf{(Equation 1.5)}$$

The same nanoconfined and additive hydride desorbs the hydrogen in a single reaction removing the intermediate step:

$$NaAlH_4 \leftrightarrow NaH + Al + \frac{3}{2} H_2. \quad \textbf{(Equation 1.6)}$$

Thus, the kinetics are faster, the thermodynamics is modified, and the reversibility is improved.

A final example concerns noble metals such as Pd and Rh which are widely used in industry as catalysts.

The Pd-H system is one of the best-known metal-hydrogen systems. In the bulk Pd, hydrogen is absorbed at ambient pressure and temperature, forming an interstitial hydride[37,38]. By decreasing the Pd nanoparticle size, the obvious size effect is observed on the Pressure-Composition-Isotherm curves. In fact, the solubility of hydrogen and the solubility limit in the solid solution phases (α phase) increases by decreasing the particle size and the solubility of hydrogen and the minimum solubility in the hydride phase (β phase) decreases with the nanoparticle size (*figure 1.14(a)*). As a result, the miscibility gap narrows, and the critical temperature decreases by decreasing the size. It has been reported that by decreasing the size of Pd nanoparticles to 2.6 and 3 nm the T_C decreases from 565 K (for bulk) to 393 and 430 K, respectively.[39–41] This behavior can be explained by a thermodynamic changes of nanosized Pd-H system.[40,42] In this context, the thermodynamic properties ($-\Delta H_{\alpha \rightarrow \beta}$ and $-\Delta S_{\alpha \rightarrow \beta}$) were studied and determined by Yamauchi *et al.* and it has been shown that by decreasing the size of the nanoparticles, $-\Delta H_{\alpha \rightarrow \beta}$ and $-\Delta S_{\alpha \rightarrow \beta}$ decreases accordingly (*figure 1.14(b)* and *(c)*) [39]. Thus, the decrease of the critical temperature of the Pd-H phase diagram and the destabilization of the Pd hydride in the nanoparticles are caused by the weak bond strength between Pd and H in nanoparticles (small $-\Delta H_{\alpha \rightarrow \beta}$).

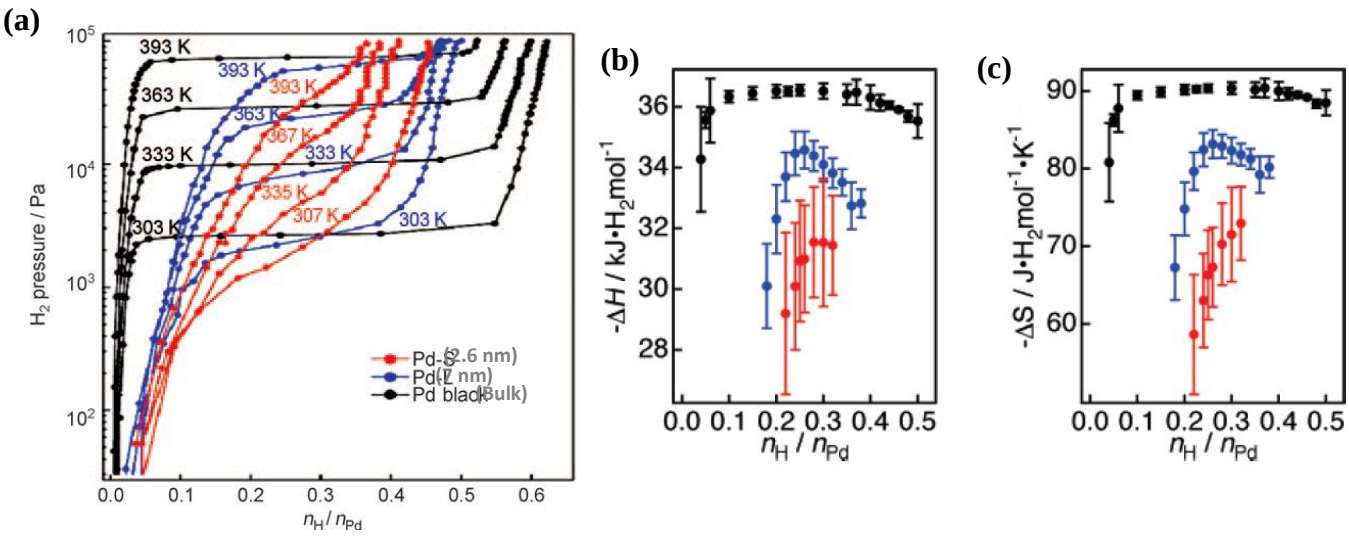

Figure 1.14: Size effect on (a) Hydrogen Pressure-Composition Isotherm curves, (b) heat of formation ($\Delta H_{\alpha\rightarrow\beta}$) and (c) standard entropy ($\Delta S_{\alpha\rightarrow\beta}$) for 2.6, 7 nm and bulk Pd. [39]

In addition, the decrease in the size of the nanoparticles influences the absorption/desorption kinetics due to the shortening of the hydrogen diffusion pathways in the nanoparticles and the increase in the specific surface area, which enhances the hydrogen sites for its dissociation and recombination. This absorption/desorption kinetics, which increases with decreasing particle size, has been confirmed by an indirect nanoplasmonic sensing method for nanoparticles of different sizes.[43] On the other hand, using Thermal-Desorption spectroscopy, the desorption kinetics were shown to be faster for 3 nm nanoparticles supported on carbon compared to bulk Pd.[1]

The decrease in particle size reduces the hydrogen storage capacity, which is directly related to the shrinking of the miscibility gap of the Pd-H phase diagram. An example that shows this size effect has been reported for Pd nanoparticles of 2.6 and 7 nm (*figure 1.14(a)*)[39]. Nanosized Pd still absorb hydrogen easily, but its storage capacity is reduced which is characterized by the decrease in the width of the pressure plateau.

In contrast with Pd, at room temperature, rhodium bulk absorbs hydrogen and forms a hydride at pressures above 40 kbar of H_2 [44–46]. The absorption of H_2 in Rh bulk is an endothermic reaction (ΔH = 17 kJ/mol [45]) and it has been demonstrated that the decrease in particle size leads to a change in the thermodynamic properties. In fact, the reduction of the Rh nanoparticle size from 10 nm to 7 nm transforms the H_2 absorption reaction from

endothermic to exothermic [47]. This change in thermodynamic properties has been explained by a change in the electronic state by decreasing the particle size[44,48].

An important size effect was also observed in the interaction of rhodium with hydrogen. It has been demonstrated by Kobayashi *et al.*[44] that by reducing the particle size below 10 nm, Rh absorbs hydrogen at room temperature and under 1 bar of H_2. Furthermore, the absorption of hydrogen by Rh nanoparticles with a size between 10 and 3 nm is accompanied by formation of solid solutions of Rh with hydrogen with a low ratio H/Rh (~ 0.1) [44]. However, it has been reported by Zlotea *et al.* that for sizes ≤ 2.3 nm, the Rh hydride is stabilized, at ambient temperature and under 1 bar H_2, with a fairly high H/Rh ratio (~ 0.4) [49]. *Figure 1.15* shows this nanosize effect on rhodium Pressure-Composition Isotherm curves. In fact, by decreasing the Rh particle size from bulk to 2.3 nm, the hydrogen absorption with hydride formation is observed at ambient pressure and temperature characterized by the pressure plateau at low pressure.

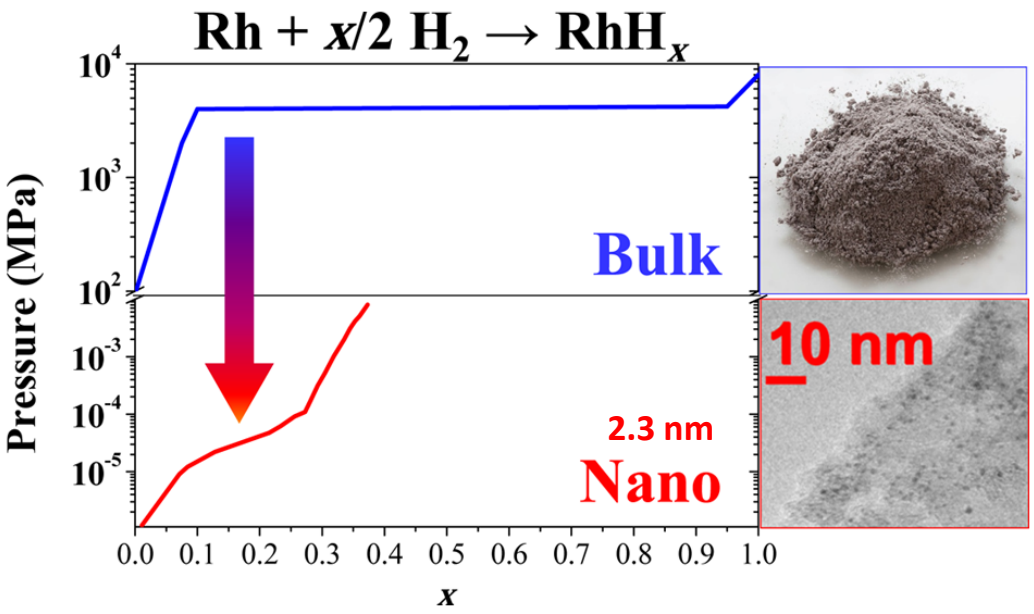

Figure 1.15: Nanosize effect on Pressure-Composition Isotherm curves for rhodium. [49]

Moreover, a strong size effect has been demonstrated for hydrogen desorption from the Rh nanosized hydride phase: the smaller the size, the lower the hydrogen desorption. Zlotea *et al.*[49] have shown, using Thermal Desorption Spectroscopy (TDS), that for RhH_x nanoparticles of 1.3 and 1.9 nm, the maximum hydrogen desorption temperature is 459 and 491 K, respectively. The same trend was also observed by Differential Scanning Calorimetry (DSC). In fact, shifts of exothermic hydrogen desorption peaks, to lower temperatures, have been

observed by reducing the size of RhH_x nanoparticles. Furthermore, the total desorption of hydrogen from the interstitial sites of the Rh hydride phase is observed along with a shrinkage of the *fcc* lattice, characterized by a small contraction of the R_{Rh-Rh}, as noticed with 1.4 nm Rh nanoparticles with X Ray Absorption Spectroscopy (XAS) [50].

In summary, nanosize effect on Pd is well-documented and understood whereas, for Rh, contradictory results are reported for the change of thermodynamics. However, they all agree to an increase of H sorption capacity and a decrease of equilibrium pressure at ~ 1 bar at room temperature with decreasing Rh nanoparticles size.

References

1. Zlotea, C. & Latroche, M. Role of nanoconfinement on hydrogen sorption properties of metal nanoparticles hybrids. *Colloids and Surfaces A: Physicochemical and Engineering Aspects* **439**, 117–130 (2013).
2. Zuttel, A., Remhof, A., Borgschulte, A. & Friedrichs, O. Hydrogen: the future energy carrier. *Philosophical Transactions of the Royal Society A: Mathematical, Physical and Engineering Sciences* **368**, 3329–3342 (2010).
3. Eberle, U., Felderhoff, M. & Schüth, F. Chemical and Physical Solutions for Hydrogen Storage. *Angewandte Chemie International Edition* **48**, 6608–6630 (2009).
4. Schlapbach, L. & Züttel, A. Hydrogen-storage materials for mobile applications. *Nature* **414**, 353–358 (2001).
5. Jongh, P. E. de, Allendorf, M., Vajo, J. J. & Zlotea, C. Nanoconfined light metal hydrides for reversible hydrogen storage. *MRS Bulletin* **38**, 488–494 (2013).
6. European Commission & Directorate General for Research. *World energy technology outlook (WETO H2)*. (EUR-OP, 2006).
7. Lavoisier, A.-L. de (1743-1794) A. du texte *et al. Méthode de nomenclature chimique , proposée par MM. de Morveau, Lavoisier, Bertholet & de Fourcroy. On y a joint un nouveau système de caractères chimiques, adaptés à cette nomenclature, par MM. Hassenfratz et Adet*. (1787).
8. Marbán, G. & Valdés-Solís, T. Towards the hydrogen economy? *International Journal of Hydrogen Energy* **32**, 1625–1637 (2007).
9. Haessig, T., Alleau, T. & Haessig, T. *L'hydrogène, énergie du futur ? / Thierry Alleau*. (EDP Sciences. Les Ulis, 2007).
10. Puiu, T. New electrolysis system produces hydrogen 30 times faster. *ZME Science* (2014).
11. Steinberg, M. Hydrogen Production from Fossil Fuels. 5
12. *18th World Hydrogen Energy Conference 2010 - WHEC 2010: proceedings. 3 part 2: Hydrogen production technologies Parallel sessions book*. (Forschungszentrum, IEF-3, 2010).
13. O'Brien, J. E. Large Scale Hydrogen Production From Nuclear Energy Using High Temperature Electrolysis. in *2010 14th International Heat Transfer Conference, Volume 8* 287–308 (ASME, 2010). doi:10.1115/IHTC14-23341

14. Müller, S., Stidl, M., Pröll, T., Rauch, R. & Hofbauer, H. Hydrogen from biomass: large-scale hydrogen production based on a dual fluidized bed steam gasification system. *Biomass Conv. Bioref.* **1**, 55–61 (2011).
15. Sharma, A. & Arya, S. K. Hydrogen from algal biomass: A review of production process. *Biotechnol Rep (Amst)* **15**, 63–69 (2017).
16. Leridon, H. Chaire Développement durable – environnement, énergie et société: Année académique 2008-2009. *La lettre du Collège de France* 9 (2009). doi:10.4000/lettre-cdf.501
17. Fayaz, H. *et al.* An overview of hydrogen as a vehicle fuel. *Renewable and Sustainable Energy Reviews* **16**, 5511–5528 (2012).
18. Office of Energy Efficiency & Renewable Energy. *Energy.gov* Available at: https://www.energy.gov/eere/office-energy-efficiency-renewable-energy. (Accessed: 4th March 2019)
19. Typy lahví. *Linde Industrial Gases* Available at: //www.linde-gas.sk/en/products_and_supply/cylinder_types/index.html. (Accessed: 5th March 2019)
20. Demirocak, D. E. Hydrogen Storage Technologies. in *Nanostructured Materials for Next-Generation Energy Storage and Conversion: Hydrogen Production, Storage, and Utilization* (eds. Chen, Y.-P., Bashir, S. & Liu, J. L.) 117–142 (Springer Berlin Heidelberg, 2017). doi:10.1007/978-3-662-53514-1_4
21. Ag, L. Modell des CooLH2 Fahrzeugtanks. 1
22. Song, C. *et al.* Using metal hydride H2 storage in mobile fuel cell equipment: Design and predicted performance of a metal hydride fuel cell mobile light. *International Journal of Hydrogen Energy* **39**, 14896–14911 (2014).
23. Zlotea, C. Nanosciences pour l'Energie. *EDP Sciences*
24. Jia, Y. *et al.* Combination of nanosizing and interfacial effect: Future perspective for designing Mg-based nanomaterials for hydrogen storage. *Renewable and Sustainable Energy Reviews* **44**, 289–303 (2015).
25. Technical System Targets: Onboard Hydrogen Storage for Light-Duty Fuel Cell Vehicles.
26. von Helmolt, R. & Eberle, U. Fuel cell vehicles: Status 2007. *Journal of Power Sources* **165**, 833–843 (2007).
27. Rouquerol, F., Rouquerol, J. & Sing, K. S. W. *Adsorption by powders and porous solids: principles, methodology, and applications*. (Academic Press, 1999).

28. Moghadam, P. Z. *et al.* Development of a Cambridge Structural Database Subset: A Collection of Metal–Organic Frameworks for Past, Present, and Future. *Chem. Mater.* **29**, 2618–2625 (2017).
29. Farha, O. K. *et al.* De novo synthesis of a metal–organic framework material featuring ultrahigh surface area and gas storage capacities. *Nature Chemistry* **2**, 944–948 (2010).
30. Sumby, C. MOF the chart: why a record-breaking surface area matters. *The Conversation* Available at: http://theconversation.com/mof-the-chart-why-a-record-breaking-surface-area-matters-9915. (Accessed: 5th March 2019)
31. Férey, G. *et al.* A Chromium Terephthalate-Based Solid with Unusually Large Pore Volumes and Surface Area. *Science* **309**, 2040–2042 (2005).
32. Zhao, Z. *et al.* Graphene-wrapped chromium-MOF(MIL-101)/sulfur composite for performance improvement of high-rate rechargeable Li–S batteries. *J. Mater. Chem. A* **2**, 13509–13512 (2014).
33. Shahi, R. R., Raghubanshi, H., Shaz, M. A. & Srivastava, O. N. Studies on the de/re-hydrogenation characteristics of nanocrystalline MgH2 admixed with carbon nanofibres. *Appl Nanosci* **2**, 195–201 (2012).
34. Li, W., Li, C., Ma, H. & Chen, J. Magnesium Nanowires: Enhanced Kinetics for Hydrogen Absorption and Desorption. *J. Am. Chem. Soc.* **129**, 6710–6711 (2007).
35. Zlotea, C. *et al.* Ultrasmall MgH2 Nanoparticles Embedded in an Ordered Microporous Carbon Exhibiting Rapid Hydrogen Sorption Kinetics. *J. Phys. Chem. C* **119**, 18091–18098 (2015).
36. Bogdanović, B. & Schwickardi, M. Ti-doped alkali metal aluminium hydrides as potential novel reversible hydrogen storage materials1Invited paper presented at the International Symposium on Metal–Hydrogen Systems, Les Diablerets, August 25–30, 1996, Switzerland.1. *Journal of Alloys and Compounds* **253–254**, 1–9 (1997).
37. Manchester, F. D., San-Martin, A. & Pitre, J. M. The H-Pd (hydrogen-palladium) System. *JPE* **15**, 62–83 (1994).
38. Frieske, H. & Wicke, E. Magnetic Susceptibility and Equilibrium Diagram of PdHn. *Berichte der Bunsengesellschaft für physikalische Chemie* **77**, 48–52 (1973).
39. Yamauchi, M., Ikeda, R., Kitagawa, H. & Takata, M. Nanosize Effects on Hydrogen Storage in Palladium. *The Journal of Physical Chemistry C* **112**, 3294–3299 (2008).
40. Narehood, D. G. *et al.* X-ray diffraction and H-storage in ultra-small palladium particles. *International Journal of Hydrogen Energy* **34**, 952–960 (2009).
41. Pundt, A. Hydrogen in Nano-sized Metals. *Adv. Eng. Mater.* **6**, 11–21 (2004).

42. Eastman, J. A., Thompson, L. J. & Kestel, B. J. Narrowing of the palladium-hydrogen miscibility gap in nanocrystalline palladium. *Phys. Rev. B* **48**, 84–92 (1993).
43. Langhammer, C., Zhdanov, V., Zoric, I. & Kasemo, B. H. Size-Dependent Kinetics of Hydriding and Dehydriding of Pd Nanoparticles. *Physical Review Letters* **104**, (2010).
44. Kobayashi, H. *et al.* Nanosize-Induced Hydrogen Storage and Capacity Control in a Non-Hydride-Forming Element: Rhodium. (2011). doi:10.1021/ja2027772
45. Tkacz, M. High pressure studies of the rhodium–hydrogen system in diamond anvil cell. 2084–2087 (1998). doi:https://doi.org/10.1063/1.475587
46. Driessen, A., Sanger, P., Hemmes, H. & Griessen, R. Metal hydride formation at pressures up to 1 Mbar. *J. Phys.: Condens. Matter* **2**, 9797–9814 (1990).
47. Kusada, K., Kobayashi, H., Ikeda, R., Morita, H. & Kitagawa, H. Changeover of the Thermodynamic Behavior for Hydrogen Storage in Rh with Increasing Nanoparticle Size. *Chem. Lett.* **42**, 55–56 (2012).
48. *Hydrogen in Metals I: Basic Properties*. (Springer-Verlag, 1978).
49. Zlotea, C. *et al.* First Evidence of Rh Nano-Hydride Formation at Low Pressure. *Nano Letters* **15**, 4752–4757 (2015).
50. Zlotea, C. *et al.* Investigation of the local structure of nanosized rhodium hydride. *Journal of Colloid and Interface Science* **524**, 427–433 (2018).

CHAPTER II

MATERIALS AND METHODS

2.1 Synthesis

2.1.1 MIL-101(Cr)

The MIL-101(Cr) synthesis consists initially in the solvothermal reaction of terephthalic acid with chromium (III) nitrate, fluorhydric acid (HF), and water, at 493 K for 8 hours. A highly crystallized green powder of the chromium terephthalate is then produced with formula $Cr_3F(H_2O)_2O[(O_2C)\text{-}C_6H_4\text{-}(CO_2)]_3.nH_2O$ (with *n* is ~25).[1]

In this project, the synthesis of two batches of MIL-101(Cr) was performed by our Romanian partner (NIRDIMT) following a green synthetic path[2]. Indeed, terephthalic acid (2.505 g) and $CrCl_3.6H_2O$ (4.02 g) dissolved in water (120 mL) was mixed without the use of dangerous substances, *i.e* fluorhydric acid which is replaced by chlorhydric acid (HCl). The reactants were loaded into a TFE pot which was placed in a stainless-steel autoclave. Then, the autoclave was placed in an electric oven and heated at 493 and 463 K for 20 and 4 hours for the first and second batch, respectively. After cooling, the resulting solid (green) was filtered through a fritted funnel to remove the unreacted terephthalic acid. Then the crude MIL-101 was isolated by successive filtration filter paper (12-15 µm) and then dried at 433 K. The as-synthesized MIL-101(Cr) was then activated by heating it in ethanol under reflux for 24 and 72 hours for the first and the second batch, respectively. The activated samples were then filtered and dried at 423 K for 10 hours.

2.1.2 Nanoparticles confinement

The insertion of metal nanoparticles, with different loading rates, within the MIL-101(Cr) pores can be carried out by various techniques reported in the literature such as, metal-organic chemical vapor deposition (MOCVD) [3–12], sol-gel [13–18], one-pot [19–22] or liquid impregnation [22–104]. *Table 2.1* lists the composites of Pd@MIL-101(Cr) synthesized by the different techniques as reported in the literature. The different Pd@MIL-101(Cr) composites were synthesized with metal loadings between 0.1 and 57.5 wt%. The average particle size varies between 1.5 and 9.2 nm and sometimes with the formation of aggregates. The smallest particle size (1.5 nm) corresponds to a composite doped with 1 wt% of Pd.

In this project, the synthesis of the different composites was carried out by a bottom-up method starting by the impregnation of the MIL-101(Cr) by precursor solutions followed by the reduction of the metal ions to allow the nucleation and the growth of the nanoparticles within the MOFs pores. The impregnation method was chosen to synthesize the desired

composites due to its relative simplicity to implement and the mastery of the technique by our laboratory.

Table 2.1: Summary of the reported Pd@MIL-101(Cr) composites.

Metal loading (wt. %)	**NP size (nm)**	**Preparation method, precursor (solvent)**	**Application**	**Ref**
1	1.5	Liquid Impregnation	Catalysis	[100]
4.9	2 - 3	Liquid Impregnation	Catalysis	[24]
0.1 - 0.9	2.5 - 4.2	Liquid Impregnation	Catalysis	[101]
1	1.9 ± 0.7	Liquid Impregnation	Catalysis	[25]
0.5	2.6 ± 0.5	Liquid Impregnation	Catalysis	[26]
9.3 - 57.5	1.7 - 11	Metal-Organic Chemical Vapor Deposition	Catalysis	[3]
3	2.1	Liquid Impregnation	Catalysis	[102]
20	2 - 3	Metal-Organic Chemical Vapor Deposition	Catalysis	[4]
4.9	2.5 ± 0.5	Liquid Impregnation	Catalysis	[103]
15	2 - 3.5	Metal-Organic Chemical Vapor Deposition	Catalysis	[5]
0.35	2.5 ± 0.5	Sol-Gel	Catalysis	[15]
2	2 - 3	Liquid Impregnation	Catalysis	[29]
4	1.8 ± 0.4	Liquid Impregnation	Catalysis	[30]
3 5	2.9 ± 0.8 Aggregation	Sol-Gel	Hydrogen storage	[13]
7.7	2 - 3	Liquid Impregnation	Hydrogen storage	[31]
2	1.8 - 5	Double Solvent Impregnation	Catalysis	[32]
0.5 4.1	2 - 3.5 4 <	Sol-Gel	Catalysis	[14]
0.4 - 1.8	6.5 - 9.2	Metal-Organic Chemical Vapor Deposition	Catalysis	[6]
27.5	6.28	Liquid Impregnation	Hydrogen storage	[19]
2	2.1 ± 0.6	Double Solvent Impregnation	Catalysis	[34]
-	2.7 ± 0.4	Liquid Impregnation	Catalysis	[35]
2.7	2.4	Double Solvent Impregnation	Catalysis	[36]
Up to 1	2.6 - 2.9	Double Solvent Impregnation	Catalysis	[37]
Up to 20	1	Double Solvent Impregnation	Hydrogen storage	[38]
Up to 6	2 - 3	Liquid Impregnation	Catalysis	[104]
0.9	2.5	Double Solvent Impregnation	Catalysis	[39]
1.5	3.3	Liquid Impregnation	Catalysis	[40]
2.5	2 - 3	Liquid Impregnation	Catalysis	[41]
3.3	1.8	Liquid Impregnation	Catalysis	[42]
1	-	Sol-Gel	Catalysis	[16]

Two impregnation methods were carried out: Liquid Impregnation[19,23–31,35,40–42,101,104] and Double Solvent Impregnation or Double Solvent Method (DSM)[32,34,36–39,97–99].

2.1.2.1 Liquid Impregnation (LI)

The synthetic method consists in impregnating MOFs with aqueous solutions of metal salts with corresponding metals amount to the targeted content of the final mass of the composite. A mass of an adsorbent was weighed and a volume of the precursor solution, corresponding to the desired metal content, was added. The mixture was stirred with constant magnetic stirring and the temperature was raised to 333 K to allow the water evaporation. The recovered solid was then dried at 333 K in air overnight.

2.1.2.2 Double Solvent Method (DSM)

In order to avoid metal nanoparticles aggregation on external surfaces of MOFs, the double solvent method was preferred. To remove the water molecules adsorbed on the surface and in the pores of MIL-101(Cr), a degassing step of the MOF at 493 K for 18 hours must be carried out before each synthesis and then handled without exposure to air. Then, the synthesis consists of the use of a mixture of a hydrophilic solvent (water), containing the metal precursor with a volume set equal or less than the pore volume of the adsorbent, and a hydrophobic excess solvent (pentane or hexane), playing an important role to suspend the adsorbent and facilitate the impregnation process. First, the freshly degassed 150 mg of MIL-101(Cr) is suspended in 30 mL of pentane in an ultrasonic bath for 20 minutes followed by 30 minutes of magnetic stirring. Then, a volume of the metal precursor solution, slightly less than the total pore volume of MIL-101(Cr), is added. The mixture was then stirred, in a beaker covered by a parafilm, under vigorous magnetic stirring (750 rpm) for 4 hours at room temperature. This step is very important because it will allow the good dispersion of the precursor solution within the MIL-101(Cr) pores. The total solvents evaporation is then carried out at room temperature by removing the parafilm and maintaining the magnetic stirring at 250 rpm. The recovered solid was dried at 343 K in an oven overnight. A schematic illustration of the synthesis method is represented in *figure 2.1*.

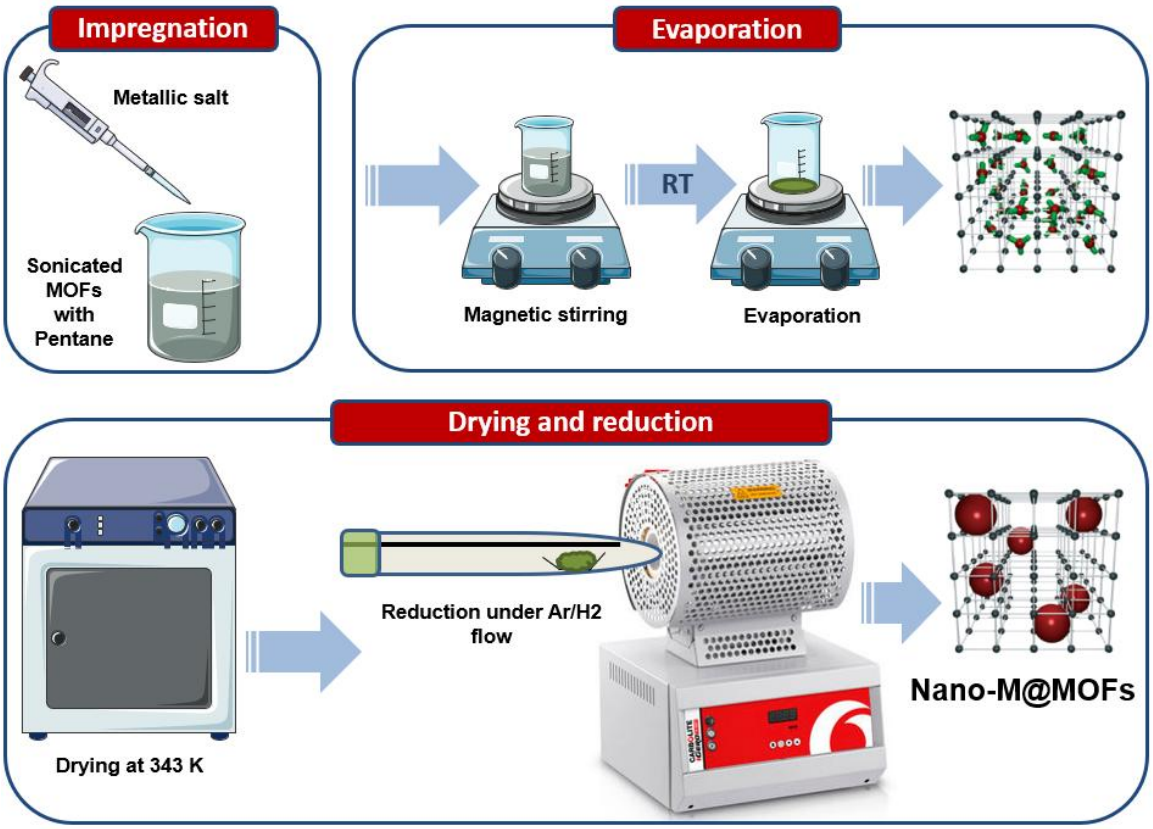

Figure 2.1: Schematic illustration of the M@MOFs synthesis.

Finally, the recovered powders after both methods are subsequently reduced under Ar/H_2 flow (0.5 L/min) at 573 K for 15 min [38]. A chemical reduction way has been also tried using $NaBH_4$. The composites were named *x-M*@MIL-101(Cr) where *x* (5, 10, 15, 20 wt.%) stands for the metal content over the entire sample mass. The optimization of the synthetic method was performed for each doping metal and discussed separately in each chapter.

2.2 Characterization

2.2.1 Physicochemical characterization

2.2.1.1 Powder X-Ray Diffraction analyses

A crystal is an organized structure formed by atoms. It is then possible to define a repeating pattern of this arrangement of atoms. The set of all nodes obtained by paving the crystallographic structure is called a network. If the network is three-dimensional, then it is possible to describe it by families of planes parallel to each other. The interplanar distance is the smallest distance between two planes of the same family. A property of electromagnetic waves is their ability to diffract when they encounter an optical network. Bragg has established a relationship between the angle of incidence of a wave, the wavelength and the interplanar distance. The diffraction condition given by the Bragg law (*figure 2.2*) is then written:

$$n\lambda = 2d\sin\theta. \qquad \textbf{(Equation 2.1)}$$

with ***d*** the interplanar distance, θ the angle between the grating surface and the incident ray ($\pi/2$-angle of incidence), and ***n*** the diffraction order. λ is the wavelength of the incident wave. θ being between 0 and $\pi/2$, the maximum value of $\sin(\theta)$ is therefore 1. For example, in the case of visible light, the minimizing wavelength d is then about 380 nm, the minimum interplanar distance for the diffraction of the visible light is then 190 nm, which is much too important regarding the known interplanar distances of the crystals, which are of the order of the angstrom. In a simplified manner, it can be noted that the diffraction condition on a network is as follows:

$$\lambda_{incident\,wave} \sim d. \qquad \textbf{(Equation 2.2)}$$

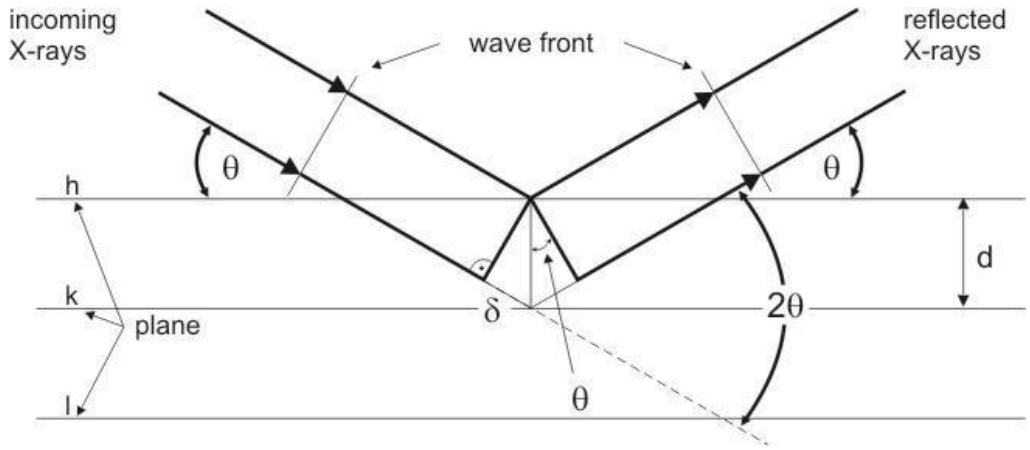

Figure 2.2: Bragg reflection for X-ray diffraction.

X-rays have the advantage of having wavelengths between 0.01 nm and 10 nm. This allows them to diffract on all the crystals. In this work, the diffractometer used is a Bruker-D8 Advance model, following the Bragg-Brentano geometry, in the 2θ range 5° to 90° at a scan rate of 1°/min (*figure 2.3*). The source used is a copper anticathode ($\lambda K_{\alpha 1}$ = 1.5406 Å) fed at 40 kV and 40 mA.

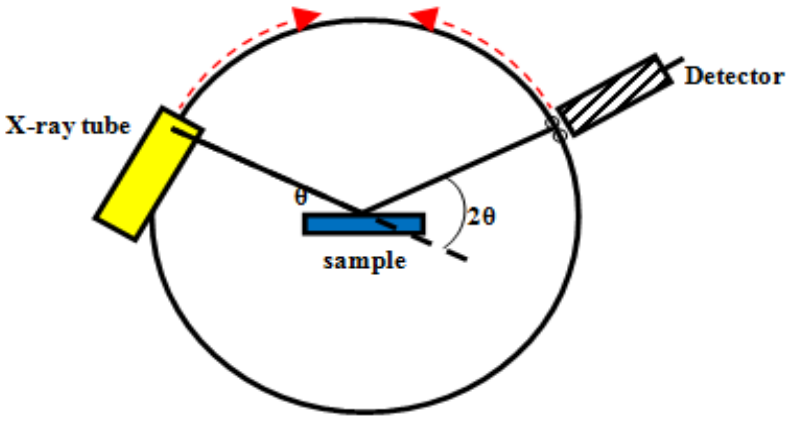

Figure 2.3: Illustration of the diffractometer (Bragg-Brentano geometry).

2.2.1.2 Scanning Electron Microscopy analyses

Scanning Electron Microscopy (SEM) is a classic technique used to observe the morphology of materials on a microscopic scale. The main use of this technique is to obtain images of the surface of the material. For this purpose, for conventional microscopes, the sample is placed in a chamber in which the vacuum is produced. In this work, scanning electron microscopy was only used to image the surface of the sample and, as such, qualitative or quantitative microanalyses were not performed using this technique. The average resolution of scanning electron microscopes is of the order of one nanometer. This last point shows that SEM images have the main utility of describing morphology rather than microstructure. A schematic illustration of a SEM is shown in *figure 2.4*.

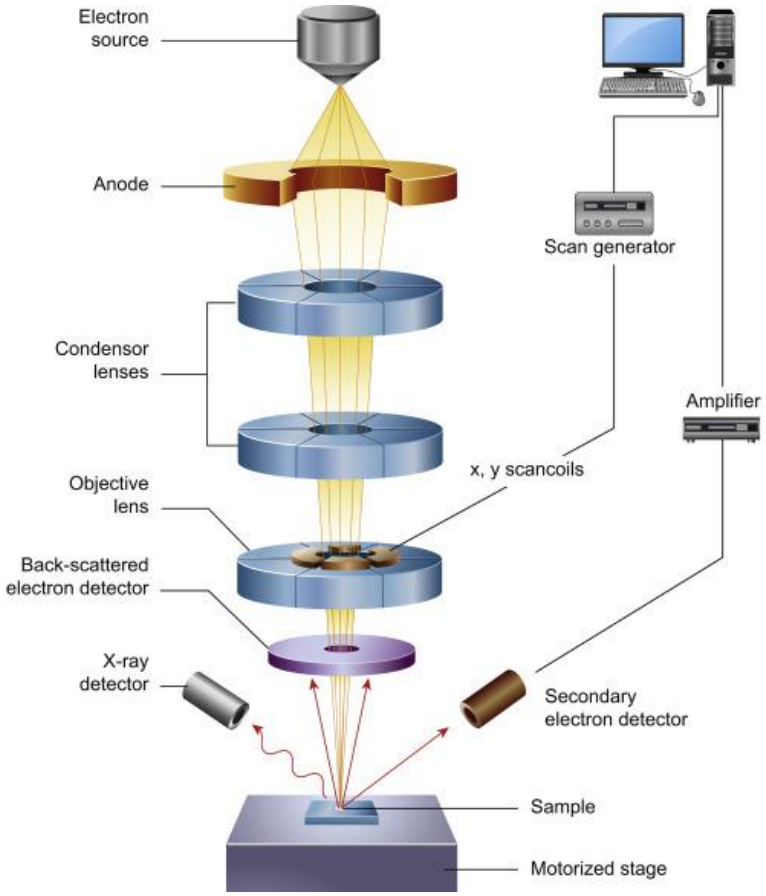

Figure 2.4: Schematic diagram of a Scanning Electron Microscope.[105]

Electrons are generated using a cathode. This can be thermionic (Tungsten filament or lanthanum hexaboride tip: LaB6) or field effect. Before interacting with the sample, the electrons are accelerated using a potential difference between the electron source and the anode. A system of magnetic lenses then allows the reduction, focusing of the electron beam on the sample and the correction of aberrations. The beam is finally brought to scan the surface of the sample through a system of coils.

The interaction of the electron beam with the sample produces secondary electrons, backscattered electrons, Auger electrons, X-rays, and visible light. For simple imaging purposes, only secondary electrons are used. These are detected using a detector with a Faraday cage to guide the electrons in the center of the detector. In this project, the SEM images were carried out at the NIRDIMT (Cluj-Napoca, Romania).

2.2.1.3 Transmission Electron Microscopy, Energy-dispersive X-Ray spectroscopy

Transmission Electron Microscopy (TEM) is used to characterize much finer samples and uses much higher voltages than those used for other microscopies such as scanning electron microscopy. The maximum acceleration voltages used in transmission electron microscopy range from 200 to 300 KV. TEM have the advantage of having resolutions much higher than those of SEM. The most recent models make it possible to distinguish the microstructure of the materials up to the scale of the atom and therefore have lower resolutions than the angstrom. The morphology of a TEM is shown in *figure 2.5*.

The image is then formed in the image space which is geometrically downstream of the sample. The radiation-matter interaction is identical to that occurring in a SEM. Nevertheless, the electrons passing through the sample can be either electrons transmitted or diffracted (elastic diffusion) or even diffused inelastically. The transmitted electrons are used for conventional TEM imaging in bright field. In this case, the areas with low electron density appear in the clear while the others are dark. The diffracted electrons are used to perform electron diffraction or dark field imaging during which one or more diffracted beams are selected. In this case, only the diffracting elements appear in the clear. This is dark field imaging. Finally, the inelastically scattered electrons make it possible to perform energy loss spectroscopy. The latter is a powerful tool allowing, in the case of a very small energy resolution, to identify the chemical nature of the elements. In addition, the X-ray photons emitted by de-excitation of the electronic cortege of the atoms of which a core electron has been ejected under the electronic impact give qualitative and quantitative chemical information of the target atom (EDS analysis: Energy Dispersive Spectroscopy). EDS analysis makes it possible to determine the composition and distribution of the chemical elements in the analyzed sample. Depending on the mode chosen, it is possible to carry out an elemental analysis at a precise point (on a volume of about 1 μm^3) or on average on a surface, to form a concentration profile over a given distance or to carry out elementary mapping of a surface.

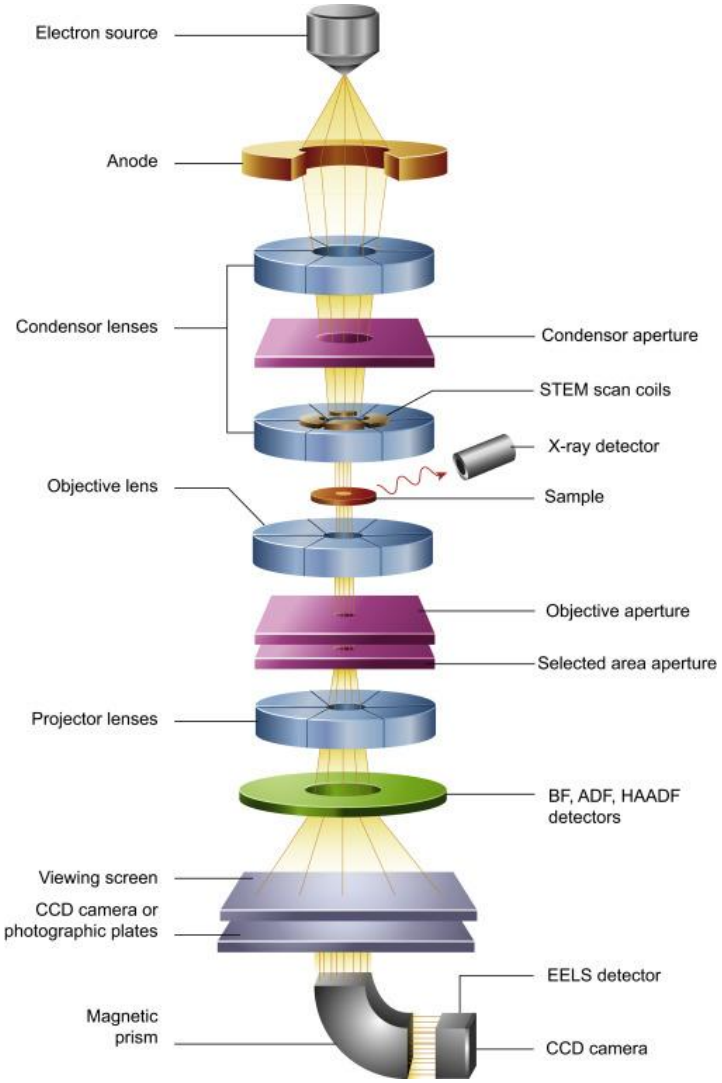

Figure 2.5: Schematic diagram of a transmission electron microscope. [105]

In the case of metal-organic frameworks composites, the materials are in the form of powders. Nevertheless, the deposition of the powder *via* an ethanol suspension on a sample holder grid allows the observation of the MOF grains. When these grains are of too large sizes to be crossed by the electron beam, they must be observed at their edges or, if they are small enough, can be observed in transmission over their entire surface. For nanoparticles confined within MOF pores, the first observable characteristic is the average size of the nanoparticles which was determined by counting manually the nanoparticle sizes from several TEM images using the ImageJ® software. Then, statistical analyzes of these nanoparticles made it possible to trace the size histograms of particle size and to propose an average size of the nanoparticles.

2.2.1.4 Specific surface area & total pore volume

Porous materials are mainly characterized by their textures. The texture is the set of geometric parameters describing the porosity of the materials (shape, size, and volumes occupied by the different pores in a material). The specific surface area of powder is estimated after degassing, by adsorption of a gas by Van der Waals binding in the open pore of the sample. In practice, the materials are characterized after the adsorption of N_2 at its normal liquefaction temperature (77 K). The physical adsorption isotherms obtained experimentally illustrates the amount adsorbed as a function of the equilibrium relative pressure P/P_0 (the ratio of the equilibrium pressure of the adsorbate gas and its saturation vapor pressure). Eight possible types of isotherms are represented in *figure 2.6* as classified by IUPAC.

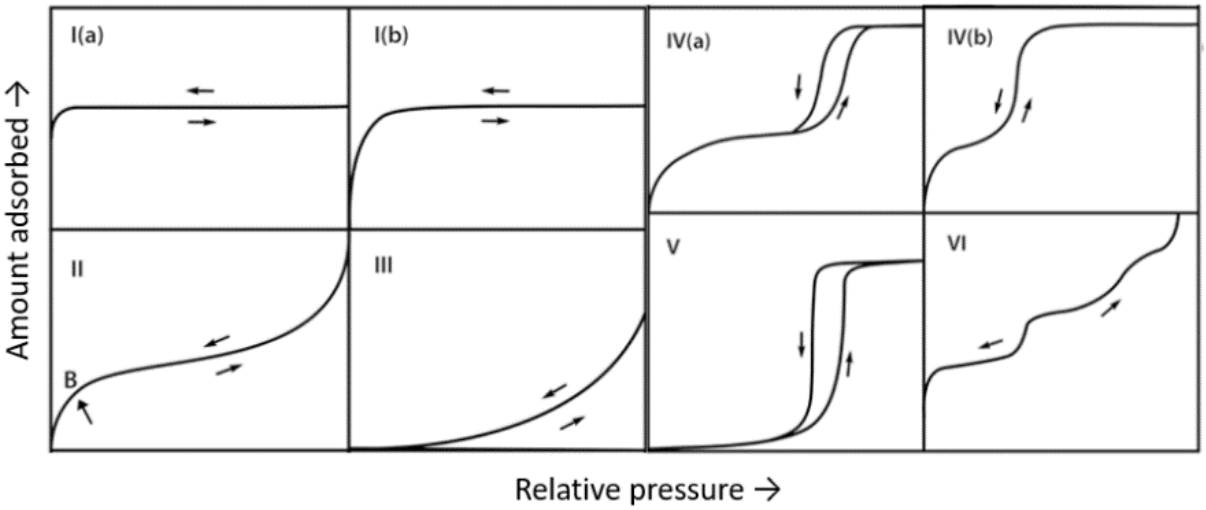

Figure 2.6: Types of physisorption isotherms upon IUPAC. [106]

Type I(a): monolayer physisorption → microporous materials with filled micropores (< ~ 1 nm);

Type I(b): monolayer physisorption → microporous materials with possibly narrow mesopores (< ~ 2.5 nm);

Type II: multilayer physisorption without capillary condensation → non-porous or macroporous materials;

Type IV(a): multimolecular physisorption → mesoporous materials in which capillary condensation takes place. The desorption of condensed nitrogen by capillarity in the mesopores is not reversible: hysteresis is generally observed between desorption and adsorption.

Type IV(b): multimolecular physisorption → mesoporous materials with conical and cylindrical mesopores closed at the tapered end.

Type III, type V: rare, very unusual convex curvature, different from types II and IV at low pressures, because of weak adsorbent/adsorbate interactions (e.g., water vapor adsorption by a hydrophobic surface).

Type VI: stepwise multilayer → adsorption on a nonporous or non-uniform surface. The different "steps" on these isotherms correspond to the formation of a new layer of the adsorbate.

In this work, the specific surface area and total pore volume of different materials were determined from nitrogen adsorption/desorption isotherms measured at liquid nitrogen temperature (77 K) with an automated volumetric device (Autosorb IQ Quantachrome). The quantity of N_2 adsorbed on the surface of the material at 77 K is measured by performing successive doses of nitrogen gas by the volumetric method. From the amount of N_2 adsorbed by the material measured for each relative pressure value P/P_0, it is possible to calculate the specific surface area as well as the total pore volume (for a relative pressure P/P_0=0.95). The results obtained are exploited, according to equation 3 established by Brunauer, Emmet, and Teller (BET method)[107].

$$\frac{1}{n[{}^{P_0}/_{P}-1]} = \frac{1}{n_m C} + \frac{C-1}{n_m C}\left(\frac{P}{P_0}\right) \qquad \textbf{(Equation 2.3)}$$

In this equation, $\boldsymbol{n}$ represents the quantity of the gas adsorbed at the relative pressure P/P_0 and $\boldsymbol{n_m}$ the quantity of the adsorbate (N_2) forming a complete monolayer. The term $\boldsymbol{C}$ is the BET constant which is related to the adsorption energy of the first layer E_1, to the liquefaction energy of the adsorbate E_L, to the temperature T of the adsorption and to the molar constant of the gases R according to the relation:

$$\boldsymbol{C = exp}\left(\frac{E_1 - E_L}{RT}\right). \qquad \textbf{(Equation 2.4)}$$

The main hypotheses considered in the BET theory:

i) the surface of the adsorbent can be covered with 1, 2, …, i adsorbate layers (multimolecular adsorption),

ii) from the second layer, the adsorption energy E_2 is equal to the liquefaction energy E_L,

iii) there is only one type of independent adsorption site and there is no interaction between the adsorbed molecules (Langmuir's basic assumptions).

By mathematical processing, the value of the S_{BET} surface area is accessed. When the surface A of the solid is completely covered with a layer of adsorbed molecules, the value of this is easily calculated from $\boldsymbol{n_m}$ (number of gas molecules adsorbed in a complete monolayer)

and $\boldsymbol{\sigma_m}$ (the area occupied by a molecule adsorbed on the surface of the solid covered with a monomolecular layer ($\boldsymbol{\sigma_m}$= 0.16257 nm^2 for the N_2)).

2.2.1.5 X-Ray Absorption Spectroscopy

X-ray absorption spectroscopy consists of following the evolution of the absorption coefficient ($\boldsymbol{\mu}$) of a sample as a function of the energy of the incident beam. The energy scanning is performed near to an absorption edge of the studied atom. When the ionization energy is reached, a core electron is ejected towards the continuum and is called a photoelectron, resulting in a sharp increase in the absorption coefficient[108].

The Beer-Lambert law allows expressing the intensity transmitted through the sample according to the incident intensity and the absorption coefficient:

$$\boldsymbol{I = I_0\, e^{-\mu(E)x}}. \qquad \textbf{(Equation 2.5)}$$

where *x* is the sample thickness.

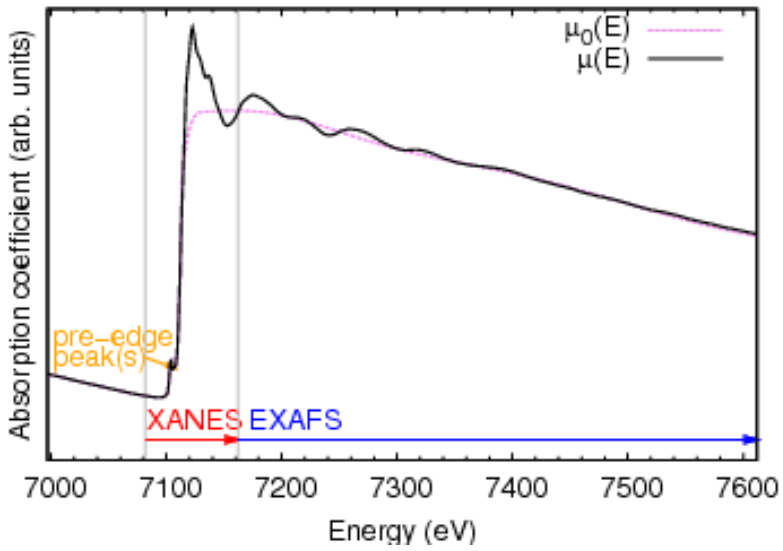

Figure 2.7: Representation of an absorption spectrum and absorption modeling. [109]

In the absorption spectrum (*figure 2.7*), three domains are distinguished: the pre-edge, the edge (X-ray Absorption Near Edge Structure "XANES") and the Extended X-Ray Absorption Fine Structure "EXAFS", which is the oscillatory component of the absorption spectrum[109].

Oscillations after the edge are related to the wave character of the emitted photoelectron. Indeed, the emitted photoelectron can be associated with a wave that propagates in the material and can be diffused by the surrounding atoms. After

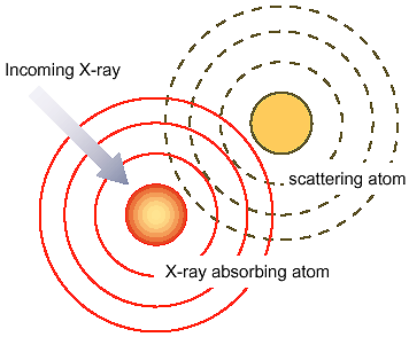

Figure 2.8: Interference of outgoing and backscattered photoelectron wave.

diffusion, there is interference[109] between the outgoing electronic wave of the central atom and those backscattered by the neighboring atoms (*figure 2.8*). These interferences are reflected on the absorption coefficient by the presence of oscillations which extend about 1000 eV after the edge. These oscillations are at the origin of the EXAFS signal. The EXAFS signal is written[108]:

$$(E) = \frac{\mu(E)-\mu 1(E)}{\Delta\mu(E_0)} \text{ with } \Delta\mu(E_0) = \mu_1(E) - \mu_0(E). \qquad \textbf{(Equation 2.6)}$$

Where: μ is the absorbance of the sample, μ_0 and μ_1 the absorbance that a single atom would have in space (atomic absorption) before and after the edge.

The EXAFS spectrum is interpreted using diffusion paths that can be of two types: single or multiple depending on the number of scattering atoms. They are characterized by their order, which corresponds to the number of steps necessary for the photoelectron to return to the absorbing atom. In the case of simple diffusion, the order is equal to two (only one diffusing atom), and in that of the multiple diffusion, it is greater than or equal to three (at least two diffusing atoms) (*figure 2.9*). The sum of the contributions of these different paths is considered in the expression of the standard EXAFS formula[108]. It is obtained by considering the propagation of the photoelectron between the atoms, the diffusion by the neighboring atoms, the inelastic losses as well as the effects of static and dynamic disorder for all the paths[109]:

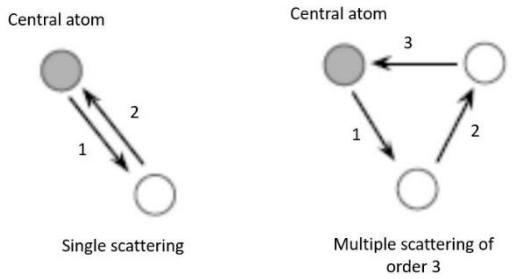

Figure 2.9: Diffusion of the wave by neighboring atoms (single and multiple diffusion).

$$k\chi(k) = -S_0^2 \Sigma[\frac{Ni}{R_i^2} |f_i(\pi,k,R)| e^{(-2\sigma^2 k2)} e^{(-2(Ri/\lambda(k)))} \sin(2kR_i + 2\partial_1(k) + \psi_i(k))] \qquad \textbf{(Equation 2.7)}$$

With: $k = \sqrt{\frac{2m_e}{\hbar^2}(h\upsilon - E_0)}$

where: k: the photoelectron wave vector, S_0: the electronic reduction factor (it considers the multielectronic effects), i: diffusion path index, N_i: the number of equivalent paths. In the case of simple diffusion, it is equal to the number of neighboring atoms located at the distance R_i of the central atom. σ is the Debye-Waller factor (accounts for the attenuation of the signal due to the disorder resulting in part from the thermal agitation), $\lambda(k)$: the mean free path of the ejected electron, it reports the photoelectron absorption, δ_1: phase shift related to the central

atom. f_i and ψ_i represent the amplitudes and the phases of diffusion by the neighboring atoms.

The local structure of Palladium and Rhodium clusters was investigated by X-ray absorption spectroscopy (XAS) in transmission mode on ROCK beamline at the SOLEIL synchrotron. The X-ray absorption spectra at the K edges of Pd (24350 eV) and Rh (23229.5 eV) was measured under H_2 and He flows (15 mL/min) at 300 K. Bulk Pd and Rh were also measured and used as a reference. The powder sample was placed inside the Lytle-type cell which was connected to a gas distribution system that allows careful control of the gas flow at atmospheric pressure[110]. The sample was pre-treated under hydrogen flow at room temperature to remove oxides at the surface of Pd and Rh nanoparticles[111]. The XAS data treatment and EXAFS refinements were performed by the help of the MAX program package (Fourier transform range 4 - 14Å^{-1} for Pd and 3 – 16Å^{-1} for Rh)[112,113]. EXAFS fit was performed on first-sphere filtered spectra. Theoretical phases and amplitudes were computed with FEFF8 on the basis of Pd and Rh metals *fcc* structure. The refined parameters are the coordination number (*N*), the Debye-Waller factor (σ^2) and the distance (R). The energy shift ΔE_0 was refined first for bulk Pd or Rh reference and then fixed for further refinements. The goodness of fit was evaluated using the quality factor (QF).

2.2.1.6 Inductively Coupled Plasma

Inductively Coupled Plasma is an analytical technique that can quantitatively measure the chemical composition of a material in a range of ppt to the weight percentage. The only elements that cannot be measured by this method are H, C, O, N and halogens. Solid samples should be dissolved, usually by acid digestion. This dissolution may optionally be assisted by microwaves or by bombs allowing a rise in temperature and high pressure. Once the sample is in solution, it is then vaporized in the core of an argon-induced plasma, which can reach temperatures of 8000 °C. At such a high temperature, any analyte undergoes atomization, ionization, and thermal excitation. It can then be detected and quantified, either with an Optical Emission Spectrometer (OES) or with a Mass Spectrometer (MS).

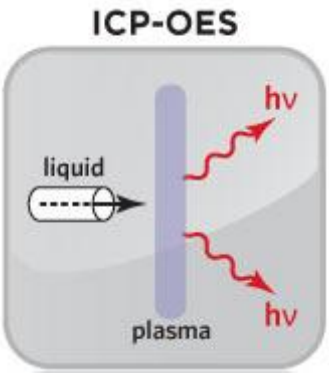

Optical Emission Spectrometry coupled with ICP (ICP-OES) is based on the thermal excitation of ions in the plasma and the analysis of the light emitted by these excited ions. Each element emits characteristic wavelengths. The

wavelengths are then separated, identified and their intensities measured by a spectrometer. The elemental concentration is then determined by comparison with external calibration.

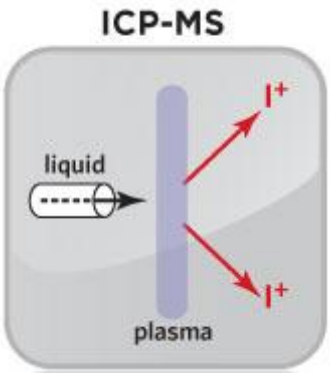

Mass spectrometry coupled with ICP (ICP-MS) relies on the separation of ions generated by argon plasma as a function of their mass-to-charge ratio *m/z*. The ions separated are then identified and counted, which allows a calculation of the elementary concentrations present in the material *via* an external calibration. Mass Spectrometry coupled with ICP offers extremely high sensitivity (and thus very low detection thresholds) for a wide range of elements.

In this work, in order to determine the metal content in the studied composites, ICP-MS was performed at NIRDIMT using an ELAN DRC-e Perkin Elmer, after calibration with a 10 µg/mL of metal in HNO_3 standard solution (Multi-element Calibration Standard 3) and digesting the samples by standard protocols in $HNO_3/HF/H_2O$.

2.2.1.7 Fourier Transform Infrared spectroscopy

Fourier transform infrared (FTIR) spectroscopy is based on infrared waves. These waves range from 12800 cm^{-1} to 10 cm^{-1} and are divided into three groups: near-infrared, mid-infrared and far-infrared. FTIR uses mean infrared ranging from 4000 cm^{-1} to 400 cm^{-1} (2.5 µm to 25 µm). When an infrared wave is sent to a molecule, the latter absorbs a part of the wave that corresponds to the bonds present in the molecule. The absorption of the infrared radiation can take place only if the wavelength corresponds to the energy associated with a particular mode of vibrations of the molecule. The instrument needs a spectrum of wavelengths between 4,000 cm^{-1} and 400 cm^{-1} because it is in this area that most organic compounds produce a single absorption spectrum. FTIR can, therefore, be considered more like a machine which gives an idea of the organic components of a sample, but which alone cannot determine the exact constitution of the sample.

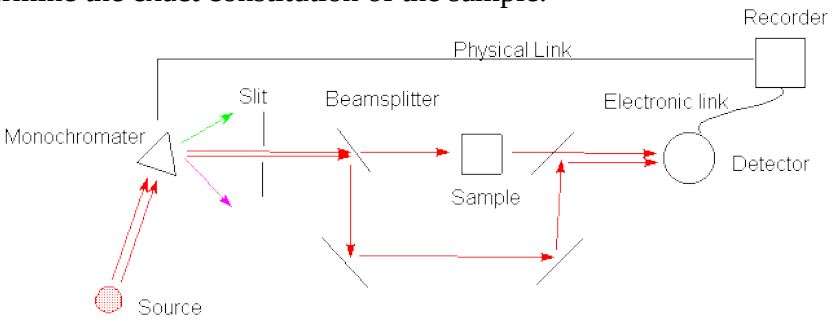

Figure 2.10: Representative scheme of the operating principle of an FTIR. [114]

The FTIR sends at the same time, two monochrome infrared waves. One passes through the sample, while the other is used as a reference. The FTIR, therefore, sends monochromatic waves of 4,000 cm^{-1} to 400 cm^{-1} and the difference in transmission between the two waves is compared (*figure 2.10*).

There are different modes of FTIR: transmission, reflection, or attenuated total reflectance (ATR). FTIR in transmission requires preparation of the sample in an infrared-transparent material: KBr pellet, NaCl cell or CIF_2, while the other modes do not require any preparation, except in some cases the sampling of part of the sample. In this work, FTIR spectroscopy studies were performed at CNR-ISC (Rome, Italy) using a Bruker Alpha FTIR apparatus in transmission mode.

2.2.1.8 Differential Thermal Analysis coupled with Thermogravimetric Analysis

Differential Thermal Analysis (DTA) is a method in which the temperature difference between a sample (T_{Sample}) and a reference material (T_{ref}) is measured as a function of time or temperature while the temperature of the sample is programmed, in a controlled atmosphere. The results obtained by DTA provide information on the production of either endothermic reactions (for melting, denaturation, dehydration, pyrolysis, etc.) or exothermic reactions (for crystallization, oxidation, polymerization, decomposition, etc.).

While, Thermogravimetric Analysis (TGA) is a method to follow the evolution of the mass of a sample depending on the heat treatment temperature. This mass variation can be either a loss (dehydration, decomposition, desorption, reduction, etc.) or a gain (adsorption, oxidation carbonation, etc.).

In this work, differential thermal analysis is coupled with thermogravimetry. The TGA-DTA coupling makes it possible to associate the mass variation with the corresponding thermal effect, *i.e* endothermic or exothermic, and to differentiate thermal effects without mass variation (fusion, transition, etc.). In addition, the use of DTA-TGA makes it possible to study the formation of bimetallic alloys confined within the MOFs pores.

The device used is the SETARAM TG-DTA SETSYS evolution type. It consists of a high-precision scale with an alumina crucible (to avoid spurious reactions), and a furnace that can reach 1600 ° C. The instrument, controlled by a computer, allows the simultaneous acquisition of the mass variation curve of the sample and the differential thermal analysis curve. The device makes it possible to work under a controlled atmosphere (Ar or air). The measurements are performed under air; the resolution is 1 µg.

2.2.2 Hydrogenation properties

2.2.2.1 Thermo-Desorption Spectroscopy

Thermo-desorption spectroscopy is used to study different molecules desorption from a material when applying a constant heating rate under high vacuum. This technique makes it possible to determine the nature of the molecules desorbed using a mass spectrometer but also different energy parameters. These desorbed molecules can originate from molecules adsorbed on the surface by weak binding forces such as Van der Wals forces as well as molecules absorbed in the volume of a material. These bonds can be destroyed by a supply of thermal energy. For an energy corresponding to the desorption activation energy of a given molecule, all these molecules will desorb by giving a peak more or less wide depending on the temperature heating rate. The shape of the peak and the area defined under this peak give access to kinetic parameters (adsorption rate, desorption rate, mean adsorption time, etc.) and energy parameters (activation desorption energies).

In this work, thermo-desorption spectroscopy was used to study the hydrogen desorption from metal hydrides. The hydrogen desorption properties were studied using a homemade instrument (*figure 2.11*) recording the H_2 partial pressure while applying a constant heating rate[115]. The gas partial pressures were followed by a quadrupole mass spectrometer (MKS Micro Vision Plus RGA) working under dynamic high vacuum (10^{-6} mbar). The temperature is monitored using a K type thermocouple in close contact with the sample. The true sample temperature is then recorded and used to plot the TDS spectra.

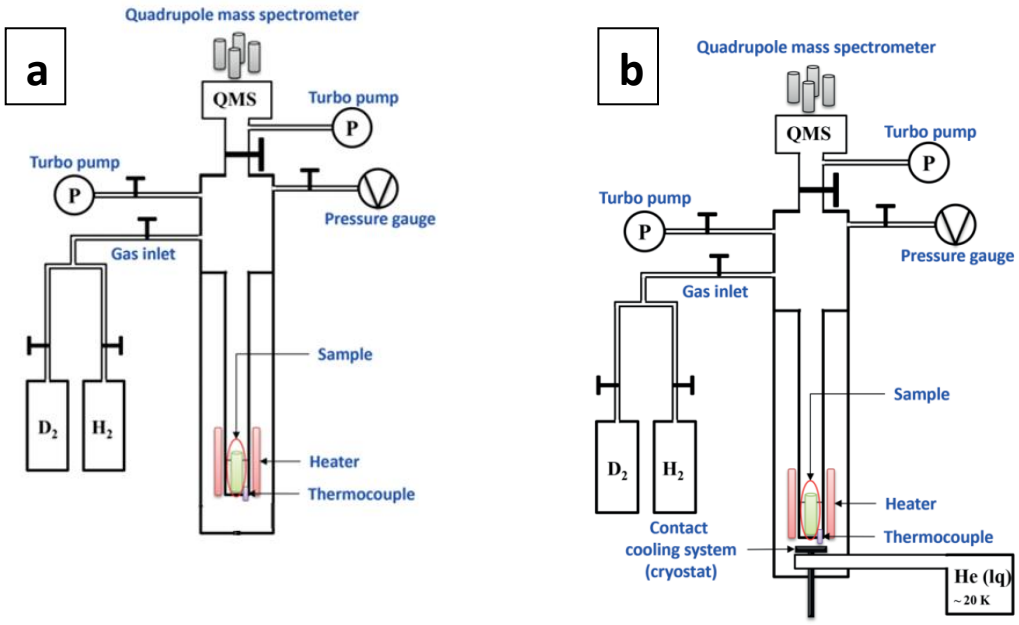

Figure 2.11: Schematic illustration of the experiment assembly of thermo-desorption spectroscopy (TDS) at (a) high and (b) low temperature.

Due to their sensitivity to air, the samples are stored and loaded in an argon glove box *via* an air-tight transfer system. Two experimental protocols have been used:

(1) Thermo-Desorption Spectroscopy at High Temperature (TDS-HT)

The samples were exposed to 1 bar of hydrogen at room temperature and subsequently evacuated under secondary vacuum. Afterward, the desorbed H_2 partial pressure was recorded while heating to 473 K with a constant temperature increase of 5 K/min (*figure 2.11(a)*).

(2) Thermo-Desorption Spectroscopy at Low Temperature (TDS-LT)

The H_2 desorption at low temperature was performed using an Oxford Instruments cryostat (ITC 5035) that uses liquid nitrogen as a coolant. The hydrogen partial pressure was recorded from 77 to 300 K (*figure 2.11(b)*). Another type of TDS-LT measurement was performed at Stuttgart from 20 to 300 K and will be detailed in the appropriate chapter.

2.2.2.2 Pressure-Composition-Isotherm

Hydrogen sorption properties have also been studied by the Sievert method, which is a static volumetric method. Measuring the PCI curves is equivalent to finding the equilibrium pressure correspondence P_{eq} and consumed hydrogen quantity for a given temperature T. Since each point of the curve corresponds to thermodynamic equilibrium, the experiment gives only one form discretized curve. The measurements are from equilibrium point to equilibrium point. In Sievert's volumetric method, two calibrated volumes are used, the reservoir and the sample holder. The reservoir contains hydrogen gas at a specified pressure and temperature, the sample holder contains the sample at a determined pressure and temperature. The opening of a valve connects the two chambers and a drop in pressure is observed due to the expansion of the gas in a larger volume. After this gas expansion, the sample is placed outside its equilibrium state. When the new equilibrium is reached, the calculation of the difference between the pressure obtained by simple expansion of the gases and the gas pressure of the new equilibrium makes it possible to obtain the quantity of hydrogen sorbed or desorbed (*figure 2.12(a)*)[116]. A PCI curve is thus constructed by measuring several points by increasing the pressure for absorption and decreasing it for desorption (*figure 2.12(b)*).[117]

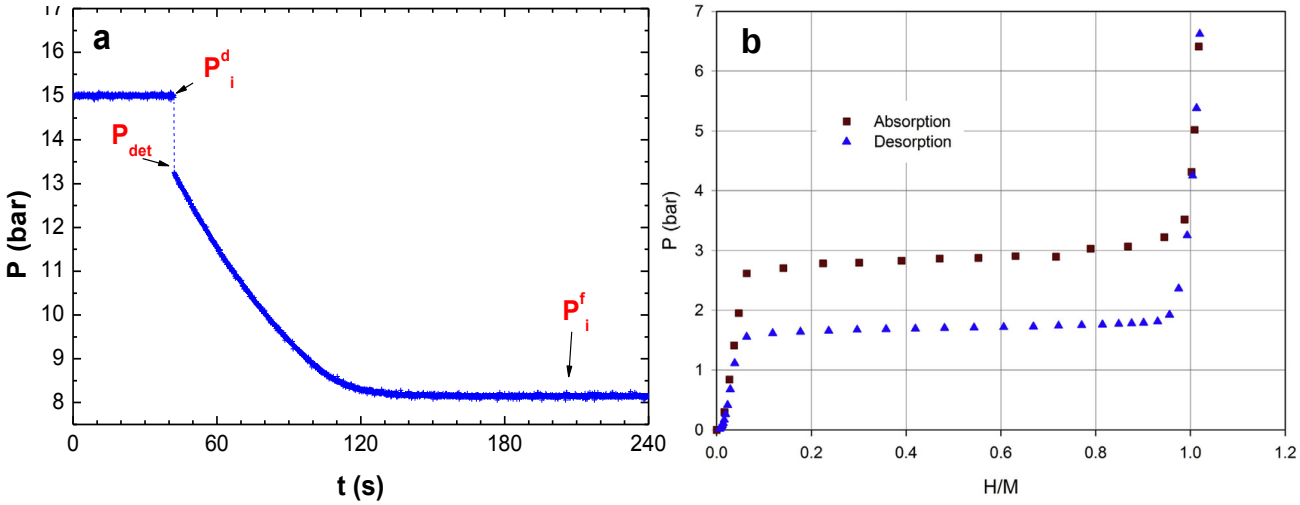

Figure 2.12: (a) Pressure variation as a function of time during an absorption point. Valve opening at t = 42 s with the immediate expansion of the gas followed by a sorption phase with a drop in pressure[116] *(b) Example of Pressure-Composition-Isotherm graph of $LaNi_5$-H_2 system at 296 K.* [117]

PCI curves are obtained by successive loading of gas to the sample at a constant temperature. The shape of the curves obtained depends on the nature of the material and the temperature of the study.

Several hydrogen sorption experiments were carried out to measure pressure-composition-isotherm (PCI) curves at different temperatures up to a maximum pressure of 0.1 MPa of hydrogen using an automated volumetric apparatus (Quantachrome Autosorb IQ). Prior to any sorption measurements, the samples were degassed under secondary vacuum at 493 K for 18 h. The sample holder is introduced into an Oxford Instruments cryostat (ITC 5035) and the temperature was controlled using liquid nitrogen as a coolant. The PCI curves were measured several times to ensure reproducibility of the measurements.

The thermodynamic properties of adsorption on a surface can be characterized by the determination of the adsorption energy, or the isosteric adsorption heat. This energy is the amount of heat involved in the adsorption of one mole of a chemical species in the gas phase on a substrate. This quantity is related to the enthalpy variation of the adsorbing gas (H_2 in our case).

The isosteric heats of adsorption for a specific adsorbate can be calculated by using the Clausius-Clapeyron equation (*equation 8*) applied to adsorption isotherms collected over wide ranges of pressure and temperature.

$$Q_{st} = -R\left(\frac{\partial(ln(P))}{\partial\left(\frac{1}{T}\right)}\right)_{n_{ads}} \qquad \textbf{(Equation 2.8)}$$

where: R is the perfect gas constant, P is the pressure, T is the temperature and n_{ads} is the adsorbed gas quantity.

This involves the graphical determination of the slope of ln (P) versus 1/T evaluated at constant n_{ads} using the above-mentioned relation. One example is given in *figure 2.13.*

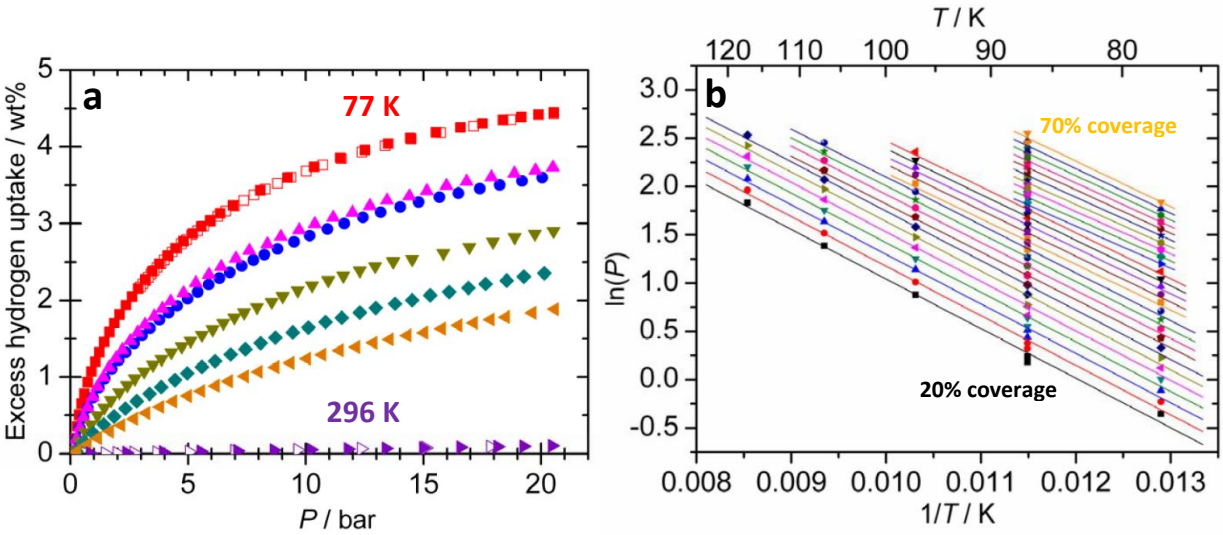

Figure 2.13: (a) Excess hydrogen adsorption (full symbols) and desorption (empty symbols) isotherms of MOF-5 performed under up to 20 bar and (b) ln(P) versus 1/T of MOF-5. [118]

The above relationship is an approximation obtained by assuming that the gas is perfect, and that the specific volume of the gas is much larger than that of the adsorbed phase.

References

1. Férey, G. *et al.* A Chromium Terephthalate-Based Solid with Unusually Large Pore Volumes and Surface Area. *Science* **309**, 2040–2042 (2005).
2. Ardelean, O. *et al.* Volumetric hydrogen adsorption capacity of densified MIL-101 monoliths. *International Journal of Hydrogen Energy* **38**, 7046–7055 (2013).
3. Hermannsdörfer, J. & Kempe, R. Selective Palladium-Loaded MIL-101 Catalysts. *Chemistry – A European Journal* **17**, 8071–8077 (2011).
4. Hermannsdörfer, J. *et al.* Ni/Pd@MIL-101: Synergistic Catalysis with Cavity-Conform Ni/Pd Nanoparticles. *Angewandte Chemie International Edition* **51**, 11473–11477 (2012).
5. Hermannsdörfer, J., Friedrich, M. & Kempe, R. Colloidal Size Effect and Metal-Particle Migration in M@MOF/PCP Catalysis. *Chemistry – A European Journal* **19**, 13652–13657 (2013).
6. Yin, D. *et al.* Efficient Pd@MIL-101(Cr) hetero-catalysts for 2-butyne-1,4-diol hydrogenation exhibiting high selectivity. *RSC Adv.* **7**, 1626–1633 (2017).
7. Hermes, S. *et al.* Metal@MOF: Loading of Highly Porous Coordination Polymers Host Lattices by Metal Organic Chemical Vapor Deposition. *Angewandte Chemie International Edition* **44**, 6237–6241 (2005).
8. Esken, D., Zhang, X., Lebedev, O. I., Schröder, F. & Fischer, R. A. Pd@MOF-5: limitations of gas-phase infiltration and solution impregnation of [Zn4O(bdc)3] (MOF-5) with metal–organic palladium precursors for loading with Pd nanoparticles. *J. Mater. Chem.* **19**, 1314–1319 (2009).
9. Zhang, M. *et al.* Chemical Vapor Deposition of Pd(C3H5)(C5H5) to Synthesize Pd@MOF-5 Catalysts for Suzuki Coupling Reaction. *Catal Lett* **142**, 313–318 (2012).
10. Hermes, S., Zacher, D., Baunemann, A., Wöll, C. & Fischer, R. A. Selective Growth and MOCVD Loading of Small Single Crystals of MOF-5 at Alumina and Silica Surfaces Modified with Organic Self-Assembled Monolayers. *Chem. Mater.* **19**, 2168–2173 (2007).
11. Müller, M., Lebedev, O. I. & Fischer, R. A. Gas-phase loading of [Zn4O(btb)2] (MOF-177) with organometallic CVD-precursors: inclusion compounds of the type [LnM]a@MOF-177 and the formation of Cu and Pd nanoparticles inside MOF-177. *J. Mater. Chem.* **18**, 5274–5281 (2008).

12. Kalidindi, S. B. *et al.* Metal@COFs: Covalent Organic Frameworks as Templates for Pd Nanoparticles and Hydrogen Storage Properties of Pd@COF-102 Hybrid Material. *Chemistry – A European Journal* **18**, 10848–10856 (2012).
13. Qin, W., Cao, W., Liu, H., Li, Z. & Li, Y. Metal-organic framework MIL-101 doped with palladium for toluene adsorption and hydrogen storage. *RSC Adv.* **4**, 2414–2420 (2014).
14. Ren, H., Li, C., Yin, D., Liu, J. & Liang, C. Pd@MIL-101 as an efficient bifunctional catalyst for hydrodeoxygenation of anisole. *RSC Adv.* **6**, 85659–85665 (2016).
15. Chen, G., Wu, S., Liu, H., Jiang, H. & Li, Y. Palladium supported on an acidic metal-organic framework as an efficient catalyst in selective aerobic oxidation of alcohols. *Green Chem.* **15**, 230–235 (2013).
16. Liu, H., Chen, G., Jiang, H., Li, Y. & Luque, R. From Alkyl Aromatics to Aromatic Esters: Efficient and Selective C□H Activation Promoted by a Bimetallic Heterogeneous Catalyst. *ChemSusChem* **5**, 1892–1896 (2012).
17. Bakuru, V. R., Velaga, B., Peela, N. R. & Kalidindi, S. B. Hybridization of Pd Nanoparticles with UiO-66(Hf) Metal-Organic Framework and the Effect of Nanostructure on the Catalytic Properties. *Chemistry – A European Journal* **0**,.
18. Zhang, M. *et al.* PVP–Pd@ZIF-8 as highly efficient and stable catalysts for selective hydrogenation of 1,4-butynediol. *Catal. Sci. Technol.* **4**, 329–332 (2014).
19. Shen, L., Wu, W., Liang, R., Lin, R. & Wu, L. Highly dispersed palladium nanoparticles anchored on UiO-66(NH2) metal-organic framework as a reusable and dual functional visible-light-driven photocatalyst. *Nanoscale* **5**, 9374–9382 (2013).
20. Zheng, S., Yang, P., Zhang, F., Chen, D.-L. & Zhu, W. Pd nanoparticles encaged within amine-functionalized metal-organic frameworks: Catalytic activity and reaction mechanism in the hydrogenation of 2,3,5-trimethylbenzoquinone. *Chemical Engineering Journal* **328**, 977–987 (2017).
21. Chen, L., Chen, X., Liu, H., Bai, C. & Li, Y. One-step encapsulation of Pd nanoparticles in MOFs via a temperature control program. *J. Mater. Chem. A* **3**, 15259–15264 (2015).
22. Kobayashi, H., Mitsuka, Y. & Kitagawa, H. Metal Nanoparticles Covered with a Metal–Organic Framework: From One-Pot Synthetic Methods to Synergistic Energy Storage and Conversion Functions. *Inorg. Chem.* **55**, 7301–7310 (2016).
23. Henschel, A., Gedrich, K., Kraehnert, R. & Kaskel, S. Catalytic properties of MIL-101. *Chem. Commun.* 4192–4194 (2008) doi:10.1039/B718371B.

24. El-Shall, M. S. *et al.* Metallic and bimetallic nanocatalysts incorporated into highly porous coordination polymer MIL-101. *J. Mater. Chem.* **19**, 7625–7631 (2009).
25. Yuan, B., Pan, Y., Li, Y., Yin, B. & Jiang, H. A Highly Active Heterogeneous Palladium Catalyst for the Suzuki–Miyaura and Ullmann Coupling Reactions of Aryl Chlorides in Aqueous Media. *Angewandte Chemie International Edition* **49**, 4054–4058 (2010).
26. Huang, Y., Lin, Z. & Cao, R. Palladium Nanoparticles Encapsulated in a Metal–Organic Framework as Efficient Heterogeneous Catalysts for Direct C2 Arylation of Indoles. *Chemistry – A European Journal* **17**, 12706–12712 (2011).
27. Li, H. *et al.* Palladium Nanoparticles Confined in the Cages of MIL-101: An Efficient Catalyst for the One-Pot Indole Synthesis in Water. *ACS Catal.* **1**, 1604–1612 (2011).
28. Zhang, D., Guan, Y., Hensen, E. J. M., Chen, L. & Wang, Y. Porous MOFs supported palladium catalysts for phenol hydrogenation: A comparative study on MIL-101 and MIL-53. *Catalysis Communications* **41**, 47–51 (2013).
29. Zhao, X., Jin, Y., Zhang, F., Zhong, Y. & Zhu, W. Catalytic hydrogenation of 2,3,5-trimethylbenzoquinone over Pd nanoparticles confined in the cages of MIL-101(Cr). *Chemical Engineering Journal* **239**, 33–41 (2014).
30. Dai, H., Su, J., Hu, K., Luo, W. & Cheng, G. Pd nanoparticles supported on MIL-101 as high-performance catalysts for catalytic hydrolysis of ammonia borane. *International Journal of Hydrogen Energy* **39**, 4947–4953 (2014).
31. Szilagyi, P. A. *et al.* Probing hydrogen spillover in Pd@MIL-101(Cr) with a focus on hydrogen chemisorption. *Phys. Chem. Chem. Phys.* **16**, 5803–5809 (2014).
32. Aijaz, A., Zhu, Q.-L., Tsumori, N., Akita, T. & Xu, Q. Surfactant-free Pd nanoparticles immobilized to a metal-organic framework with size- and location-dependent catalytic selectivity. *Chem. Commun.* **51**, 2577–2580 (2015).
33. Zhao, Y. *et al.* Preparation and hydrogen storage of Pd/MIL-101 nanocomposites. *Journal of Alloys and Compounds* **772**, 186–192 (2019).
34. Liu, Y. *et al.* Synthesis of highly dispersed metallic nanoparticles inside the pores of MIL-101(Cr) via the new double solvent method. *Catalysis Communications* **70**, 44–48 (2015).
35. Zhang, L. *et al.* PdNi nanoparticles supported on MIL-101 as high-performance catalysts for hydrogen generation from ammonia borane. *Journal of Alloys and Compounds* **677**, 87–95 (2016).

36. Shang, N. *et al.* Palladium nanoparticles encapsulated inside the pores of a metal–organic framework as a highly active catalyst for carbon–carbon cross-coupling. *RSC Adv.* **4**, 54487–54493 (2014).
37. Anderson, A. E., Baddeley, C. J. & Wright, P. A. Tuning Pd-nanoparticle@MIL-101(Cr) Catalysts for Tandem Reductive Amination. *Catal Lett* **148**, 154–163 (2018).
38. Malouche, A. *et al.* Hydrogen absorption in 1 nm Pd clusters confined in MIL-101(Cr). *J. Mater. Chem. A* (2017) doi:10.1039/C7TA07159K.
39. Yang, Q., Chen, Y.-Z., Wang, Z. U., Xu, Q. & Jiang, H.-L. One-pot tandem catalysis over Pd@MIL-101: boosting the efficiency of nitro compound hydrogenation by coupling with ammonia borane dehydrogenation. *Chem. Commun.* **51**, 10419–10422 (2015).
40. Xu, S. *et al.* Dynamic kinetic resolution of amines by using palladium nanoparticles confined inside the cages of amine-modified MIL-101 and lipase. *Journal of Catalysis* **363**, 9–17 (2018).
41. Sun, Q., Chen, M., Aguila, B., Nguyen, N. & Ma, S. Enhancing the biofuel upgrade performance for Pd nanoparticles via increasing the support hydrophilicity of metal–organic frameworks. *Faraday Discuss.* **201**, 317–326 (2017).
42. Li, H., Zhao, W. & Fang, Z. Hydrophobic Pd nanocatalysts for one-pot and high-yield production of liquid furanic biofuels at low temperatures. *Applied Catalysis B: Environmental* **215**, 18–27 (2017).
43. Zhang, F. *et al.* Palladium nanoparticles incorporated within sulfonic acid-functionalized MIL-101(Cr) for efficient catalytic conversion of vanillin. *J. Mater. Chem. A* **3**, 17008–17015 (2015).
44. Huang, Y. *et al.* Facile synthesis of palladium nanoparticles encapsulated in amine-functionalized mesoporous metal–organic frameworks and catalytic for dehalogenation of aryl chlorides. *Journal of Catalysis* **292**, 111–117 (2012).
45. Carson, F. *et al.* Influence of the Base on Pd@MIL-101-NH2(Cr) as Catalyst for the Suzuki–Miyaura Cross-Coupling Reaction. *Chemistry – A European Journal* **21**, 10896–10902 (2015).
46. Pascanu, V. *et al.* Sustainable Catalysis: Rational Pd Loading on MIL-101Cr-NH2 for More Efficient and Recyclable Suzuki–Miyaura Reactions. *Chemistry* **19**, 17483–17493 (2013).
47. Szilágyi, P. Á. *et al.* Functionalised metal–organic frameworks: a novel approach to stabilising single metal atoms. *J. Mater. Chem. A* **5**, 15559–15566 (2017).

48. Yin, D., Ren, H., Li, C., Liu, J. & Liang, C. Highly selective hydrogenation of furfural to tetrahydrofurfuryl alcohol over MIL-101(Cr)-NH2 supported Pd catalyst at low temperature. *Chinese Journal of Catalysis* **39**, 319–326 (2018).
49. Chen, J., Liu, R., Guo, Y., Chen, L. & Gao, H. Selective Hydrogenation of Biomass-Based 5-Hydroxymethylfurfural over Catalyst of Palladium Immobilized on Amine-Functionalized Metal–Organic Frameworks. *ACS Catal.* **5**, 722–733 (2015).
50. Hwang, Y. K. *et al.* Amine Grafting on Coordinatively Unsaturated Metal Centers of MOFs: Consequences for Catalysis and Metal Encapsulation. *Angewandte Chemie International Edition* **47**, 4144–4148 (2008).
51. Gu, X., Lu, Z.-H., Jiang, H.-L., Akita, T. & Xu, Q. Synergistic Catalysis of Metal–Organic Framework-Immobilized Au–Pd Nanoparticles in Dehydrogenation of Formic Acid for Chemical Hydrogen Storage. *J. Am. Chem. Soc.* **133**, 11822–11825 (2011).
52. Huang, Y. *et al.* Palladium Nanoparticles Supported on Mixed-Linker Metal–Organic Frameworks as Highly Active Catalysts for Heck Reactions. *ChemPlusChem* **77**, 106–112 (2012).
53. Huang, Y. *et al.* Palladium nanoparticles supported on amino functionalized metal-organic frameworks as highly active catalysts for the Suzuki–Miyaura cross-coupling reaction. *Catalysis Communications* **14**, 27–31 (2011).
54. Zlotea, C. *et al.* Pd Nanoparticles Embedded into a Metal-Organic Framework: Synthesis, Structural Characteristics, and Hydrogen Sorption Properties. *J. Am. Chem. Soc.* **132**, 2991–2997 (2010).
55. Huang, G., Yang, Q., Xu, Q., Yu, S.-H. & Jiang, H.-L. Polydimethylsiloxane Coating for a Palladium/MOF Composite: Highly Improved Catalytic Performance by Surface Hydrophobization. *Angewandte Chemie International Edition* **55**, 7379–7383 (2016).
56. Li, X. *et al.* Controlling Catalytic Properties of Pd Nanoclusters through Their Chemical Environment at the Atomic Level Using Isoreticular Metal–Organic Frameworks. *ACS Catalysis* **6**, 3461–3468 (2016).
57. Guan, Q. *et al.* Comparison of Pd-UiO-66 and Pd-UiO-66-NH2 catalysts performance for phenol hydrogenation in aqueous medium. *Fuel* **205**, 130–141 (2017).
58. Cai, X. *et al.* Pd/UiO-66(Hf): A highly efficient heterogeneous catalyst for the hydrogenation of 2,3,5-trimethylbenzoquinone. *Catalysis Communications* **113**, 23–26 (2018).

59. Shang, N.-Z., Feng, C., Gao, S.-T. & Wang, C. Ag/Pd nanoparticles supported on amine-functionalized metal–organic framework for catalytic hydrolysis of ammonia borane. *International Journal of Hydrogen Energy* **41**, 944–950 (2016).
60. Zhang, F. *et al.* Synergetic catalysis of palladium nanoparticles encaged within amine-functionalized UiO-66 in the hydrodeoxygenation of vanillin in water. *Green Chem.* **18**, 2900–2908 (2016).
61. Coupry, D. E. *et al.* Controlling embedment and surface chemistry of nanoclusters in metal–organic frameworks. *Chem. Commun.* **52**, 5175–5178 (2016).
62. Chen, L., Chen, H., Luque, R. & Li, Y. Metal−organic framework encapsulated Pd nanoparticles: towards advanced heterogeneous catalysts. *Chem. Sci.* **5**, 3708–3714 (2014).
63. Li, Y.-A. *et al.* Pd(0)@UiO-68-AP: chelation-directed bifunctional heterogeneous catalyst for stepwise organic transformations. *Chem. Commun.* **52**, 6517–6520 (2016).
64. Koo, W.-T. *et al.* Heterogeneous Sensitization of Metal–Organic Framework Driven Metal@Metal Oxide Complex Catalysts on an Oxide Nanofiber Scaffold Toward Superior Gas Sensors. *J. Am. Chem. Soc.* **138**, 13431–13437 (2016).
65. Dang, T. T. *et al.* Palladium Nanoparticles Supported on ZIF-8 As an Efficient Heterogeneous Catalyst for Aminocarbonylation. *ACS Catal.* **3**, 1406–1410 (2013).
66. Villajos, J. A., Orcajo, G., Calleja, G., Botas, J. A. & Martos, C. Beneficial cooperative effect between Pd nanoparticles and ZIF-8 material for hydrogen storage. *International Journal of Hydrogen Energy* **41**, 19439–19446 (2016).
67. Yang, Q., Xu, Q., Yu, S.-H. & Jiang, H.-L. Pd Nanocubes@ZIF-8: Integration of Plasmon-Driven Photothermal Conversion with a Metal–Organic Framework for Efficient and Selective Catalysis. *Angew. Chem. Int. Ed.* **55**, 3685–3689 (2016).
68. Tong, Y. *et al.* Interfacial coupling between noble metal nanoparticles and metal–organic frameworks for enhanced catalytic activity. *Nanoscale* **10**, 16425–16430 (2018).
69. Zhao, C. *et al.* A single palladium site catalyst as a bridge for converting homogeneous to heterogeneous in dimerization of terminal aryl acetylenes. *Mater. Chem. Front.* **2**, 1317–1322 (2018).
70. Gole, B., Sanyal, U., Banerjee, R. & Mukherjee, P. S. High Loading of Pd Nanoparticles by Interior Functionalization of MOFs for Heterogeneous Catalysis. *Inorg. Chem.* **55**, 2345–2354 (2016).

71. Cheon, Y. E. & Suh, M. P. Multifunctional Fourfold Interpenetrating Diamondoid Network: Gas Separation and Fabrication of Palladium Nanoparticles. *Chemistry – A European Journal* **14**, 3961–3967 (2008).
72. Moon, H. R. & Suh, M. P. Flexible and Redox-Active Coordination Polymer: Control of the Network Structure by Pendant Arms of a Macrocyclic Complex. *European Journal of Inorganic Chemistry* **2010**, 3795–3803 (2010).
73. Cheon, Y. E. & Suh, M. P. Enhanced Hydrogen Storage by Palladium Nanoparticles Fabricated in a Redox-Active Metal–Organic Framework. *Angewandte Chemie International Edition* **48**, 2899–2903 (2009).
74. Shen, L., Luo, M., Huang, L., Feng, P. & Wu, L. A Clean and General Strategy To Decorate a Titanium Metal–Organic Framework with Noble-Metal Nanoparticles for Versatile Photocatalytic Applications. *Inorg. Chem.* **54**, 1191–1193 (2015).
75. Liang, R., Jing, F., Shen, L., Qin, N. & Wu, L. M@MIL-100(Fe) (M = Au, Pd, Pt) nanocomposites fabricated by a facile photodeposition process: Efficient visible-light photocatalysts for redox reactions in water. *Nano Res.* **8**, 3237–3249 (2015).
76. Xu, B., Li, X., Chen, Z., Zhang, T. & Li, C. Pd@MIL-100(Fe) composite nanoparticles as efficient catalyst for reduction of 2/3/4-nitrophenol: Synergistic effect between Pd and MIL-100(Fe). *Microporous and Mesoporous Materials* **255**, 1–6 (2018).
77. Pascanu, V. *et al.* Selective Heterogeneous C−H Activation/Halogenation Reactions Catalyzed by Pd@MOF Nanocomposites. *Chemistry – A European Journal* **22**, 3729–3737 (2016).
78. Pascanu, V. *et al.* Double-Supported Silica-Metal–Organic Framework Palladium Nanocatalyst for the Aerobic Oxidation of Alcohols under Batch and Continuous Flow Regimes. *ACS Catal.* **5**, 472–479 (2015).
79. Jayaramulu, K. *et al.* Honeycomb Porous Framework of Zinc(II): Effective Host for Palladium Nanoparticles for Efficient Three-Component (A3) Coupling and Selective Gas Storage. *ChemPlusChem* **77**, 743–747 (2012).
80. Chen, G.-J. *et al.* Pd@Cu(II)-MOF-Catalyzed Aerobic Oxidation of Benzylic Alcohols in Air with High Conversion and Selectivity. *Inorg. Chem.* **55**, 3058–3064 (2016).
81. Pan, Y. *et al.* Uncoordinated carbonyl groups of MOFs as anchoring sites for the preparation of highly active Pd nano-catalysts. *J. Mater. Chem.* **22**, 10834–10839 (2012).
82. Huang, Y.-B. *et al.* Water-medium C–H activation over a hydrophobic perfluoroalkane-decorated metal-organic framework platform. *Journal of Catalysis* **333**, 1–7 (2016).

83. Kleist, W., Maciejewski, M. & Baiker, A. MOF-5 based mixed-linker metal–organic frameworks: Synthesis, thermal stability and catalytic application. *Thermochimica Acta* **499**, 71–78 (2010).
84. Gao, S., Zhao, N., Shu, M. & Che, S. Palladium nanoparticles supported on MOF-5: A highly active catalyst for a ligand- and copper-free Sonogashira coupling reaction. *Applied Catalysis A: General* **388**, 196–201 (2010).
85. Dang, T. T. *et al.* Atmospheric pressure aminocarbonylation of aryl iodides using palladium nanoparticles supported on MOF-5. *Chem. Commun.* **48**, 1805–1807 (2012).
86. Park, Y. K. *et al.* Catalytic nickel nanoparticles embedded in a mesoporous metal–organic framework. *Chem. Commun.* **46**, 3086–3088 (2010).
87. Sabo, M., Henschel, A., Fröde, H., Klemm, E. & Kaskel, S. Solution infiltration of palladium into MOF-5: synthesis, physisorption and catalytic properties. *J. Mater. Chem.* **17**, 3827–3832 (2007).
88. Opelt, S. *et al.* Preparation of palladium supported on MOF-5 and its use as hydrogenation catalyst. *Catalysis Communications* **9**, 1286–1290 (2008).
89. Kim, J. Y. *et al.* In situ-generated metal oxide catalyst during CO oxidation reaction transformed from redox-active metal-organic framework-supported palladium nanoparticles. *Nanoscale Res Lett* **7**, 461 (2012).
90. Roy, A. S. *et al.* Pd-grafted porous metal–organic framework material as an efficient and reusable heterogeneous catalyst for C–C coupling reactions in water. *Applied Catalysis A: General* **469**, 320–327 (2014).
91. Martis, M., Mori, K., Fujiwara, K., Ahn, W.-S. & Yamashita, H. Amine-Functionalized MIL-125 with Imbedded Palladium Nanoparticles as an Efficient Catalyst for Dehydrogenation of Formic Acid at Ambient Temperature. *J. Phys. Chem. C* **117**, 22805–22810 (2013).
92. Gulcan, M., Zahmakiran, M. & Özkar, S. Palladium(0) nanoparticles supported on metal organic framework as highly active and reusable nanocatalyst in dehydrogenation of dimethylamine-borane. *Applied Catalysis B: Environmental* **147**, 394–401 (2014).
93. Li, G. *et al.* Hydrogen storage in Pd nanocrystals covered with a metal–organic framework. *Nature Materials* **13**, 802–806 (2014).
94. Li, X. *et al.* Metal–Organic-Framework-Derived Carbons: Applications as Solid-Base Catalyst and Support for Pd Nanoparticles in Tandem Catalysis. *Chemistry – A European Journal* **23**, 4266–4270 (2017).

95. Panahi, L., Naimi-Jamal, M. R. & Mokhtari, J. Ultrasound-assisted Suzuki-Miyaura reaction catalyzed by Pd@Cu2(NH2-BDC)2(DABCO). *Journal of Organometallic Chemistry* **868**, 36–46 (2018).
96. Lin, A., Ibrahim, A. A., Arab, P., El-Kaderi, H. M. & El-Shall, M. S. Palladium Nanoparticles Supported on Ce-Metal–Organic Framework for Efficient CO Oxidation and Low-Temperature CO2 Capture. *ACS Appl. Mater. Interfaces* **9**, 17961–17968 (2017).
97. Sun, D. & Li, Z. Double-Solvent Method to Pd Nanoclusters Encapsulated inside the Cavity of NH2–Uio-66(Zr) for Efficient Visible-Light-Promoted Suzuki Coupling Reaction. *J. Phys. Chem. C* **120**, 19744–19750 (2016).
98. Wang, X.-D. *et al.* Allenylphosphine Oxides as Starting Materials for the Synthesis of Conjugated Enynes: Boosting the Catalytic Performance by MOF Encapsulated Palladium Nanoparticles. *Advanced Synthesis & Catalysis* **360**, 3518–3525 (2018).
99. Wang, D. & Li, Z. Coupling MOF-based photocatalysis with Pd catalysis over Pd@MIL-100(Fe) for efficient N-alkylation of amines with alcohols under visible light. *Journal of Catalysis* **342**, 151–157 (2016).
100. Henschel, A., Gedrich, K., Kraehnert, R. & Kaskel, S. Catalytic properties of MIL-101. *Chem. Commun.* 4192–4194 (2008) doi:10.1039/B718371B.
101. Pan, Y., Yuan, B., Li, Y. & He, D. Multifunctional catalysis by Pd@MIL-101: one-step synthesis of methyl isobutyl ketone over palladium nanoparticles deposited on a metal-organic framework. *Chem. Commun.* **46**, 2280–2282 (2010).
102. Li, H. *et al.* Palladium Nanoparticles Confined in the Cages of MIL-101: An Efficient Catalyst for the One-Pot Indole Synthesis in Water. *ACS Catalysis* **1**, 1604–1612 (2011).
103. Zhang, D., Guan, Y., Hensen, E. J. M., Chen, L. & Wang, Y. Porous {MOFs} supported palladium catalysts for phenol hydrogenation: A comparative study on MIL-101 and MIL-53. *Catalysis Communications* **41**, 47–51 (2013).
104. Liu, H., Li, Y., Luque, R. & Jiang, H. A Tuneable Bifunctional Water-Compatible Heterogeneous Catalyst for the Selective Aqueous Hydrogenation of Phenols. *Advanced Synthesis & Catalysis* **353**, 3107–3113 (2011).
105. Inkson, B. J. 2 - Scanning electron microscopy (SEM) and transmission electron microscopy (TEM) for materials characterization. in *Materials Characterization Using Nondestructive Evaluation (NDE) Methods* (eds. Hübschen, G., Altpeter, I., Tschuncky, R. & Herrmann, H.-G.) 17–43 (Woodhead Publishing, 2016). doi:10.1016/B978-0-08-100040-3.00002-X.

106. Thommes, M. *et al.* Physisorption of gases, with special reference to the evaluation of surface area and pore size distribution (IUPAC Technical Report). *Pure and Applied Chemistry* **87**, 1051–1069 (2015).
107. Rouquerol, F., Rouquerol, J. & Sing, K. S. W. *Adsorption by powders and porous solids: principles, methodology, and applications*. (Academic Press, 1999).
108. Ankudinov, A. L., Nesvizhskii, A. I. & Rehr, J. J. Dynamic screening effects in x-ray absorption spectra. *Phys. Rev. B* **67**, 115120 (2003).
109. Ankudinov, A. L., Ravel, B., Rehr, J. J. & Conradson, S. D. Real-space multiple-scattering calculation and interpretation of x-ray-absorption near-edge structure. *Phys. Rev. B* **58**, 7565–7576 (1998).
110. La Fontaine, C., Barthe, L., Rochet, A. & Briois, V. X-ray absorption spectroscopy and heterogeneous catalysis: Performances at the SOLEIL's SAMBA beamline. *Catalysis Today* **205**, 148–158 (2013).
111. Ghimbeu, C. M. *et al.* Understanding the mechanism of hydrogen uptake at low pressure in carbon/palladium nanostructured composites. *J. Mater. Chem.* **21**, 17765–17775 (2011).
112. Alain, M., Jacques, M., Diane, M.-B. & Karine, P. MAX: Multiplatform Applications for XAFS. *Journal of Physics: Conference Series* **190**, 012034 (2009).
113. Michalowicz, A., Moscovici, J., Muller-Bouvet, D. & Provost, K. MAX (Multiplatform Applications for XAFS) New Features. *J. Phys.: Conf. Ser.* **430**, 012016 (2013).
114. FTIR instrumentation and theory. https://chemistry.oregonstate.edu/courses/ch361-464/ch362/irinstrs.htm.
115. Zlotea, C. *et al.* Synthesis of small metallic Mg-based nanoparticles confined in porous carbon materials for hydrogen sorption. *Faraday Discuss.* **151**, 117–131 (2011).
116. Latroche, M. Notice feuille de calcul Excel 'Banc-type'. (2015).
117. Mohammadshahi, S. S., Gray, E. MacA. & Webb, C. J. A review of mathematical modelling of metal-hydride systems for hydrogen storage applications. *International Journal of Hydrogen Energy* **41**, 3470–3484 (2016).
118. Schmitz, B. *et al.* Heat of Adsorption for Hydrogen in Microporous High-Surface-Area Materials. *ChemPhysChem* **9**, 2181–2184 (2008).

CHAPTER III

MIL-101(Cr) DOPED WITH PALLADIUM NANOPARTICLES

3.1 Synthesis optimization

The insertion of the palladium nanoparticles in the pores of the MIL-101(Cr) was carried out by impregnation of the porous matrix with the palladium precursor followed by a reduction step to obtain confined metallic nanoparticles. Two impregnation techniques, as well as two reduction techniques, have been compared to validate the one that gives the best dispersion of the nanoparticles in a homogeneous way. On the other hand, the effect of degassing the MOF and its handling away from air before impregnation with the precursor solution was also studied.

3.1.1 Impregnation and reduction method

The liquid impregnation (LI) and the impregnation by double solvent method (DSM), as well as the reduction under Ar/H_2 flow at 300°C and a chemical one by $NaBH_4$ have been carried out. Three main combinations were tested: LI + Ar/H_2, DSM + $NaBH_4$, and DSM + Ar/H_2. In all three synthesis, the used MIL-101(Cr) is not degassed. The structural characterization of pristine MIL-101(Cr), as well as different 10-Pd@MIL-101(Cr) composites, was performed by X-ray diffraction and the results are shown in *figure 3.1*.

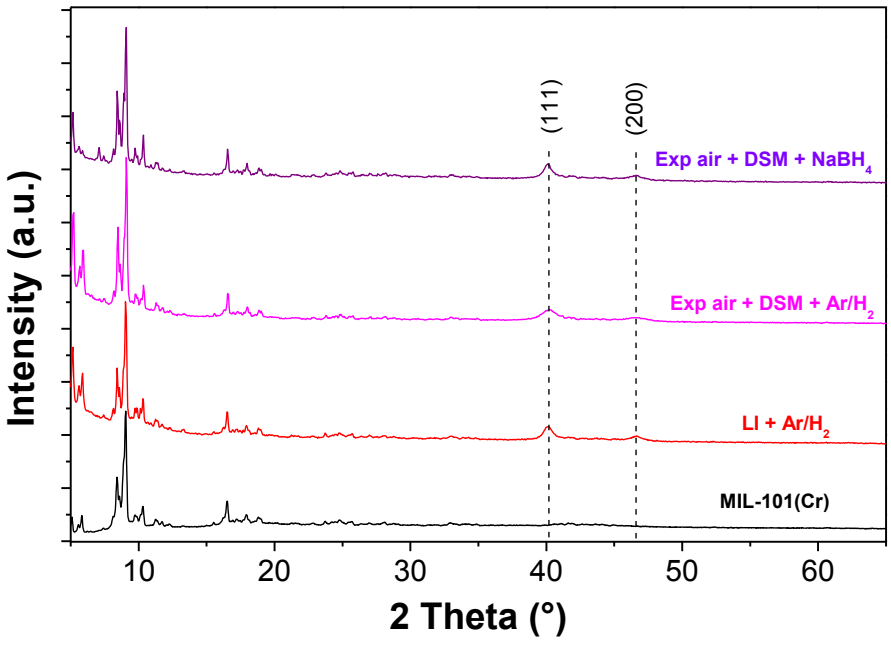

Figure 3.1: XRD patterns of MIL-101(Cr) and 10-Pd@MIL-101(Cr) composites synthesized by different methods.

For the different synthetic techniques, MIL-101(Cr) keeps its crystalline structure, characterized by main diffraction peaks between 5 and 25°. In addition, two characteristic diffraction peaks of Pd, which crystallize in a *fcc (Fm-3m)* system, are visible for the different 10-Pd@MIL-101(Cr) composites.

The microstructural characterization of the different materials was carried out by Transmission Electron Microscopy (TEM) to evaluate the homogeneity of nanoparticles distribution (*figure 3.2*). The pristine MIL-101(Cr) also is shown in *figure 3.2(d)*.

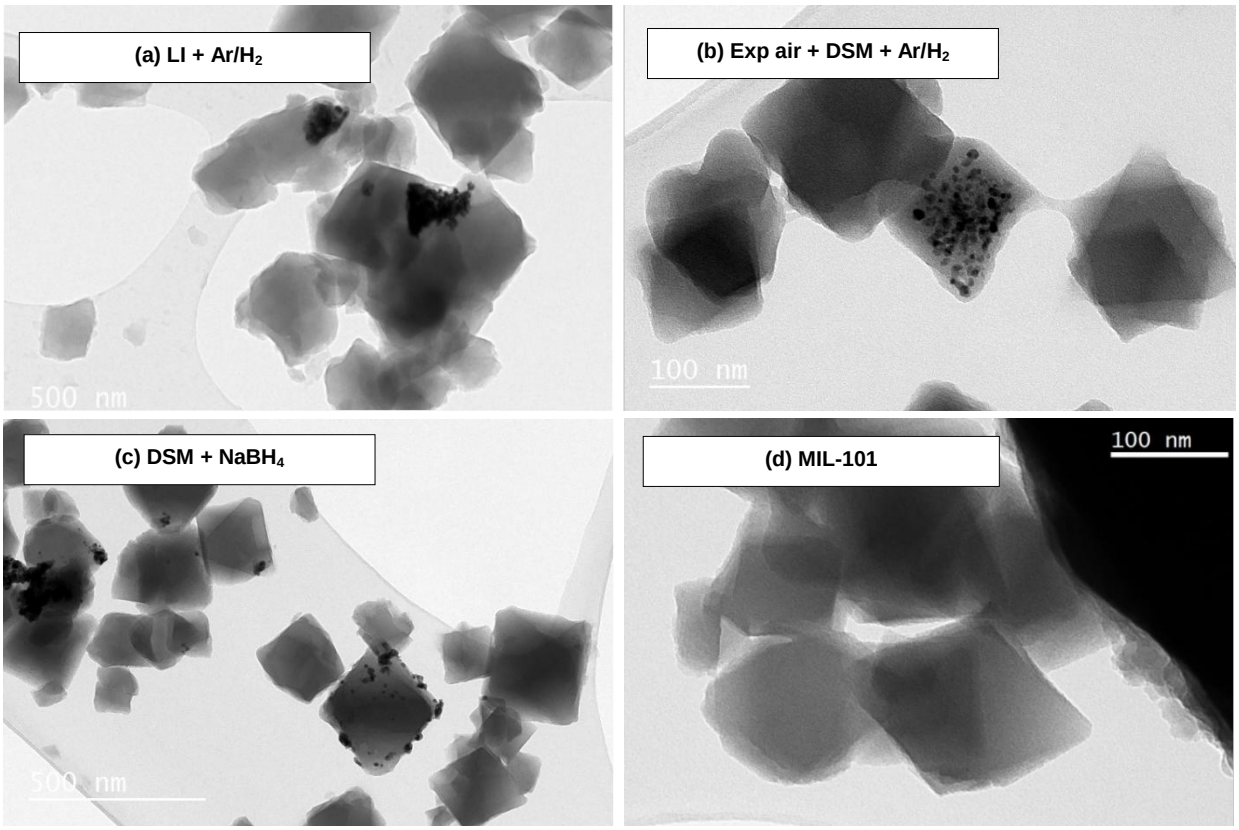

Figure 3.2: (a), (b), (c) Typical TEM images of 10-Pd@MIL-101(Cr) composites synthesized by different methods and (d) the pristine MIL-101(Cr).

For the material synthesized by LI and reduced under Ar/H_2 flow, the TEM images show a very heterogeneous distribution of the nanoparticles with the presence of very large aggregates, most probably formed outside the pores (*figure 3.2(a)*). The same aggregates were observed for the 10-Pd@MIL-101(Cr) composite synthesized by DSM with a non-degassed MIL-101(Cr) and reduced under Ar/H_2 flow (*figure 3.2(b)*). Finally, the material synthesized by DSM and reduced by $NaBH_4$ shows the presence of large nanoparticles (around 100 nm) (*figure 3.2(c)*). In all the cases, a heterogeneous dispersion of nanoparticles is observed.

In conclusion, these conditions need to be optimized to obtain homogeneous nanoparticles dispersion. One way will be explored by previously degassing the porous host since this MIL-101(Cr) has very large surface area and is known to absorb rapidly large amount of H_2O upon air exposure. This might block the porosity to metal precursor.

3.1.2 Degassing effect

In order to study the effect of degassing the MOF and handling it away from air before impregnation with the palladium precursor solution, a 10-Pd@MIL-101(Cr) was synthesized by DSM using a degassed MIL-101(Cr) under secondary vacuum at 493 K for 18 hours and further handled in a glove box under argon atmosphere. The reduction was then carried out under an Ar/H_2 flow at 573 K for 15 min.

The structural characterization of pristine MIL-101(Cr) and 10-Pd@MIL-101(Cr) composites (with and without degassing) was performed by X-ray diffraction and the results are shown in *figure 3.3*.

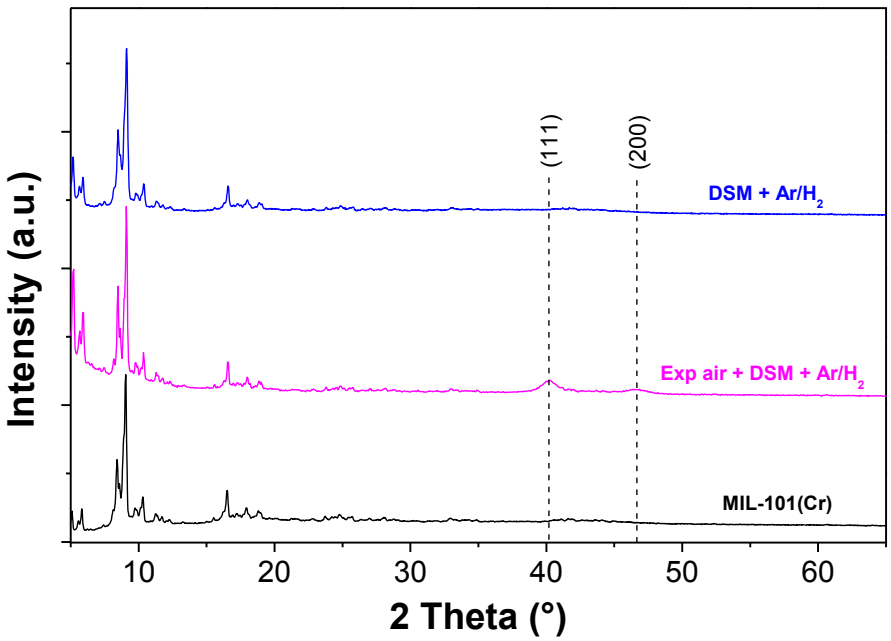

Figure 3.3: XRD patterns of MIL-101(Cr) and 10-Pd@MIL-101(Cr) composites synthesized by different methods.

As was shown for the 10-Pd@MIL-101(Cr) composite synthesized by DSM with a non-degassed MIL-101(Cr), the MOF structure of the material synthesized with a degassed MIL-101(Cr) and handled away from air, retains its crystallinity after synthesis, characterized by diffraction peaks between 5 and 25 °. However, no characteristic Pd diffraction peak occurs

for the Pd@MIL-101(Cr) composite synthesized with an outgassed MIL-101(Cr) by DSM and reduced under Ar/H_2 flow. *Figure 3.4* shows the TEM images of the latter 10-Pd@MIL-101(Cr) material.

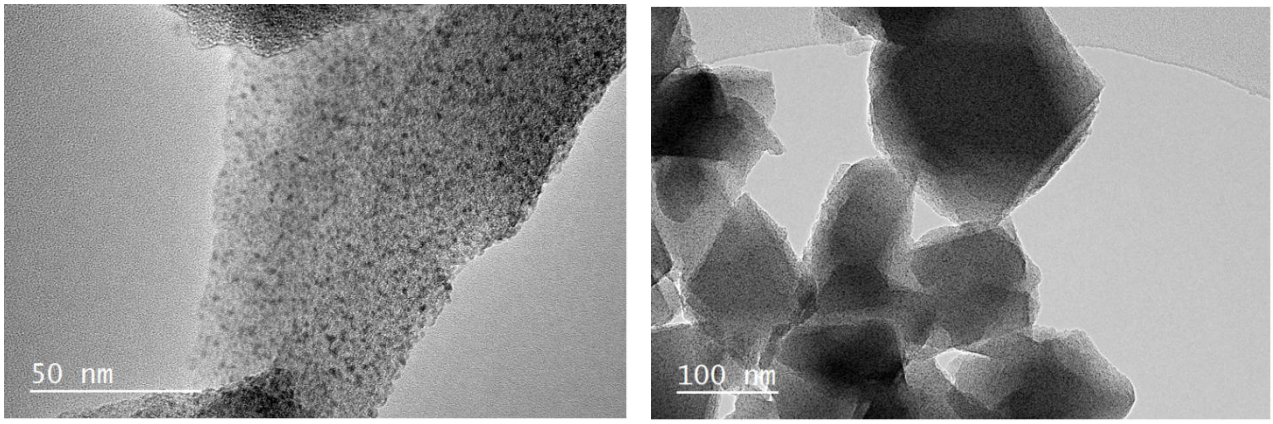

Figure 3.4: Typical TEM images of 10-Pd@MIL-101(Cr) composites synthesized by DSM using a degassed MIL-101(Cr) followed by a reduction under Ar/H_2 flow.

TEM images of this composite show a homogeneous distribution of nanoparticles within the MIL-101(Cr) pores with sizes smaller than the size of the pores (2.9 and 3.4 nm) (*figure 3.4*). In conclusion, the outgas of MIL-101(Cr) followed by its impregnation using the double solvent method as well as the reduction under Ar/H_2 flow provide the optimal synthesis conditions for obtaining a material formed by metal nanoparticles confined in a homogeneous way within the MOF pores. This optimized synthesis method has been validated and chosen to prepare the materials to be studied in the next sections.

3.2 Palladium doping: Variable metal loading

Once the synthetic method optimized, four *x*-Pd@MIL-101(Cr) composites with the different metal loadings (*x* = 5, 10, 15 and 20 wt.%) were synthesized and characterized to study the effect of metal loading on the structural, nanostructural and textural properties. The hydrogen sorption properties will be then discussed, and the nanosize effect will be determined. It should be noted that the maximum metal loading has been imposed by the solubility limit of the precursor salt into water.

3.2.1 X-Ray Diffraction

The *x*-Pd@MIL-101(Cr) composites, with *x* = 5 – 20 wt.%, are obtained by the optimized DSM approach. The structural characterization of the synthesized hybrid materials was carried out by X-ray diffraction. The angular domain 2θ chosen for these studies is 5-65°. The bulk palladium crystallizes in a face-centered cubic system (*fcc*) with the space group *Fm-3m*.

The X-ray diffraction patterns of pristine MIL-101(Cr) and *x*-Pd@MIL-101(Cr) composites with different metal loading, are plotted in *figure 3.5*. The Miller indices of expected diffraction peaks in the Pd *fcc* crystal structure are also indicated as dotted lines.

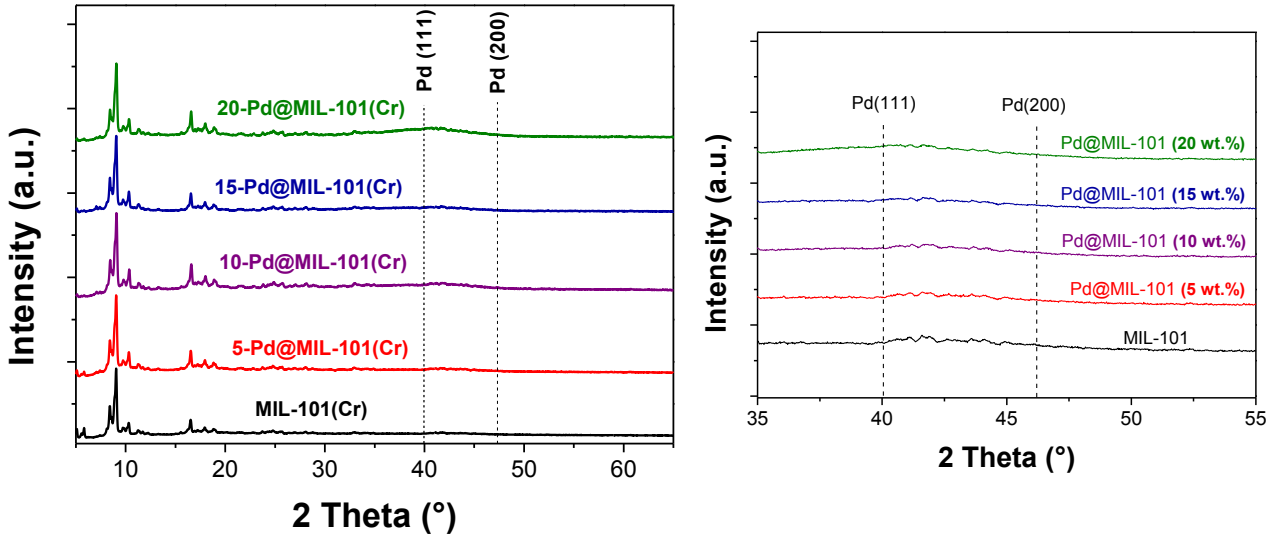

Figure 3.5: XRD patterns of pristine MIL-101(Cr) and x-Pd@MIL-101(Cr) composites (left) and a zoom between [35-55°] (right).

The MIL-101(Cr) structure retains its crystallinity after synthesis of Pd nanoparticles. In addition, there is no Pd diffraction peak, despite the large metal content, up to 20 wt.%. *Figure 3.5(b)* represents a zoom of the different diffractograms and confirms the absence of

the diffraction peaks of Pd. This suggests that either amorphous Pd or ultra-small nanoparticles with too short coherence length to diffract X-rays. The latter hypothesis will be further confirmed by TEM.

3.2.2 Fourier Transform Infrared Spectroscopy

FTIR characterization was carried out to detect the identity of the MIL-101(Cr) functional groups and the effect of doping. The FT-IR spectra, performed by Annalisa PAOLONE at CNR-ISC (Rome, Italy), are shown in *figure 3.6*. All materials were handled in air.

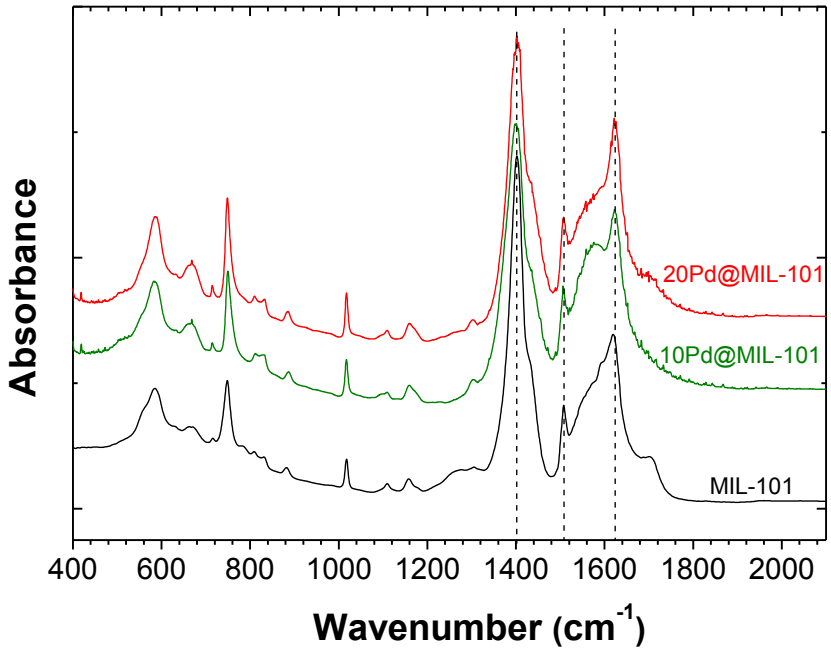

Figure 3.6: Infrared spectra of MIL-101(Cr) and x-Pd@MIL-101(Cr) (x = 10 and 20).

For MIL-101(Cr), the band at 1625 cm^{-1} indicates the presence of adsorbed water. The bands at 1404 cm^{-1} correspond to the symmetric (O-C-O) vibrations, implying the presence of dicarboxylate within the MIL-101(Cr) framework. The other bands between 600 and 1600 cm^{-1} are attributed to benzene, including the stretching vibration (C=C) at 1508 cm^{-1} and deformation vibration (C-H) at 750, 884,1017 and 1160 cm^{-1}. In accordance with XRD results, no change in the FTIR spectra of the Pd@MIL-101(Cr) composites is observed. These results confirm that the MIL-101(Cr) framework did not transform after Pd doping despite the large metal content, up to 20 wt.%.

3.2.3 Transmission Electron Microscopy

The nanostructural characterization of Pd nanoparticles was performed by Transmission Electron Microscopy (TEM) to examine the dispersion of the particles in the MOF, to determine the particle size distribution and the average size of these particles.

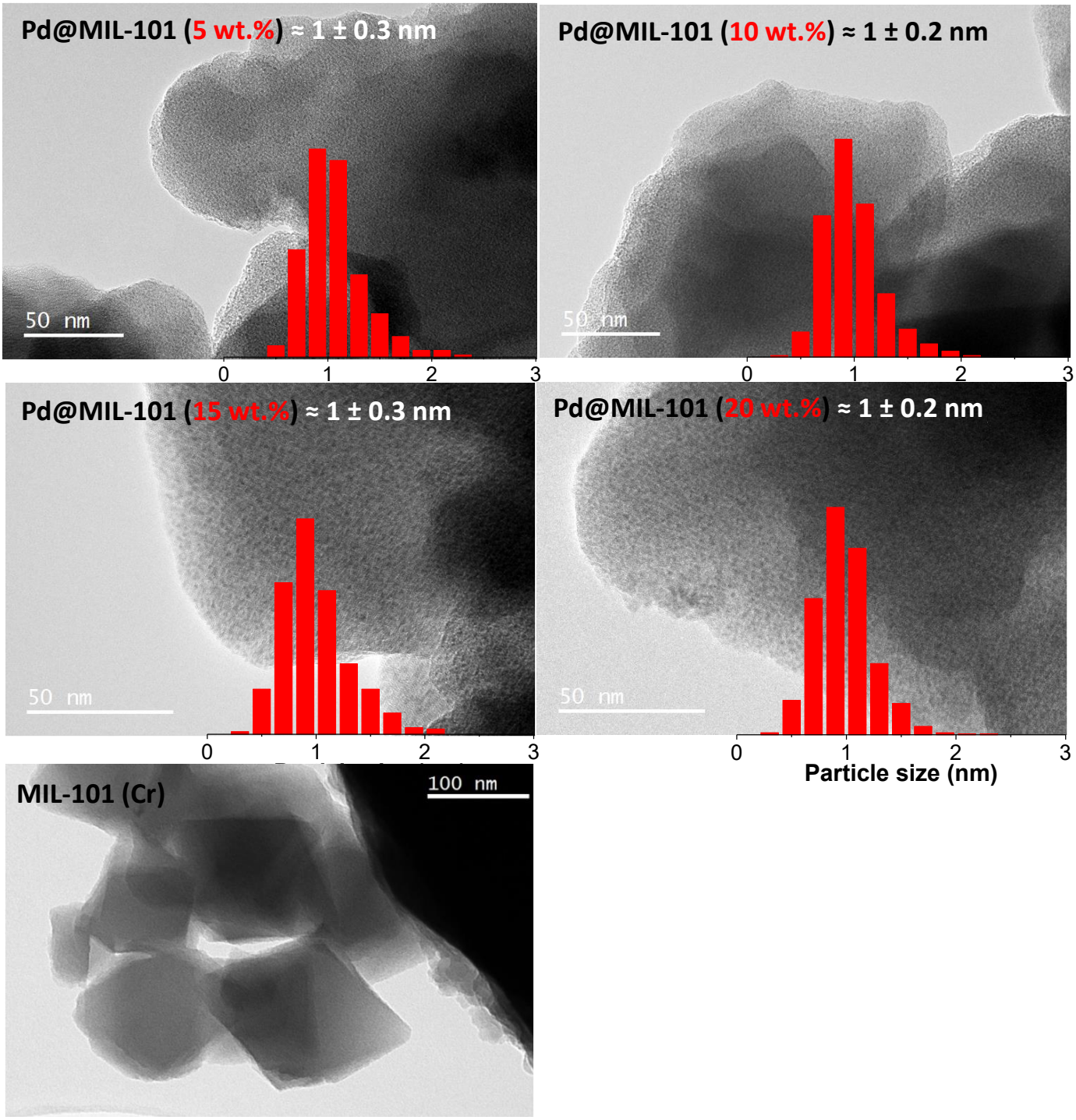

Figure 3.7: Typical TEM images of x-Pd@MIL-101(Cr) composites (x = 5, 10, 15 and 20 wt.%) with Pd particle size histograms as well as the pristine MIL-101(Cr).

F*igure 3.7* shows the TEM images of the Pd composites with the different metal loading and pristine MIL-101(Cr). The analysis of several TEM images allows drawing the histograms of particle size presenting the size distribution of the nanoparticles. The average particle size was proposed following the statistical analysis of the histograms.

The images show black spots that correspond to Pd clusters very well dispersed in the pores of MIL-101(Cr). The size distribution of the nanoparticles of Pd of the different metal loading is between 0.5 and 2.5 nm and the average size of the clusters of the different composites is 1 nm irrespective of the metal loading. This very small size explains the absence of X-ray diffraction peaks of the Pd. It is noted that this average particle size is the smallest ever reported in the literature for these composites and at this Pd loadings.

High-Resolution Transmission Electron Microscopy (HR-TEM) images were carried out, by Jaysen NELAYAH at MPQ-CNRS (Paris, France), to better identify the clusters and to closely observe their dispersion in the pores of the MIL-101(Cr). HR-TEM investigations show the presence, not only of well-dispersed 1 nm Pd clusters within the pores of MIL-101(Cr) but also few larger particles located on the surface (*figure 3.8*). Moreover, HR-TEM images demonstrate that the large Pd clusters located outside are crystalline. Indeed, lattice planes can be noticed for Pd clusters embedded into the MIL-101(Cr) pores. Typical interplanar distances, as measured for selected Pd nanoparticles, are 2.25 – 2.29 Å, which are close to d_{111}= 2.245 Å of bulk Pd[1]. Thus, we hypothesize that Pd clusters adopt the typical *fcc* structure of the bulk metal.

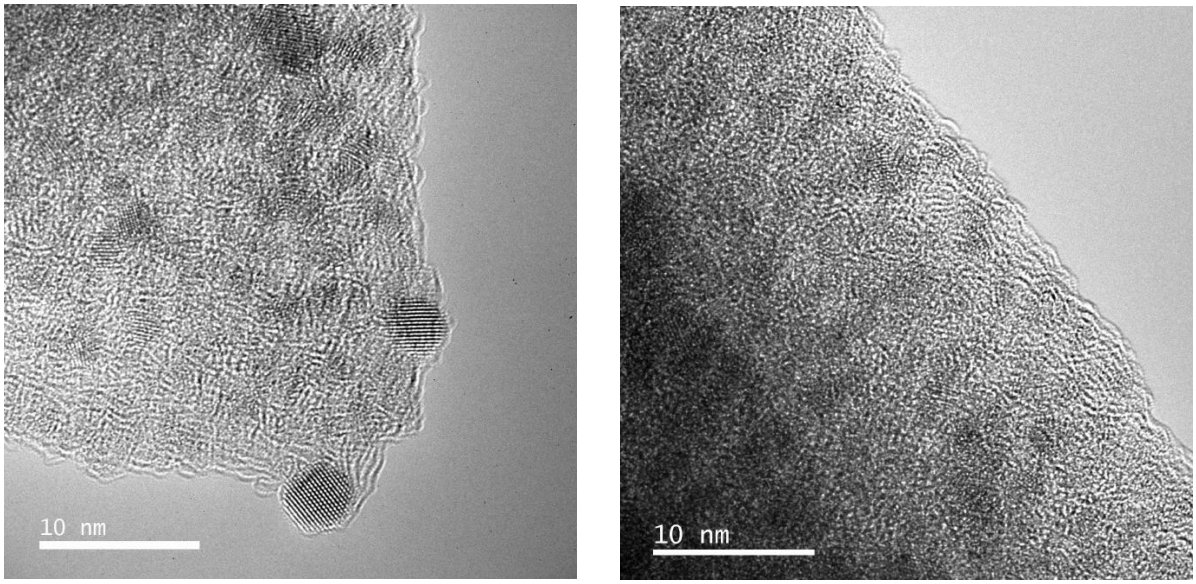

Figure 3.8: HR-TEM images of 10-Pd@MIL-101 composite.

3.2.4 Scanning Electron Microscopy

To further study the structural properties of the Pd@MIL-101(Cr) materials, some images were performed by Scanning Electron Microscopy (SEM). *Figure 3.9* shows the SEM images of the Pd composites with the different metal loadings.

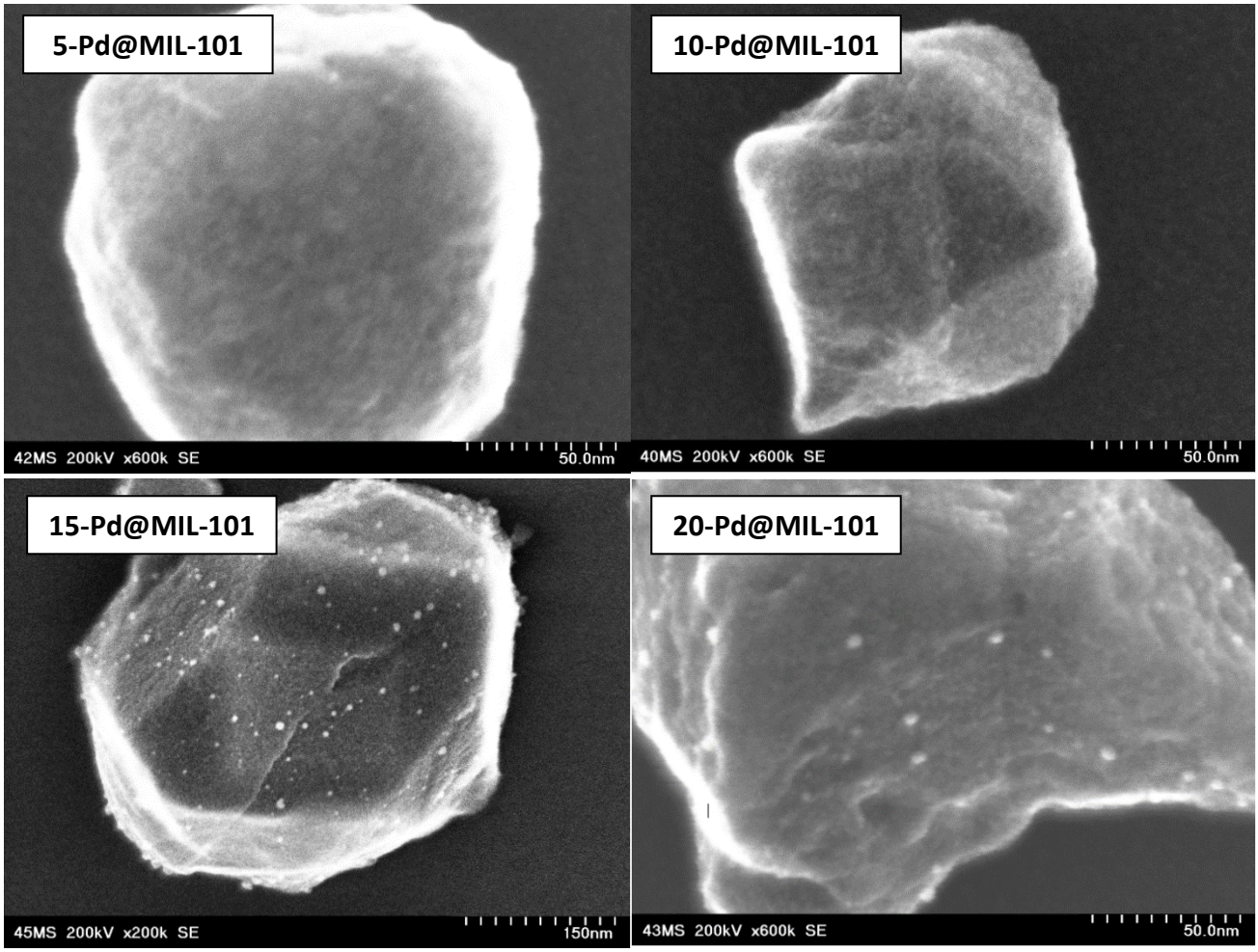

Figure 3.9: Typical SEM images of x-Pd@MIL-101(Cr) composites (x = 5, 10, 15 and 20 wt.%).

The SEM images show that, by increasing the Pd loading, some particles are deposited on the surface of MIL-101 (Cr). The number of these particles on the surface remains small compared to the number of particles observed by TEM. The deposition of the nanoparticles on the outer surface of the MOF may be explained by the obstruction of the pores at the high metal content.

In conclusion, our optimized method allows preparation of well confined Pd nanoparticles with average size around 1 nm for loadings up to 20 wt.% of Pd.

3.2.5 Specific surface area & total pore volume

The characterization of the textural properties was carried out by N_2 adsorption/desorption measurements. *Figure 3.10* shows the N_2 adsorption curves for MIL-101(Cr) and the different Pd doped MIL-101(Cr) composites with different metal loadings. The obtained isotherms for MIL-101 (Cr) as well as for *x*-Pd@MIL-101(Cr), represented in *figure 3.10(a)*, are of type IV (a small hysteresis, above 0.3 P/P_0, is present in all curve), *i.e.* corresponding to mesoporous materials. The evolution of the specific surface area and the total pore volume as a function of the Pd amount has also been represented in *figure 3.10(b)* and *(c)*. The specific surface area and the pore volume decrease with the insertion of Pd clusters into the pores of MIL-101(Cr). In fact, the specific surface area and total pore volume of the pristine MIL-101(Cr) decreased from 3300 m^2/g and 1.64 cc/g to 2200 m^2/g and 1.05 cc/g for the most loaded composites (15 and 20 wt.%). This decrease can be explained by the increase in the total mass of the composite after the insertion of the Pd clusters and by blocking the accessible pores.

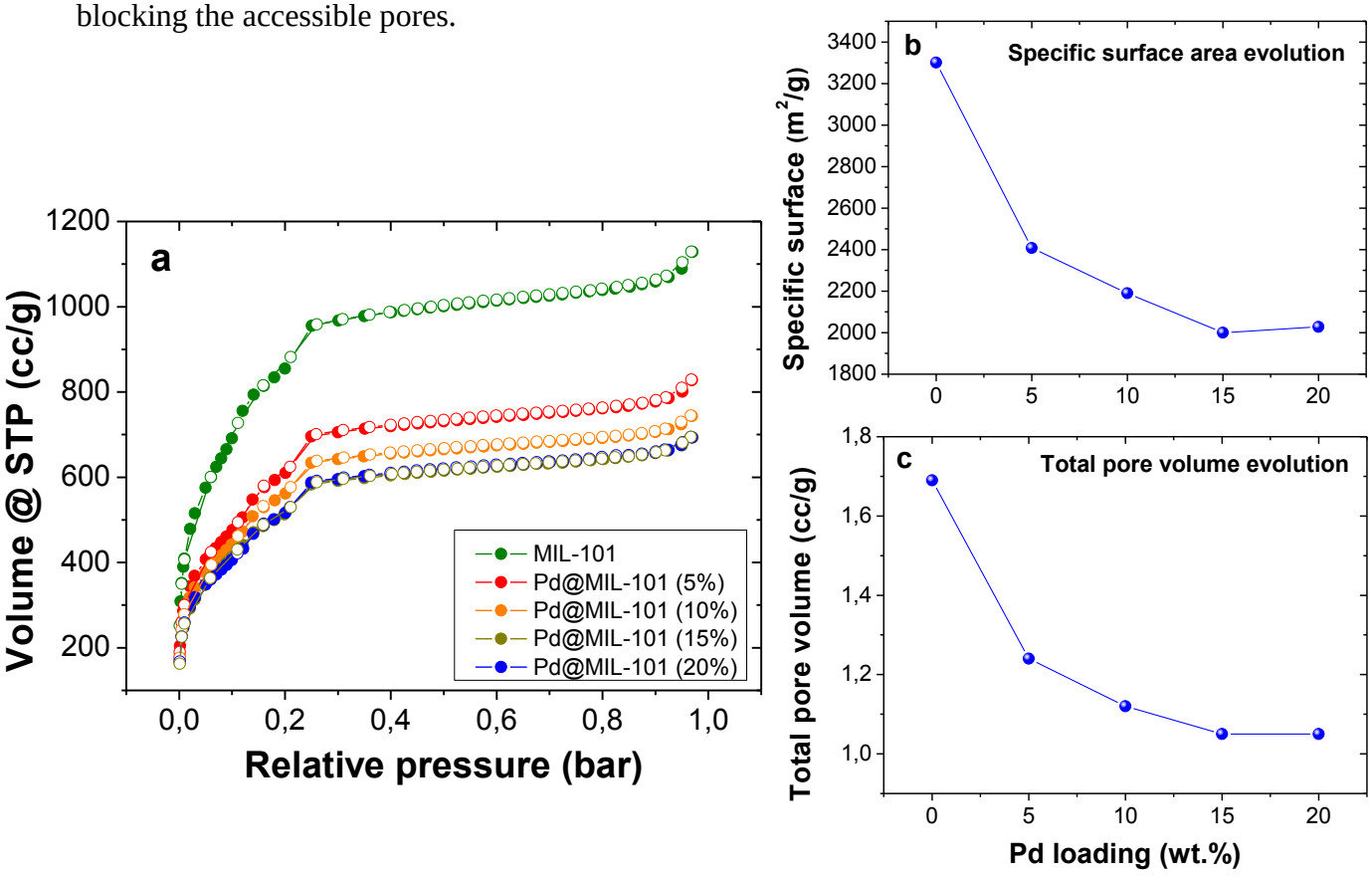

Figure 3.10: (a) N_2 adsorption/desorption curves of MIL-101(Cr) and x-Pd@MIL-101(Cr) composites and the evolution of (b) the specific surface area and (c) total pore volume as a function of Pd amount.

Moreover, it is surprising that the textural properties of composites with 15 and 20 wt.% Pd are very close as shown in *figure 3.10(b)* and *(c)*, since they are expected to constantly decrease with increasing Pd loading. This discrepancy cannot be accounted by the formation of Pd nanoparticles outside the pores of MIL-101(Cr) since only a few nanoparticles could be detected on the external surface of the porous support (*figure 3.9*). One possible explanation might be that the probed surface area by N_2 adsorption is composed of both the MIL-101(Cr) porous surface and Pd nanoparticle surface. Under the hypothesis of perfect spherical nano-objects, Pd nanoparticles with 1 nm size possess a specific surface area of around 500 m^2/g. Thus, increasing the Pd content has a twofold effect: it decreases the available porosity of MIL-101(Cr) but also it increases the surface area available on Pd nanoparticles, which is no longer negligible with increasing the metal content. Consequently, these two opposite effects might compensate for a certain Pd loading, and experimentally almost constant textural properties can be measured for samples with different Pd loadings.

In addition, from the density of the Pd, which is equal to 12.02 g/cc, the volume of Pd inserted into the pores of MIL-101(Cr) was determined and the theoretical available volume after doping was calculated. For example, for 20 wt.% composite, the volume occupied by Pd represents only 1 % of the total initial volume available of the MIL-101(Cr) (1.64 cc/g). This means that 99 % of porous volume is still theoretically available after Pd insertion. This is in contrast with the total pore volume determined by N_2 adsorption (*figure 3.10 (c)*) which shows a strong decrease after 5 wt.% Pd doping. This difference can be explained by the clogging of the windows of the pores of 1.2 and 1.6 nm aperture diameter. Thus, the theoretically available total pore volume leaves the possibility of further doping MIL-101(Cr) with Pd nanoparticles to higher metal loadings by successive impregnation. It should be recalled that in the context of this study, the maximum metal loading was imposed by the solubility limit of the precursor salt in the solvent.

3.2.6 Inductively Coupled Plasma - Mass spectroscopy

The Pd concentration in the different composites was determined by ICP-MS and the results were reported in *table 3.1*. Chemical analysis reveals the presence of the Pd element. The overall analysis confirms the good agreement of chemical composition for the different composites with the nominal values.

Table 3.1: Chemical analysis of x-Pd@MIL-101 composites (x= 5, 10, 15 and 20).

Sample	Pd content (wt%) ICP-MS
5-Pd@MIL-101	4.8 (±0.2)
10-Pd@MIL-101	8.3 (±0.4)
15-Pd@MIL-101	13.3 (±0.7)
20-Pd@MIL-101	19.8 (±0.9)

3.3 Interaction with Hydrogen

The hydrogenation properties of the Pd@MIL-101(Cr) composites with the different Pd loadings were studied by Pressure Composition Isotherm, Thermo-Desorption Spectroscopy and *in situ* X-Ray Absorption Spectroscopy.

3.3.1 Pressure-Composition-Isotherm at high pressure and low temperature (77 K)

Hydrogen sorption PCI curves for both MIL-101(Cr) and 10-Pd@MIL-101(Cr) have been measured at 77 K up to 80 bar (*figure 3.11*).

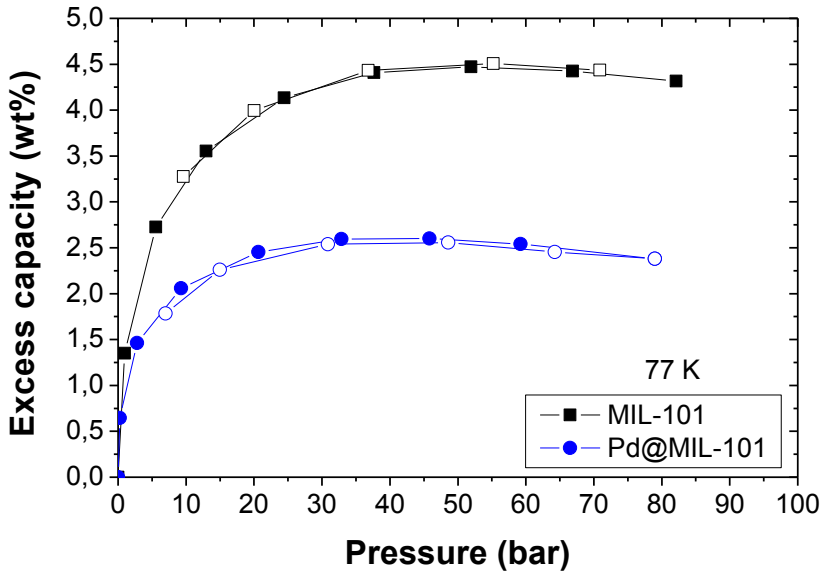

Figure 3.11: The PCI curve recorded at 77 K up to 80 bar for both MIL-101(Cr) (square) and 10-Pd@MIL-101(Cr) (circle). The adsorption and desorption are marked as full and empty symbols, respectively.

Adsorption of hydrogen is completely reversible for both MIL-101(Cr) and 10-Pd@MIL-101(Cr), irrespective of the temperature. This clearly points out that the hydrogen interaction in these pressure and temperature conditions is based on adsorption at the surface since hydrogen absorption in Pd is not expected at such low temperatures. The pristine porous material has a maximum excess capacity of 4.5 wt.% at around 40 bar whereas the 10-Pd@MIL-101(Cr) composite shows a decrease of excess capacity to around 2.5 wt.% at a similar pressure. This reduced value of excess capacity can be understood in terms of the decrease of the specific surface area and porous volume after Pd insertion. In fact, it is well known that the hydrogen adsorption capacity of porous materials at 77 K and high pressure can be linearly correlated to their specific surface area and microporous volume.[2–4] The present adsorption capacities are on line with this trend and are in good agreement with previously reported values of MOF's with similar textural properties (*figure 3.12*).[3]

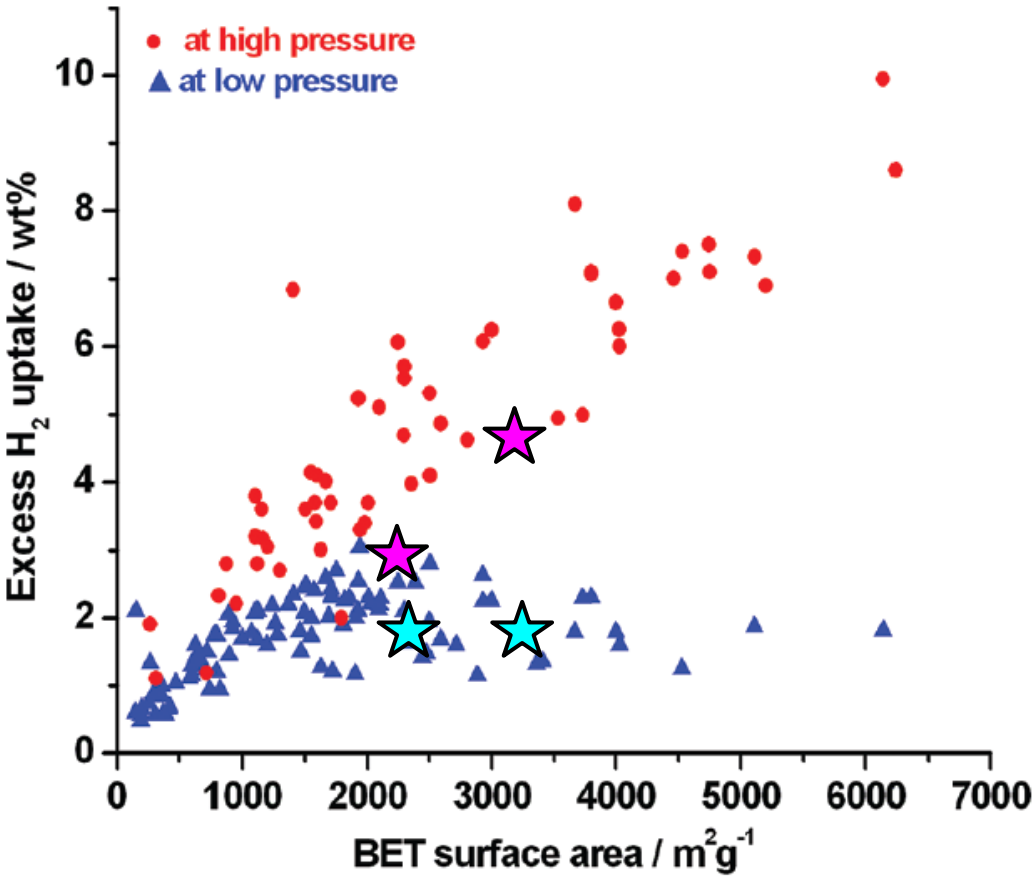

Figure 3.12: Evolution of excess H_2 uptake as a function of BET surface area for MOFs at high (red circle) and low pressure (blue triangle). The present MIL-101(Cr) as well as 10-Pd@MIL-101(Cr) values are represented with stars.

3.3.2 Pressure-Composition-Isotherm at low pressure and low temperature (78 – 107 K)

PCI measurements at low pressure and cryogenic temperatures for both MIL-101(Cr) and Pd@MIL-101(Cr) have been carried out up to 1 bar (*figure 3.13(a) and (b)*). From these curves, the isosteric heat of adsorption for both materials has been calculated using the Clausius-Clapeyron equation (*figure 3.13(c)*)[5]. It varies from 6 to 4 kJ/mol for MIL-101(Cr) with increasing hydrogen excess capacity with an average of 5.2 kJ/mol. This parameter was determined only up to 1 bar hydrogen pressure. This value is in good agreement with previous studies on hydrogen cryo-adsorption in MIL-101(Cr).[6,7]

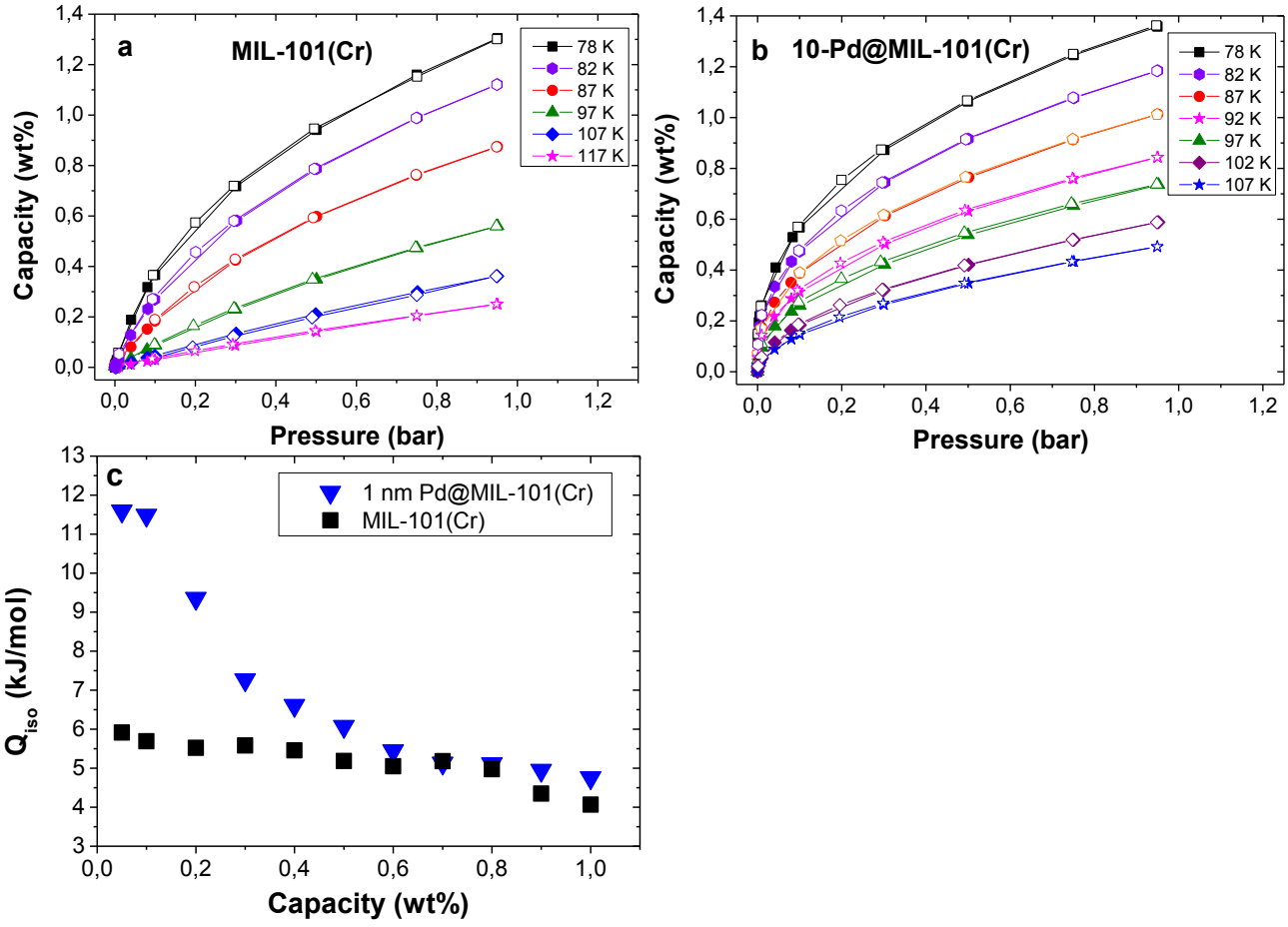

Figure 3.13: (a) PCI curves recorded at several cryogenic temperatures for MIL-101(Cr) and (b) 10-Pd@MIL-101(Cr) where the adsorption and desorption are marked as full and empty symbols, respectively;(c) The isosteric heat of adsorption versus hydrogen excess capacity for both MIL-101(Cr) (square) and 10-Pd@MIL-101(Cr) (triangle).

The isosteric heat of adsorption for 10-Pd@MIL-101(Cr) was also calculated up to 1 wt.% hydrogen sorption capacity. Interestingly, the isosteric heat of adsorption for the 10-Pd@MIL-101(Cr) is around 11.5 kJ/mol at very low capacity (<0.05), which is almost two times higher than 6 kJ/mol for pristine MIL-101(Cr) at similar capacity. However, this value

strongly decreases in the coverage range of 0.05 - 0.2 and reaches similar values at higher sorption capacity. Moreover, this behavior is also observed for other composites with different Pd loadings (*Annex 2*). This proves an enhancement of the hydrogen interaction with Pd doped MIL-101(Cr) relative to pristine material for the first interactions with H_2 molecules, comparable to MIL-101(Cr) doped with $[Mo_6Br_8F_6]^{2-}$ metal atoms clusters[6] and carbon template doped with 3 nm Pd nanoparticles[8]. This feature was confirmed for MIL-101(Cr) doped with $[Mo_6Br_8F_6]^{2-}$ metal atoms clusters by both Clausius-Clapeyron equation and calorimetric measurements whereas the latter method was used to prove the increase of heat of adsorption in carbon template doped with 3 nm Pd nanoparticle, confirming the synergistic effect between metal nanoparticles and porous hosts. The 10-Pd@MIL-101(Cr) shows a steeper increase of capacity at a low pressure relative to MIL-101(Cr) although both materials reach comparable capacity at 1 bar. However, at 1 bar the slope of MIL-101(Cr) is steeper than 10-Pd@MIL-101(Cr) forecasting larger capacity at high pressure of pristine porous solid as compared to the doped material, as experimentally confirmed by high-pressure measurements (*figure 3.11*). Similar trend was observed by Masika *et al.* on nanoparticles of Pd loaded in a zeolite-templated carbon (ZTC) with a loading of 0.2-2wt% and a particle size of 2-5 nm[9].

Thereafter, in order to check the effect of Pd nanoparticle size on the isosteric heat of adsorption, another 10-Pd@MIL-101(Cr) composite has been prepared under slightly different synthetic conditions. In fact, after degassing and prior to liquid impregnation, the powder MIL-101(Cr) was handled in air. The nanoparticles were successfully embedded into the pores of MIL-101(Cr) but their average particle size was 4.5 nm exceeding the pore sizes of the pristine porous host (*Annex 3*). The isosteric heat of adsorption of the latter sample was determined similarly to MIL-101(Cr) and 1 nm 10-Pd@MIL-101(Cr) (*figure 3.14*). A small increase of isosteric heat of adsorption is noticed at low coverage for 4.5 nm Pd@MIL-101(Cr) to 7.5 kJ/mol followed by a fast decrease to the same values as pristine MIL-101(Cr).

The isosteric heat of adsorption of 4.5 nm Pd doped MIL-101(Cr) doesn’t show the impressive rise observed for 1 nm Pd doped sample at low coverage. Therefore, the presence of well dispersed ultra-small Pd nanoparticles is essential for enhancing the hydrogen interaction with porous MIL-101(Cr).

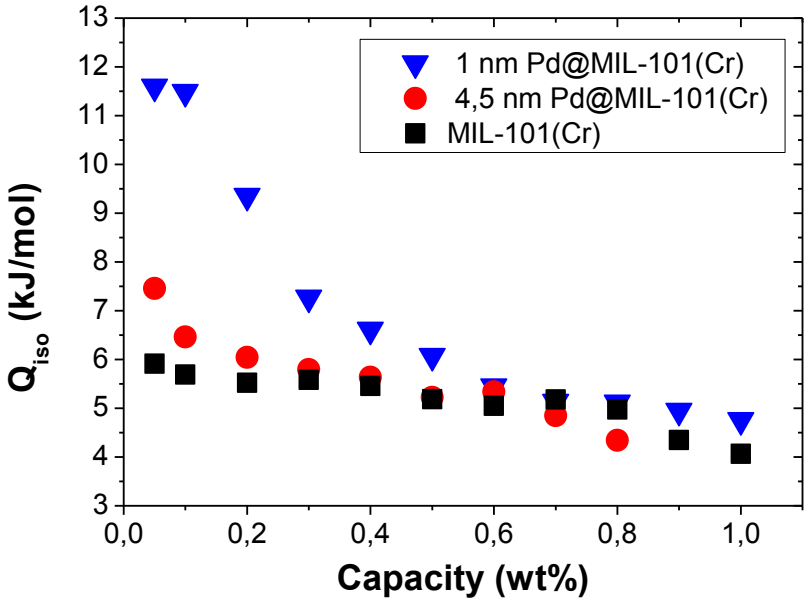

Figure 3.14: Isosteric heat of adsorption as a function of hydrogen excess capacity (expressed in wt%) for two different composites: 10-Pd-1nm@MIL-101(Cr) and 10-Pd-4.5nm@MIL-101(Cr).

3.3.3 Pressure-Composition-Isotherm at low pressure and room temperature

Hydrogen sorption for different Pd@MIL-101(Cr) composites at 300 K up to 1 bar is expected to include both H_2 adsorption on the internal surface of the material and hydrogen absorption in Pd nanoparticles, as already experienced for other Pd doped MOFs[10,11]. The adsorption on the porous scaffold is small under these conditions (<0.01 wt.%) and consequently the hydrogen capacity can be entirely attributed only to Pd nanoparticles.

We have chosen to present here only the PCI curve for the highest Pd loading (20 wt.%) since no real differences could be observed among the composites (*Annex 4*) (*figure 3.15*). The choice was motivated by the aim to ensure high accuracy of PCI volumetric measurements. It is well known that the system volume to sample active mass ratio is one of the most important factors affecting the accuracy of volumetric PCI measurements.[12–14] Thus, the highest Pd loading is necessary to guarantee the smallest uncertainties of the measurement.

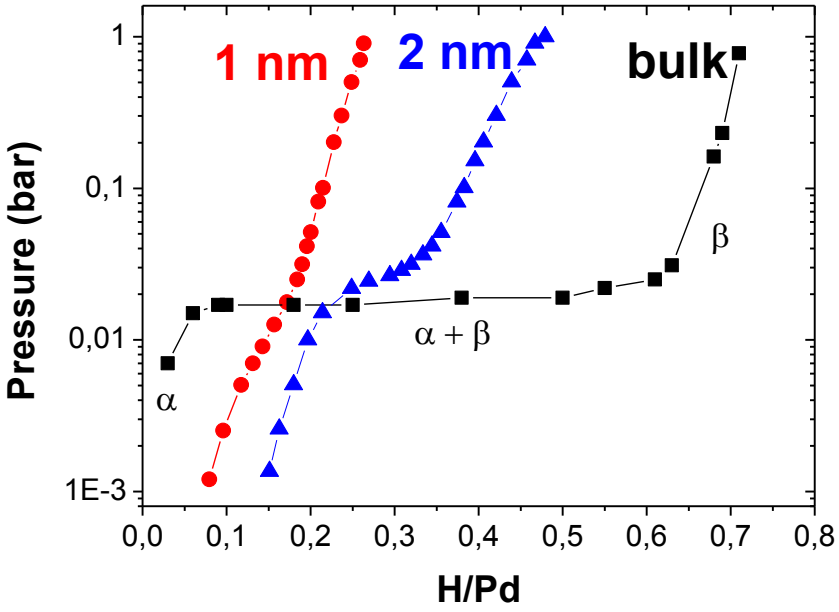

Figure 3.15: PCI curves of bulk Pd (square), 2 nm Pd nanoparticles (triangle)[15] *and 1 nm Pd clusters (circle) performed at 300 K up to 1 bar H_2 pressure. The capacity is expressed as H/Pd.*

The PCI curves of the bulk and 1 nm Pd (20-Pd@MIL-101(Cr)) at 300 K are shown in *figure 3.15*. For comparison purpose, the PCI curve of 2 nm Pd nanoparticles supported on carbon[15] was also plotted, as measured by the same instrument. Interestingly, no plateau pressure could be observed for 1 nm Pd clusters suggesting that such ultra-small nanoparticles do not form a hydride phase contrary to the bulk that forms interstitial hydride under these conditions. This result is also in contrast with 2-3 nm Pd nanoparticles, showing hydride formation under these conditions[16]. The absence of the pressure plateau with the 1 nm Pd cluster can be understood by the decrease of the critical temperature (T_C) of the two-phase region (α-β) below RT, as suggested earlier for nanocrystalline Pd systems[17–20]. *Figure 3.16* represents a schematic evolution of the biphasic zone of the Pd-H phase diagram as a function of nanoparticles size. The T_C for bulk Pd is around 573 K, it decreases for nanoparticles of 2.6 nm, which has been shown by Yamauchi *et al.*[17] and the T_C is 423 K. To confirm the decrease of the critical temperature for the present 1 nm clusters below 300 K, a low-temperature hydrogen desorption study was performed (see paragraph 3.3.5.2).

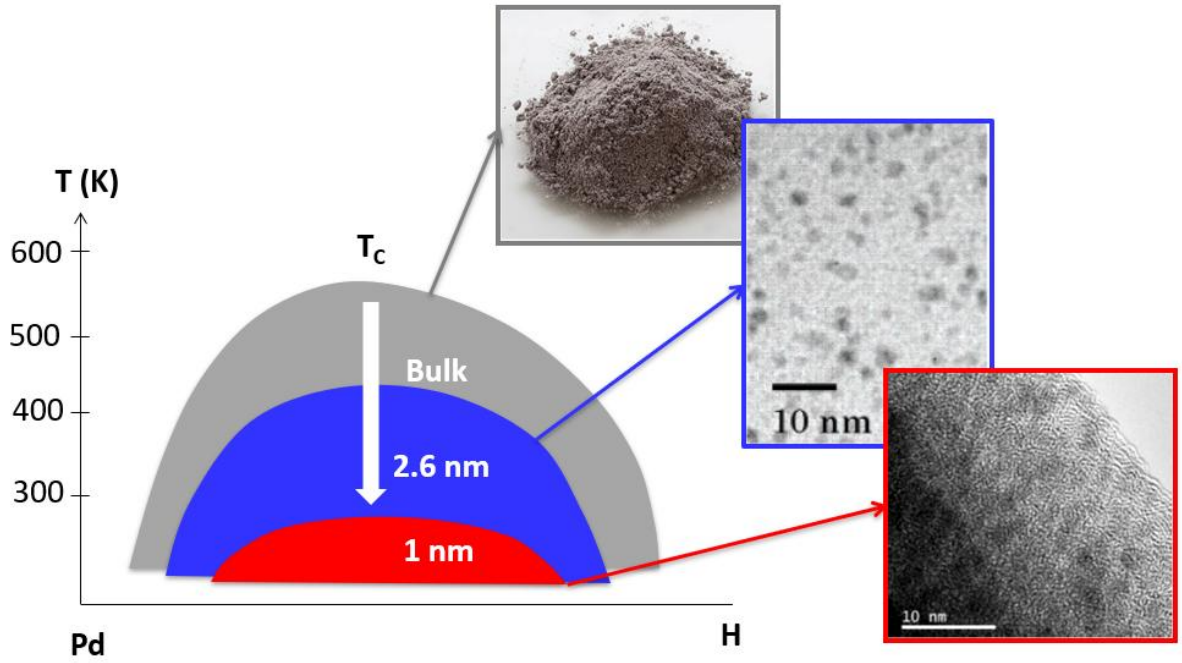

Figure 3.16: Size effect on Pd-H phase diagram: Decrease of the Tc of the miscibility gap by decreasing the particle size.

3.3.4 In-situ X-Ray Absorption Spectroscopy

In order to investigate the local structure in 1 nm Pd clusters under different gaseous environments, *in situ* XAS was carried out under 1 bar H_2 and He at room temperature on the ROCK beamline at SOLEIL synchrotron. The 10-Pd@MIL-101(Cr) composite was chosen for this experiment to optimize the absorption coefficient at the Pd K edge (24350 eV) in transmission mode. The XANES regions show a negligible shift, irrespective of the sample and gas atmosphere as shown in *figure 3.17*. This might suggest that Pd nanoparticles have negligible interaction with the porous MIL-101(Cr), in good agreement with the literature.[21,22]

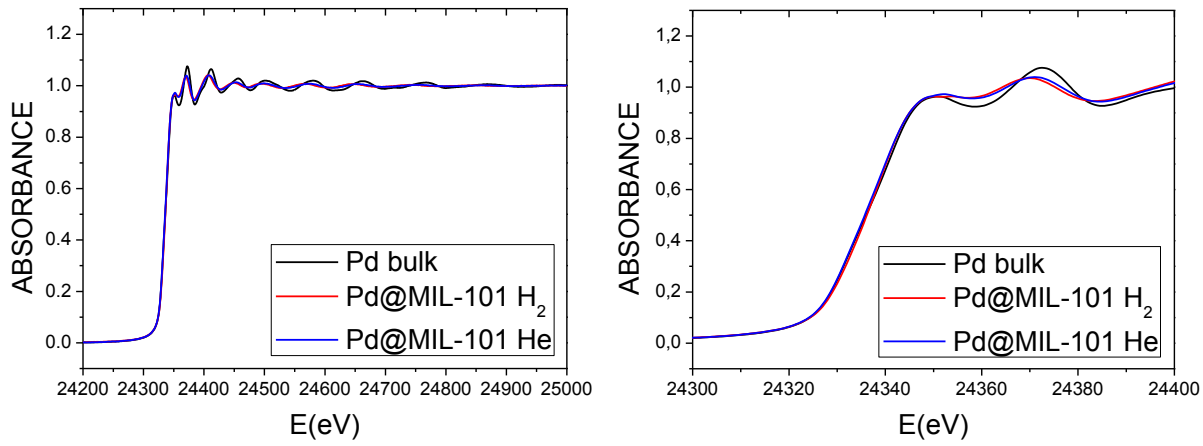

Figure 3.17: (a) XAS and (b) XANES spectra for Pd bulk under air (black) and Pd@MIL-101 under 1 bar He (blue) and H_2 (red) at 300 K.

Figure 3.18 depicts the EXAFS signal and the corresponding modules of the Fourier transform for bulk Pd and 1 nm clusters under a He and H_2 atmosphere. Under an inert atmosphere, the main FT peak of 1 nm Pd diminishes as compared to that of the bulk. Moreover, the FT of 1 nm Pd almost vanishes for large distances. This suggests a negligible contribution from higher atomic shells to 1 nm nanoparticles, in agreement with their ultra-small size.

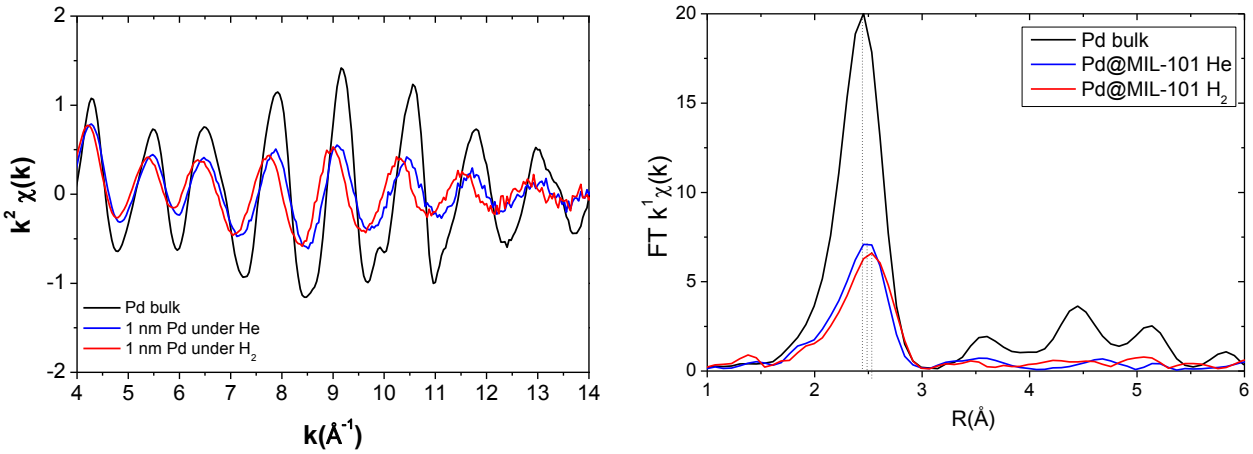

Figure 3.18: (a) Experimental EXAFS spectra at the Pd K edge and (b) the corresponding module of the Fourier transform (FT) of bulk Pd (black) and 1 nm Pd under He (blue) and H_2 (red) at 300 K. The dotted lines indicate the positions of the main FT peak.

The EXAFS refinement results for all samples under different environments are listed in *table 3.2*. The *fcc* crystalline structure typical for bulk Pd was used for first shell EXAFS refinements of 1 nm clusters.

Moreover, the first neighbor distance ($R_{Pd\text{-}Pd}$) of 1 nm Pd clusters under inert gas is slightly larger as compared to that of bulk Pd, in very good agreement with the interplanar expansion observed from HR-TEM.

Table 3.2: Results of EXAFS refinements for the first shell of ~ 1 nm Pd clusters under different gaseous environments at 300 K: coordination number (N), Debye-Waller factor (σ^2), nearest neighbor distance (R_{Pd-Pd}) and the quality of fit (QF).

Sample	Gas	Pd K edge			
		N	σ^2 (Å^2)	R_{Pd-Pd} (Å)	QF
Pd bulk	air	12	0.0078(1)	2.744(1)	0.02
	H_2 [23]	12	0.0080	2.840	-
Pd@MIL-101	He	7(0.5)	0.0103(3)	2.755(3)	0.21
	H_2	7(0.5)	0.0105(4)	2.786(4)	0.17

The refinement values obtained for bulk Pd are in very good agreement with results published earlier.[23] Typical refinement results for bulk and 1 nm Pd clusters under He environment are shown in *figure 3.19*.

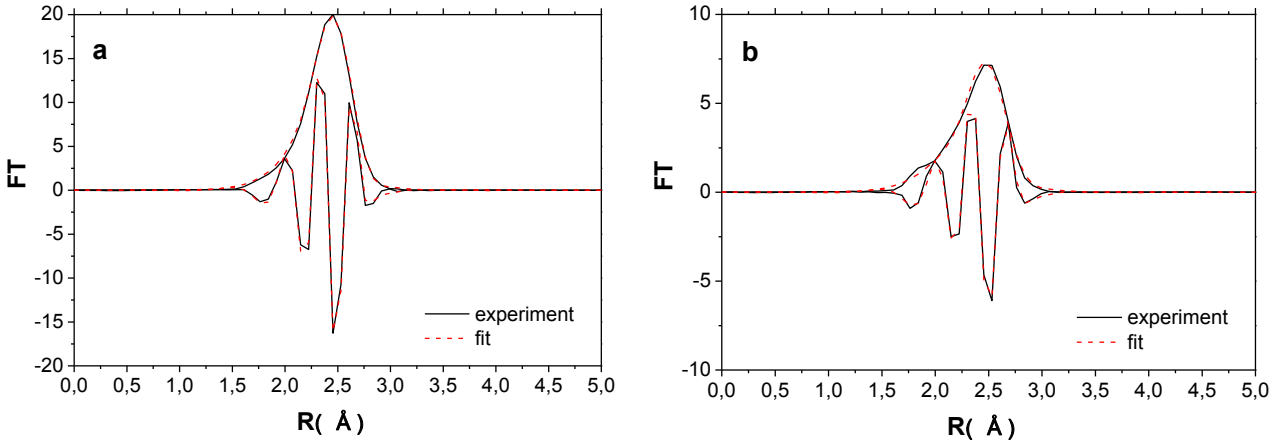

Figure 3.19: Comparison between FT experimental (black) and fitted (red) by EXAFS refinements at Pd K edge for (a) bulk Pd and (b) Pd@MIL-101 under He.

From EXAFS refinements, a decrease of the coordination number is noticed from 12 to 7 from the bulk to 1 nm nanoparticles, as expected for nano-objects.[24,25] Jentys has demonstrated that the coordination number of the first shell of *fcc* metal clusters does not significantly depend on the particle shape, and therefore this value can be used to estimate the average particle size.[26] He proposed a hyperbolic function to determine the coordination number of each *i* shell:

$$N_i = \frac{aN_{at}}{b+N_{at}} + \frac{cN_{at}}{d+N_{at}}$$

where for the first shell (i = 1) a = 8.910, b = 9.640, c = 3.026 and d = 1462.61. Thus, for N_1 = 7 the *fcc* metal clusters comprise approximately 30-40 atoms, which is typical for spherical clusters with 1 nm diameter. This size is below the sizes of the MIL-101(Cr) mesopores (2.9 and 3.4 nm) and consequently, the crystalline structure of the MIL-101(Cr) is maintained, as demonstrated by XRD and FTIR. This value agrees well with the average nanoparticle size of 1 nm obtained by direct observation of TEM images.

The Debye-Waller factor strongly increases from the bulk to 1 nm clusters. Lower coordination numbers are correlated with the increased static disorder in the first shell metal-metal bond lengths, as already suggested for Pt nanoparticles.[27] This can be explained by the relaxation of bond length at the surface, which undergoes substantial strain due to the high curvature of the solid.

Under an H_2 atmosphere, the main FT peak of the Pd clusters is slightly shifted to larger distances, as compared to nanoparticles under an inert gas as shown in *figure 3.18*. Moreover, the intensities of the FT peaks decrease under H_2 gas. This is due to the increased disorder by hydrogen insertion, as also suggested by the increase of the Debye-Waller factor (*Table 3.2*). A similar increase is observed for bulk upon hydrogenation.[8] From EXAFS refinements, an expansion of the $R_{Pd\text{-}Pd}$ distances from 2.75 to 2.78 Å under He and H_2 gas (ΔR = 0.03 Å), respectively, is noticed clearly proving the occurrence of hydrogen absorption in these ultra-small nanoparticles at room temperature and under 1 bar of H_2. Moreover, from previous EXAFS experience on hydrogen absorbing Pd-based nanoparticles, an increase of ΔR around 0.03 Å is in agreement with solid solution formation[21,22] whereas the hydride phase is accompanied by larger expansion ($\Delta R \geq$ 0.05 Å for 2.0 nm Pd nanoparticles forming hydride)[22,23].

3.3.5 Hydrogen desorption properties

The hydrogen desorption properties of MIL-101(Cr) and 10-Pd@MIL-101(Cr) were investigated by the Thermo-Desorption Spectroscopy technique, by applying a constant heating rate of 5 K/min from 22 to 300 K, in which the partial pressures were followed by a mass spectrometer. Several desorption were recorded by TDS at low temperature on pristine MIL-101(Cr) and 10-Pd@MIL-101(Cr) composite. Several desorption protocols were used, depending on the temperature range to be studied and the desired study of the interaction of hydrogen with the material. Four protocols have been established:

(1) The first protocol was carried out by Michael HIRSCHER at Max Planck Institute for Intelligent Systems in Stuttgart (Germany) and was used to study the hydrogen desorption at a temperature range between 22 and 120 K. Prior to the measurement, the samples were degassed at 473 K for 10 h under high vacuum, while an additional H_2 treatment was taken for 10-Pd@MIL101(Cr). Both samples were exposed for 10 min at different temperature (300, 200, 77 and 30 K), and then cooled down to 22 K under hydrogen atmosphere. The desorbed H_2 partial pressure was then recorded while applying a constant heating rate (6 K/min)

(2) The second protocol, as well as the two following, were carried out at ICMPE. The desorbed samples were exposed to 1 bar of hydrogen at room temperature then cooled under gas pressure to 78 K and subsequently evacuated under secondary vacuum. Then, the desorbed H_2 partial pressure was recorded while applying different constant heating rates (from 2 to 12 K/min) up to 310 K. The activation energy of desorption is subsequently calculated using the Kissinger method [28] illustrated by the equation below:

$$ln\left(\frac{\beta}{T_m^2}\right) = -\frac{E_a}{RT_m} + ln(k_0) \qquad \textbf{(Equation 3.1)}$$

where: E_a is the activation energy, β is the heating rate, T_m is maximum temperature corresponding to the peak of desorption, R is the gas constant and k_0 is a pre-exponential factor.

(3) The third protocol was carried out to check the hydrogen diffusion and hydride formation in different materials as a function of temperature. The desorbed samples were exposed to 1 bar of hydrogen at different temperature (78, 100, 125, 150, 200 and 300 K) and cooled to 78 K under gas. Afterward, they were evacuated under secondary vacuum and the desorbed H_2 was recorded while applying a constant heating rate of 5 K/min up to 310 K.

(4) The forth protocol was performed to check the hydride formation at a fixed temperature without cooling under H_2 gas to 78 K. The desorbed sampled were exposed to 1 bar of hydrogen at a series of temperatures (150, 200, 225 and 240 K) for 5 min, without further cooling to 78 K. Afterwards, they were evacuated under secondary vacuum at a fixed temperature and the desorbed H_2 was recorded while heating with a constant temperature increase of 2 K/min up to 310 K.

3.3.5.1 Hydrogen desorption for MIL-101(Cr)

In order to study the physisorption interactions in the temperature range of 22 – 120 K, measurements following protocol no. 1 were carried out and represented in *figure 3.20*. For pristine MIL-101(Cr), three hydrogen desorption peaks occur at 35 K, 45 K and 70 K, while no significant desorption peak was observed above 120 K, in agreement with previous TDS result of MIL-101(Cr).[6] These three desorption peaks could be clearly assigned to specific adsorption positions in the MIL-101(Cr) structure.

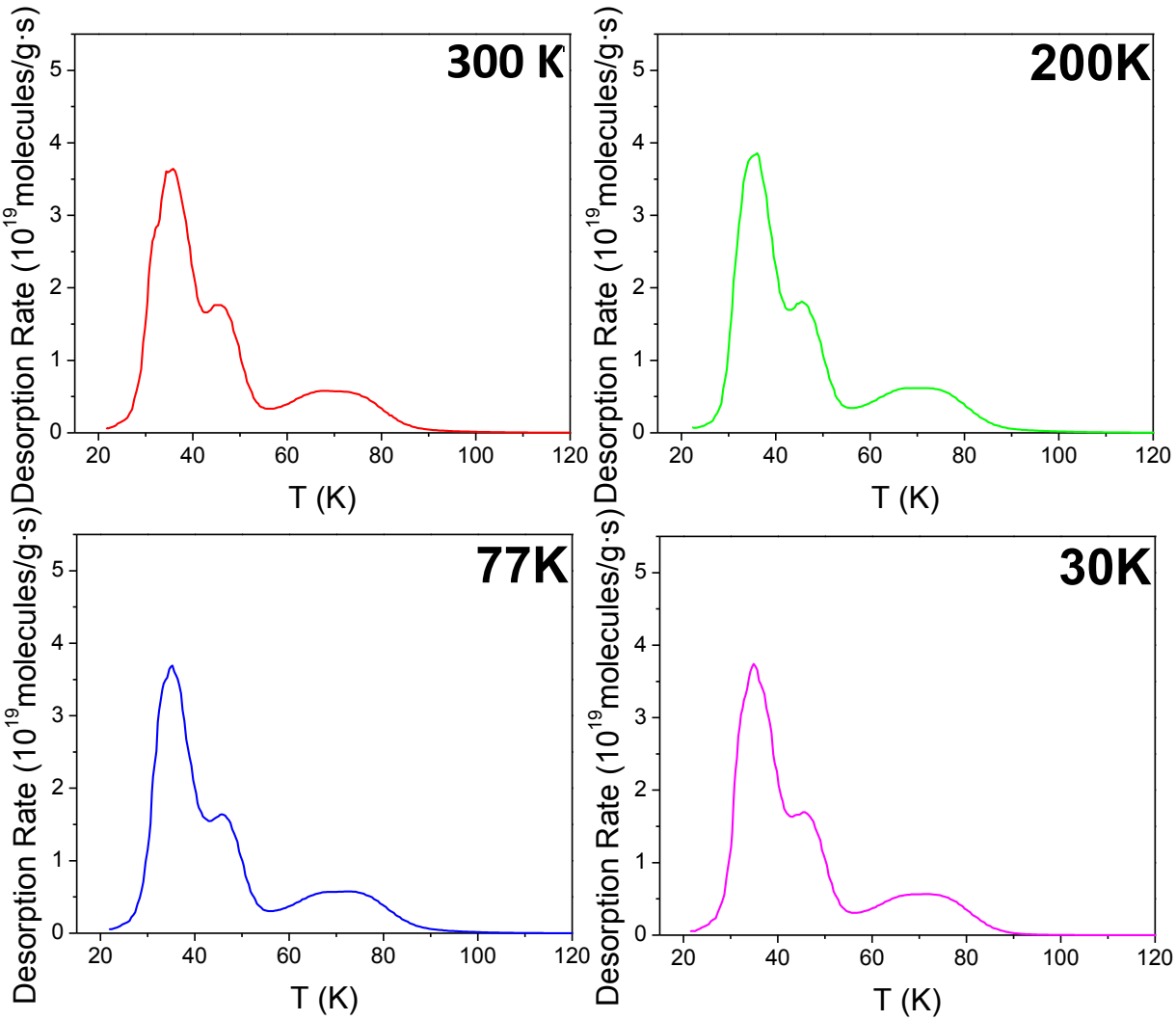

Figure 3.20: Thermo-desorption spectra of MIL-101(Cr) with a heating rate of 5 K/min. The samples were previously loaded with H_2 at 300 K, 200 K, 77 K and 30 K followed by cooling under H_2 to 22 K.

MIL-101(Cr) is a MOF based on SBU (secondary building units) of type μ_3-oxo-centered trimers of octahedral Cr(III) formed by the assembly of three octahedra sharing a μ_3-O common vertex, connected by phenylene rings.[29] Its adsorption sites are associated with the

secondary building units and the linker. Its chemical composition is $(Cr_3O)X(H_2O)_2[O_2C\text{-}C_6H_4\text{-}CO_2]_3$ and exhibits a cationic framework with a negative default charge per trimer of Cr(III) octahedra, which is compensated by one fluorine ion ($X=F^{-1}$, Cl^{-1}, OH^{-1}). [29,30] Thus, in the present case, the terminal molecules on two of the three Cr(III) octahedral are water molecules and Cl^{-1} on the third. These terminal water molecules are removable from the framework by degassing under vacuum at a temperature above 423 K, leading to the two Cr(III) CUS (coordinative unsaturated sites – *figure 3.21*).

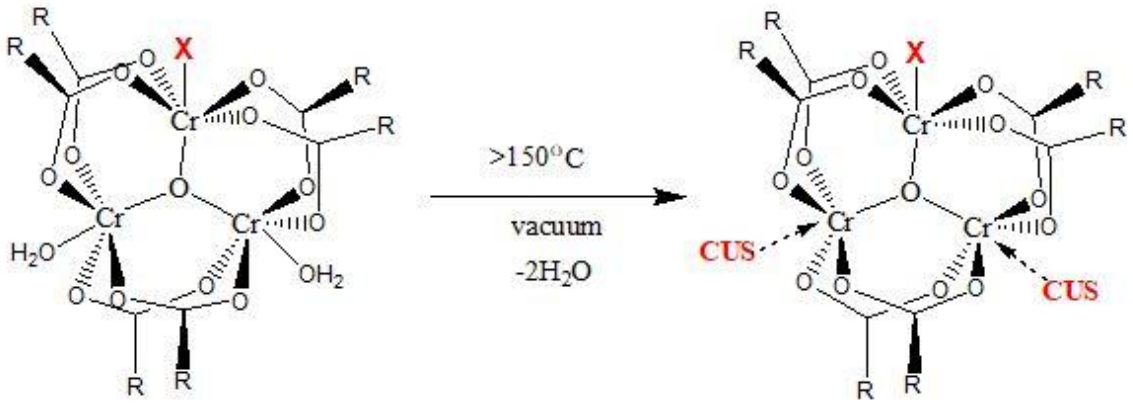

Figure 3.21: Hydrogen adsorption sites in MIL-101(Cr): CUS (red) sites ascribed to the high energy adsorption sites (~ 70 K in TDS spectra)

On a descending scale of the strength of interaction with hydrogen, the first adsorption sites are these two CUSs which can accommodate 2 hydrogen molecules (1 molecule/CUS) which are desorbed at ~ 70 K (*figure 3.20*). Similarly to the adsorption sited in MOF-5 [31,32] we have identified additional adsorption sites in MIL-101(Cr). Thus, the second adsorption sites, also in number of two, are the positions at the center of the three CrO_3 triangular faces, termed the "CUP sites" (*figure 3.22*). They can accommodate 2 hydrogen molecules (1 molecule/site), which might be assigned to the desorption peak at ~ 45 K (*Figure 3.19*).

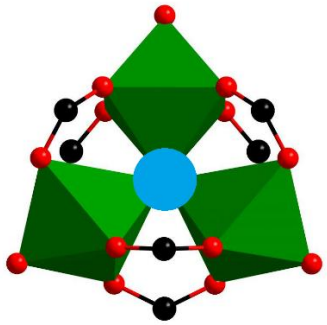

Figure 3.22: Hydrogen adsorption sites in MIL-101(Cr): CUP sites (blue) identified as medium energy sites (~ 45 K in TDS spectra).

In addition, the adsorption sites include the site on top of single CrO_3 triangle (noted CrO_3 site, in number of 12/SBU), the site just above the edge of a CrO_6 octahedron (noted CrO_3 site, in number of 12/SBU), the site above phenylene face (2/phenylene ring) and the site on the phenylene edge (2/phenylene ring) (*figure 3.23*). The hydrogen accommodated in these (less strong) sites should be desorbed at lower temperatures and could be assigned to the peak ~ 35 K.

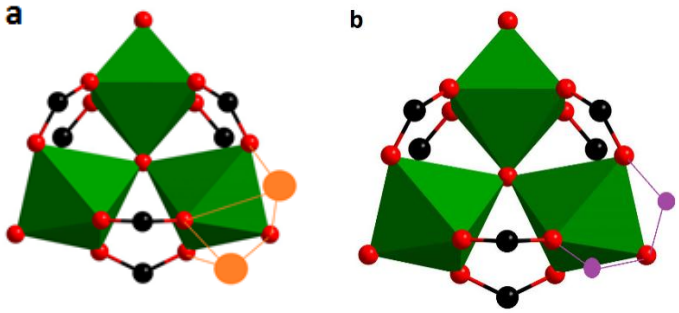

Figure 3.23: Hydrogen adsorption sites in MIL-101(Cr): Other adsorption sites: the positions marked in orange and purple identified as low energy sites (~ 35 K in TDS spectra).

Under the hypothesis that the peak area corresponds to the amount of hydrogen desorption from each type of site, we have performed a fitting of TDS signal of MIL-101(Cr) with 3 Gaussian curves (*figure 3.24*) and extracted the corresponding area of the peaks for all temperature conditions (see table below).

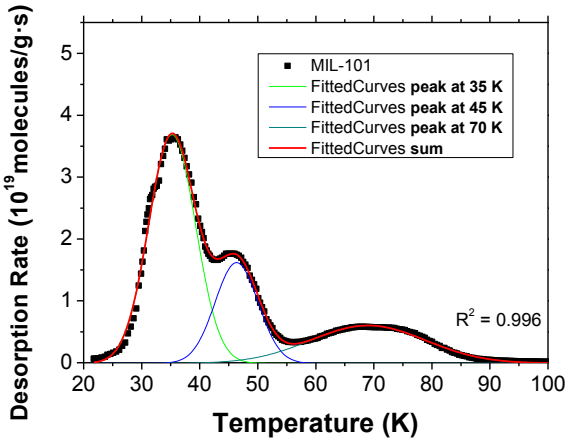

	MIL-101(Cr)		
H_2 loading T (K)	Peak at 35 K	Peak at 45 K	Peak at 70 K
30	33.5	17.9	14.2
77	34.4	17.9	15.7
200	34.4	17.9	15.8
300	37.5	15.1	15.2
Average	34.9	17.2	15.2
Percent %	52	25	23

Figure 3.24: Fitting results of the TDS spectra from MIL-101(Cr) loaded with hydrogen at 300 K and the table summarizing the area of the desorption peaks as calculated from TDS spectra for MIL-101(Cr) recorded at different hydrogen loading temperatures.

The low energy peak consists of around 50 % of the total TDS signal, whereas the medium and high energy peaks are approximately 25 % each. Thus, the latter two sites can adsorb a similar amount of H_2, in agreement with geometrical consideration: 2 H_2 molecules

are desorbed from both CUSs and CUPs. The other various low energy sites can store two times more hydrogen than CUS or CUP sites (~50 %).

3.3.5.2 Hydrogen desorption for 10-Pd@MIL-101(Cr) composite

As for the MIL-101(Cr), hydrogen desorption from 10-Pd@MIL-101(Cr) was carried out by TDS using the protocol no. 1 and represented in *figure 3.25*.

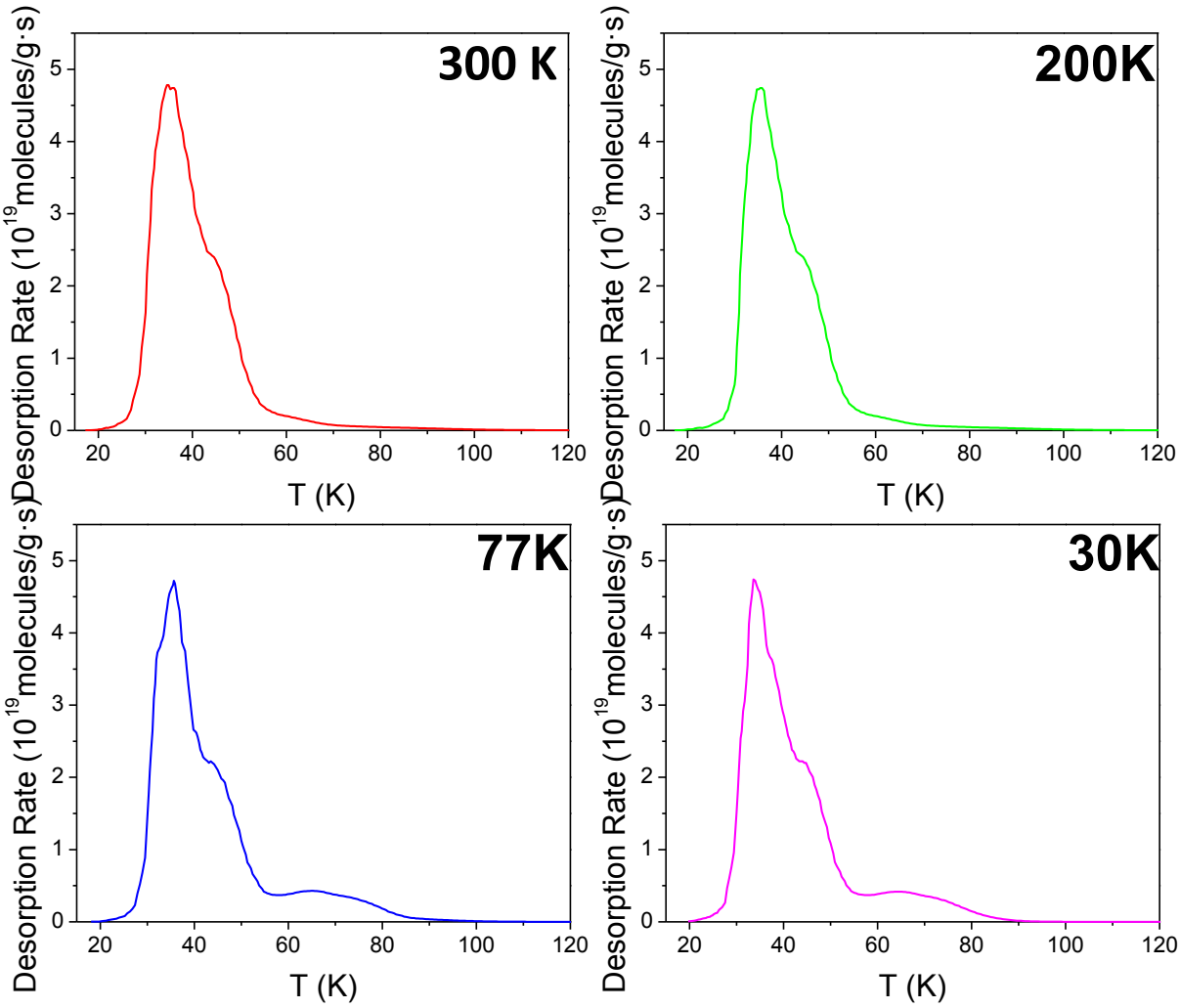

Figure 3.25: Thermo-desorption spectra of 10-Pd@MIL-101(Cr) with a heating rate of 5 K/min. The samples were previously loaded with H_2 at 300 K, 200 K, 77 K and 30 K followed by cooling under H_2 to 22 K.

The physisorption phenomenon was studied at first in temperature range of 20-120 K. The TDS spectra of 10-Pd@MIL101(Cr) exhibits similar first two low temperature signals to MIL-101(Cr) at around 35 to 45 K whereas, the desorption peak at 70 K disappears for measurements performed with a H_2 exposure at 200 and 300 K (*figure 3.25*). This might suggest that these high energy sites are shadowed by the presence of Pd clusters. Another

interesting feature of 10-Pd@MIL-101(Cr) is the occurrence of an additional desorption peak at around 66 K when this sample is charged with hydrogen at 30 and 77 K (*figure 3.25*).

Since the crystalline structure of MIL-101(Cr) is preserved by Pd doping, we expect similar adsorption sites in 10-Pd@MIL-101(Cr). The first two low-temperature signals around 35 and 45 K are still active, irrespective of hydrogenation conditions (*figure 3.25*). On the contrary, the high energy sites are very sensitive to the hydrogenation conditions. Upon charging with hydrogen at 30 and 77 K the high energy sites are active with a maximum at 66 K, although the relative contribution of this peak to the total desorbed H_2 amount (*figure 3.26*) is reduced (15 %) relative to pure MIL-101(Cr) (23%). On the contrary, when 10-Pd@MIL-101(Cr) is hydrogenated at high temperatures such as, 200 and 300 K, the TDS spectra did not show any high energy desorption peak (*figure 3.25*). This finding is unexpected and might suggest that high energy sites are "hindered" by the presence of Pd clusters. One hypothesis is based on the favorite location of Pd clusters close to the CUS sites that might become inaccessible when clusters are hydrogenated.

The fitting of the TDS signal from 10-Pd@MIL-101(Cr) was performed with 2 or 3 Gaussian curves, depending on the hydrogenation conditions, and the related peak areas have been calculated (*figure 3.26*). One example of fitting of the spectra loaded with hydrogen at 300 K is shown in *figure 3.26*. The average amount of medium energy sites overpasses the one of low energy sites, except the loading at 77 K.

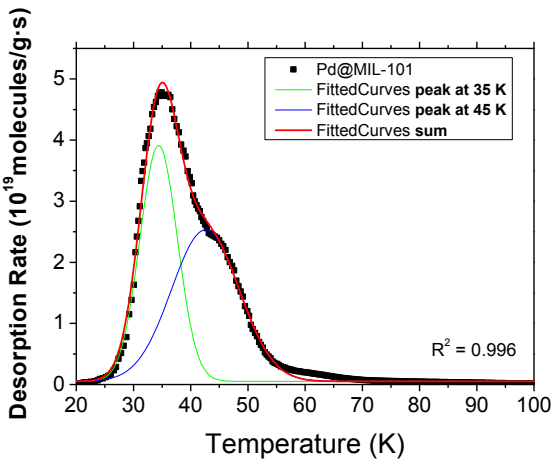

	10-Pd@MIL-101(Cr)		
H_2 loading T (K)	Peak at 35 K	Peak at 45 K	Peak at 66 K
30	24.3	37.6	10
77	35.7	25.7	11.6
Average ≤ 77 K	30	31.6	10.8
Percent %	41.4	43.6	15
200	26.5	36.9	0
300	31.7	36.7	0
Average > 77 K	29.1	36.8	0
Percent %	44.2	55.8	0

Figure 3.26: Fitting results of the TDS spectra from 10-Pd@MIL-101(Cr) loaded with hydrogen at 300 K and the table summarizing the area of the desorption peaks as calculated from TDS spectra for 10-Pd@MIL-101(Cr) recorded at different hydrogen loading temperatures.

Another important aspect is the link between results obtained from PCI and TDS. Using the former technique, it was demonstrated that the isosteric heat of adsorption in Pd@MIL-101(Cr) is increased at low coverage relative to pristine MIL-101(Cr). Thus, one could expect changes in the TDS spectra from 10-Pd@MIL-101(Cr), *i.e.* extra desorption peaks at high temperature. However, we did not observe such behavior for 10-Pd@MIL-101(Cr). One possible explanation of this apparent contradiction is the fundamental difference between these two techniques: TDS is mainly exploring desorption kinetic properties, whereas the PCI curves are measured under thermodynamic equilibrium conditions.

Hydrogen desorption from the bulk and 1 nm Pd clusters was studied in the temperature range of 78-300 K. The spectra of both bulk powder and 1 nm clusters following the protocol no. 2 (with 2 K/min) are shown in *figure 3.27*. In fact, TDS spectra of both 1 nm clusters and bulk Pd show similar two-peak desorption: the first peak at low temperature is smaller than the second one occurring at a higher temperature. The two-peak shape is a common feature for hydrogen desorption from hydride forming bulk Pd powders: the first desorption peak (at a lower temperature) points to the desorption from the β phase and the most intense peak corresponds to desorption that accompanies the β to α phase transformation. Thus, the presence of two peaks for 1 nm Pd clusters clearly indicates hydrogen desorption from the hydride phase formed during cooling to 78 K under hydrogen.

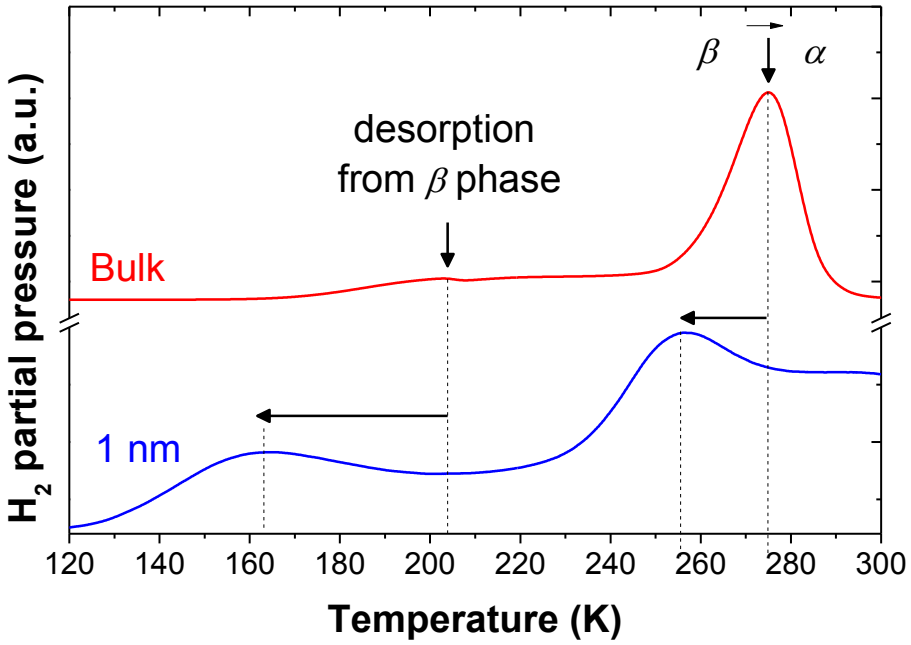

Figure 3.27: Thermo-desorption spectra of the bulk and 1 nm Pd with a heating rate of 2 K/min following protocol no.2.

The positions of these couples of peaks are 163 and 225 K for 1 nm cluster and 204 and 275 K for the bulk counterpart. These temperatures are lower for 1 nm clusters as compared to those of bulk powder proving faster desorption in 1 nm clusters than the bulk counterpart.

The area of the TDS signal corresponds to the total amount of desorbed hydrogen in 1 nm Pd cluster. A value of H/Pd = 0.3 (±0.01) was calculated considering the bulk $PdH_{0.7}$ spectrum as a reference at the same heating rate. This value is in agreement with previous capacities reported for hydride forming 2-3 nm Pd nanoparticles.[10,17,33]

3.3.5.3 Hydrogen diffusion

The hydride formation in 1 nm Pd clusters strongly depends on the hydrogen loading conditions. *Figure 3.28* shows the TDS spectra from 1 nm Pd clusters recorded following the protocol no. 3. The TDS spectra for samples exposed to H_2 below 100 K do not show any clear desorption peaks. This demonstrates that 1 nm Pd hydride cannot be formed below 100 K, in agreement with the low hydrogen diffusion in Pd at cryogenic temperatures.

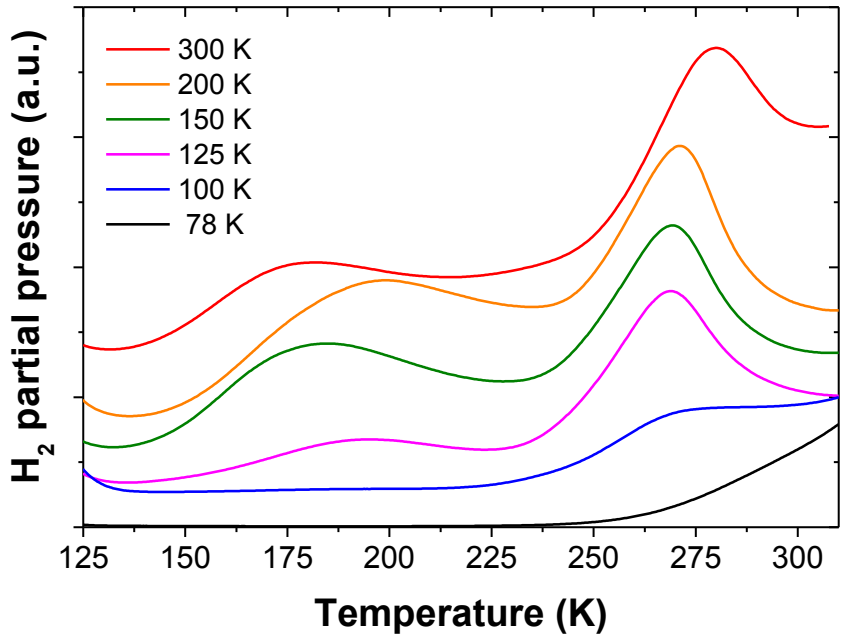

Figure 3.28: Thermo-desorption spectra of 1 nm Pd clusters exposed to H_2 at different temperatures (78, 100, 125, 150, 200 and 300 K) performed at 5 K/min following protocol no 3.

3.3.5.4 Hydride formation

The TDS spectra of 1 nm Pd recorded following the protocol no. 4 are plotted in *figure 3.29*. The presence of the desorption peak corresponding to β → α transformation for H_2 exposure between 150 and 225 K along with the absence of desorption peak for exposure to H_2 at 240 K proves that the hydride phase forms and stabilizes at temperatures ≤ 225 K. The exposure to higher temperature only forms solid solutions with hydrogen in Pd, in agreement with PCI and *in situ* EXAFS investigations. Therefore, the *Tc* of the two-phase region of Pd clusters is located between 225 and 240 K.

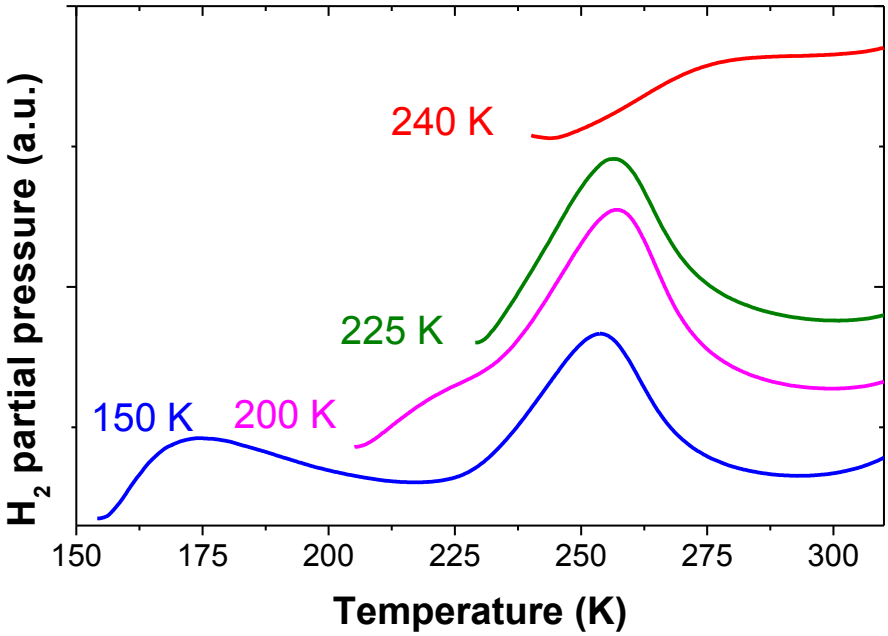

Figure 3.29: Thermo-desorption spectra performed at 2 K/min of 1 nm Pd clusters exposed to H_2 at fixed temperatures (150, 200, 225 and 240 K) without cooling to 78 K following protocol no 4.

3.3.5.5 Activation energy of desorption

The TDS technique allows the calculation of the activation energy of desorption by applying the Kissinger equation (*equation 8*). This method uses the characteristic temperature T_m at which the desorption rate reaches its maximum at different linear heating rates, β (*figure 3.30*).

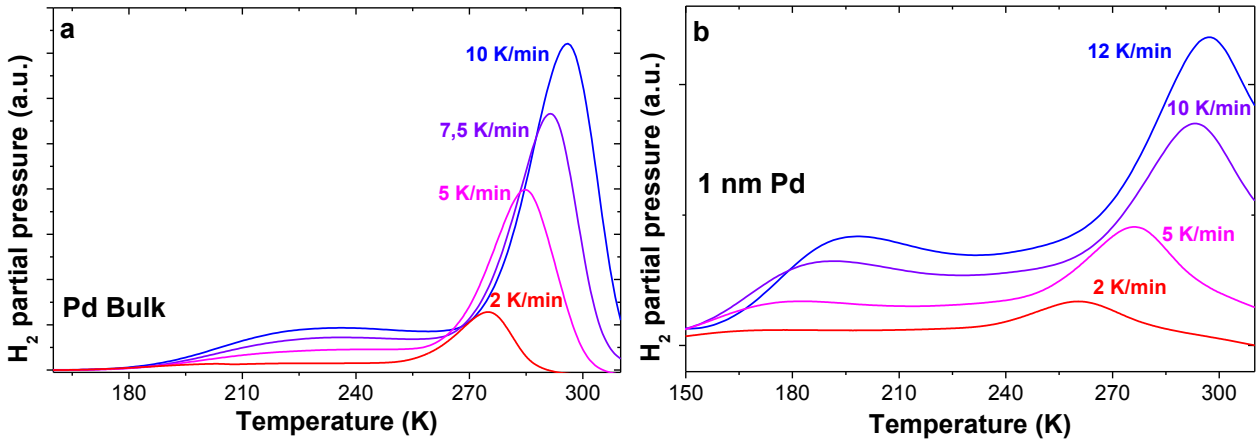

Figure 3.30: Thermo-desorption spectra performed at different heating rates following protocol no 2 for (a) Pd bulk and (b) 1 nm Pd clusters.

Therefore, the logarithmic plot of $\frac{\beta}{T_m^2}$ *vs.*$1/T_m$ gives a straight line with a slope equal to $\frac{E_a}{R}$. A comparison of the Kissinger plots for 1 nm and bulk Pd is displayed in the *figure 3.31*. This analysis was applied for the main desorption peak, corresponding to the hydrogen desorption from the hydride.

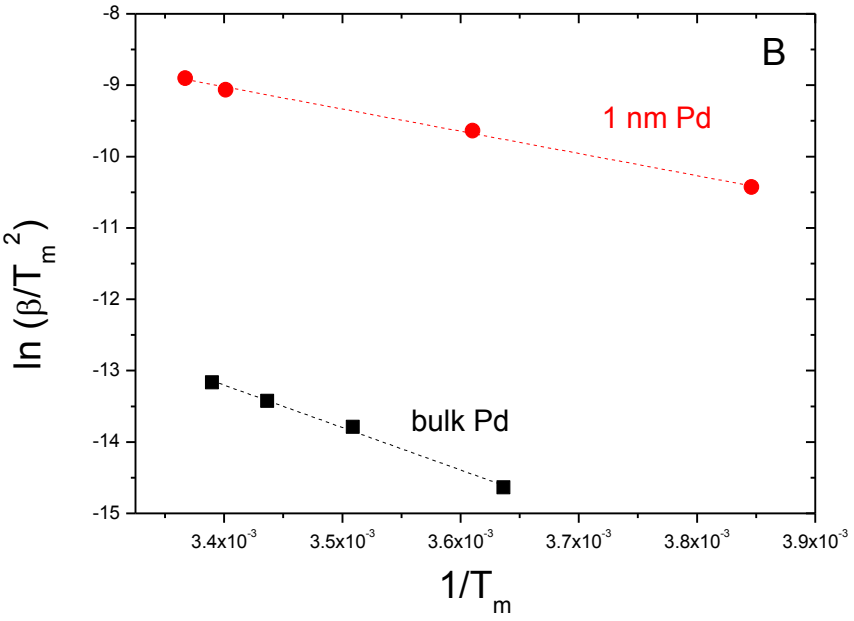

Figure 3.31: The Kissinger plots for bulk powder and 1 nm Pd clusters. The correlation coefficients for the linear regressions are R= 0.99 for both the bulk and 1 nm Pd.

The calculated values of E_a are 0.27(2) and 0.51(2) eV for 1 nm and bulk Pd powder, respectively. The value obtained for bulk Pd powder is in good agreement with previous

results.[34] This strong decrease of the activation energy of desorption from the bulk to 1 nm Pd clusters indicates that the latter have lower thermal stability as compared to the bulk metal which may suggest a change in the rate limiting step of the desorption reaction. The kinetics of desorption include the following processes: bulk diffusion, phase transformation and surface processes. Previously Stern *et al.* demonstrated that hydrogen desorption from bulk Pd powder is limited by surface reactions.[35] A more recent study has thoroughly calculated the activation energies for different desorption steps in bulk Pd.[34] During the desorption from the hydride phase (before β →α transformation) the rate limiting step of desorption is a surface recombination mechanism with rather high activation energy (0.87 eV). During the two-phase region, the rate limiting step is β →α phase transformation with an activation energy of 0.57 eV, close to the value found presently for bulk Pd powder. However, the value found for 1 nm Pd clusters is much smaller (0.27 eV) and intriguingly close to the activation energy of diffusion of hydrogen into either α and β phases (0.23 eV[36] and 0.22 eV[35,37], respectively). This suggests a change of the rate limiting step from surface recombination or β → α phase transformation in bulk Pd powder to hydrogen diffusion into α and β phases in 1 nm clusters. The fact that surface processes are not anymore, the rate limiting reactions is not surprising since 1 nm Pd clusters possess an extremely large surface area of around 500 m^2g^{-1}, under the hypothesis of a spherical morphology of clusters. Moreover, β →α phase transformation is also unexpected to be the rate limiting step of desorption from such small nanoparticles. Very recently Baldi *et al.* have proven sharp transitions between α and β phases in individual Pd nanocrystals that is consistent with a coherent process in which two phase coexistence is suppressed.[20] Likely, the β →α transition in 1 nm Pd clusters must take place instantly since the formation of incoherent interfaces is energetically unfavorable below a critical size of 30 nm[20] and the critical size of the coherent precipitate in bulk Pd is around 4 nm.[38]

3.4 Conclusion

In this chapter, a study of the structural and nanostructural properties of a hybrid material formed by ultra-small palladium nanoparticles confined in the pores of MIL-101 (Cr), as well as the properties of hydrogen sorption was carried out.

The first part of this chapter consists of the preparation of Pd@MIL-101(Cr) materials with different loadings up to 20 wt%. Indeed, after an optimization step, the synthesis technique chosen is the double solvent impregnation (DSM) followed by a reduction under Ar/H_2 flow at 573 K associated with the proper degassing of initial MIL-101(Cr).

The second part of this chapter focused on the physicochemical characterization of the synthesized hybrids. Structural, nanostructural and textural characterization confirmed the careful control of the synthetic conditions allowing the successful preparation of ultra-small Pd nanoparticles of 1 nm size effectively embedded in the mesopores of MIL-101(Cr) for high metal loading. To the best of our knowledge, this is the first time that Pd clusters containing approximately 30-40 atoms are stabilized into a MOF solid.

The last part of this chapter has been devoted to the determination of the hydrogen sorption properties of the Pd@MIL-101(Cr) materials by means of both laboratory and synchrotron facilities. The 1 nm Pd clusters do not form a hydride phase at 300 K and atmospheric pressure, in contrast with bulk and 2 nm sized Pd, as proven by PCI curves. A decrease of the critical temperature below room temperature due to extreme nanosizing can be at the origin of this behavior. However, they absorb hydrogen and form solid solutions under these conditions, as confirmed by *in situ* EXAFS at RT. At lower temperature (125-240 K) they can form a hydride phase, as demonstrated by thermal-desorption spectroscopy. The hydrogenated Pd clusters have lower thermal stability as compared to bulk material most probably due to shorter diffusion path and larger surface area. At lower temperature, the 1 nm Pd clusters can form a hydride phase, as demonstrated by hydrogen desorption spectroscopy. These hydride clusters have lower activation energy of desorption as compared to the bulk material. This suggests a change of the rate limiting step from surface recombination or $\beta \rightarrow \alpha$ phase transformation in bulk Pd powder to hydrogen diffusion into α and β phases in 1 nm clusters.

The presence of 1 nm Pd clusters into the pores of MIL-101(Cr) increases the isosteric heat of H_2 adsorption at low coverage, in contrast with the same material doped with 4.5 nm

Pd particles that does not show any remarkable rise. This is a very interesting result that may open the route to a new synthetic strategy for improving the interaction between H_2 and porous host, *i.e.* ultra-dispersion of Pd into the form of single atoms into the pores of a solid host, comparable to the very recent promising concept of "single-atom catalyst" in the field of heterogeneous catalysis[39].

3.5 Perspectives

The perspectives of this part of the project are mainly related to further characterize the hydrogen sorption properties and to confirm the formation of Pd hydride at low temperature with a second analytical technique. A low-temperature XAS measurement may provide additional information on the interaction of hydrogen with the 1 nm Pd cluster. In addition, it would be interesting to continue the synthesis optimization of Pd@MIL-101(Cr) composites, in order to increase even further Pd doping since porous volume is still available, by successively impregnations, for example.

Moreover, as palladium is an interesting material not only for hydrogen storage, but also in catalysis, using the ultra-small nanoparticles developed in this project in heterogeneous catalytic reactions will provide further study on the efficiency and selectivity of 1 nm Pd clusters. Two catalytic reactions were carried out with Pd@MIL-101(Cr) as catalyst. The catalytic properties of the composite were studied firstly for the Suzuki-Miyaura coupling reaction, which is one of the most important and effective methods for C-C bond formation[40–42]. In this context, bromobenzene and phenylboronic acid were coupled, using 5-Pd@MIL-101(Cr) as catalyst, to form corresponding biaryl products (*Annex 5*). This study was carried out at ICMPE (Thiais, France) in collaboration with Benjamin LE DROUMAGUET. However, despite a successful C-C cross-coupling reaction with Pd nanoparticles doped MIL-101(Cr), an optimization of the experimental protocol of the catalytic reaction is necessary because the catalyst is degraded at the end of the reaction.

The second example of a catalytic reaction (H_2 production from formic acid) is given in the *annex 6* with a study of the catalytic properties of 10-Pd@MIL-101(Cr) composite done in collaboration with our Romanian partner, Gabriela BLANITA, and her team. It has been shown that 1 nm Pd clusters have catalytic activity in decomposition of HCOOH by promoting the dehydrogenation pathway. Interestingly, the Pd doped MIL-101(Cr) retains its crystalline structure during this reaction, in contrary with Suzuki-Miyaura coupling reaction.

References

1. Pallassana, V., Neurock, M., Hansen, L. B., Hammer, B. & Nørskov, J. K. Theoretical analysis of hydrogen chemisorption on Pd(111), Re(0001) and Pd ML / R e (0001) , Re ML / P d (111) pseudomorphic overlayers. *Physical Review B* **60**, 6146–6154 (1999).
2. Collins, D. J. & Zhou, H.-C. Hydrogen storage in metal–organic frameworks. *J. Mater. Chem.* **17**, 3154–3160 (2007).
3. Suh, M. P., Park, H. J., Prasad, T. K. & Lim, D.-W. Hydrogen Storage in Metal–Organic Frameworks. *Chem. Rev.* **112**, 782–835 (2012).
4. Hirscher, M. & Panella, B. Hydrogen storage in metal–organic frameworks. *Scripta Materialia* **56**, 809–812 (2007).
5. Rouquerol, F., Rouquerol, J. & Sing, K. S. W. *Adsorption by powders and porous solids: principles, methodology, and applications*. (Academic Press, 1999).
6. Dybtsev, D. *et al.* Influence of [Mo6Br8F6]2− Cluster Unit Inclusion within the Mesoporous Solid MIL-101 on Hydrogen Storage Performance. *Langmuir* **26**, 11283–11290 (2010).
7. Blanita, G., Coldea, I., Misan, I. & Lupu, D. Hydrogen cryo-adsorption by hexagonal prism monoliths of MIL-101. *International Journal of Hydrogen Energy* **39**, 17040–17046 (2014).
8. Zlotea, C. & Latroche, M. Role of nanoconfinement on hydrogen sorption properties of metal nanoparticles hybrids. *Colloids and Surfaces A: Physicochemical and Engineering Aspects* **439**, 117–130 (2013).
9. Masika, E., Bourne, R. A., Chamberlain, T. W. & Mokaya, R. Supercritical CO2 Mediated Incorporation of Pd onto Templated Carbons: A Route to Optimizing the Pd Particle Size and Hydrogen Uptake Density. *ACS Appl. Mater. Interfaces* **5**, 5639–5647 (2013).
10. Zlotea, C. *et al.* Pd Nanoparticles Embedded into a Metal-Organic Framework: Synthesis, Structural Characteristics, and Hydrogen Sorption Properties. *J. Am. Chem. Soc.* **132**, 2991–2997 (2010).
11. Szilagyi, P. A. *et al.* Probing hydrogen spillover in Pd@MIL-101(Cr) with a focus on hydrogen chemisorption. *Phys. Chem. Chem. Phys.* **16**, 5803–5809 (2014).
12. Broom, D. P. The accuracy of hydrogen sorption measurements on potential storage materials. *International Journal of Hydrogen Energy* **32**, 4871–4888 (2007).

13. Webb, C. J. & Gray, E. MacA. Analysis of the uncertainties in gas uptake measurements using the Sieverts method. *International Journal of Hydrogen Energy* **39**, 366–375 (2014).
14. Hurst, K. E., Parilla, P. A., O'Neill, K. J. & Gennett, T. An international multi-laboratory investigation of carbon-based hydrogen sorbent materials. *Appl. Phys. A* **122**, 42 (2016).
15. Bastide, S., Zlotea, C., Laurent, M., Latroche, M. & Cachet-Vivier, C. Direct assessment from cyclic voltammetry of size effect on the hydrogen sorption properties of Pd nanoparticle/carbon hybrids. *Journal of Electroanalytical Chemistry* **706**, 33–39 (2013).
16. F.A. Lewis. The Palladium-Hydrogen System. *Johnson Matthey Technology Review* Available at: https://www.technology.matthey.com/article/26/3/121-128/. (Accessed: 23rd May 2019)
17. Yamauchi, M., Ikeda, R., Kitagawa, H. & Takata, M. Nanosize Effects on Hydrogen Storage in Palladium. *The Journal of Physical Chemistry C* **112**, 3294–3299 (2008).
18. Weissmuller, J. & Lemier, C. On the size dependence of the critical point of nanoscale interstitial solid solutions. *Philosophical Magazine Letters* **80**, 411–418 (2000).
19. Griessen, R., Strohfeldt, N. & Giessen, H. Thermodynamics of the hybrid interaction of hydrogen with palladium nanoparticles. *Nature Materials* **15**, 311–317 (2016).
20. Baldi, A., Narayan, T. C., Koh, A. L. & Dionne, J. A. In situ detection of hydrogen-induced phase transitions in individual palladium nanocrystals. *Nature Materials* **13**, 1143–1148 (2014).
21. Zlotea, C., Oumellal, Y., Provost, K. & Ghimbeu, C. M. Experimental Challenges in Studying Hydrogen Absorption in Ultrasmall Metal Nanoparticles. *Front. Energy Res.* **4**, (2016).
22. Oumellal, Y., Provost, K., Ghimbeu, C. M., Yuso, A. M. de & Zlotea, C. Composition and size dependence of hydrogen interaction with carbon supported bulk-immiscible Pd–Rh nanoalloys. *Nanotechnology* **27**, 465401 (2016).
23. Zlotea, C. *et al.* Size-Dependent Hydrogen Sorption in Ultrasmall Pd Clusters Embedded in a Mesoporous Carbon Template. *Journal of the American Chemical Society* **132**, 7720–7729 (2010).
24. Evans, J. & Tromp, M. Interaction of small gas phase molecules with alumina supported rhodium nanoparticles: anin situspectroscopic study. *J. Phys.: Condens. Matter* **20**, 184020 (2008).

25. Sanchez, S. I. *et al.* The emergence of nonbulk properties in supported metal clusters: negative thermal expansion and atomic disorder in Pt nanoclusters supported on gamma-Al2O3. *J. Am. Chem. Soc.* **131**, 7040–7054 (2009).
26. Jentys, A. Estimation of mean size and shape of small metal particles by EXAFS. *Phys. Chem. Chem. Phys.* **1**, 4059–4063 (1999).
27. Frenkel, A. I., Hills, C. W. & Nuzzo, R. G. A View from the Inside: Complexity in the Atomic Scale Ordering of Supported Metal Nanoparticles. *The Journal of Physical Chemistry B* **105**, 12689–12703 (2001).
28. Blaine, R. L. & Kissinger, H. E. Homer Kissinger and the Kissinger equation. *Thermochimica Acta* **540**, 1–6 (2012).
29. Férey, G. *et al.* A Chromium Terephthalate-Based Solid with Unusually Large Pore Volumes and Surface Area. *Science* **309**, 2040 (2005).
30. Vimont, A. *et al.* Investigation of Acid Sites in a Zeotypic Giant Pores Chromium(III) Carboxylate. *J. Am. Chem. Soc.* **128**, 3218–3227 (2006).
31. Rowsell, J. L. C., Spencer, E. C., Eckert, J., Howard, J. A. K. & Yaghi, O. M. Gas Adsorption Sites in a Large-Pore Metal-Organic Framework. *Science* **309**, 1350 (2005).
32. Yildirim, T. & Hartman, M. R. Direct Observation of Hydrogen Adsorption Sites and Nanocage Formation in Metal-Organic Frameworks. *Phys. Rev. Lett.* **95**, 215504 (2005).
33. Pundt, A. & Kirchheim, R. HYDROGEN IN METALS: Microstructural Aspects. *Annu. Rev. Mater. Res.* **36**, 555–608 (2006).
34. Leardini, F., Fernández, J. F., Bodega, J. & Sánchez, C. Isotope effects in the kinetics of simultaneous H and D thermal desorption from Pd. *Journal of Physics and Chemistry of Solids* **69**, 116–127 (2008).
35. Stern, A., Resnik, A. & Shaltiel, D. Thermal desorption spectra of the PdH x system in a powder form. *J. Phys. F: Met. Phys.* **14**, 1625 (1984).
36. *Hydrogen in Metals I: Basic Properties*. (Springer-Verlag, 1978).
37. Seymour, E. F. W., Cotts, R. M. & Williams, W. D. NMR Measurement of Hydrogen Diffusion in $\ensuremath{\beta}$-Palladium Hydride. *Phys. Rev. Lett.* **35**, 165–167 (1975).
38. Pundt, A. *et al.* Hydrogen sorption in elastically soft stabilized Pd-clusters. *Journal of Alloys and Compounds* **293–295**, 480–483 (1999).
39. Qiao, B. *et al.* Single-atom catalysis of CO oxidation using Pt_1/FeO_x. *Nature Chemistry* **3**, 634–641 (2011).

40. Miyaura, Norio. & Suzuki, Akira. Palladium-Catalyzed Cross-Coupling Reactions of Organoboron Compounds. *Chem. Rev.* **95**, 2457–2483 (1995).
41. Fairlamb, I. J. S. Metal-Catalyzed Cross-Coupling Reactions and More. 3 Volume Set. Edited by Armin de Meijere, Stefan Bräse and Martin Oestreich. *Angewandte Chemie International Edition* **53**, 13001–13002 (2014).
42. Yin & Liebscher, J. Carbon−Carbon Coupling Reactions Catalyzed by Heterogeneous Palladium Catalysts. *Chem. Rev.* **107**, 133–173 (2007).

CHAPTER IV

MIL-101(Cr) DOPED WITH RHODIUM NANOPARTICLES

4.1 Synthesis optimization by double solvent method

The synthesis of *x*-Rh@MIL-101(Cr) composites was carried out by double solvent impregnation as it was validated for palladium-based materials. However, optimization of the reduction conditions was necessary to form totally reduced Rh particles. Two parameters were studied: the temperature and the time of the reduction. It should be noted that for rhodium-based materials, a second batch of MIL-101(Cr) was used, which has larger textural properties than the one used for Pd doping : S_{BET} = 3549 m^2/g, V_{pore} = 1.75 cc/g. Improved porous properties are due to the optimization of the synthesis conditions and activation of MIL-101(Cr) by our Romanian partner. This second batch of MIL-101(Cr) was synthesized at 463 K for 4 hours instead of 493 K for 20 hours, and the activation was carried out for 72 hours instead of 24 hours.

4.1.1 Reduction temperature effect

The reduction of rhodium chloride to rhodium metal was carried out under H_2/Ar flow. The temperature and the duration are the same as initially tested with success for Rh@C material[1]: 448 K for 15 min. However, these conditions do not seem to be the best for complete reduction of Rh@MIL-101(Cr) as reviled by EXAFS at Rh K edge (23229.5 eV). The *figure 4.1* depicts the comparison between the experimental EXAFS spectra (*figure 4.1(a)*) of Rh clusters reduced under the above conditions and bulk Rh under N_2 flow (15 mL/min) at room temperature as well as the corresponding modules of the Fourier Transform (*figure 4.1(b)*).

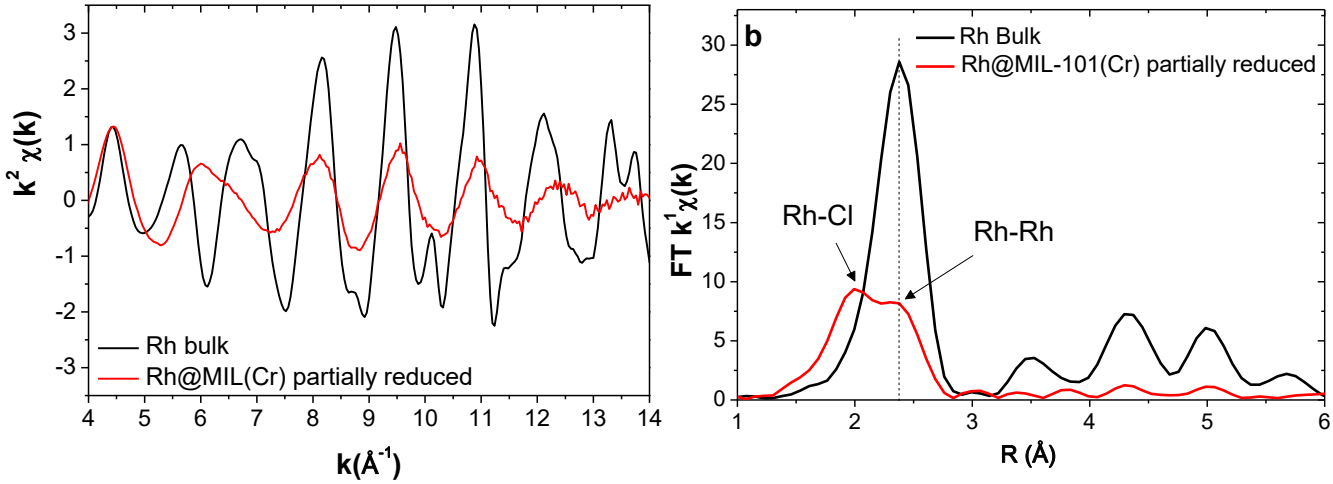

Figure 4.1: (a) Experimental EXAFS spectra at the Rh K edge and (b) the corresponding module of the Fourier transform (FT) of bulk Rh (black) and Rh clusters (red) under N_2 at 298 K.

As for the local structure study of the 1 nm Pd cluster, the XAS was performed on the ROCK beamline at SOLEIL synchrotron and data treatment and EXAFS refinements were carried out with the MAX program package (E_0 = 23229.5 eV for the Rh K edge, Fourier transform range = 4 – 14 $Å^{-1}$)[2,3]. Surprisingly, the EXAFS spectra for Rh bulk and nanometric Rh are not in phase. Furthermore, the main FT signal of the nanometric Rh, diminishes as compared to that of the bulk, and shows two peaks in contrast to the main peak of the bulk Rh. The first peak corresponds to the distance $R_{Rh\text{-}Cl}$ characterizing the presence of rhodium chloride (*monoclinic C2/m*) and the second peak of FT corresponds to the $R_{Rh\text{-}Rh}$ distance typical of rhodium metal (*fcc Fm-3m*). This finding proves that the reduction at 448 K for 15 min under Ar/H_2 flow was only partial. Thus, a thermal treatment under N_2 flow was applied to check the reduction of Rh precursor by *in-situ* XAS. The 10-Rh@MIL-101(Cr) material was monitored during heating from 298 to 543 K (2 K/min) under N_2 flow (*figure 4.2*).

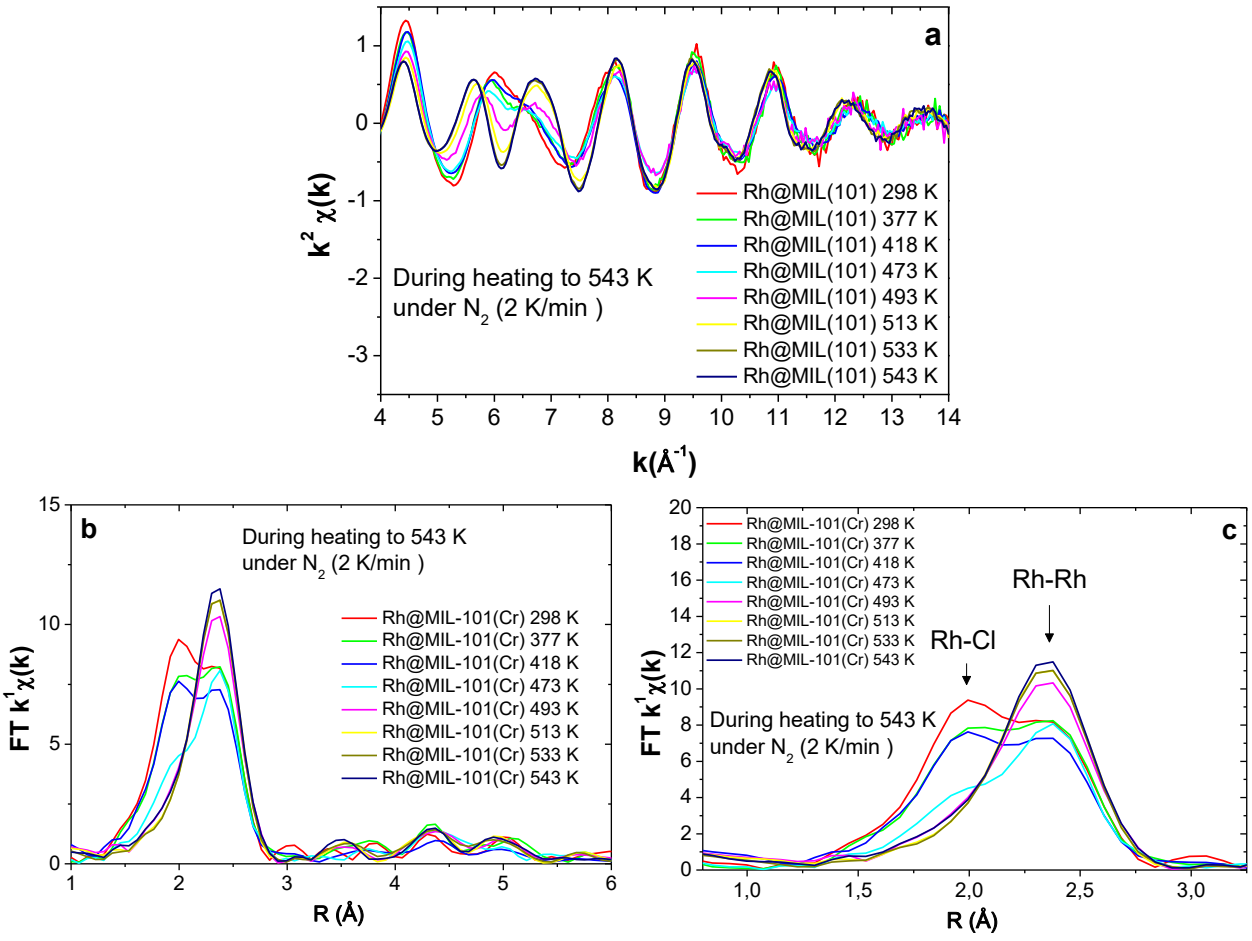

Figure 4.2: (a) Experimental EXAFS spectra at the Rh K edge, (b) the corresponding module of the Fourier transform (FT)and (c) a zoom of this FT module between [1-3.5 Å] of Rh clusters under N_2 as a function of the temperature.

The EXAFS spectra recorded between 298 and 543 K, shown in *figure 4.2(a)*, depict an evolution of the material by increasing the temperature. This evolution is also observed on spectra of Fourier transforms in *figures 4.2(b) and (c)*. In fact, by increasing the temperature, the peak amplitude of the $R_{Rh\text{-}Rh}$ increases on the expense of the peak of $R_{Rh\text{-}Cl}$ until its total disappearance at 513 K, as shown in *figure 4.2(b) and (c)* characterizing the total reduction of rhodium chloride to rhodium metal.

EXAFS fitting was performed on first (*Rh-Cl*) and second-sphere (*Rh-Rh*) filtered spectra up to 513 K. Theoretical phases and amplitudes were computed with FEFF8 based on the Rh metal *fcc* structure and Rh chloride *monoclinic* structure. The refined parameters are the coordination number (*N*) and the first-neighbor distance ($R_{Rh\text{–}Cl}$ for the first shell and $R_{Rh\text{–}Rh}$ for the second one), and the Debye-Waller factor (σ^2).

The evolution of the coordination number (*N*), as well as that of the distance for the first and the second shell ($R_{Rh\text{-}Cl}$ and $R_{Rh\text{-}Rh}$ respectively) as a function of the temperature, are represented in *figure 4.3*.

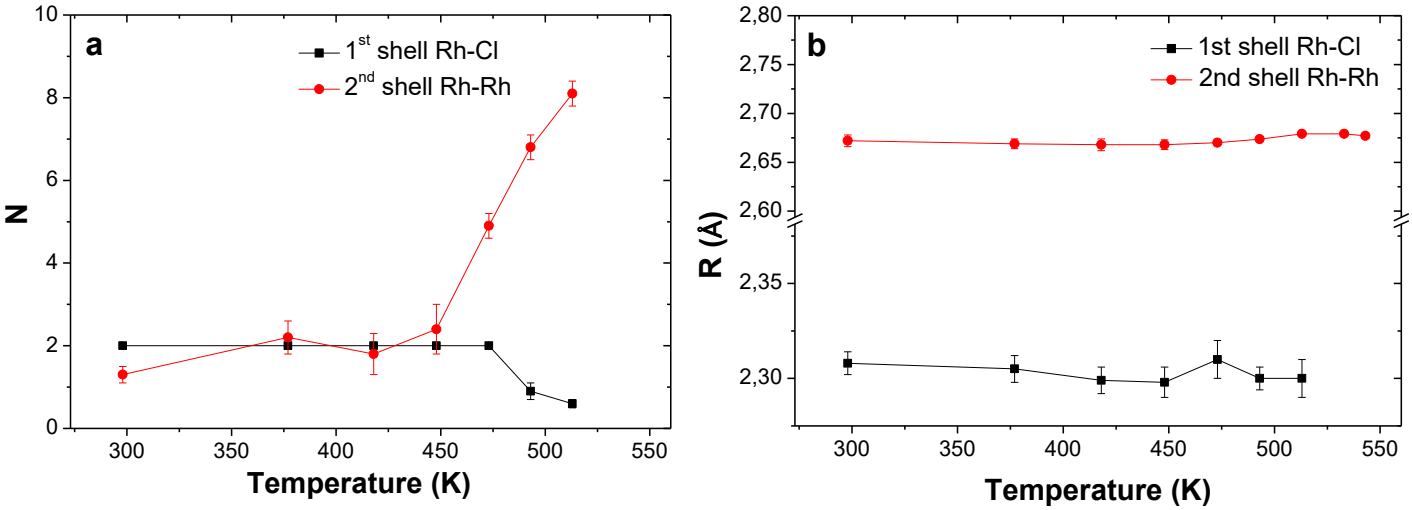

Figure 4.3: Evolution of (a) the coordination number and (b) the distance between first neighbors determined for the 1st and the 2nd shell.

At a temperature below 450 K, the coordination number (*N*) for the two shells is almost the same (around 2). However, beyond 450 K, *N* of the 2nd shell (*Rh-Rh*) increases on the expense of the coordination number (*N*) of the 1st shell (*Rh-Cl*) which vanishes at 513 K. For the 1st shell (*Rh-Cl*), the coordination number (*N*) and the distance $R_{Rh\text{-}Cl}$ are in good agreement with the theoretical values, 2 and 2.29 Å respectively, at a temperature below 450 K. In the same range of temperature, a strong decrease of *N* of the 2nd shell (*Rh-Rh*), from

12, for the bulk, to 1.8 is noticed. A small contraction of the $R_{Rh\text{-}Rh}$, from 2.68 to 2.67 Å, is also observed, as expected for nano-objects.[4,5] Then, beyond 450 K, the noticed increase of the coordination number (*N*) for the (*Rh-Rh*) shell, up to 8, can be ascribed to the *in situ* decomposition of the $RhCl_3$ and the growth of pure metallic Rh.

The structural and nanostructural properties of the recovered material after XAS analysis were determined by X-ray diffraction (XRD) and Transmission Electron Microscopy (TEM) and compared to pristine MIL-101(Cr) and the composite before the heat treatment under N_2 flow at 513 K. *Figure 4.4* shows the diffractograms of the pristine MIL-101(Cr) and the 10-Rh@MIL-101(Cr) composite partially and fully reduced. First, the diffractograms of the different composites, show that the MIL-101(Cr) retains its crystallinity after synthesis and after the XAS measurements under N_2 atmosphere and up to 543 K. Moreover, no diffraction peak of Rh, which crystallizes in a *fcc* system, is observed for the partially reduced material. The absence of the diffraction peak might be explained by a very small particle size of Rh. However, a weak diffraction signal of Rh appears for the composite recovered after fully reduction at 543 K.

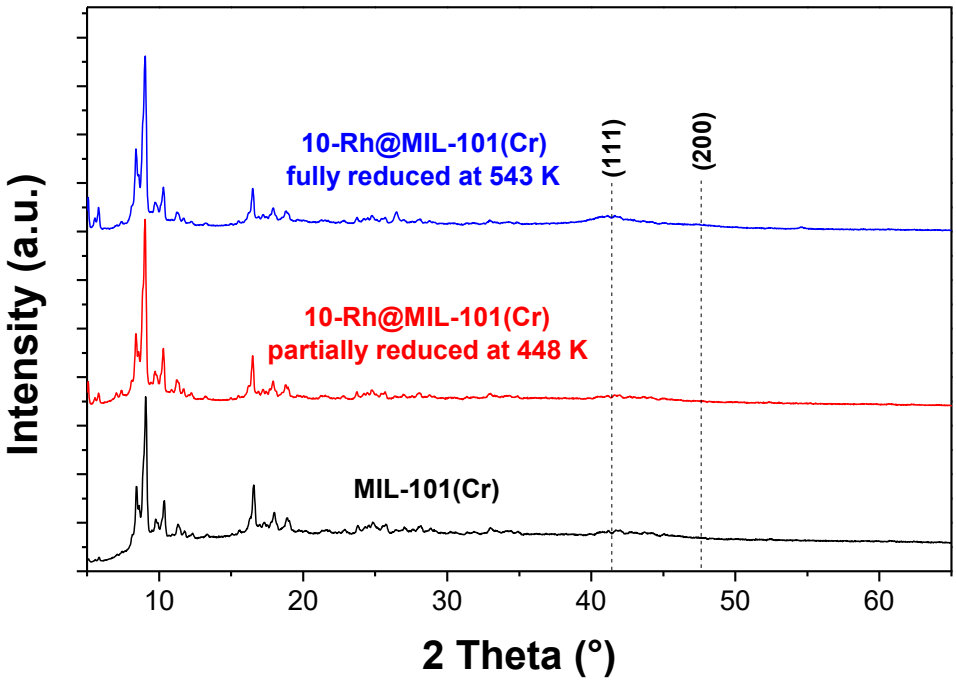

Figure 4.4: XRD patterns of pristine MIL-101(Cr) and 10-Rh@MIL-101(Cr) partially and fully reduced.

The TEM images performed for the Rh@MIL-101(Cr) composite before (partially reduced) and after XAS (fully reduced), as well as the size distribution histograms, are shown in *figure 4.5*.

For both composites, partially and fully reduced, the dispersion of the nanoparticles is very homogeneous. However, their average particle size has significantly increased from 0.7 to 3 nm, in agreement with the X-ray diffraction results.

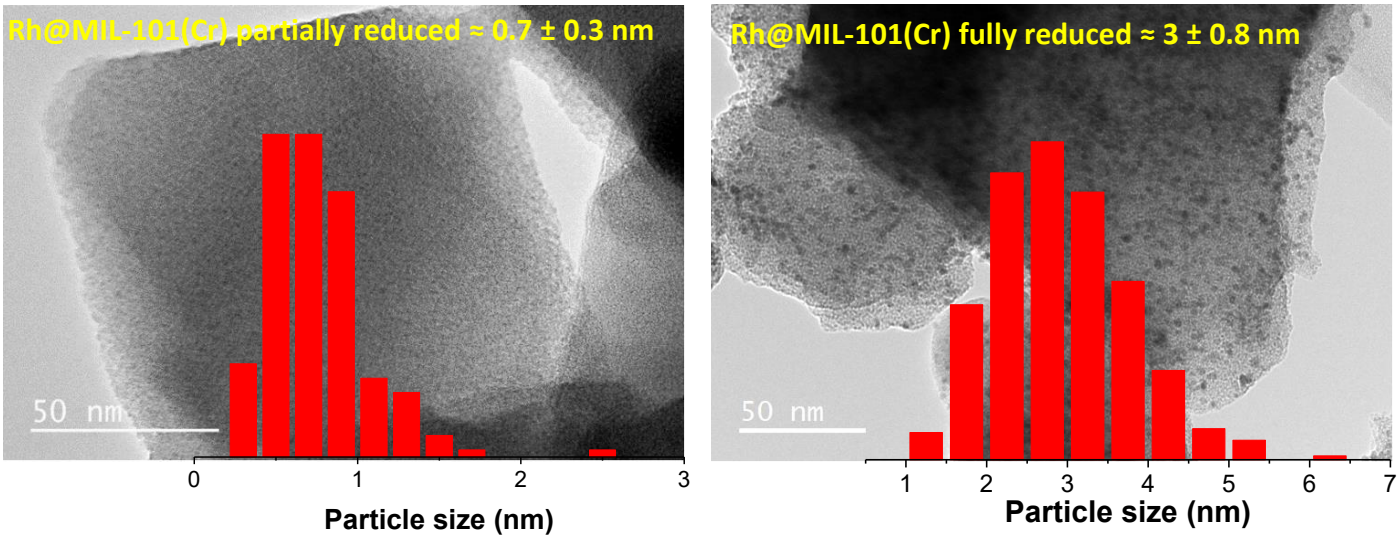

Figure 4.5: Typical TEM image of 10-Rh@MIL-101(Cr) (a) partially reduced at 448 K and (b) fully reduced at 543 K.

In conclusion, X-ray absorption spectroscopy has shown that the temperature conditions of reduction used in the literature (at 448 K) are not enough to completely decompose rhodium chloride inside the MIL-101(Cr) pores and to obtain metal nanoparticles. Thus, our reduction conditions used to fully reduce the Rh inside MIL-101(Cr) pores are T = 573 K for 2 hours under Ar/H_2 flow, as confirmed further.

In order to study the difference in decomposition behavior of the rhodium chloride, differential scanning calorimetry measurements were performed under Ar atmosphere with a heat rate of 5 K/min up to 673 K. *Figure 4.6* represents a comparison between the results obtained for undoped MIL-101(Cr), rhodium chloride salt, a carbon (High Surface Area Graphite) and a MIL-101(Cr) freshly impregnated with a solution of rhodium chloride and MIL-101(Cr) doped with Rh nanoparticles obtained after a reduction step at 573 K for 2h.

The decrease in heat flow below 373 K corresponds to an endothermic loss of water for all samples. The most visible loss of H_2O is observed for pristine MIL-101(Cr) (*figure 4.6(a)*) and fully reduced 20-Rh@MIL-101(Cr) (*figure 4.6(e)*). At higher temperatures, the peak at 413 K for rhodium chloride salt (*figure 4.6(b)*) and freshly impregnated carbon (*figure 6(c)*) corresponds to the decomposition of the salt. However, the freshly impregnated MIL-101(Cr)

(*figure 4.6(d)*) shows different behavior. The decomposition of rhodium chloride in this latter sample occurs at a higher temperature, 523 K, in agreement with the results of XAS. Finally, the curve obtained with metal rhodium nanoparticles confined in the pores of MIL-101(Cr) (*figure 4.6(e)*) shows the absence of the peak corresponding to the decomposition of rhodium chloride confirming the total reduction of rhodium chloride at 573 K.

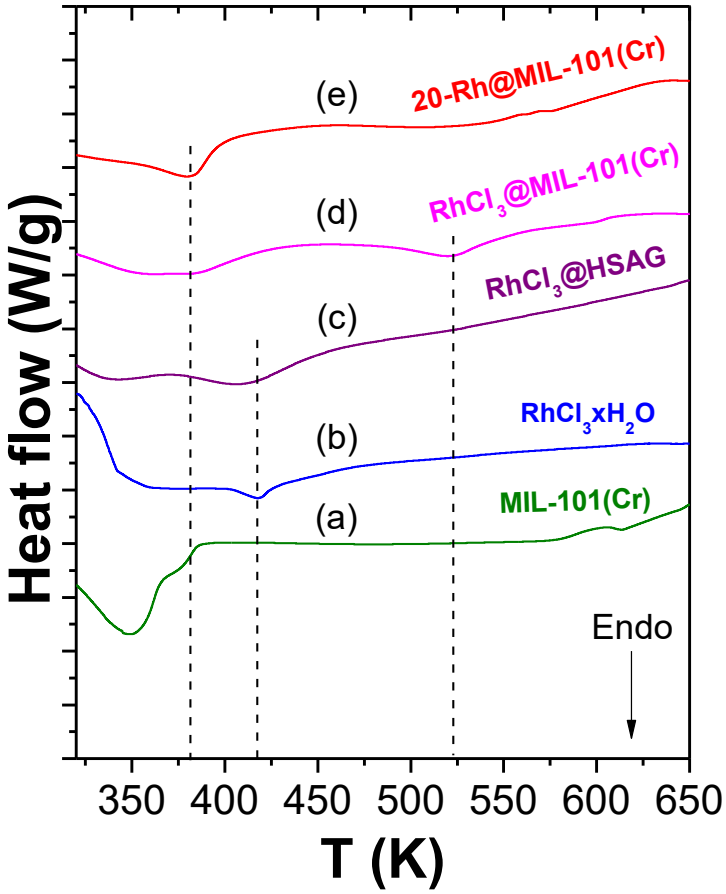

Figure 4.6: DSC curves for (a) pristine MIL-101(Cr), (b) rhodium chloride, (c) $RhCl_3$@HSAG, (d) RhCl3@MIL-101(Cr) and (e) 20-Rh@MIL-101(Cr).

These results show the different behavior of the reduction of $RhCl_3$ in Rh as a function of the support. In fact, the nanoconfinement of rhodium chloride in the pores of MIL-101(Cr) stabilizes the salt and requires a higher temperature to fully reduce it to rhodium metal. Since MIL-101 (Cr) is a material that starts to decompose at 623 K, the maximum reduction temperature was set at 573 K. The parameter to be optimized next is, therefore, the time of the reduction.

4.1.2 Reduction time effect

In order to track the state of reduction of rhodium nanoparticles, Energy-dispersive X-ray spectroscopy-TEM was used to follow the atomic ratio of chlorine, in the different samples according to the reduction time. To simplify the comparison, chlorine, rhodium, and chromium compositions will be followed. Pristine MIL-101(Cr) initially contains a Cl/Cr ratio of 11 at% from the use of chloridic acid instead of fluoridic acid during the synthesis. To conclude that the rhodium chloride salt is totally decomposed inside the composite, the Cl/Cr ratio must be close to 11 at.%. Indeed, the Cl/Cr ratios obtained for the 10-Rh@MIL-101(Cr) composites, reduced at 573 K, as a function of the reduction time are 15.5, 14 and 11.5 at.% for a reduction time of 5, 15 and 120 min respectively. Thus, the reduction at 573 K for 120 min seems to be the best conditions for obtaining fully reduced Rh nanoparticles.

In conclusion, after the various synthesis optimization steps of the Rh@MIL-101(Cr) composites, the preparation of the materials by the DSM impregnation followed by the reduction under Ar/H_2 flow at 573 K for 120 min has been validated.

4.2 Rhodium doping: Variable metal loading

In order to study the effect of metal loading on the structural, nanostructural and textural properties, four *x*-Rh@MIL-101(Cr) composites with the different metal loadings (*x* = 5, 10, 15 and 20 wt.%) were synthesized by our optimized method. The synthesized Rh composites were subsequently characterized, and the hydrogen sorption properties are discussed. It should be noted that the maximum metal loading has been imposed by the solubility limit of the precursor salt in water.

4.2.1 X-Ray Diffraction

As for the Pd@MIL-101(Cr) materials, the structural characterization of the various rhodium-doped MIL-101(Cr) composites was carried out by X-ray diffraction. The angular domain 2θ chosen for these studies is 5-65°. The bulk rhodium crystallizes in a face-centered cubic system (*fcc*) with the space group *Fm-3m* with main diffraction peaks of (111) and (200) at around 40.9 and 47.6° respectively.

The X-ray diffraction patterns of pristine MIL-101(Cr) and *x*-Rh@MIL-101(Cr) composites with different rhodium loadings are plotted in *figure 4.7*. The expected Miller indices of diffraction peaks in the Rh *fcc* crystal structure are also indicated as dotted lines.

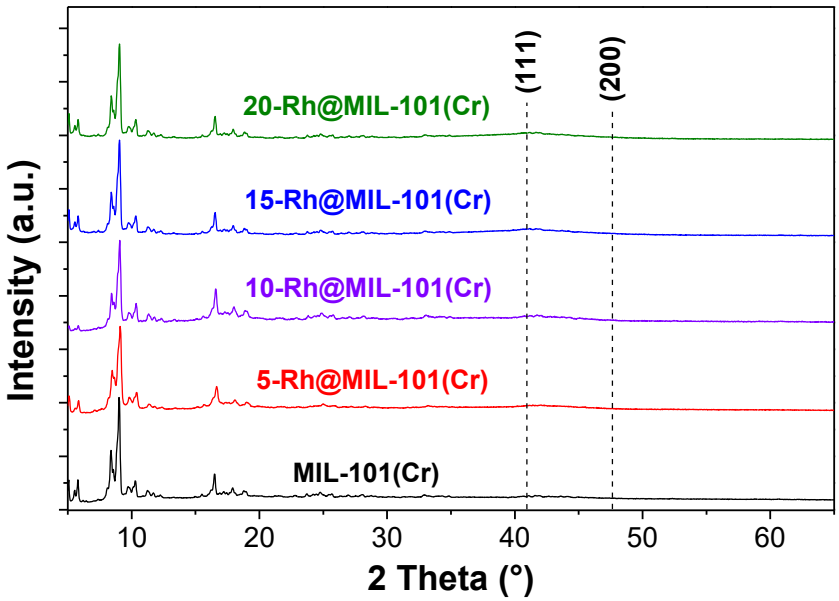

Figure 4.7: XRD patterns of pristine MIL-101(Cr) and x-Rh@MIL-101(Cr) composites (x = 5, 10, 15 and 20wt.%).

The MIL-101(Cr) structure retains its crystallinity after synthesis of Rh nanoparticles. In addition, there is no Rh diffraction peak, despite the large metal content, up to 20 wt.%. This can be explained by the very small size of the Rh clusters, as confirmed further by TEM.

4.2.2 Transmission Electron Microscopy

The nanostructural characterization of Rh clusters doped MIL-101(Cr) was performed by Transmission Electron Microscopy (TEM) to examine the dispersion of the particles in the MOFs, to determine the particle size distribution and the average size of these particles.

Figure 4.8 shows the TEM images of the Rh composites with the different metal loadings. The analysis of several TEM images allows drawing the histograms presenting the size distribution of the nanoparticles. The average particle size was proposed following statistical analysis of the histograms.

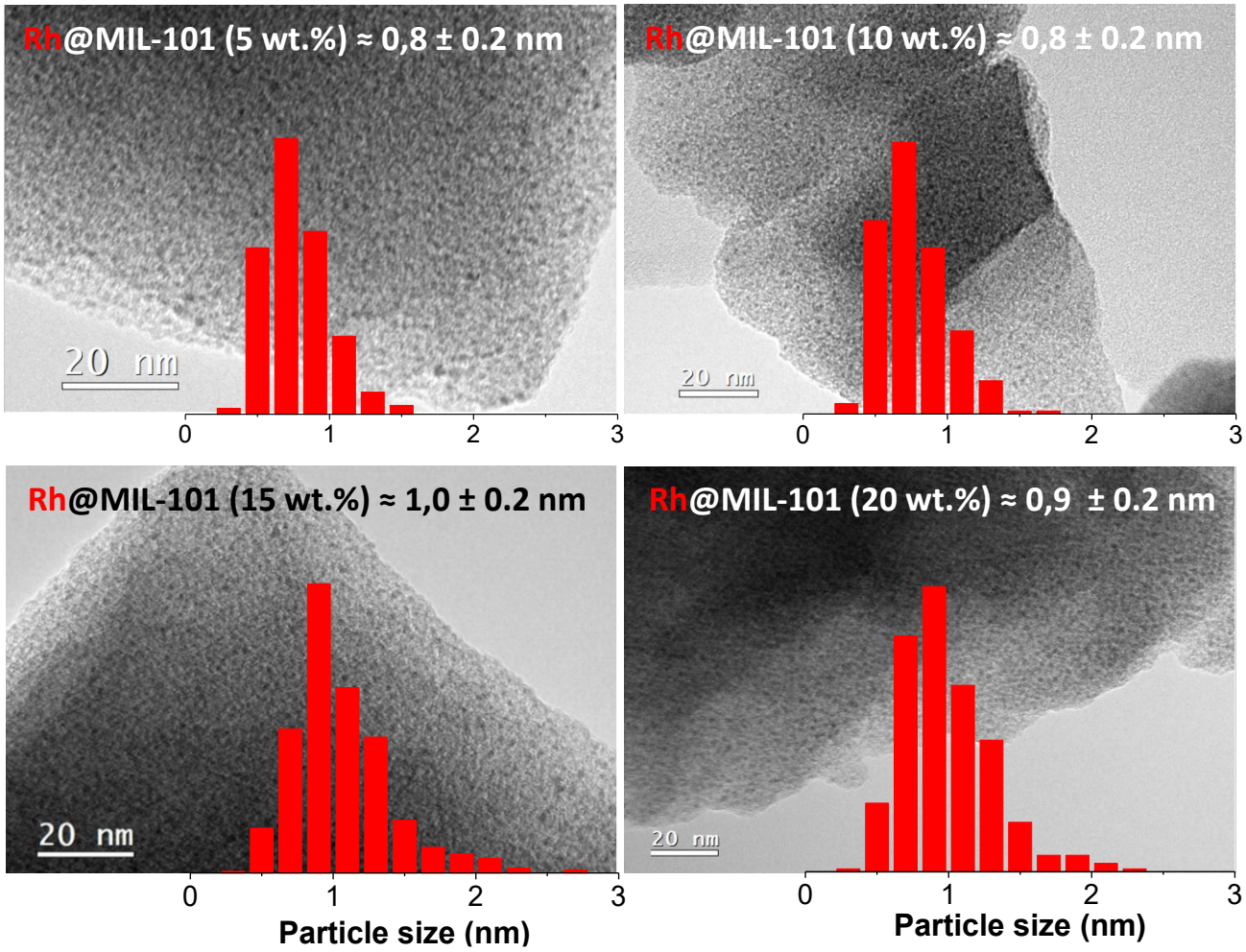

Figure 4.8: Typical TEM images of x-Rh@MIL-101(Cr) composites (x = 5, 10, 15 and 20 wt.%), with Rh particle size histograms.

The images show very small black spots that correspond to Rh clusters very well dispersed in the pores of MIL-101(Cr). The size distribution of the nanoparticles of Rh of the different metal loadings is between 0.25 and 2.75 nm and the average size of the clusters of

the different composites is between 0.8 and 1 nm despite the high metal loadings (20 wt%). This very small size explains the absence of an X-ray diffraction peak of the Rh.

4.2.3 Specific surface area & total pore volume

The textural properties characterization of the *x*-Rh@MIL-101(Cr) composites was performed by N_2 adsorption measurements. *Figure 4.9* shows the N_2 adsorption/desorption curves for MIL-101(Cr) and the different *x*-Rh@MIL-101(Cr) composites. The obtained isotherms for MIL-101(Cr) as well as for *x*-Rh@MIL-101(Cr), represented in *figure 4.9(a)*, are of type IV (with a small hysteresis), *i.e.* corresponding to mesoporous materials. The evolution of the specific surface area and the total pore volume as a function of the Rh amount are also represented in *figure 4.9(b)* and *(c)*. As for the *x*-Pd@MIL-101(Cr) composites, the specific surface area and the total pore volume decrease with the insertion of Rh clusters, up to 10 wt.%. In fact, the specific surface area and the total pore volume of the pristine MIL-101(Cr) decreased from 3549 m^2/g and 1.75 cc/g to 2180 m^2/g and 1.01 cc/g for the 10-Rh@MIL-101(Cr). This decrease can be explained by the increase in the total mass of the composite after the insertion of the Rh clusters and by blocking the accessible pores.

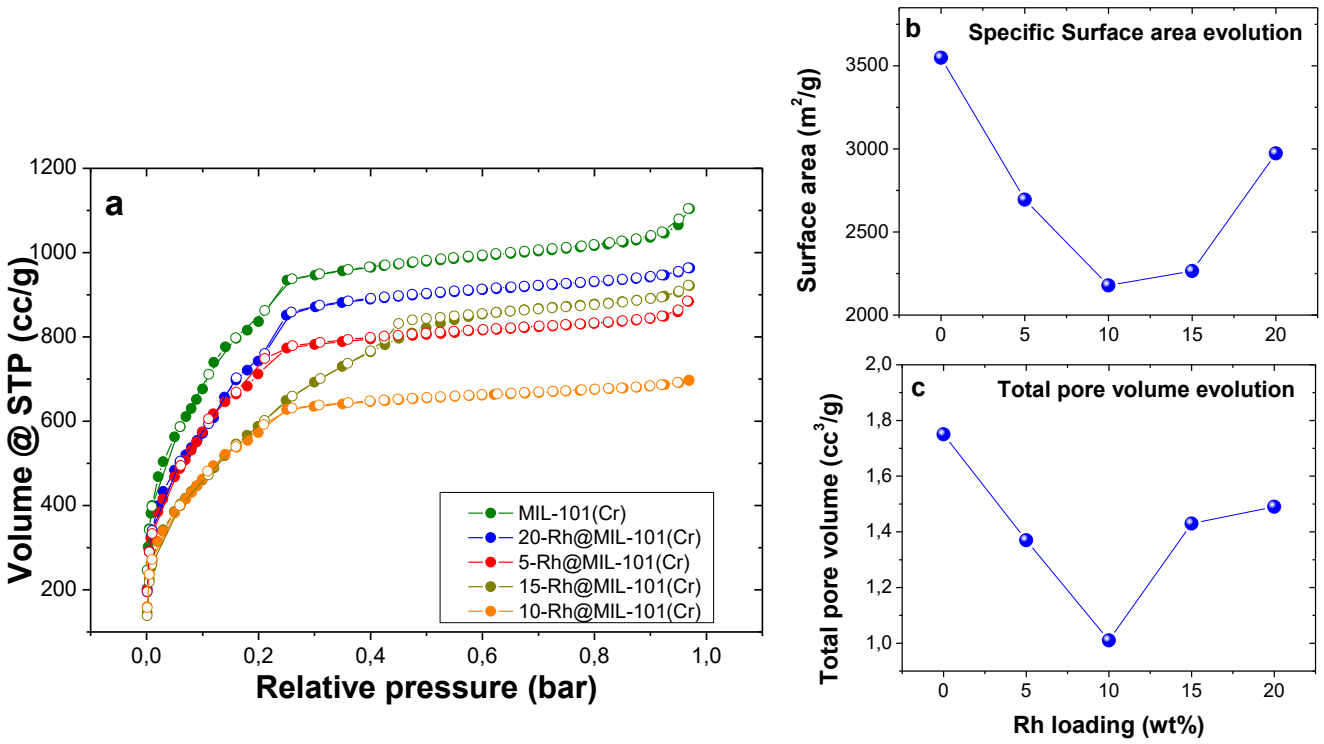

Figure 4.9: (a) N_2 adsorption/desorption curves of MIL-101(Cr) and x-Rh@MIL-101(Cr) composites and the evolution of (b) the specific surface area and (c) total volume as a function of Rh amount.

However, by increasing the rhodium content beyond 10 wt%, the specific surface area and the total pore volume increase significantly. This increase might be explained by the contribution of two phenomena mainly: the pores of MIL-101(Cr) remained partially accessible and the windows were not blocked by the nanoparticles as well as the contribution of the specific surface of the Rhodium clusters of 1 nm which is around 500 m^2/g.

4.3 Hydrogen sorption properties

In this chapter, the study of the hydrogen interaction with 1 nm Rh clusters confined within the MIL-101(Cr) composites has been studied and the size effect is discussed. The characterization of hydrogen sorption properties was carried out by Pressure-Composition-Isotherm and Thermo-Desorption-Spectroscopy measurements.

4.3.1 Pressure-Composition-Isotherm at low temperature (78 – 107 K)

PCI measurements at low pressure and cryogenic temperatures have been carried out, as for pristine MIL-101(Cr) (second batch, different than that used in the synthesis of Pd composites) and 10-Rh@MIL-101(Cr) up to 1 bar of hydrogen (*figure 4.10(a)* and *(b)*). Adsorption and desorption are fully reversible due to a H_2 physisorption phenomenon on the internal surface of the materials. The isosteric heat of adsorption was determined using the Clausius-Clapeyron equation (*figure 4.10(c)*).

The energy of adsorption varies from 8.5 to 4.5 kJ/mol for the pristine MIL-101(Cr) and from 10 to 4.5 kJ/mol for the 10-Rh@MIL-101(Cr) composites by increasing the sorption capacity of H_2. At low capacity (0.05 – 0.2 wt.%), the isosteric heat strongly decreases for both materials and reaches similar values at higher sorption capacities. At low coverage, the energy increases with the insertion of Rh nanoparticles within the MIL-101(Cr) pores which proves an enhancement of the hydrogen interaction relative to pristine material, confirming a synergistic effect between metal nanoparticles and porous hosts as also shown for Pd@MIL-101(Cr).

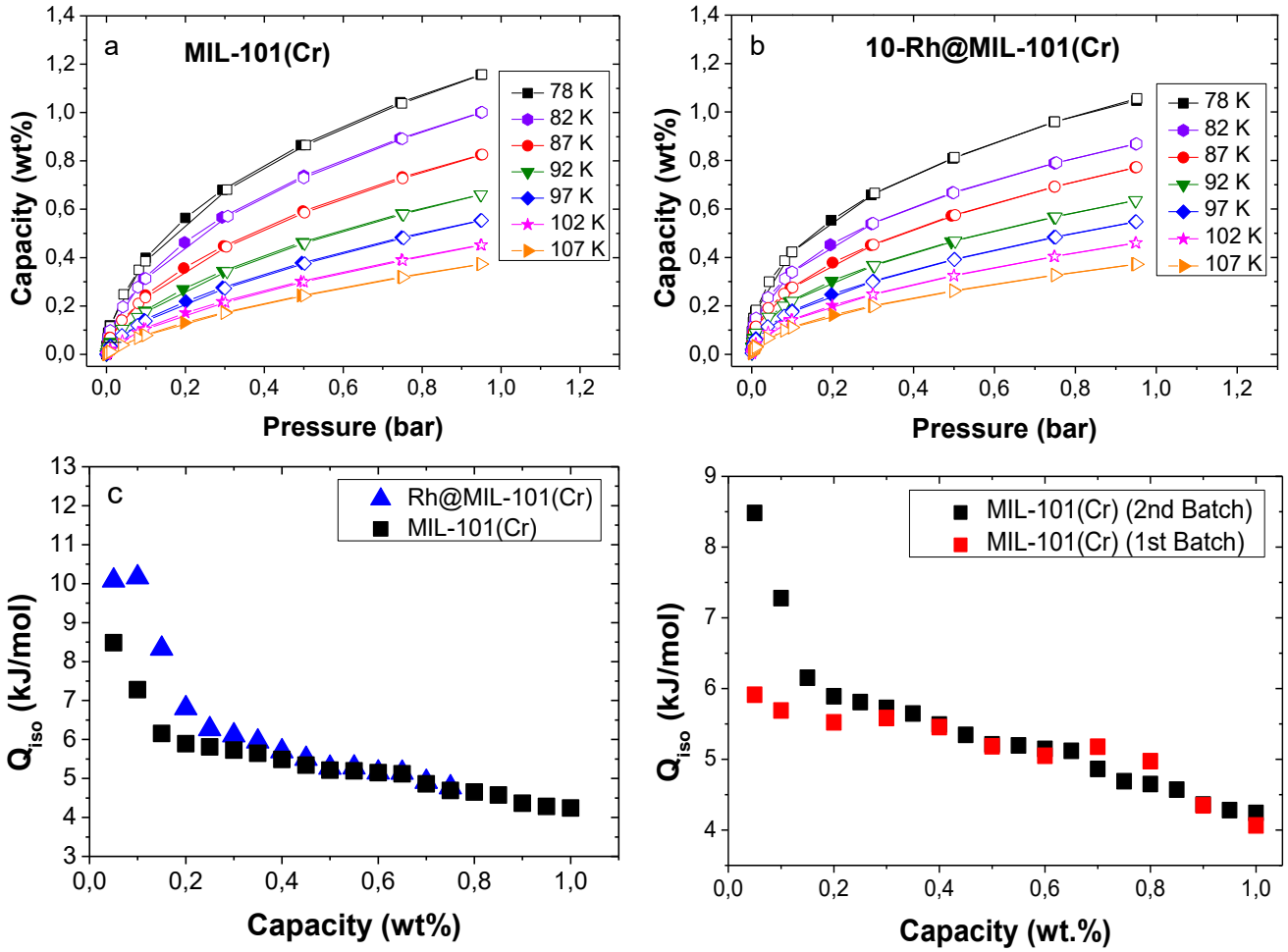

Figure 4.10: PCI curves recorded at several cryogenic temperatures for (a) MIL-101(Cr)(2nd batch) and (b) 10-Rh@MIL-101(Cr) where the adsorption and desorption are marked as full and empty symbols, respectively; The isosteric heat of adsorption versus hydrogen sorption capacity for (c) both MIL-101(Cr) (square) and 10-Rh@MIL-101(Cr) (triangle) and (d) both MIL-101(Cr) batches used for Pd@MIL-101(Cr) (red) and Rh@MIL-101(Cr) (black) materials.

Moreover, the comparison of the isosteric heat of the two batches of MIL-101(Cr) shows a difference at low sorption capacities as shown in *figure 4.10(d)*. The first batch of MIL-101(Cr) used to confine the nanoparticles of Pd shows a maximum of adsorption heat equal to 6 kJ/mol at low adsorption capacity. However, the MIL-101(Cr) used in Rh@MIL-101(Cr) materials shows a significant increase in Q_{isos}, at low sorption capacity, reaching 8.5 kJ/mol. The differences of the two MIL-101(Cr) batches can be explained by the structural and textural differences. The MIL-101(Cr) used to confine Pd nanoparticles, has a S_{BET} = 3300 m^2/g and V_{pore} = 1.64 cc/g *versus* S_{BET} = 3549 m^2/g and V_{pore} = 1.75 cc/g for the batch used for the insertion of Rh nanoparticles. Considering that MIL-101(Cr) can reach

surfaces of 4200 m^2/g and pore volume of 2.0 cm^3/g [6], the most obvious explanation is that the latter batch has a better-formed structure (closer to the ideal structure), which certainly has effects on the adsorption positions. Comparing the X-ray diffraction patterns of the two batches recorded under the same conditions, the Bragg reflections are better defined in the second sample, especially those between 3-3.5°, which confirms the higher degree of crystallinity and better structural quality (*figure 4.11*).

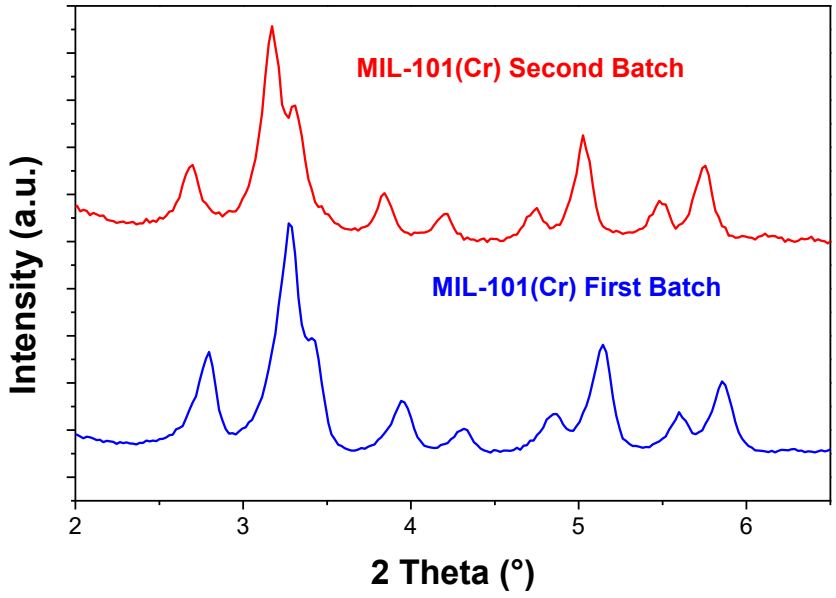

Figure 4.11: XRD patterns of first batch of MIL-101(Cr) used in Pd@MIL-101(Cr) (blue) and second batch used in Rh@MIL-101(Cr) (red).

Thus, the two batches of MIL-101(Cr), synthesized by two different methods, have different properties and the second batch, prepared by an optimized synthesis method and used to confine the particles of Rh, has better structural and textural properties.

4.3.2 Pressure-Composition-Isotherm at low pressure and room temperature

The PCI curves of the MIL-101(Cr) as well as the 10 and 20-Rh@MIL-101(Cr) composites were measured, up to 1 bar of hydrogen at room temperature, and are shown in *figure 4.12*. Before each measurement, the materials were degassed at 493 K for 18 hours to remove water molecules, with an additional hydrogen pretreatment step prior to degassing for doped materials. The PCI curves are represented in weight capacity to compare the Rh composites curves with the pristine MIL-101(Cr) curve.

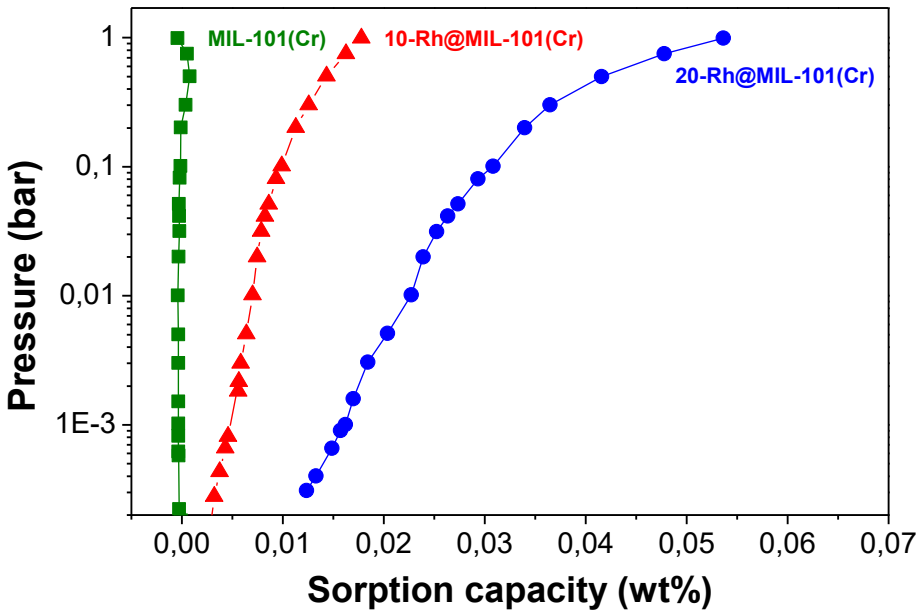

Figure 4.12: The PCI curve recorded at room temperature up to 1 bar for MIL-101(Cr) (square), 10-Rh@MIL-101(Cr) (triangle) and 20-Rh@MIL-101(Cr) (circle).

At room temperature and at pressures up to 1 bar H_2, the hydrogen adsorption capacity by the pristine MIL-101(Cr) is negligible, in agreement with the literature[7]. However, by inserting rhodium nanoparticles in the pores of MIL-101(Cr) hydrogen sorption capacity increases with the Rh loading, *i.e.* the higher Rh loading, the higher the sorption capacity. It should be noted that these measurements are repeatable under the same analysis conditions *i.e.* an outgas at 493 K for 2 hours was carried out before each measurement.

Moreover, no pressure plateau is observed for the two composites of 1 nm Rh clusters characterizing the absence of the hydride formation at room temperature and up to 1 bar of H_2, in contrast with the 2.3 nm Rh nanoparticles, showing hydride formation under these conditions[1]. The absence of a pressure plateau with 1 nm Rh nanoparticles and the increase of the sorption capacity by increasing the Rh loading allow to propose two working hypotheses: the interaction of hydrogen with Rh nanoparticles consists of a surface phenomenon with dissociative chemisorption on the surface, or a volume phenomenon with the formation of solid solutions with hydrogen at room temperature and up to 1 bar H_2. The coexistence of both phenomena is also possible.

In order to further study the hydrogen sorption properties of the Rh@MIL-101(Cr) composites, hydrogen desorption measurements were performed.

4.3.3 Hydrogen desorption properties

The hydrogen desorption properties of 20-Rh@MIL-101(Cr) were investigated by the Thermal-Desorption Spectroscopy technique, by applying a constant heating rate of 5 K/min from room temperature to 473 K and the partial pressures of evolved gaseous species were recorded by a mass spectrometer.

4.3.3.1 Hydrogen desorption for Rh@MIL-101(Cr) composite

First, a study of the interaction of the composite of 20-Rh@MIL-101(Cr) with H_2 and D_2 was carried out. For this, before starting the desorption, three different exposures to gas were performed. The first desorption was carried out after exposure to 1 bar of H_2 for 8 hours. The second one was recorded after exposure to 1 bar of D_2 for 8 hours. The last desorption was carried out after exposure for 8 hours to 1 bar of an equimolar mixture of H_2 and D_2. *Figure 4.13* illustrates the obtained results.

After each exposure of the material to the pure gases (H_2, D_2,), the most intense recorded desorption peak corresponds to the used gas. Indeed, following the exposure of 20-Rh@MIL-101(Cr) to H_2 or D_2, the recorded desorption showed 1 peak, at about the same temperature (≈ 365 K), for H_2 and D_2 respectively (*figure 4.13(a)* and *(b)*). However, by exposing the composite to 1 bar of an equimolar mixture of H_2 and D_2, 3 desorption peaks are recorded at about the same temperature range: 2 peaks of H_2 and D_2 together with a third more intense of HD (*figure 4.13(c)*). It should be noted that, regardless of the exposed gas, the recorded desorption for the pristine MIL-101(Cr) is negligible, confirming that the MIL-101(Cr) does not desorb hydrogen under our conditions [7].

The desorption temperature recoded, whatever the gas exposed (H_2, D_2 or their mixture), is almost the same, suggesting a similar desorption kinetics of the two gases, as previously demonstrated by Yates *et al.* for Rh (111) surfaces[8]. Moreover, the recorded HD peak, following exposure of the material to a mixture of H_2 and D_2, characterizes a phenomenon of random recombination at the surface of Rh nanoparticles. In fact, adsorbed on the surface, the molecules of H_2 and D_2 are dissociated before diffusing and establishing chemical bonds with Rh. Then, by heating under secondary vacuum, a random recombination is produced on the surface before desorbing molecules of H_2, D_2 and HD, as noticed in *figure 4.13(c)*.

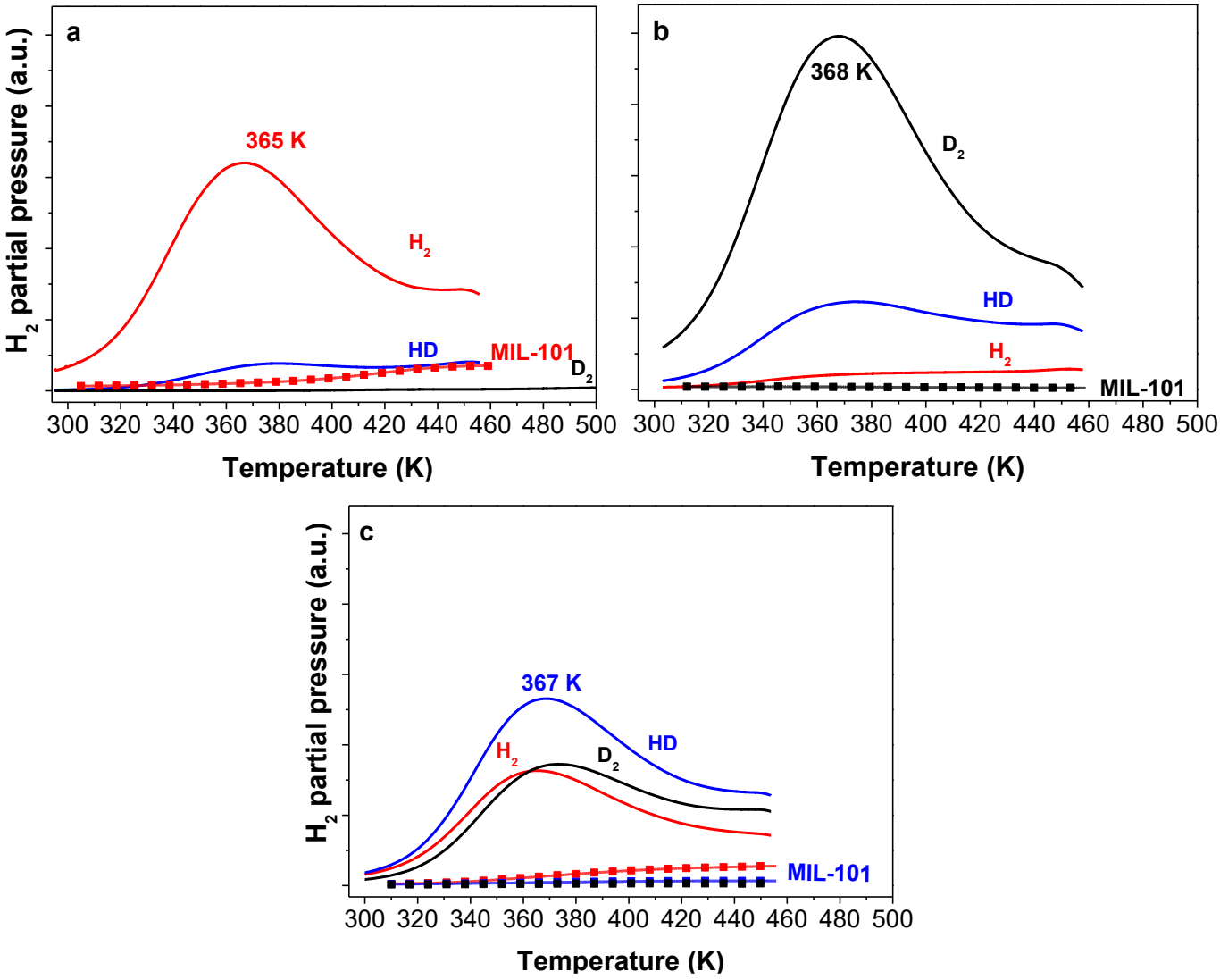

Figure 4.13: Thermo-desorption spectra of Rh@MIL-101(Cr) carried out after exposure to (a) hydrogen, (b) deuterium and (c) equimolar mixture of hydrogen and deuterium

These desorption results confirmed the interaction of hydrogen with the 1 nm Rh clusters confined in the pores of MIL-101(Cr). Nevertheless, both working hypotheses, proposed as a result of PCI measurements, are maintained and none can be eliminated. In fact, the desorption peaks at ~ 365 K can be attributed to desorption of gas from absorbed hydrogen forming solid solutions at room temperature up to 1 bar or that chemisorbed at the surface. Further analyzes are therefore needed to better understand the interaction of hydrogen with the 1 nm Rh nanoparticles.

It should be noted that studies of H2 desorption from chemisorbed hydrogen on Rh (111), Rh (100) and Rh(110) were carried out[8–10]. However, no comparison of the desorption temperature is possible since the measurements are performed under different conditions than ours (different heating rate mainly).

4.3.3.2 Air exposure effect

So far, the desorption measurements are performed with clean materials, *i.e.* which have not been exposed to air. In order to check the air exposure effect on hydrogen desorption properties, additional TDS experiments were performed following the protocols reported previously.[11] Three desorption experiments were performed: (1) after H_2 exposure (8 hours) without air exposure (directly from glove box), (2) after H_2 exposure (8 hours) followed by a short air exposure (5 min) and (3) after short air exposure (5 min) followed by H_2 pre-treatment at RT and additional exposure to H_2 (8 hours). The H_2 pretreatment consisted of three cycles of 1 bar H_2 exposure for 5 min at RT, followed by degassing under dynamic secondary vacuum in order to remove H_2O molecules formed at the metal surface by oxide reduction upon exposure to H_2. The desorption results are reported in *figure 4.14*.

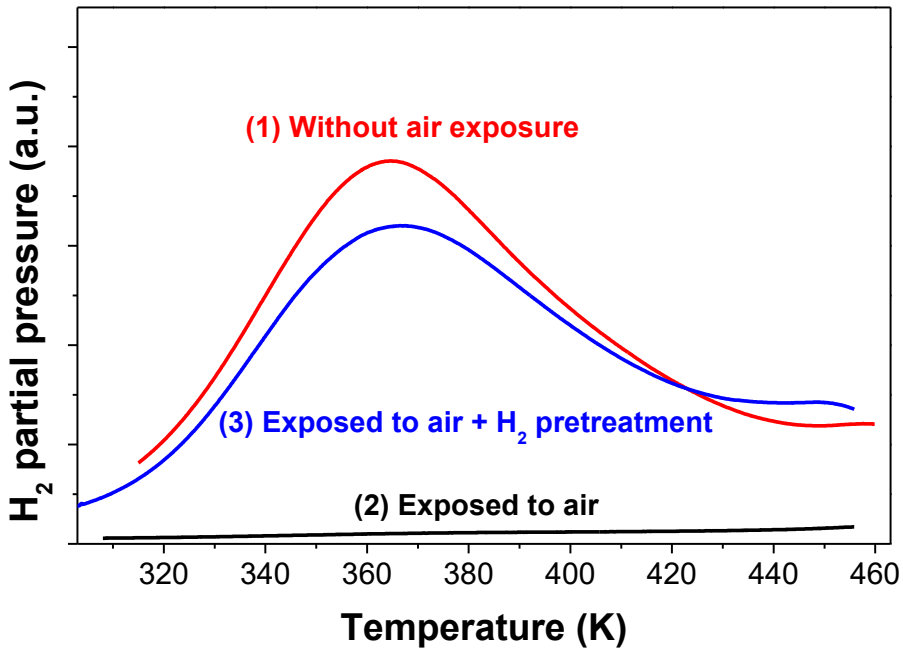

Figure 4.14: Thermo-desorption spectra of 20-Rh@MIL-101(Cr) for three sample conditionings: desorption recorded after hydrogen exposure and without air exposure (red), after hydrogen exposure followed by air exposure (black) and after air exposure followed by hydrogen pretreatment and H_2 exposure (blue)

Hydrogen desorption from Rh nanoparticles unexposed to air shows a unique desorption peak with a maximum at around 365 K. Interestingly, after H_2 exposure followed by air exposure of the composite, no hydrogen desorption is detected, whereas the hydrogen desorption behavior is recorded when the air-exposed material is subsequently treated under H_2 atmosphere at RT. This might be explained by the formation of H_2O at the surface of Rh

nanoparticles. This same phenomenon was observed by Jòzwiak[12] with Rh nanoparticles supported on carbon. The H_2O formation at the Rh nanoparticles surface might be explained by the combination of oxygen atoms in the air with hydrogen atoms, adsorbed by chemisorption, or absorbed in the interstitial sites of Rh. In both cases, no hydrogen desorption signal may be recorded after air exposure of hydrogenated Rh nanoparticles. Moreover, these results depict that it is possible to recover the material after air exposure and to have the same desorption properties initially observed. This is in good agreement with the results obtained for 1.4 nm Rh nanoparticles on carbon support.[11]

However, at this level, the results do not allow to decide whether the interaction of hydrogen with 1 nm Rh clusters is an absorption of H_2 with solid solution formation at room temperature under 1 bar of H_2 or it is dissociative chemisorption on the surface.

4.3.3.3 Nanosize *effect* and the scaling law

To further study the nanoscale effect on Rh particles in the interaction with hydrogen, a comparison between the desorption spectra of Rh nanoparticles with different sizes was carried out with the same heating rate (*figure 4.15(a)*). Thus, four materials with different Rh average particle sizes: three composites, already reported [1], formed by Rh nanoparticles supported on a carbon matrix with an average particle size of 2.3, 1.9 and 1.3 nm respectively, and the fourth is that of 1 nm Rh particles confined in MIL-101(Cr). The T_{max} of the different desorption peaks were then plotted *vs. 1/r* (r = radius of nanoparticle) as shown in *figure 4.15(b)*.

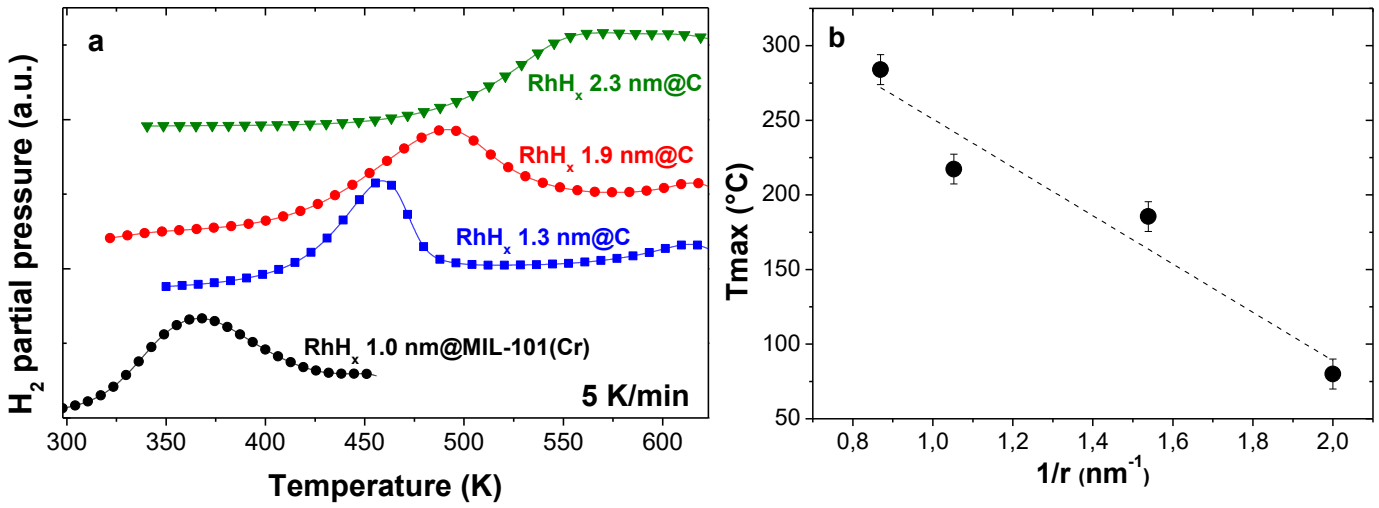

Figure 4.15: (a) TDS spectra of materials with different Rh particle size and (b) the T_{max} vs. 1/r plot.

The recorded desorption results show that by increasing the size of the nanoparticles, hydrogen is desorbed at higher temperatures (*figure 4.15(a)*). Moreover, by plotting the T_{max} of desorption as a function of the inverse of the particle size, a linear dependence is obtained obeying the inverse size scaling law[13] as showing in *figure 4.15(b)*. The scaling law highlights a linear relation between the inverse size and the different properties of the particles (thermodynamic, kinetic…). For example, a linear dependence of melting temperature of confined indium nanoparticles was reported in the literature.[13] In this perspective, the linear dependence of T_{max} of H_2 desorption with size of the particles is due to a volume phenomenon, therefore of diffusion of hydrogen in the interstitial sites. Otherwise, if the interaction of the hydrogen with the nanoparticles of Rh was dissociative chemisorption on the surface, which is a phenomenon independent of particle size, the H_2 desorption T_{max} should have been the same, whatever the size, but with a decrease in the intensity of the desorption peaks by increasing the size, *i.e.* decreasing the total area of the particles. Nevertheless, for a diffusion phenomenon, the larger the particle size, the longer the diffusion paths traveled by the hydrogen and the higher the energy required for diffusion and recombination, *i.e.* requires a higher temperature to desorb the absorbed hydrogen in the interstitial sites.

Thus, the formation of rhodium solid solutions with hydrogen is suggested by the different TDS measurements and the comparison of the desorption results with other materials. The transition from the solid solution to the metal phase (during desorption) seems to obey the inverse size scaling law.

4.3.3.4 Cycling effect

The 1 nm Rh clusters were exposed to 1 bar of H_2 or D_2 at room temperature several times and TDS was recorded thereafter. These desorption measurements were performed on the same portion of the material. The aim is to study the effect of cycling (sorption/desorption) on the interaction of hydrogen with Rh clusters. Thus, the peak areas were determined for each cycle and were plotted in *figure 4.16*.

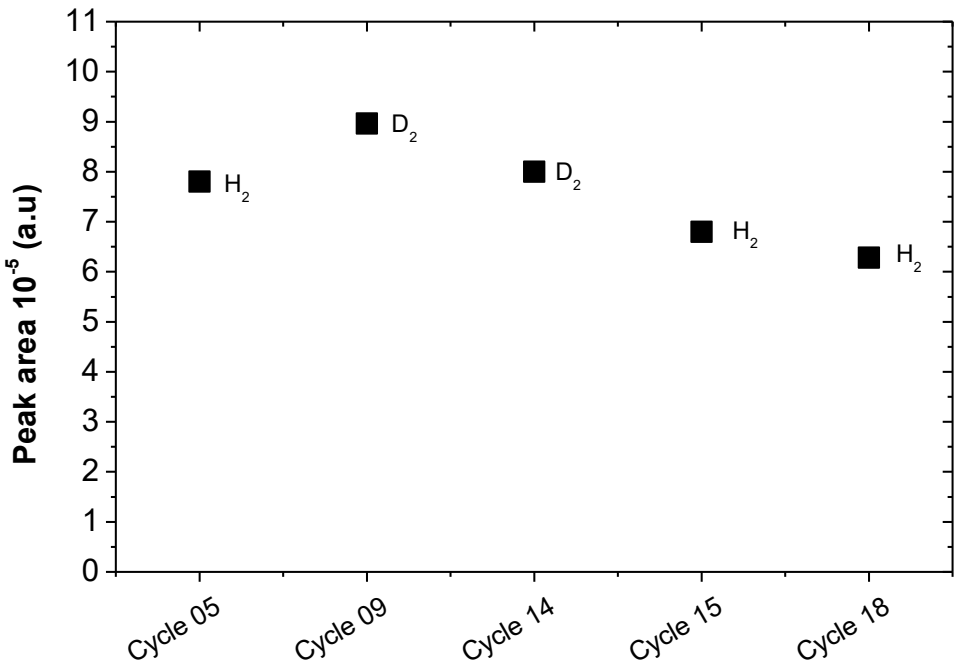

Figure 4.16: Desorption peak areas of Rh nanoparticles as a function of the gas.

Whatever the gas to which the Rh particles was exposed (H_2 or D_2), the areas of the desorption peaks, which translates roughly the amount of desorbed hydrogen, are comparable.

Thus, in order to check the stability of the material to cycling, TEM images were performed on the 20-Rh@MIL-101(Cr) composite recovered after the 20 cycles. The Rh nanoparticles retained their good dispersion in the MIL-101(Cr) with a stable average size (~ 1 nm) as shown in *figure 4.17*.

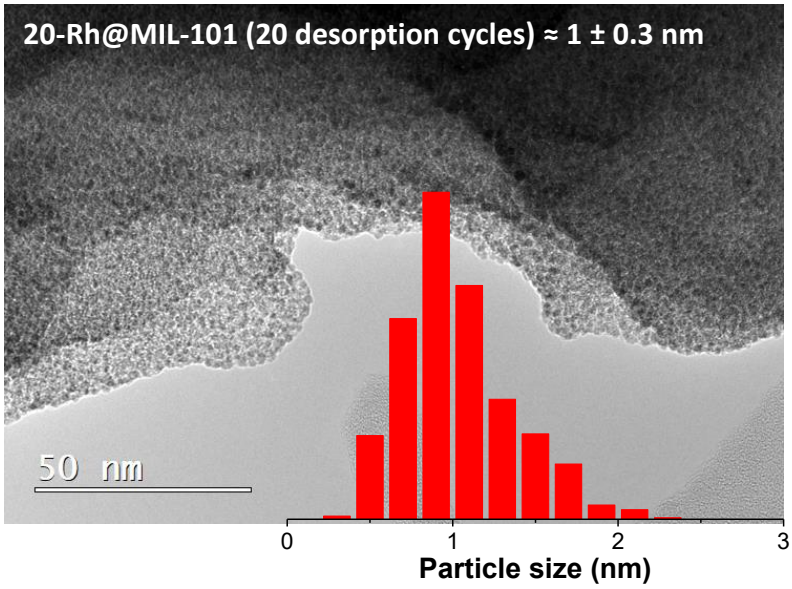

Figure 4.17: Typical TEM images of 20-Rh@MIL-101(Cr) composite after 20 desorption cycles with Rh particle size histograms

4.4 Conclusion

In this chapter, a study of the structural and nanostructural properties of a composite material formed by ultra-small rhodium nanoparticles confined within the pores of MIL-101(Cr), as well as the hydrogen sorption properties was carried out.

The first part of this chapter consists of the synthesis of Rh@MIL-101(Cr) materials with different loadings up to 20 wt.%. The synthesis technique used for the preparation of the Pd@MIL-101(Cr) materials, *i.e.* the double solvent impregnation followed by a reduction under Ar/H_2 flow, was optimized. Then, the physicochemical characterization of the synthesized materials was carried out. Structural, nanostructural and textural characterization confirmed the good insertion and dispersion of the 1 nm Rh particles within the pores of MIL-101(Cr) even for high metal loadings.

The last part of this chapter focused on the determination of the hydrogen sorption properties of Rh@MIL-101(Cr) materials. Firstly, a study of hydrogen adsorption was carried out at low temperature and the isosteric heat was determined and compared to that of MIL-101(Cr). Interestingly, as for 10-Pd@MIL-101(Cr) in *chapter III*, an increase in isosteric heat at low coverage has been observed. Then, the study of the hydrogen sorption at room temperature was carried out. First, PCI curves, performed at room temperature and up to 1 bar H_2, showed that no pressure plateau was observed assuming no formation of the hydride phase under these measurement conditions and suggesting two working hypotheses: the interaction of hydrogen with Rh nanoparticles consists of a dissociative chemisorption on the surface, or a solid solutions formation with hydrogen at room temperature and up to 1 bar H_2, or both. Afterward, the H_2 desorption study was carried out by the thermal desorption spectroscopy. These H_2 desorption measurements were insufficient to decide on the phenomenon involved in the interaction of hydrogen with 1 nm Rh clusters. But, by comparing the desorption results with the Rh@MIL-101(Cr) with other Rh mono materials with different particle sizes, the formation of solid solution in 1 nm Rh was suggested.

The difficulty of characterizing the 1 nm Rh particles should be noted and emphasized. Because of the laboratory facilities are limited to characterize 1 nm Rh particles and study their hydrogen sorption properties, interpretations and conclusions are drawn and discussed indirectly. In fact, apart from the TEM images which made it possible to clearly identify the Rh nanoparticles, all the other used characterization techniques made it possible to interpret the results and to draw conclusions indirectly. The conclusion of the hydrogen interaction with 1 nm Rh nanoparticles are mainly based on hypotheses. However, confirmation of the

obtained results in this study may be performed by *in situ* XAS measurements. Indeed, due to its very high sensitivity of the X-ray absorption spectroscopy, supplementary information on the local structure of 1 nm Rh clusters in a H_2 environment can be given.

References

1. Zlotea, C. *et al.* First Evidence of Rh Nano-Hydride Formation at Low Pressure. *Nano Letters* **15**, 4752–4757 (2015).
2. Alain, M., Jacques, M., Diane, M.-B. & Karine, P. MAX: Multiplatform Applications for XAFS. *Journal of Physics: Conference Series* **190**, 012034 (2009).
3. Michalowicz, A., Moscovici, J., Muller-Bouvet, D. & Provost, K. MAX (Multiplatform Applications for XAFS) New Features. *J. Phys.: Conf. Ser.* **430**, 012016 (2013).
4. Evans, J. & Tromp, M. Interaction of small gas phase molecules with alumina supported rhodium nanoparticles: anin situspectroscopic study. *J. Phys.: Condens. Matter* **20**, 184020 (2008).
5. Sanchez, S. I. *et al.* The emergence of nonbulk properties in supported metal clusters: negative thermal expansion and atomic disorder in Pt nanoclusters supported on gamma-Al2O3. *J. Am. Chem. Soc.* **131**, 7040–7054 (2009).
6. Ferey, G. A Chromium Terephthalate-Based Solid with Unusually Large Pore Volumes and Surface Area. *Science* **309**, 2040–2042 (2005).
7. Juan-Alcan, J. *et al.* Interplay of Linker Functionalization and Hydrogen Adsorption in the Metal−Organic Framework MIL-101. *J. Phys. Chem. C* 8 (2014).
8. Yates, J. T., Thiel, P. A. & Weinberg, W. H. The chemisorption of hydrogen on Rh(111). *Surface Science* **84**, 427–439 (1979).
9. Castner, D. G., Sexton, B. A. & Somorjai, G. A. Leed and thermal desorption studies of small molecules (H2, O2, CO, CO2, NO, C2H4, C2H2 AND C) chemisorbed on the rhodium (111) and (100) surfaces. *Surface Science* **71**, 519–540 (1978).
10. Kreuzer, H. J. *et al.* Thermal desorption kinetics of hydrogen on rhodium (110). *Surface Science* **303**, 1–15 (1994).
11. Zlotea, C. *et al.* Investigation of the local structure of nanosized rhodium hydride. *Journal of Colloid and Interface Science* **524**, 427–433 (2018).
12. Jóźwiak, W. K. Temperature-programmed desorption of hydrogen from Rh/C catalysts. *React Kinet Catal Lett* **33**, 155–159 (1987).
13. Roduner, E. Size matters: why nanomaterials are different. *Chem. Soc. Rev.* **35**, 583–592 (2006).

CHAPTER V

MIL-101(Cr) DOPED WITH BIMETALLIC NANOPARTICLES

5.1 Bimetallic nanoparticles doping

In this chapter, a study of composites formed by bimetallic nanoparticles confined in the pores of MIL-101(Cr) was carried out. Indeed, three 10-*M*@MIL-101(Cr) materials (*M* = $Pd_{50}Rh_{50}$, $Pd_{50}Pt_{50}$ and $Rh_{50}Ir_{50}$) were synthesized by double-solvent impregnation of the previously degassed MIL-101(Cr) (second batch) followed by reduction under Ar/H_2 flux at 573 K for 2 hours. It should be noted that the bulk binary system of Pd-Rh, Pd-Pt and Rh-Ir have large miscibility gaps with very high critical temperatures (1203[1,2], 1043[3] and 1123 K[4] respectively). Moreover, studies on these particles has been carried out in the literature for the same composition of bimetallic nanoparticles (50:50). For the Pd-Rh and Pd-Pt systems, metastable alloys were formed, under synthetic conditions similar to those used in this project, with particles sizes of 2.9 ± 0.6[5], 1.8 ± 0.6[6] and 3.2 ± 1.0 nm[2,7] for the first system and 7.8 ± 0.9[8] and 6.3 nm[9] for the second. To serve as a reference, 10-Pd@MIL-101(Cr), 10-Rh@MIL-101(Cr), 10-Pt@MIL-101(Cr) and 10-Ir@MIL-101(Cr) were also synthesized by the same method. The different composites have been characterized in order to study the nature of the formed bimetallic nanoparticles. The latter can exist in three forms: separated monometallic nanoparticles, bimetallic nanoparticles in the form of metastable alloy, or bimetallic nanoparticles in the form of core-shell. Our main objective here is to characterize the formation or not of solid solutions of bulk-immiscible metals at nanoscale and confined into the pores of MIL-101(Cr).

5.1.1 X-Ray Diffraction (XRD)

The 10-*M*@MIL-101(Cr) composites (*M* = Pd, Rh, Pt, Ir, Pd_{50}-Rh_{50}, Pd_{50}-Pt_{50} and Rh_{50}-Ir_{50}) were obtained by the optimized DSM approach. The structural characterization of the synthesized hybrid materials was carried out by X-ray diffraction. The angular domain 2θ chosen for this study is 5-65°. The different bulk metals crystallize in a face-centered cubic system (*fcc*) with the space group *Fm-3m*.

The X-ray diffraction patterns of pristine MIL-101(Cr) and 10-*M*@MIL-101(Cr) composites are plotted in *figure 1*. *Figure 5.1(a), (b)* and *(c)* depicts the XRD patterns for *M* = Pd, Pd_{50}-Rh_{50}, Rh, *M* = Pd, Pd_{50}-Pt_{50}, Pt and *M* = Rh, Rh_{50}-Ir_{50}, Ir respectively. The Miller indices of expected peaks of different metal are also indicated as dotted lines.

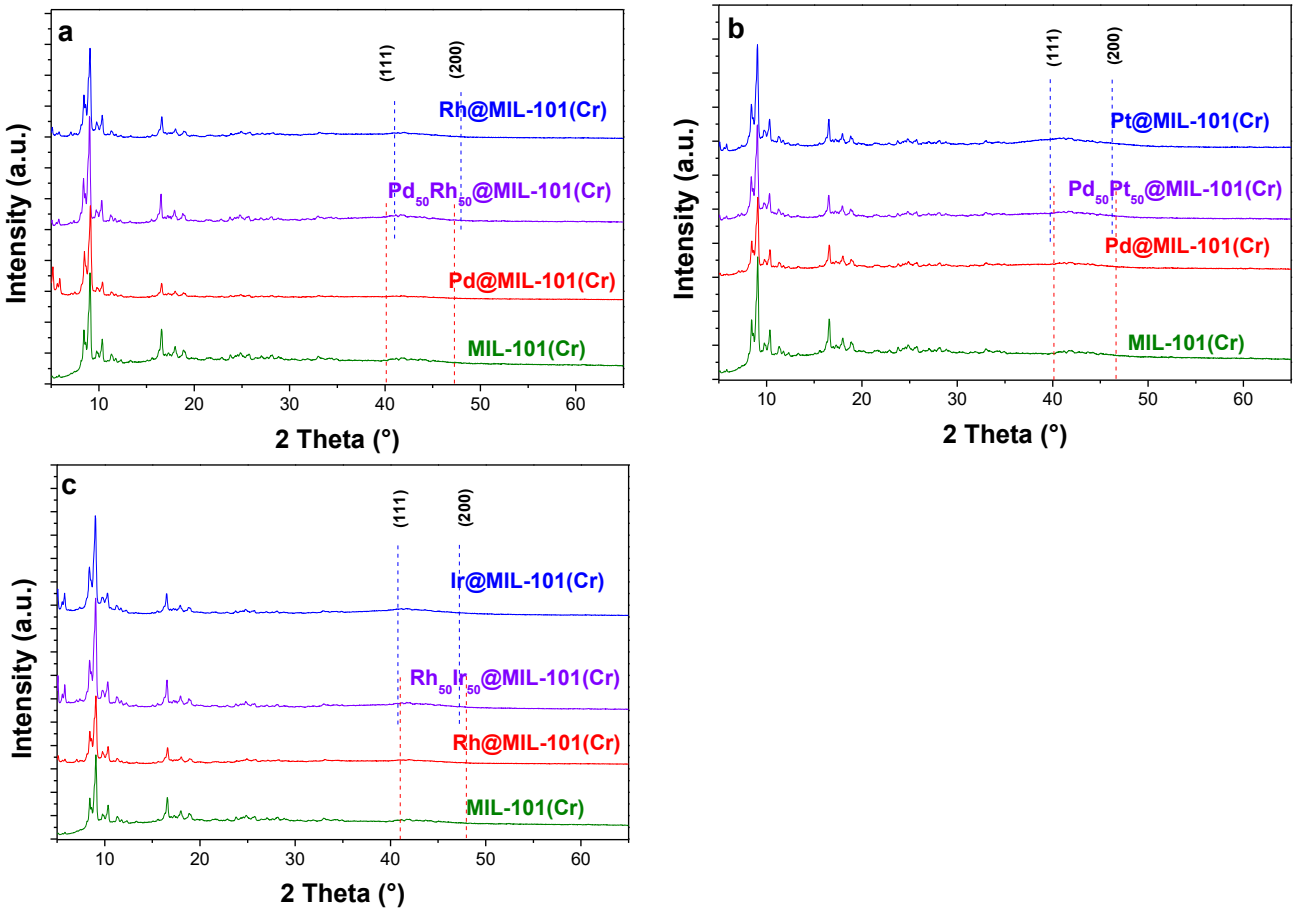

Figure 5.1: XRD patterns of pristine MIL-101(Cr) and 10-M@MIL-101(Cr) ((a) M = Pd, Pd_{50}-Rh_{50} and Rh (b) M = Pd, Pd_{50}-Pt_{50} and Pt (c) M = Rh, Rh_{50}-Ir_{50} and Ir).

The MIL-101(Cr) structure retains its crystallinity after synthesis of metallic nanoparticles whatever the composite. In addition, there is no metal diffraction peak for the different 10-*M*@MIL-101(Cr) composites as observed in *figure 5.1(a), (b)* and *(c)*. This can be explained by the very small size of the Pd clusters, as further confirmed by TEM.

5.1.2 Transmission Electron Microscopy (TEM)

The nanostructural characterization of 10-*M*@MIL-101(Cr) was performed by Transmission Electron Microscopy (TEM) to examine the dispersion of the nanoparticles in the MOFs, to determine the particle size distribution and the average size of these particles. *Figure 5.2* shows the TEM images of the monometallic composites (10-*M*@MIL-101(Cr) with *M* = Pd, Pt, Rh and Ir). The analysis of several TEM images allows drawing the histograms of particle size presenting the size distribution of the nanoparticles. The average particle size was proposed following the statistical analysis of the histograms.

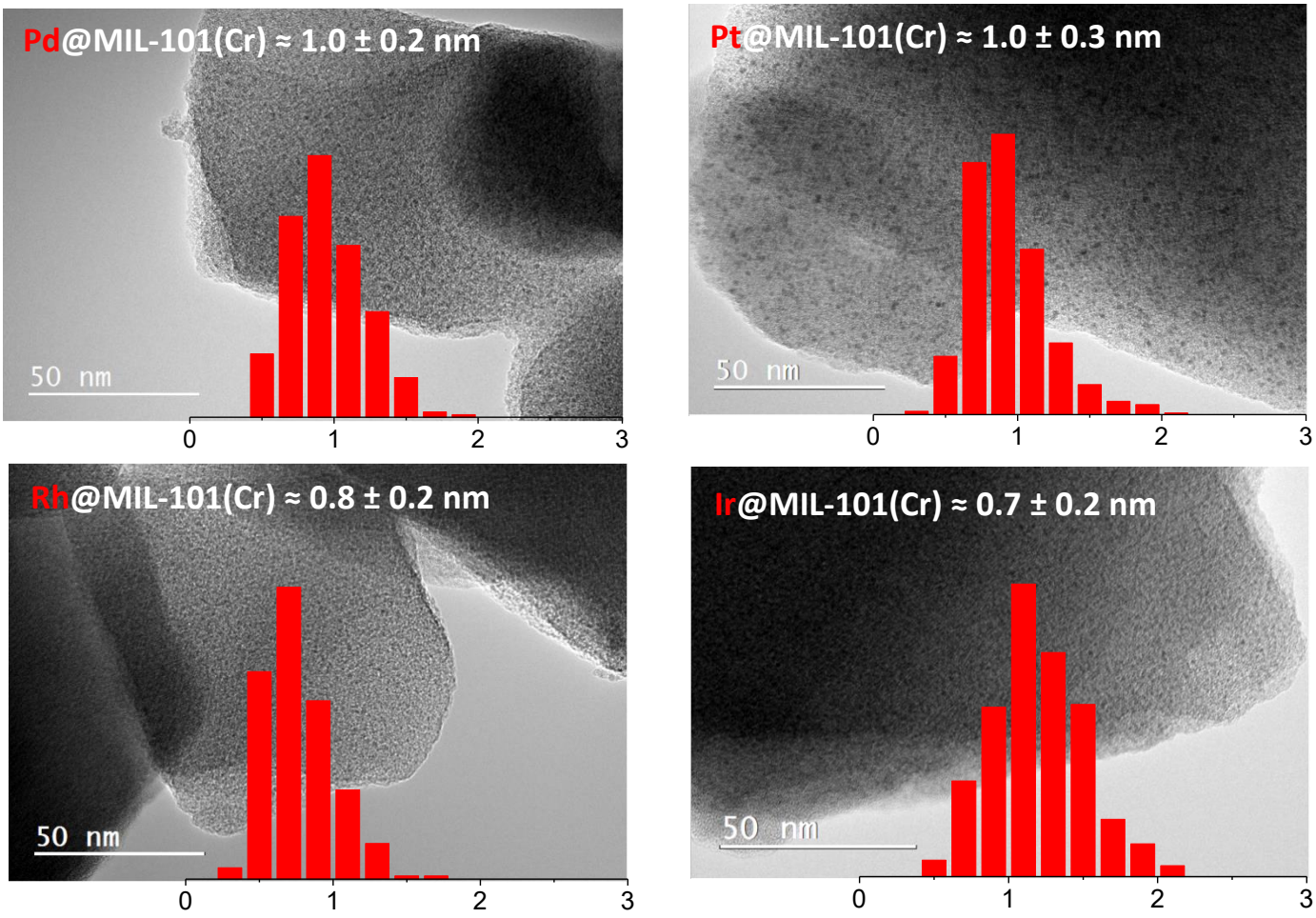

Figure 5.2: Typical TEM images of 10-M@MIL-101(Cr) composites (M = Pd, Pt, Rh and Ir), with metallic particle size histograms.

The images show black spots that corresponds to Pd, Pt, Rh and Ir clusters very well dispersed in the pores of MIL-101(Cr). The size distribution of the nanoparticles of Pd, Pt, Rh and Ir is mainly between 0.5 and 2.0 nm and the average size of the metallic clusters of the different 10-*M*@MIL-101(Cr) composites is around 1.0 nm. This very small size explains the absence of X-ray diffraction peaks of the different metals.

Materials formed by bimetallic nanoparticles were also characterized. *Figure 5.3* shows the TEM images of the 10-*M*@MIL-101(Cr) composites (*M* = Pd_{50}-Pt_{50}, Pd_{50}-Rh_{50} and Rh_{50}-Ir_{50}).

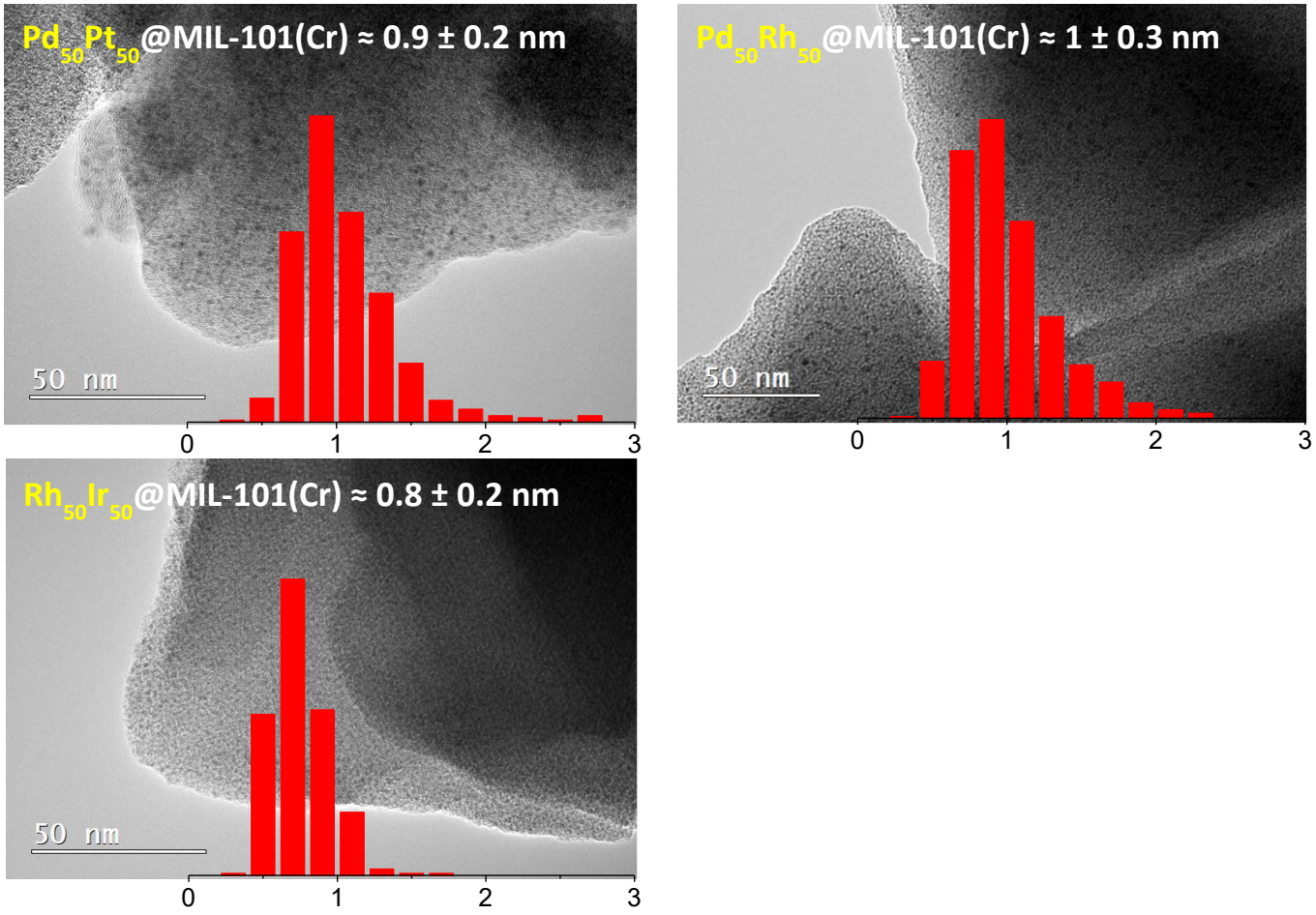

Figure 5.3: Typical TEM images of 10-M@MIL-101(Cr) composites (M = Pd_{50}-Pt_{50}, Pd_{50}-Rh_{50} and Rh_{50}-Ir_{50}), with metallic particle size histograms.

As for monometallic materials, the TEM images of bimetallic ones show black spots corresponding to very well dispersed metallic clusters in the pores of MIL-101(Cr). The size distribution of the bimetallic nanoparticles is mainly between 0.5 and 2.5 nm and the average metallic particle size is around 1 nm which explains the absence of metal X-ray diffraction peaks.

5.1.3 Energy-Dispersive X-ray spectroscopy (EDX)

The metal composites with bimetallic nanoparticles were synthesized with an equimolar composition. In order to verify this composition, chemical analyzes by Energy-Dispersive X-ray spectroscopy were performed and the results reported in *table 5.1*. For each composite, chemical analysis reveals the presence of the metals close to equimolar composition, in good agreement with nominal values.

Table 5.1 : Chemical analysis of 10-M@MIL-101(Cr) (M = Pd_{50}-Rh_{50}, Pd_{50}-Pt_{50} and Rh_{50}-Ir_{50}).

Sample	M_1 (at. %)	M_2 (at. %)
Pd_{50}-Rh_{50}@MIL-101(Cr)	**51.0 (± 4.5)**	**49.0 (± 4.2)**
Pd_{50}-Pt_{50}@MIL-101(Cr)	**50.0 (± 4.4)**	**50.0 (± 3.8)**
Rh_{50}-Ir_{50}@MIL-101(Cr)	**58.0 (± 2.2)**	**42.0 (± 2.0)**

It should be noted that the state of reduction of the mono and bimetallic nanoparticles was checked by EDX by determining the chlorine content in each composite and comparing it with the pristine MIL-101(Cr), as explained in the *chapter IV*. The chlorine content measured after the synthesis of the various materials is equal to or slightly higher than the initial rate in the pristine MIL-101(Cr), confirming the total or almost total reduction of the metallic nanoparticles.

5.1.4 Differential Thermal Analysis coupled with Thermogravimetric Analysis (DTA-TGA)

In order to study the nature of bimetallic nanoparticles, based on their thermal stability, differential thermal analysis coupled with thermogravimetric analysis (DTA-TGA) were performed under air with a temperature rate of 10 K/min.

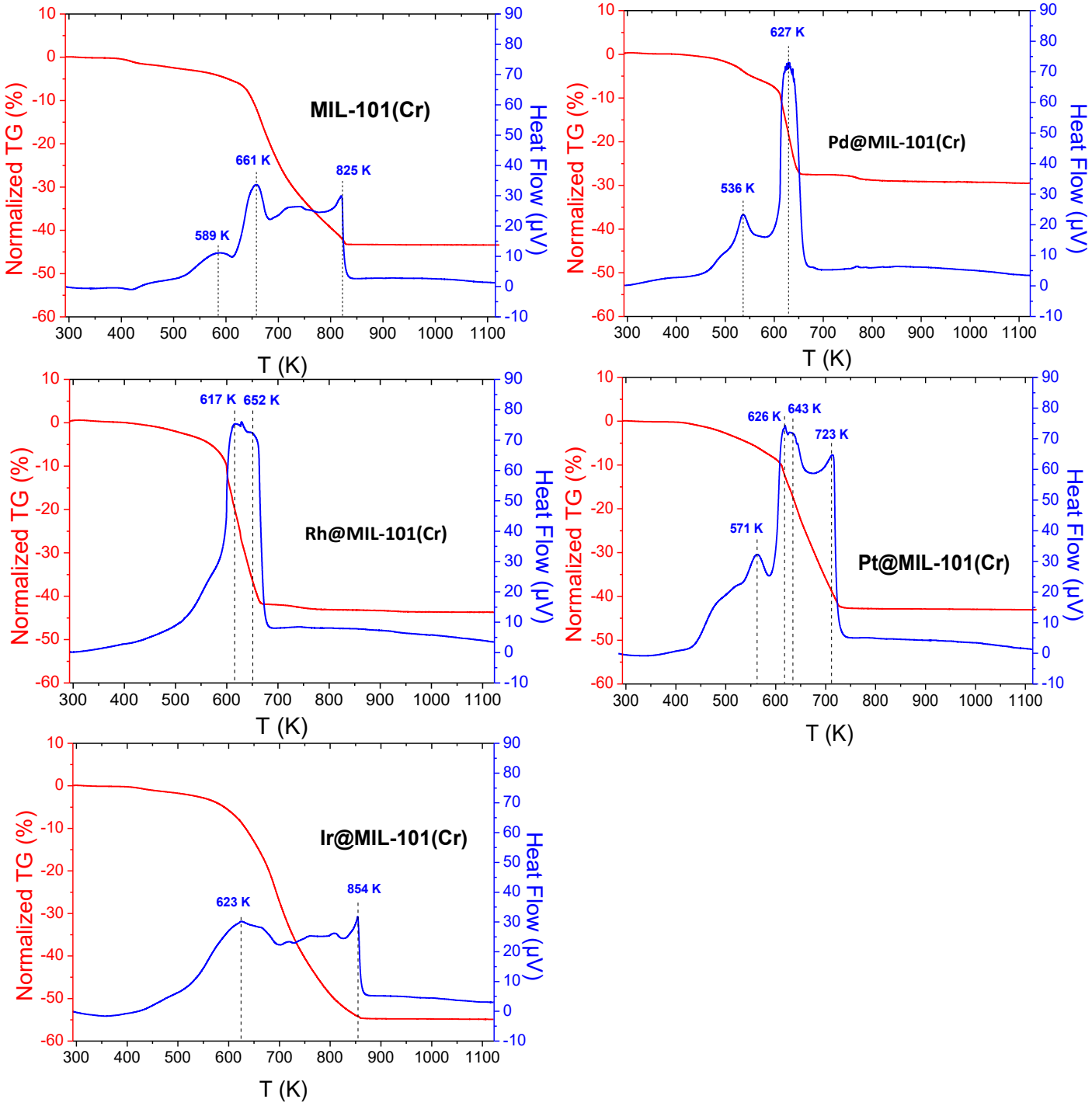

Figure 5.4: DTA(blue)-TGA(red) curves of pristine MIL-101(Cr) and 10-M@MIL-101(Cr) composites (M = Pd, Rh, Pt and Ir).

Initially, composites with monometallic nanoparticles as well as pristine MIL-101(Cr) were analyzed for reference and the results are shown in *figure 5.4*. First, the pristine MIL-101(Cr) was analyzed. At first step, adsorbed water molecules in large cages (3.4 nm), which constitute around 5 wt.% of MIL-101(Cr), were evaporated between 298 and 473 K. Then, water molecules in the small cages (2.9 nm) were removed between 473 and 650 K leading to a weight loss of around 25%. Finally, the elimination of OH/Cl groups was occurred between 650 and 823 K causing the decomposition of the framework and loss of around 40 wt.% of MIL-101(Cr). In addition, the DTA curve shows several large peaks. A similar profile is obtained with the 10-Ir@MIL-101(Cr) composite. However, the composites with nanoparticles of Pd, Pt and Rh show a faster degradation (from 623 to 673 K) characterized by a strong decrease of TGA and sharper DTA signal. Then, the composites with bimetallic nanoparticles were analyzed and the results are shown in *figure 5.5*.

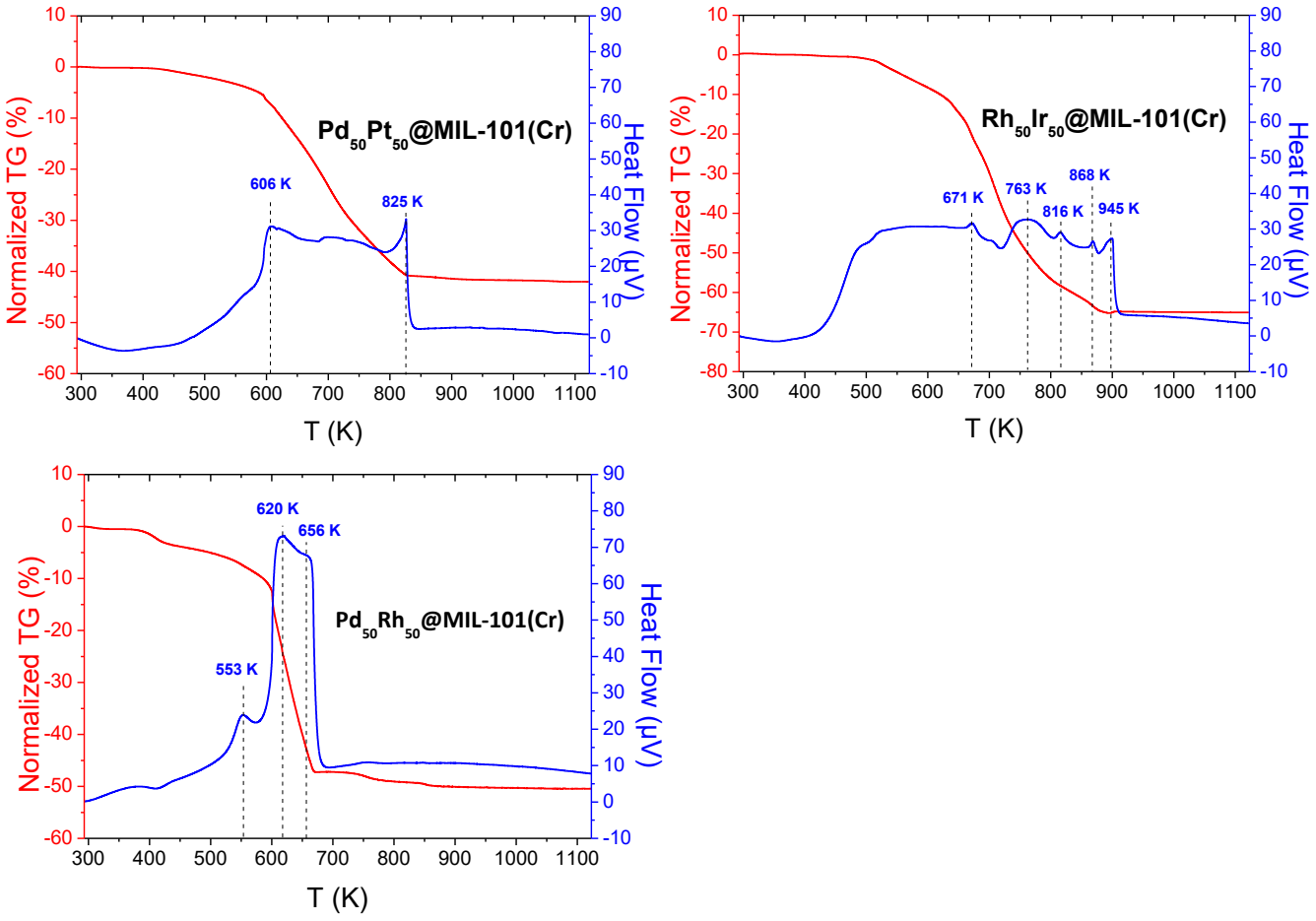

Figure 5.5: DTA(blue)-TGA(red) curves of 10-M@MIL-101(Cr) composites (M = Pd_{50}-Pt_{50}, Pd_{50}-Rh_{50} and Rh_{50}-Ir_{50}).

The 10-Pd_{50}-Pt_{50}@MIL-101(Cr) and 10-Rh_{50}-Ir_{50}@MIL-101(Cr) composites show a slow oxidation (between 520 and 850 K) characterized by the smooth decrease of the TGA signal and a broad DTA profile with several temperature peaks. The degradation of the 10-$Pd_{50}Rh_{50}$@MIL-101(Cr) composite appears faster than the 2 previous materials (between 600 and 650 K).

The oxidation of composites with nanoparticles of Pd, Rh and Pt was fast due to a catalytic effect of these metals. However, the insertion of Ir nanoparticles has no remarkable effect on the degradation of the 10-Ir@MIL-101(Cr) composite.

In order to determine the nature of the bimetallic nanoparticles, a comparison between the DTA-TGA results obtained with the mono and bimetallic clusters was carried out. The 10-Pd@MIL-101(Cr) and 10-Pt@MIL-101(Cr) composites showed a relatively fast degradation characterized by a rapid mass loss and a sharp profile of the DTA signal. However, the 10-$Pd_{50}Pt_{50}$@MIL-101(Cr) composite oxidizes more slowly and gives a DTA signal profile comparable to that of pristine MIL-101 (Cr). Under the hypothesis of full reduction of both metallic precursors, we suggest that this change in TGA-DTA profile might be due to the formation of bimetallic nanoparticles (alloys or core-shell). To this same composition, it has been reported that nanoparticles of 6.3[9] and 7.8 nm[8] form alloys while others of 11.2 nm[8] are in the form of core-shell.

For the 10-$Rh_{50}Ir_{50}$@MIL-101(Cr) composite, the same conclusion may be drawn. Indeed, the 10-Rh@MIL-101(Cr) composite show a fast oxidation while no effect is observed on the MIL-101(Cr) degradation by inserting Ir nanoparticles into the pores. Nevertheless, the oxidation of the 10-Rh_{50}-Ir_{50}@MIL-101(Cr) material became slower (between 500 and 900 K) with broad DTA signal profile.

However, for the 10-Pd_{50}-Rh_{50}@MIL-101(Cr) composite, a mass loss comparable to that of 10-Pd@MIL-101(Cr) and 10-Rh@MIL-101 (Cr) is observed on the TGA curve with a DTA profile resembling that of 10-Pd@MIL-101(Cr) and 10-Rh@MIL-101(Cr). This suggests that the nanoparticles present in the 10-Pd_{50}-Rh_{50}@MIL-101(Cr) composite are separated monometallic Pd and Rh particles dispersed in the porous matrix. In contrast to these results, metastable Pd-Rh nanoalloys were previously formed, under same synthetic conditions, with nanoparticles of 1.8[2,6], 2.9[5] and 3.2 nm[2,7] on carbon or PVP supports.

To summarize, among the three bimetallic composites, only 10-Pd_{50}-Pt_{50}@MIL-101(Cr) and 10-Rh_{50}-Ir_{50}@MIL-101 (Cr) materials seem to contain bimetallic nanoparticles. The 10-Pd_{50}-Rh_{50}@MIL-101(Cr) composite is likely to contain separately dispersed monometallic Pd and Rh nanoparticles.

5.1.5 Specific surface area & total pore volume

The characterization of the textural properties of the mono- and bimetallic nanoparticles doped MIL-101(Cr) was carried out by N_2 adsorption/desorption measurements. *Figure 5.6* shows the N_2 adsorption/desorption curves for monometallic (*figure 5.6(a)*) and bimetallic materials (*figure 5.6(b)*) and compared to pristine MIL-101(Cr). The obtained isotherms for MIL-101(Cr) (2nd batch) as well as for 10-*M*@MIL-101(Cr) are of type IV (a small hysteresis is present in all curve), *i.e.* corresponding to mesoporous materials.

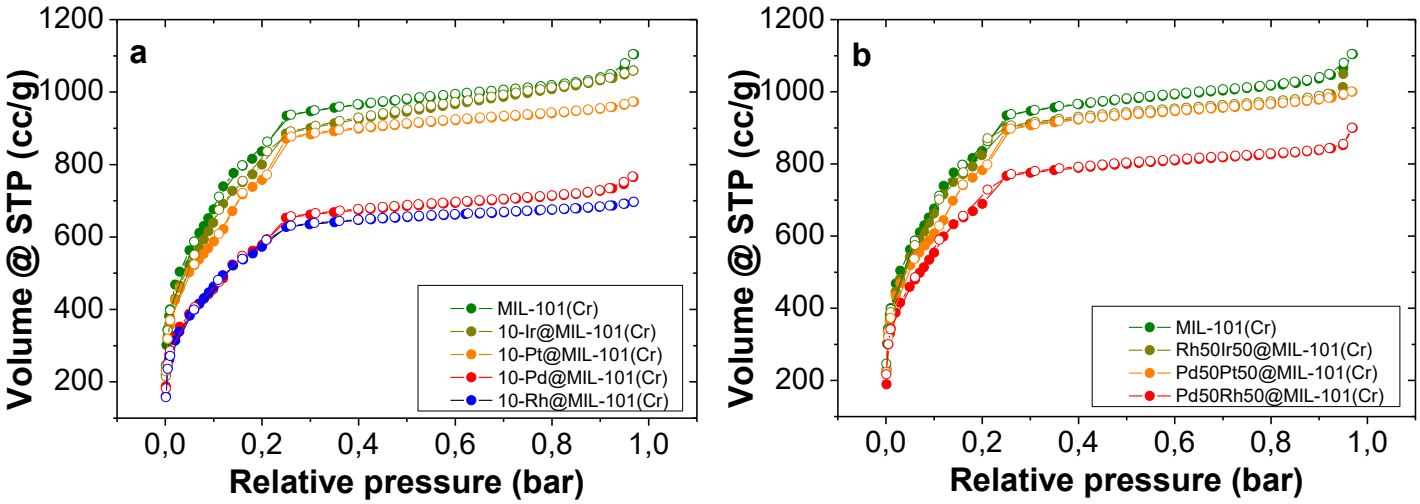

Figure 5.6: N_2 adsorption/desorption curves of 10-M@MIL-101(Cr) ((a) M = Ir, Pt, Pd and Rh and (b) M = Rh_{50}-Ir_{50}, Pd_{50}-Pt_{50} and Pd_{50}-Rh_{50}) compared to MIL-101(Cr).

Table 5.2 summarizes the results of N_2 adsorption/desorption for pristine MIL-101(Cr) and 10-*M*@MIL-101(Cr). The specific surface area and the total pore volume decrease with the insertion of mono and bimetallic nanoparticles into the pores of MIL-101(Cr). Results for 10-Pd@MIL-101(Cr) and 10-Rh@MIL-101(Cr) composites have already been discussed in chapter 3 and 4. For the other composites, the decrease in the specific surface area and the total pore volume is almost stable for the other composites (around 3100 m^2/g and 1.5 cc/g respectively), except for 10-Pd_{50}-Rh_{50}@MIL-101(Cr) with a specific surface area and total pore volume is comparable to the 10-Pd@MIL-101(Cr) and 10-Rh@MIL-101(Cr) (around

2660 m^2/g and 1.3 cc/g). As discussed in previous chapters, this decrease can be explained by the increase in the total mass of the composite after the insertion of the Pd clusters and by blocking the accessible pores.

Table 5.2 : Summary of the N_2 adsorption results of pristine MIL-101(Cr) and 10-M@MIL-101(Cr) (M = Pd, Rh, Pt, Ir, $Pd_{50}Pt_{50}$, Pd_{50}-Rh_{50} and Rh_{50}-Ir_{50}).

Sample	Particle size (nm)	Surface area (m^2/g)	Total pore volume (cc/g)
MIL-101(Cr)	-	3550	1.75
10-Pd@MIL-101(Cr)	1.0 ± 0.2	2200	1.10
10-Rh@MIL-101(Cr)	0.8 ± 0.2	2200	1.08
10-Pt@MIL-101(Cr)	1.0 ± 0.3	3020	1.49
10-Ir@MIL-101(Cr)	0.7 ± 0.2	3080	1.62
10-$Pd_{50}Pt_{50}$@MIL-101(Cr)	0.9 ± 0.2	3100	1.54
10-$Pd_{50}Rh_{50}$@MIL-101(Cr)	1.0 ± 0.3	2660	1.32
10-$Rh_{50}Ir_{50}$@MIL-101(Cr)	0.8 ± 0.2	3140	1.57

5.2 Interaction with Hydrogen

The hydrogenation properties of the 10-*M*@MIL-101(Cr) (*M* = Pd, Rh, Pt, Ir, Pd_{50}-Rh_{50}, Pd_{50}-Pt_{50} and Rh_{50}-Ir_{50}) composites were studied by Pressure Composition Isotherm and Thermo-Desorption Spectroscopy techniques.

5.2.1 Pressure-Composition-Isotherm at low pressure and room temperature

The PCI curves of the pristine MIL-101(Cr) as well as the 10-*M*@MIL-101(Cr) composites (*M* = Pd, Rh, Pt, Ir, Pd_{50}-Rh_{50}, Pd_{50}-Pt_{50} and Rh_{50}-Ir_{50}) were measured, up to 1 bar H_2 pressure at room temperature, and are shown in *figure 5.7* (and *annex 7*). Before each measurement, the materials were degassed at 493 K for 18 hours to remove water molecules adsorbed by MIL-101(Cr), with an additional hydrogen pretreatment step prior to degassing for all doped materials.

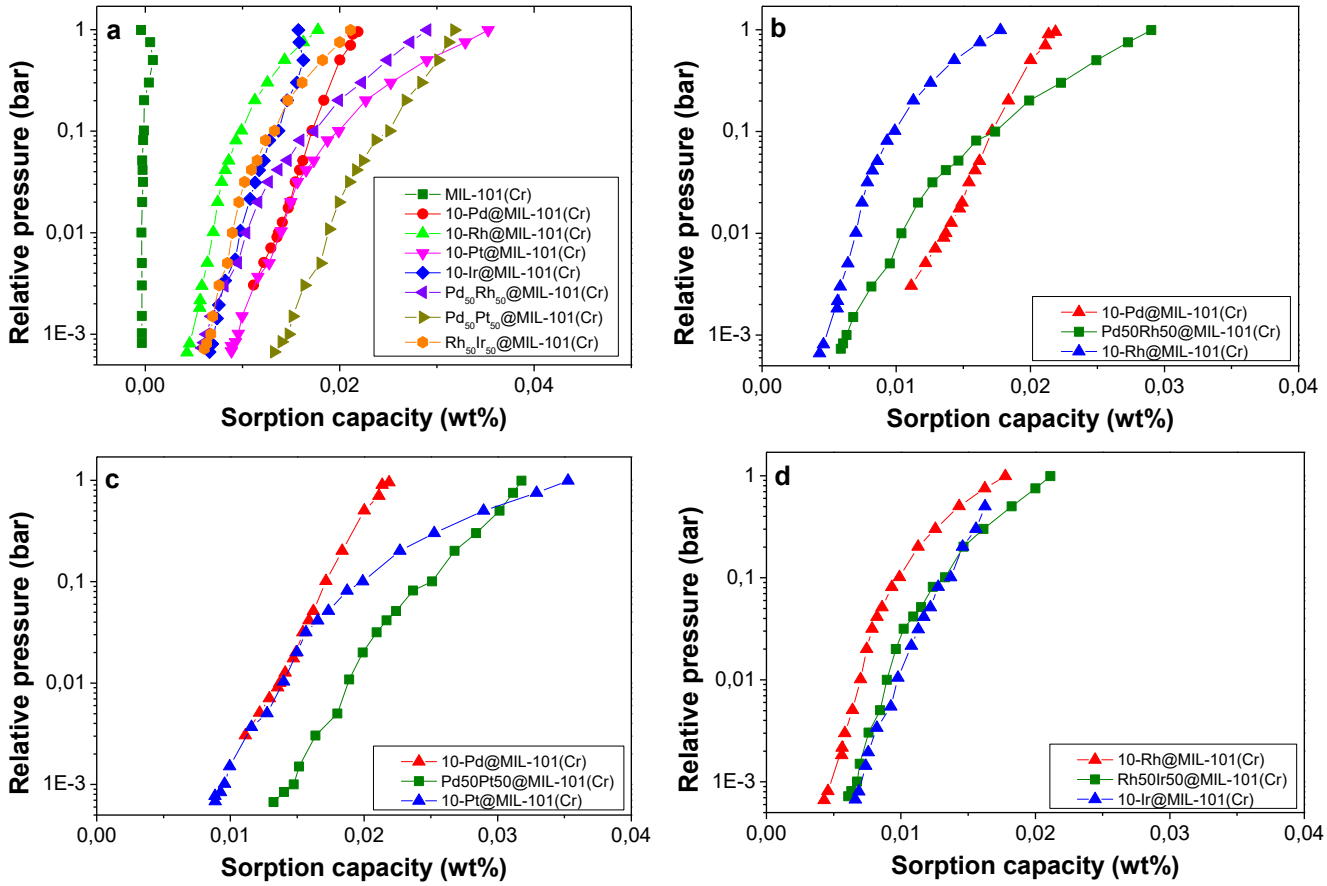

Figure 5.7: The PCI curves recorded at 300 K up to 1 bar for: (a) MIL-101(Cr) and 10-M@MIL-101(Cr) (M = Pd, Rh, Pt, Ir, Pd_{50}-Rh_{50}, $Pd_{50}Pt_{50}$ and Rh_{50}-Ir_{50}) (b) 10-M@MIL-101(Cr) (M = Pd, Rh and Pd_{50}-Rh_{50}) (c) 10-M@MIL-101(Cr) (M = Pd, Pt and Pd_{50}-Pt_{50}) (d) 10-M@MIL-101@MIL-101(Cr) (M = Rh, Ir and Rh_{50}-Ir_{50}).

The PCI curves are represented in weight capacity to compare the 10-*M*@MIL-101(Cr) composites curves with the pristine MIL-101(Cr) curve (*figure 5.7(a)*). At room temperature and up to 1 bar H_2, the hydrogen adsorption capacity by the pristine MIL-101(Cr) is negligible, as already shown in *chapter IV*. The insertion of the different metallic nanoparticles in the pores of MIL-101(Cr) increases the hydrogen sorption capacity. Moreover, no pressure plateau is observed for the different doped materials characterizing the absence of the hydride formation at room temperature up to 1 bar H_2, in good agreement with the literature[6–8]. It should be noted that these measurements are repeatable under the same analysis conditions *i.e.* an outgas at 493 K for at least 2 hours was performed between each measurement.

Thereafter, *figure 5.7(b), (c)* and *(d)* illustrate the PCI curves of 10-M^1@MIL-101(Cr), 10-M^2@MIL-101(Cr) and 10-M^1_{50}-M^2_{50}@MIL-101(Cr) (M^1_{50}-M^2_{50} = Pd_{50}-Rh_{50}, Pd_{50}-Pt_{50} and Rh_{50}-Ir_{50}). Unfortunately, despite the increase in hydrogen sorption capacity by inserting metallic nanoparticles within the pores of MIL-101(Cr), this capacity remains very low (< 0.1 wt%). Moreover, no interpretable trend is possible from the PCI curves of the various 10-*M*@MIL-101(Cr) composites. To further study the hydrogen sorption properties for these different materials, other characterization techniques are needed, such as *in-situ* XAS at both metals' edges.

5.2.2 Hydrogen desorption properties

The hydrogen desorption properties of 10-*M*@MIL-101(Cr) (*M* = Pd, Pt, Rh, Ir, Pd_{50}-Rh_{50}, Pd_{50}-Pt_{50} and Rh_{50}-Ir_{50}) were investigated by the Thermal-Desorption Spectroscopy technique in order to confirm the nature of the nanoparticles confined within the pores of MIL-101(Cr). Two experimental protocols were used, depending on the metals to be studied. The 1 nm Pd clusters desorb hydrogen at a temperature below 300 K (*Chapter III*). Therefore, Pd-containing composites are characterized by TDS at low temperature by exposing them to 1 bar H_2 at room temperature and during cooling at 78 K. The desorption is then recorded by heating to 310 K with a constant heating rate of 5 K/min. On the other hand, the desorption of H_2 for 1 nm Rh clusters was observed at a temperature above 300 K. The TDS measurements for the composites containing Rh was then carried out by exposing them to 1 bar H_2 at room temperature. Thereafter, the desorption is recorded by heating at 573 K with a constant heating rate of 5 K/min. The hydrogen desorption results by pristine MIL-101(Cr) as well as 10-*M*@MIL-101(Cr) composites are shown in *figure 5.8*.

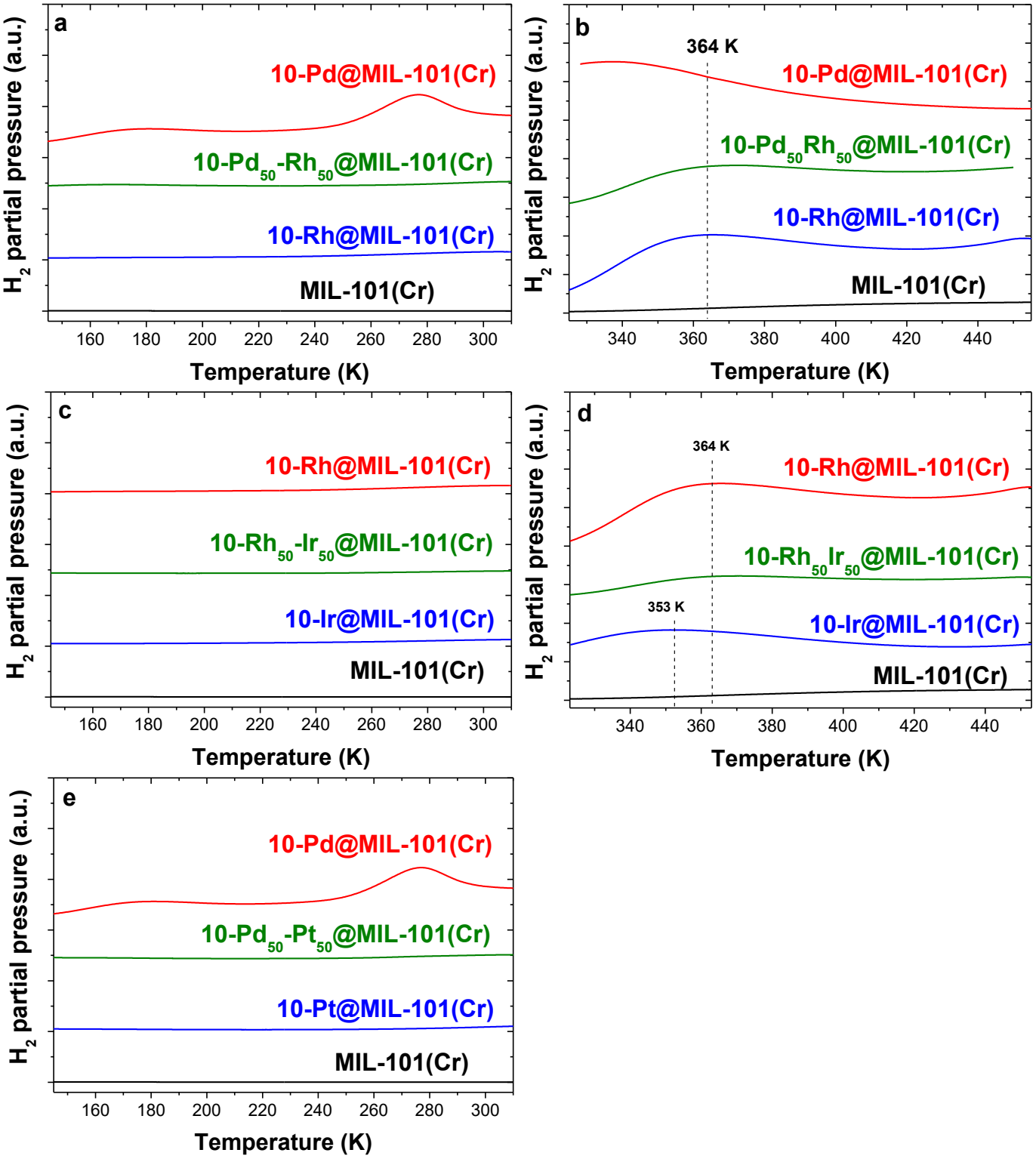

Figure 5.8: Thermo-desorption spectra of MIL-101(Cr) and 10-M@MIL-101(Cr) at low and high temperature ((a) and (b) Pd-Rh system, (c) and (d) Rh-Ir system and (e) Pd-Pt system.

At high and low temperatures, no hydrogen desorption from MIL-101(Cr) is observed (*figure 5.8*). Therefore, any recorded hydrogen desorption necessarily results from 10-*M*@MIL-101(Cr) composites. *Figures 5.8(a)* and *(b)* illustrate the desorption results for 10-*M*@MIL-101(Cr) composites (*M* = Pd, Rh and Pd_{50}-Rh_{50}) at low and high temperature. At low temperature, the only material that desorbs hydrogen is 10-Pd@MIL-101(Cr) with the two peaks recorded for desorption from the β phase and the transformation β → α (*Chapter III*). At high temperature, a peak of hydrogen desorption is mainly observed for 10-Rh@MIL-101(Cr) at ~ 365 K. A less intense peak is also noticed for 10-Pd_{50}-Rh_{50}@MIL-101(Cr) at around the same temperature (~ 365 K).

The hydrogen desorption results recorded at low and high temperature for 10-*M*@MIL-101(Cr) materials (*M* = Rh, Ir and Rh_{50}-Ir_{50}) are shown in *figures 5.8(c)* and *(d)*. At low temperature, no hydrogen desorption peak is observed for the 3 materials. However, at high temperature, the Ir and Rh monometallic composites desorb hydrogen with a desorption peak at ~ 350 and ~ 365 K respectively, with less intense peak for Ir than for Rh. By mixing the two metals, the bimetallic material no longer desorbs hydrogen characterized by the disappearance of the desorption peak. Finally, for the last composites of 10-*M*@MIL-101(Cr) (*M* = Pd, Pt and Pd_{50}-Pt_{50}) the comparison of the desorption of H_2 was carried out only at low temperature (*figure 5.8(e)*). In contrast to 10-Pd@MIL-101(Cr), neither 10-Pt@MIL-101(Cr) nor 10-Pd_{50}-Pt_{50}@MIL-101(Cr) desorb hydrogen characterized by the absence of desorption peaks of H_2.

The bimetallic Pd_{50}-Pt_{50} and Rh_{50}-Ir_{50} nanoparticles showed a hydrogen desorption spectrum different from that of the monometallic ones. Indeed, the absence of hydrogen desorption peaks at high temperature for Rh_{50}-Ir_{50} particles contrary to Rh and Ir can be explained by the formation of alloy or core-shell bimetallic nanoparticles, characterized by a different behavior to that of monometallic particles. The same trend has been observed with nanoparticles Pd_{50}-Pt_{50}, which does not desorb hydrogen at low temperature, while Pd does.

However, a different desorption trend of H_2 was observed for the Pd_{50}-Rh_{50} nanoparticles. At high temperature, the desorption peak of H_2 for the Pd_{50}-Rh_{50} particles which appears at the same temperature but with a lower intensity can be explained by a desorption contribution of the particles of Rh, dispersed separately from the Pd ones in the 10-$Pd_{50}Rh_{50}$@MIL-101(Cr) composite, especially since no desorption peak of H_2 from the Pd particles is observed.

In conclusion, the H_2 desorption results are in good agreement with the results of DTA-TGA. Alloys or core-shells might be formed for 1nm clusters of Pd_{50}-Pt_{50} and Rh_{50}-Ir_{50}. However, monometallic particles of Rh and Pd are probably dispersed separately in the material 10-$Pd_{50}Rh_{50}$@MIL-101(Cr).

5.3 Conclusion

In this chapter, a study of the structural, nanostructural and textural properties of three materials formed by ultra-small bimetallic nanoparticles confined within the pores of MIL-101(Cr), as well as determination of the nature of the synthesized bimetallic nanoparticles and the hydrogen sorption properties was carried out.

The first part of this chapter consists of the synthesis of 10-*M*@MIL-101(Cr), with *M* = Pd_{50}-Rh_{50}, Pd_{50}-Pt_{50} and Rh_{50}-Ir_{50}. The synthesis technique used is the DSM approach followed by a reduction under Ar/H_2 at 573 K for 2 hours and a previously degassed MIL-101(Cr).

The physicochemical characterization of the synthesized materials was carried out. Structural, nanostructural and textural characterization confirmed the good insertion and dispersion of ~ 1 nm metallic nanoparticles within the pores of MIL-101(Cr). Moreover, it has been shown, using coupled DTA-TGA, that 10-$Pd_{50}Pt_{50}$@MIL-101(Cr) and 10-$Rh_{50}Ir_{50}$@MIL-101(Cr) might contain bimetallic nanoparticles in the core-shell form or metastable alloys. However, 10-$Pd_{50}Rh_{50}$@MIL-101(Cr) material might be formed by nanoparticles of Pd and Rh dispersed separately.

The last part of this chapter focused on the determination of the hydrogen sorption properties of 10-*M*@MIL-101(Cr) materials (*M* = $Pd_{50}Rh_{50}$, $Pd_{50}Pt_{50}$ and Rh_{50}-Ir_{50}). First, the effect of the insertion of the bimetallic nanoparticles into the pores of MIL-101(Cr) on hydrogen sorption was analyzed by PCI curves at room temperature and up to 1 bar H_2. Whatever the composite, the presence of metal nanoparticles increases the sorption capacity of hydrogen without the formation of a hydride. However, due to the low sorption capacity recorded, it was not possible to obtain more information from PCI curves. Then, the study of H_2 desorption was performed by thermal-desorption spectroscopy below and above 300 K. These hydrogen desorption measurements provided additional information in determining the nature of the nanoparticles confined in the pores of MIL-101(Cr) and were in good agreement with the coupled DTA-TGA results.

As mentioned in *chapter IV*, the very small size of nanoparticles makes their characterization difficult. The available facilities to characterize the 1 nm bimetallic nanoparticles are insufficient for a more precise study. In this project, only TEM made it possible to clearly identify the presence and the size of nanoparticles. The discussions and conclusions of the nature of bimetallic composites are mainly based on hypothesis and indirect measurements. Other more powerful characterization techniques for characterizing such small particles (~ 1 nm) are needed, such as XAS.

References

1. Gossé, S., Dupin, N., Guéneau, C., Crivello, J.-C. & Joubert, J.-M. Thermodynamic assessment of the PdRhRu system using calphad and first-principles methods. *Journal of Nuclear Materials* **474**, 163–173 (2016).
2. Oumellal, Y. *et al.* Synthesis and stability of Pd–Rh nanoalloys with fully tunable particle size and composition. *Nano-Structures & Nano-Objects* **7**, 92–100 (2016).
3. Binary Alloy Phase Diagrams, 2nd Edition - ASM International. Available at: https://www.asminternational.org/online-catalog/alloy-phase-diagrams/-/journal_content/56/10192/57718G/PUBLICATION. (Accessed: 5th September 2019)
4. Tripathi, S. N., Bharadwaj, S. R. & Chandrasekharaiah, M. S. The Ir-Rh (Iridium-Rhodium) system. *JPE* **12**, 606–608 (1991).
5. Kobayashi, H. *et al.* Nanosize-Induced Drastic Drop in Equilibrium Hydrogen Pressure for Hydride Formation and Structural Stabilization in Pd–Rh Solid-Solution Alloys. *J. Am. Chem. Soc.* **134**, 12390–12393 (2012).
6. Zlotea, C., Oumellal, Y., Provost, K. & Ghimbeu, C. M. Experimental Challenges in Studying Hydrogen Absorption in Ultrasmall Metal Nanoparticles. *Front. Energy Res.* **4**, (2016).
7. Oumellal, Y., Provost, K., Ghimbeu, C. M., Yuso, A. M. de & Zlotea, C. Composition and size dependence of hydrogen interaction with carbon supported bulk-immiscible Pd–Rh nanoalloys. *Nanotechnology* **27**, 465401 (2016).
8. Kobayashi, H. *et al.* Atomic-Level Pd−Pt Alloying and Largely Enhanced Hydrogen-Storage Capacity in Bimetallic Nanoparticles Reconstructed from Core/Shell Structure by a Process of Hydrogen Absorption/Desorption. *J. Am. Chem. Soc.* **132**, 5576–5577 (2010).
9. Alicia, M. de Y., Oumellal, Y., Zlotea, C., Vidal, L. & Camelia, M. G. In-situ Pd–Pt nanoalloys growth in confined carbon spaces and their interactions with hydrogen. *Nano-Structures & Nano-Objects* **9**, 1–12 (2017).

GENERAL CONCLUSION

&

PERSPECTIVES

The objective of this Ph.D. thesis work was to study the nanoscale effect of metals/alloys on their physicochemical and hydrogen sorption properties. The main idea consists in combining absorption and adsorption by inserting mono and bimetallic nanoparticles into the mesoporous Metal-Organic Framework for solid storage applications. In this context, MIL-101(Cr) has been chosen to serve as a porous matrix for confining metallic nanoparticles. Three systems of materials were studied:

Firstly, Pd@MIL-101(Cr) composites with different metal loadings (up to 20 wt.%) were prepared and characterized. The double solvent impregnation (DSM) followed by reduction at 573 K under H_2/Ar flow for 15 min makes it possible to form well dispersed 1 nm Pd clusters confined within the pores of MIL-101(Cr), despite the high metal loading. The hydrogen sorption properties of the synthesized composites were then studied. In contrast to bulk and 2 nm Pd nanoparticles, 1 nm Pd clusters do not form hydride at room temperature and up to 1 bar H_2, but rather solid solutions as was shown by PCI curves and *in situ* EXAFS. However, at lower temperature (125-240 K), the hydride phase may be formed, as demonstrated by TDS. A decrease of the critical temperature of the biphasic region in the Pd-H phase diagram below room temperature due to extreme nanosizing may be the origin of this behavior. A change of the rate limiting step from surface recombination of $\beta \rightarrow \alpha$ phase transformation in bulk Pd powder to hydrogen diffusion into α and β phases in 1 nm clusters was demonstrated. Moreover, an increase of the isosteric heat of H_2 adsorption at low coverage was observed by inserting 1 nm Pd nanoparticles in MIL-101(Cr), confirming a synergistic effect between the metal nanoparticles and the porous host.

Thereafter, Rh@MIL-101(Cr) with different metal loadings (up to 20 wt.%) were synthesized by the DSM approach followed by reduction at 573 K under H_2/Ar flow for 120 min. Well dispersed 1 nm Rh clusters are inserted within the pores of MIL-101(Cr). The characterization of the hydrogen sorption properties shows that the Rh particles of 1 nm do not form a hydride at 300 K up to 1 bar H_2. Therefore, two working hypotheses may be suggested: the interaction of hydrogen with Rh nanoparticles consists of a dissociative chemisorption on the surface, or a solid solutions formation with hydrogen up to 1 bar H_2, or both. Comparison of the hydrogen desorption results, recorded at temperature above 300 K with 1 nm particles and other Rh nanoparticles with different sizes reported previously, made it possible to suggest the formation of solid solutions between 1 nm Rh clusters and hydrogen.

Finally, three bimetallic composites were prepared by the same synthetic method and characterized in order to determine the nature of the synthesized nanoparticles. 10-*M*@MIL-101(Cr) (*M* = Pd_{50}-Rh_{50}, Pd_{50}-Pt_{50} and Rh_{50}-Ir_{50}) materials were prepared with well dispersed 1 nm nanoparticles confined within the MIL-101(Cr) pores. Characterization by coupling DTA-TGA shows that 10-*M*@MIL-101(Cr) (*M* = Pd_{50}-Pt_{50} and Rh_{50}-Ir_{50}) can be formed by metallic nanoparticles in the core-shell form or metastable alloys. However, the 10-$Pd_{50}Rh_{50}$@MIL-101(Cr) seems to be formed by dispersed monometallic Pd and Rh nanoparticles. The same trend was confirmed by TDS measurements recorded below and above 300 K.

In perspective, further characterizations of the hydrogen sorption properties of the different metallic composites is suggested. In fact, a low temperature *in situ* XAS measurement may provide additional information on the interaction of hydrogen with 1 nm Pd clusters in order to confirm the hydride formation. Moreover, because of the very small size of Rh and bimetallic nanoparticles, *in situ* XAS measurements under H_2 gas may be used to confirm the solid solution formation (Rh-H) and the nature of bimetallic phases (Pd-Pt, Rh-Ir, Pd-Rh), respectively.

Furthermore, a study of the catalytic activity of the synthesized composites of Pd and Rh may be carried out. The catalytic reaction of hydrogen production from HCOOH was successfully tested in this project with the 10-Pd@MIL-101(Cr) material. The Rh@MIL-101(Cr) composite, as well as the various bimetallic composites, might also be tested and the catalytic yields compared.

Finally, increasing the density of the synthesized materials might improve the hydrogen sorption properties, by increasing the metals loading by two possible methods. The first technique is to increase the loading of metal in the MIL-101(Cr) pores by successive loadings. In this Ph.D. thesis, metal loading was limited to 20 wt.%, because of the solubility limit of the precursor salt in the solvent. The second technique consists in compacting the synthesized materials in the form of pellets (under pressure), with preserving the crystallinity and the porosity of composites.

ANNEX

Annex 1

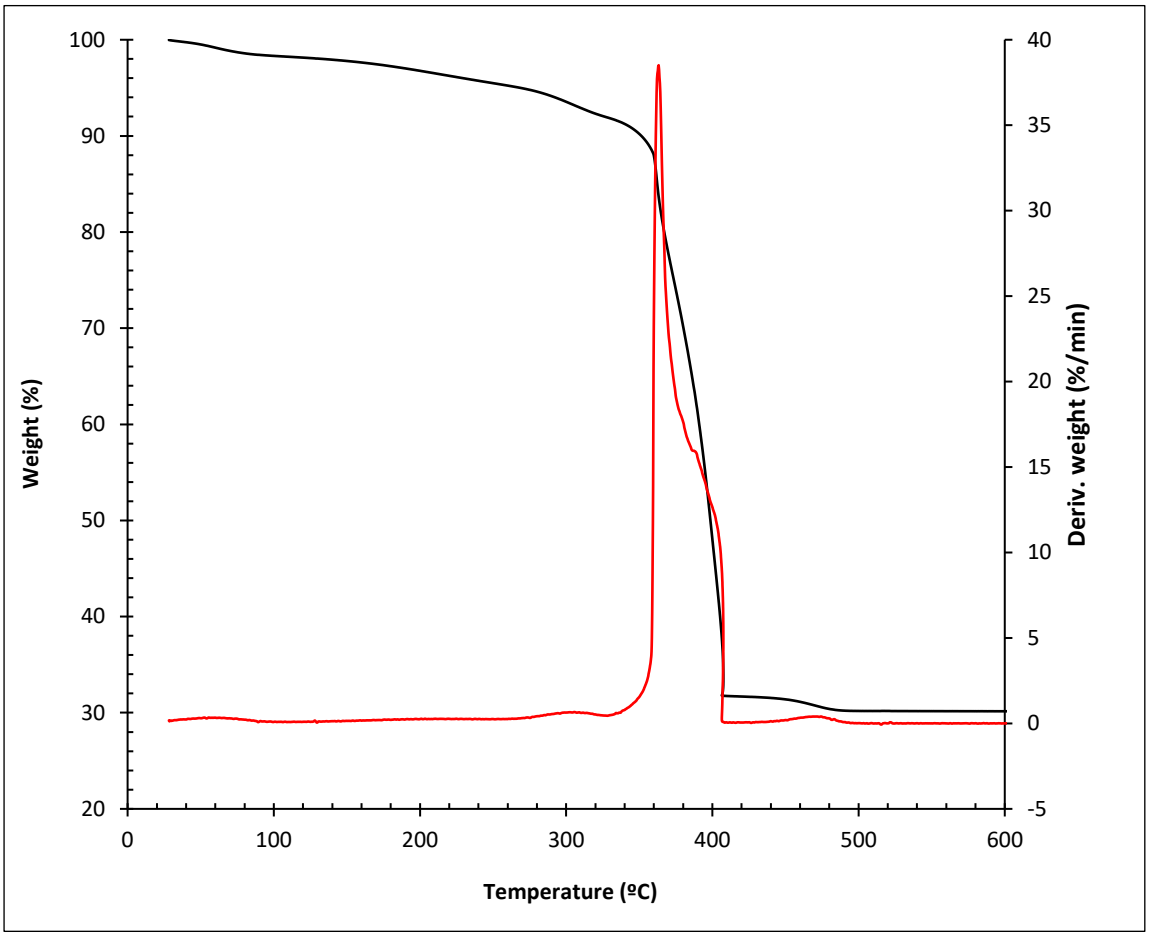

Annex 1: DTA/TGA of pristine MIL-101(Cr)

Annex 2

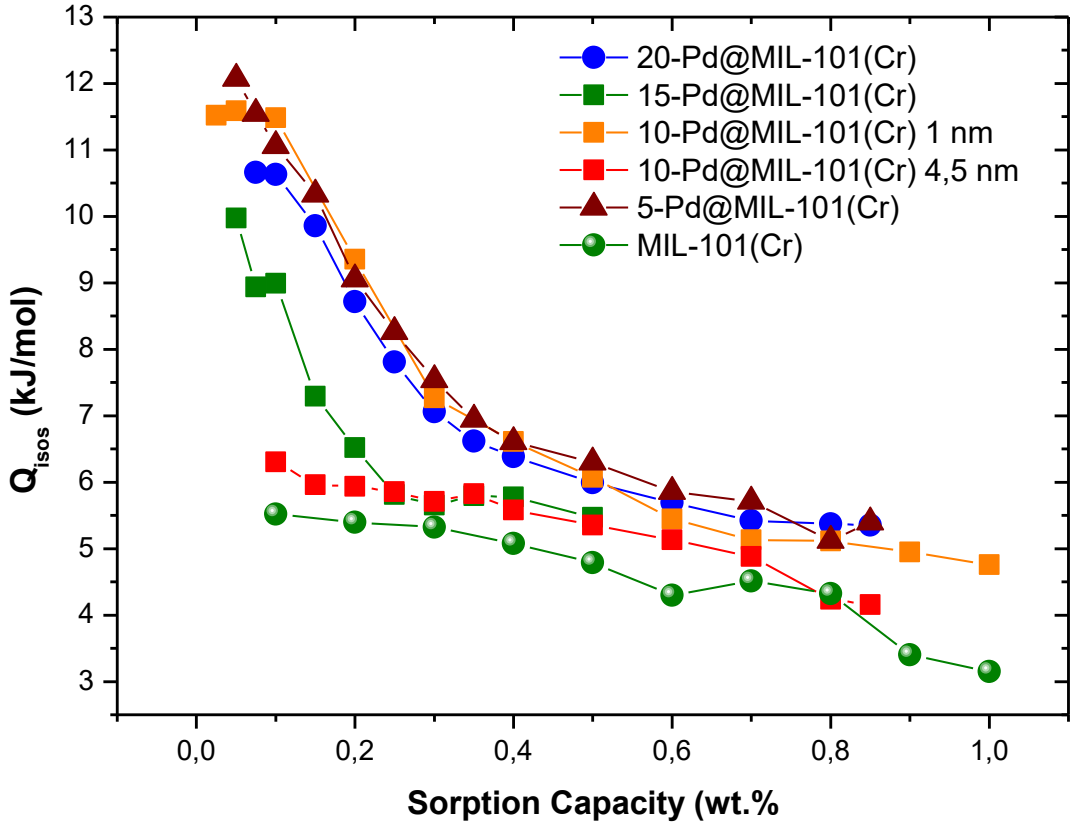

Annex 2: Isosteric heat of adsorption as a function of hydrogen excess capacity (expressed in wt%) for all composites: (5, 10, 15 and 20 wt.%) Pd-1nm@MIL-101 and 10 wt.% Pd-4.5nm@MIL-101.

Annex 3

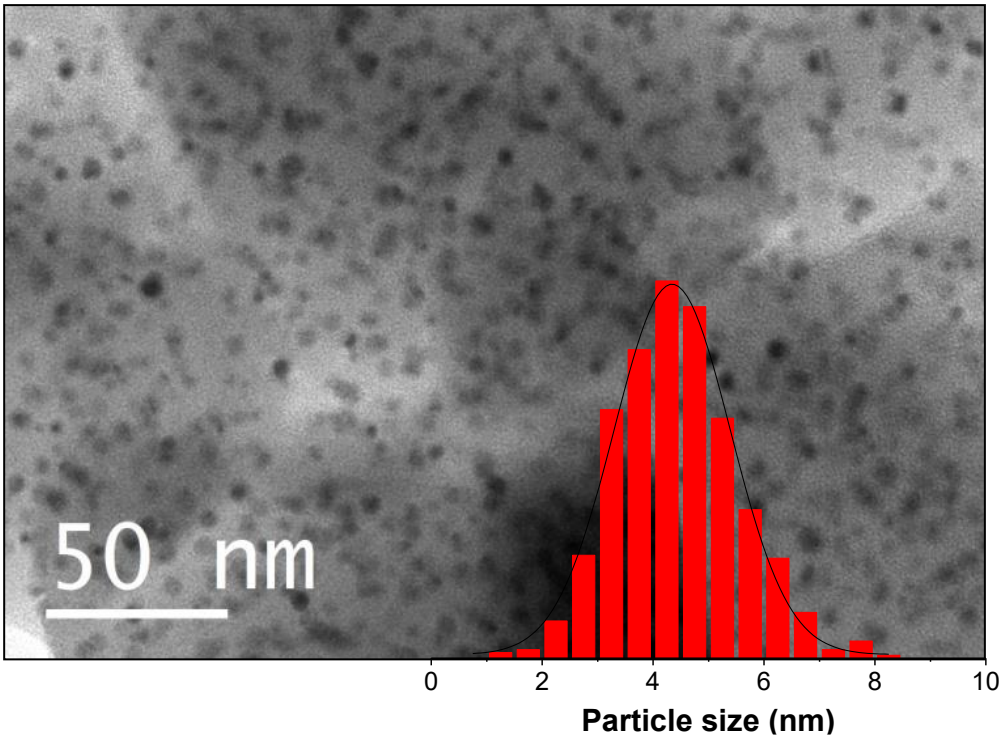

Annex 3: Typical TEM image and related particle size histogram of 4.5 nm Pd nanoparticles inserted into MIL-101(Cr).

Annex 4

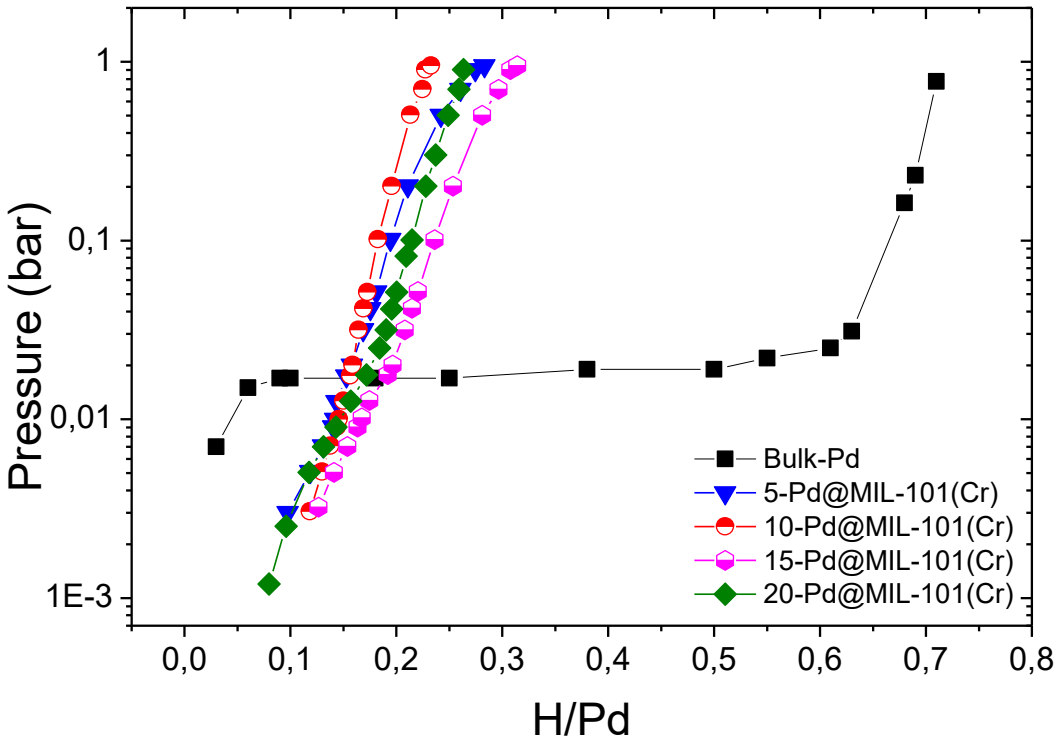

Annex 4: PCI curves of bulk Pd and 1 nm Pd clusters with 5, 10, 15 and 20 wt.% performed at 300 K up to 1 bar H_2 pressure. The capacity is expressed as H/M.

Annex 5

Suzuki-Miyaura Coupling reaction

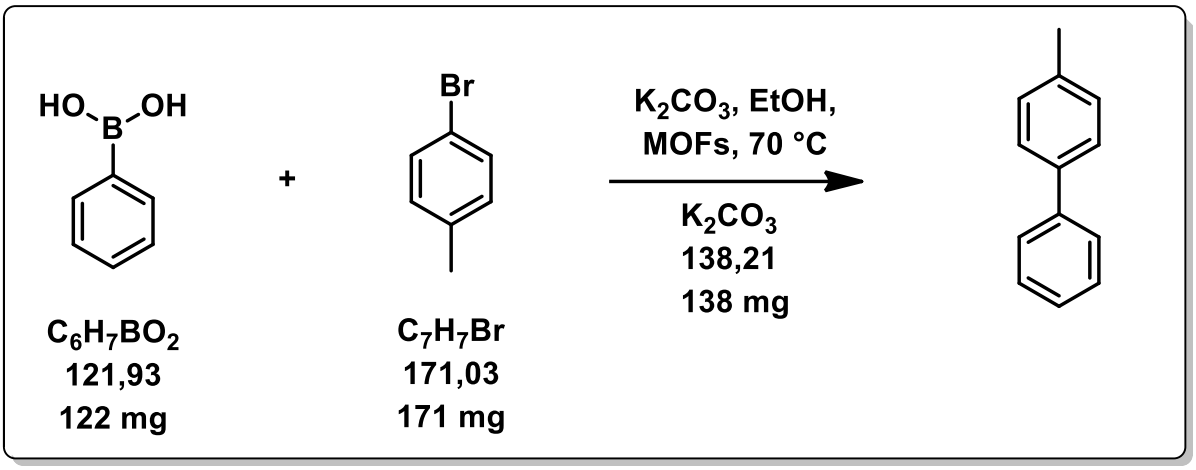

Annex 5.1: Suzuki-Miyaura Coupling reaction : mixture of benzene boronic acid, 4-bromotoluene and K_2CO_3 in ethanol. 5-Pd@MIL-101(Cr) was used as catalyst to form biphenyl.

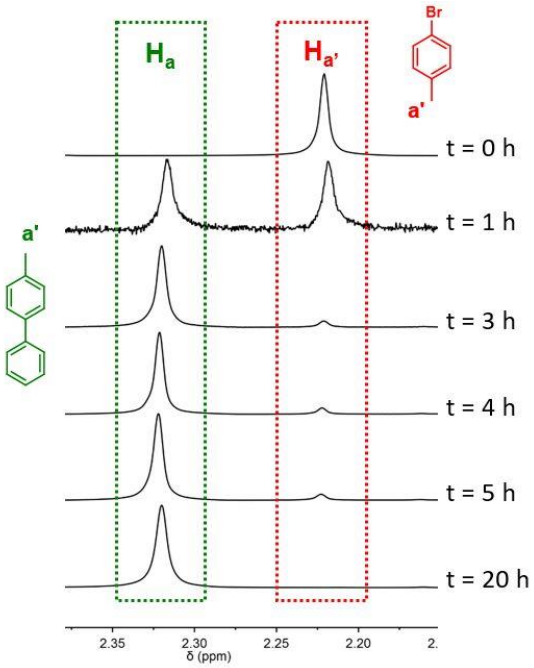

Annex 5.2: ^1H NMR spectra of the reaction mixture recorded at different reaction time using 5-Pd@MIL-101(Cr) as catalyst: monitoring of the vanishing of methyl protons from the reactant (4-bromotoluene) and appearing of methyl protons from the product of the C-C cross-coupling reaction.

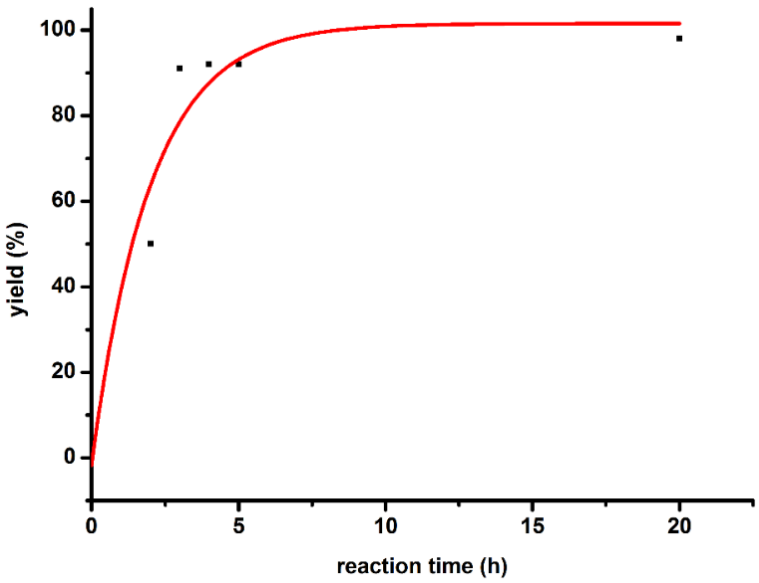

Annex 5.3: Kinetic investigation for the Suzuki-Miyaura coupling reaction using 5-Pd@MIL-101(Cr) catalyst: experimentally, yield ~ 90 % after only 3h but then 20 hours to reach total conversion with a selectivity of 100 %.

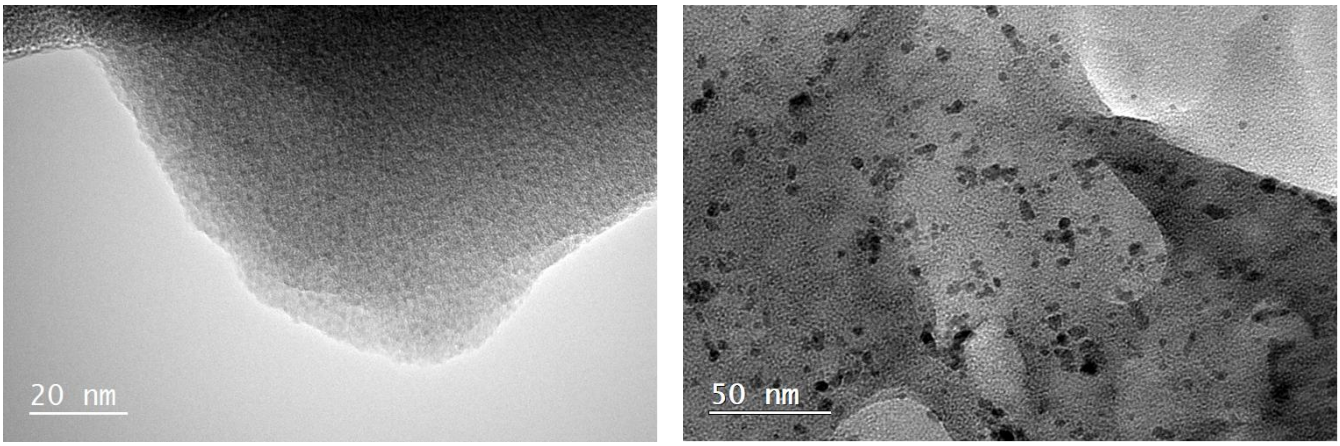

Annex 5.4: Typical TEM images of 5-Pd@MIL-101(Cr) before (left) and after (right) Suzuki-Miyaura catalytic reaction. Pd nanoparticles aggregation after the reaction. The catalyst is not recyclable.

Annex 6

Hydrogen production from formic acid

Hydrogen storage systems based on organic liquid hydrogen carrier (LC) have attracted considerable attention, because most organic materials are light and inexpensive, and they are normally liquid under ambient conditions. Basically, hydrogen storage by LC involves their conversion from a rich-energy state to a low-energy state by dehydrogenation. Ideally, the process is reversible[1].

Chemical hydrogen storage can become competitive if the storage material fulfils some requirements: 1) high gravimetric and volumetric hydrogen content under ambient conditions, 2) energy-efficient reversible charge and discharge, 3) the absence of byproducts, 4) long-term stability, 5) low toxicity, 6) easily available at a large scale and at a low price[2]. The challenge is to find suitable organic carriers.

Formic acid (FA) is a promising candidate for hydrogen storage[3]. With a hydrogen content of 4.4 wt.% and 53 g/L, it has high stability, low toxicity and can be easily handled and stored. FA is a major product of biomass processing. In general, the decomposition of HCOOH follows two pathways: one involves the formation of H_2 and CO_2.

$$HCOOH \leftrightarrow CO_2 + H_2 \qquad \Delta G = -48.4 \text{ kJ mol}^{-1} \qquad (1)$$

and the other involves the formation of CO and H_2O

$$HCOOH \leftrightarrow CO + H_2O \qquad \Delta G = -28.5 \text{ kJ mol}^{-1} \qquad (2)$$

the first one being important for hydrogen storage.

Dehydrogenation of formic acid are generally made using homogeneous catalysis[4]. However, the generation of hydrogen from formic acid with heterogenous catalysts in aqueous media remains less developed[5]. Generally, the heterogeneous catalysis is more desirable to be used widely because it is easy to be control and the catalyst can be easily removed from reaction medium, reactivated and recycled. Therefore, there is a strong desire to develop heterogeneous catalysts with high activity and selectivity for the formic acid decomposition under mild conditions.

1 Experimental

1.1 Materials

All starting materials and solvents were obtained from commercial suppliers and used without further purification.

1.2 Catalytic activity tests

Catalytic activity tests were carried out under ambient atmosphere of air using a simple experimental set-up formed by a round bottom flask, thermostated by a silicon oil bath, and connected to a gas burette in order to quantify the volume of evolved gases. Typically, 10 mg of the 10-Pd@MIL-101(Cr) catalyst was placed inside the flask together with a Teflon coated magnetic bar, while the reaction was considered started after addition of the selected volume of formic acid solution (FA, different molar concentrations) and stirring. A reflux condenser was used in order to avoid evaporation of the reaction mixture (especially when performing the reaction at higher temperatures).

The influence of several parameters on the catalytic activity of the Pd/TC catalyst in the dehydrogenation of formic acid were investigated: Pd:FA ratio, reaction temperature and concentration of formic acid solution.

For each catalytic test, the volume of the evolved gases was measured at ambient temperature, while calculations of reaction parameters (FA conversion, TOFs) were carried out by use of corrected gas volumes to 298 K.

The FA conversion and the initial turnover frequency (TOF initial) values were calculated according to the following equations:

$$x_{FA} = \frac{P_{atm} \cdot V_{gas}}{2R \cdot T \cdot n_{FA}} \; x \; 100, \quad (\%) \tag{3}$$

where P_{atm} is the atmospheric pressure (101325 Pa), V_{gas} is the generated volume of (H_2 + CO_2) gas, R is the universal gas constant (8.3145 m^3.Pa.$mol^{-1}K^{-1}$), *T* is the temperature (K) and n_{FA} is the mole number of formic acid.

Turnover frequencies (TOFs) were calculated at low conversion values (<15 %), on the basis of total metal atoms in the catalyst sample, using the following equation:

$$TOF_{initial} = \frac{P_{atm} \cdot V_{gas}}{2R \cdot T \cdot n_{Pd} \cdot t}, \quad (h^{-1}) \tag{4}$$

where n_{Pd} is the number of Pd moles in the catalyst sample, while t is the reaction time.

Qualitative analysis of the evolved gases was carried out by a quadrupole mass spectrometer (QMS, Pfeiffer Vacuum, Germany) connected to the experimental set-up. In this particular case, Ar was used as carrier gas (20 mL/min) in order to collect the evolved gases during formic acid decomposition. The experimental procedure consisted in the following steps: the catalyst sample was placed in a three-neck round bottom flask together with a Teflon coated magnetic bar, Ar was passed over the catalyst until no air was detectable by

MS, then the selected amount of formic acid solution was injected through a septum over the catalyst. The reaction was considered started after turning on the magnetic stirring.

2 Results and discussions

2.1 Pd:FA ration

In the first set of experiments were established the optimum of Pd:FA ratio. In this regard, the HCOOH decomposition was studied at room temperature on 10 mg 10-Pd@MIL-101(Cr) using identical volume of FA aqueous solutions (5 ml) of concentration of different concentration, except of the Pd:FA=1:35 case. *Table 1* summarizes the obtained results.

The best conversion was obtained for Pd:FA ratio of 1:400: 36.7% at 24h and 37.9% at 48h. Despite the fact that the TOF at 5 minutes has close values for Pd: FA ratios of 1:400, 1:800 and 1:1600, the rate of decomposition of formic acid decreases much in the last two situations, making them even smaller. From the evolved gas volume point of view, a plateau is installed after approx. 400 minutes, except the Pd:FA of 1:400 case, where the plateau is installed after approx. 25 h (*figure 1*).

As expected, using formic acid solutions of the same concentration (0.25 M), conversion increases with decreasing Pd:FA ratio. (*Table 1*) The situation is valid at 24 h, while at 6 h the conversions are similar.

Table 1 Catalytic performance of 10-Pd@MIL-101(Cr) in the dehydrogenation of FA at different concentrations (10 mg of catalyst, 5 mL of FA solution, 303 K).

Entry	FA concentration (M)	Pd:FA ratio	Conversion (%)		TOF (h^{-1})[a]
			X_{FA}^{6h}	X_{FA}^{24h}	
1	0.25	1:50	3.1	6.9	3.9
2	0.25	1:200	3.3	4.7	8
3	0.5	1:400	12.5	36.7	16
4	1.0	1:800	1.3	1.9	15.73
5	1.5	1:1200	2.5	3.9	7.7
6	2.0	1:1600	0.9	1	15.43

[a] Initial TOF after 5 min.

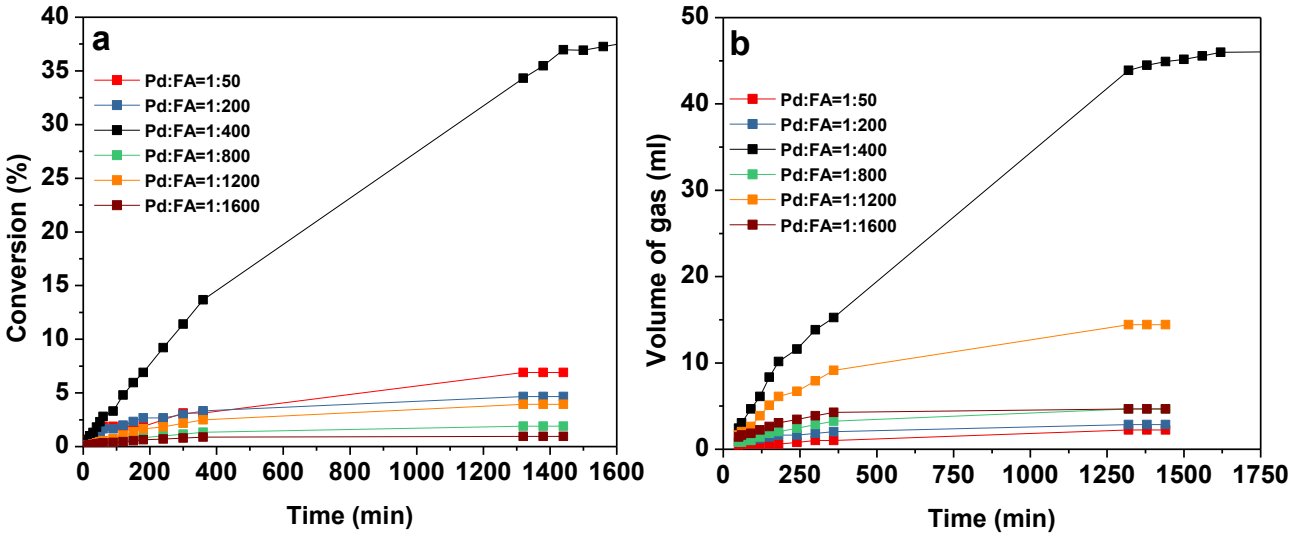

Figure 1: (a) Conversion and (b) volume of gas profiles in the dehydrogenation of FA catalyzed by 10-Pd@MIL-101(Cr) at different Pd:FA ratio (10 mg of catalyst, 5 mL of FA solution, 303 K).

The used catalyst in reaction at Pd:FA ratio of 1:400, was separated from reaction mixture by filtration, washed with water and dried at room temperature. After that its structural characteristics were investigated by powder X-ray diffraction (*figure 2*). MIL-101(Cr), the catalyst support, retains its structure during reaction.

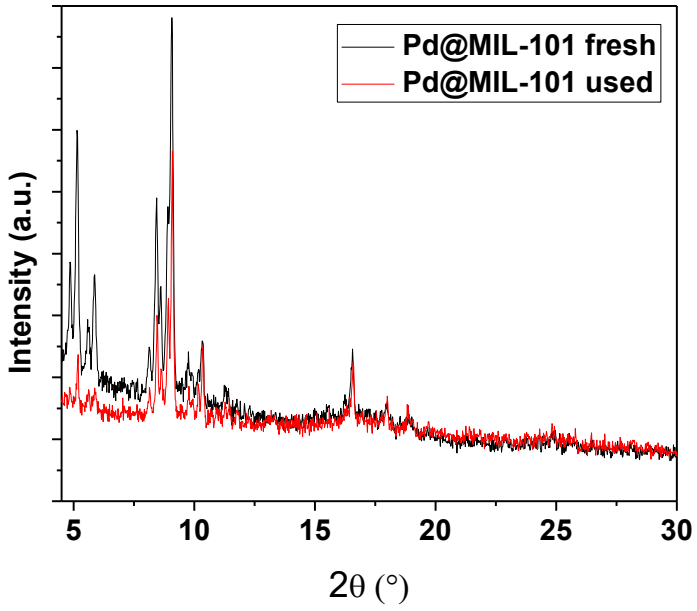

Figure 2: The PXRD diffraction patterns of 10-Pd@MIL-101(Cr) catalyst fresh (black) and used (red).

2.2 Temperature influence

The influence of reaction temperature was studied using FA 0.5 M solutions and Pd:FA ratios of 1:400. Thus, the FA decomposition was performed at temperatures of 313, 323, 333 and 343 K. The results obtained are presented in *figure 3* and *table 2*. As expected, at temperature of 333 and 343 K TOF increase, reaching values of 137 and 130 h^{-1}, respectively. Moreover, the TOF at 2 min. is 155 h^{-1}. In terms of volume of evolved gas at 343, 323 and 313 K, the plateau is installed at 120, 240 and 360 minutes, respectively. The best FA conversions at 6 h and 24 h are obtained at 333 and 303 K, respectively.

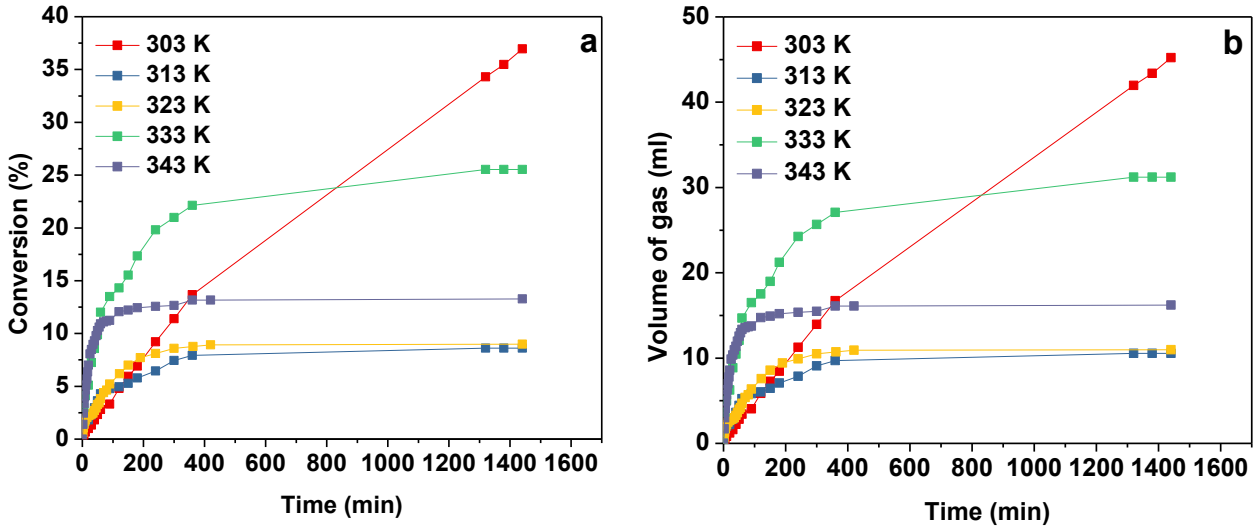

Figure 3: (a) Conversion and (b) volume of gas profiles in the dehydrogenation of FA catalyzed by 10-Pd@MIL-101(Cr) at different temperatures (Pd:FA=1:400, 10 mg of catalyst, 5 mL of FA solution, 303 K).

Table 2 Catalytic performance of 10-Pd@MIL-101(Cr) in the dehydrogenation of FA at different temperatures (Pd:FA=1:400, 10 mg of catalyst, 5 mL of FA 0.5 M solution).

Entry	Temperature (K)	Conversion (%)		TOF (h^{-1})[a]
		X_{FA}^{6h}	X_{FA}^{24h}	
1	303	12.5	36.7	16
2	313	7.9	8.6	69.8
3	323	8.8	9	56
4	333	22.1	25.5	137
5	343	13.2	13.3	130

[a] Initial TOF after 5 min.

2.3 Concentration influence

This study was mas performed at Pd:FA ratio of 1:400 and 303 K, using FA solutions of 0.25, 0.5, 1, 1.5 and 2 M concentration. The results are presented in *figure 4* and *table 3*.

As in the other cases, the best conversion of formic acid decomposition is obtained on FA 0.5 M solution. The reaction starts harder in FA solutions of 1, 1.5 and 2 M. The first evolved gas volume was measured after 10, 38, and 15 min., respectively, after timer was started.

Table 3 Catalytic performance of Pd(10wt.%)@MIL-101(Cr) in the dehydrogenation of FA at different concentration of FA solution (Pd:FA=1:400, 10 mg of catalyst, 5 mL of FA 0.5 M solution, 303 K).

Entry	FA concentration (M)	Conversion (%)		TOF (h^{-1})[a]
		X_{FA}^{6h}	X_{FA}^{24h}	
1	0.25	2.42	2.44	7.5
2	0.5	12.5	36.7	16
3	1	3	3.6	0
4	1.5	1.2	1.75	0
5	2	2.5	3.24	0

[a] Initial TOF after 5 min.

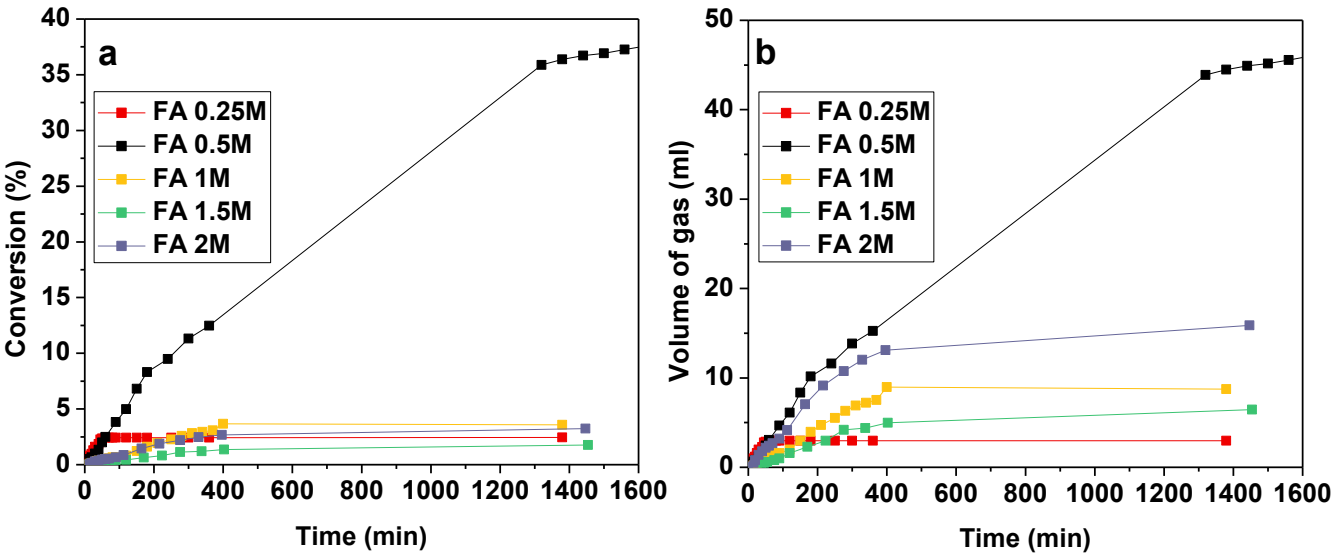

Figure 4: (a) Conversion and (b) volume of gas profiles in the dehydrogenation of FA catalyzed by 10-Pd@MIL-101(Cr) at different concentration of FA solution (Pd:FA=1:400, 10 mg of catalyst, 5 mL of FA solution, 303 K).

2.4 The nature of evolved gases

Qualitative analysis of evolved gases performed by MS reveal that H_2 (m/z = 2) and CO_2 (m/z = 44) are the constituent components of the gas mixture, with no detectable traces of CO (m/z = 24) (*figure 5(a)* and *(b)*). The peak at m/z = 28 observable in the insert picture of *figure 5(a)* is given by nitrogen present in the residual air, and not CO, proven by the characteristic fingerprint for air in the MS spectrum (mass numbers 28 and 32). Also, as can be seen in *figure 5(b)*, the m/z = 28 component has a similar evolution with the oxygen (m/z = 32). Therefore, it may be concluded that decomposition of formic acid proceeds via dehydrogenation in the presence of 10-Pd@MIL-101(Cr) catalyst, confirmed, as well, by the evolution in time of the gas composition.

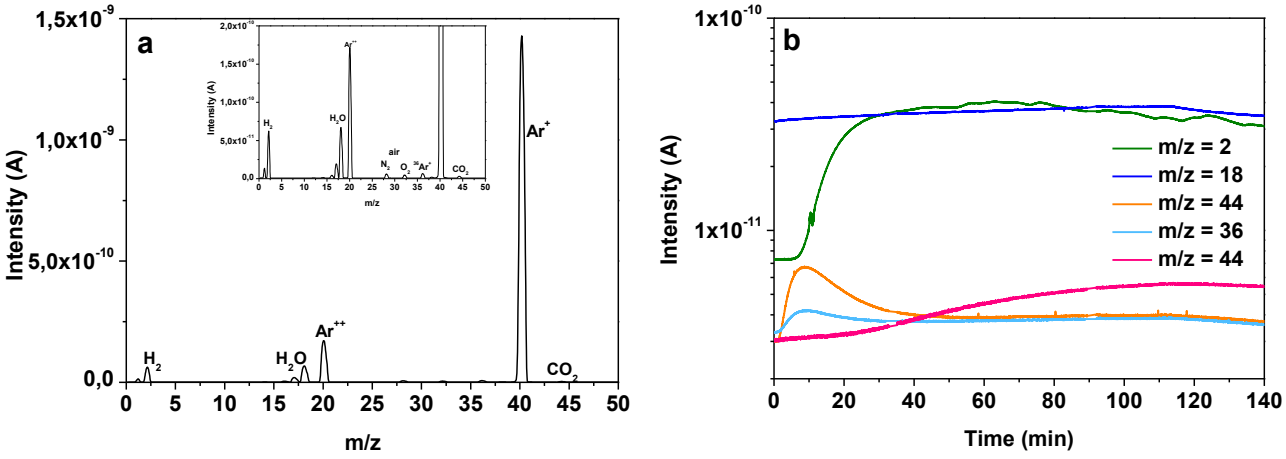

Figure 5: (a) The composition of the effluent gases following the decomposition reaction of the formic acid and (b) the evolution over time of the resulting gaseous mixture (303 K, FA 0.5 M, Pd:FA =1:400).

3 Conclusions

Pd nanoparticles of 1 nm size, confined in MIL-101(Cr), have catalytic activity in decomposition of HCOOH. They promote the dehydrogenation pathway. The best results are obtained using solution of FA 0.5 M, Pd:FA ratio of 1:400 and reaction temperature of 303 K: conversion of 36.7% at 24 h, and 37.9% at 48 h. MIL-101(Cr) maintained its structure during the reaction.

References

1. Teichmann, D., Arlt, W., Wasserscheid, P. & Freymann, R. A future energy supply based on Liquid Organic Hydrogen Carriers (LOHC). *Energy Environ. Sci.* **4**, 2767–2773 (2011).

2. Mellmann, D. *et al.* Base-Free Non-Noble-Metal-Catalyzed Hydrogen Generation from Formic Acid: Scope and Mechanistic Insights. *Chemistry – A European Journal* **20**, 13589–13602 (2014).
3. New and Future Developments in Catalysis - 1st Edition. Available at: https://www.elsevier.com/books/new-and-future-developments-in-catalysis/suib/978-0-444-53882-6. (Accessed: 16th July 2019)
4. Fujita, E., Muckerman, J. T. & Himeda, Y. Interconversion of CO2 and formic acid by bio-inspired Ir complexes with pendent bases. *Biochimica et Biophysica Acta (BBA) - Bioenergetics* **1827**, 1031–1038 (2013).
5. Wang, X. *et al.* Recent progress in hydrogen production from formic acid decomposition. *International Journal of Hydrogen Energy* **43**, 7055–7071 (2018).

Annex 7

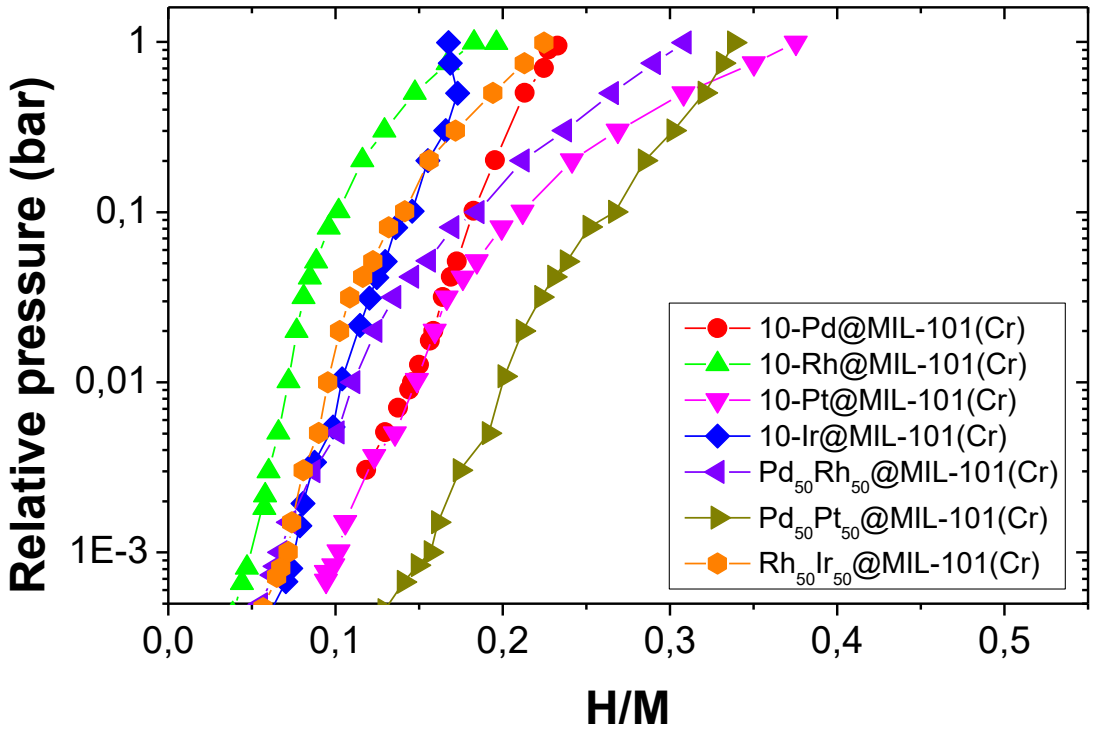

Annex 8: PCI curves performed at 300 K up to 1 bar H_2 pressure of 10-M@MIL-101(Cr) (M = Pd, Rh, Pt, Ir, Pd_{50}-Rh_{50}, $Pd_{50}Pt_{50}$ and Rh_{50}-Ir_{50}). The capacity is expressed as H/M.

METAL DOPED MOFs FOR HYDROGEN STORAGE

Due to their very large surface area and ordered crystalline structure, Metal-Organic Framework (MOF) are of great interest in various fields, such as catalysis, drug transport and hydrogen storage. In addition, the pores of MOFs have an important role in the nanoconfinement of metal particles. Indeed, the ordered porosity ensures the monodispersion of the nanoparticles and the control of their size, their stabilization against coalescence and the change of the kinetic and thermodynamic properties of hydrogen absorption.

The purpose of this PhD project is to determine the effect of nanoparticle size on physicochemical and hydrogenation properties. Indeed, 1 nm palladium, rhodium and bimetallic (Pd-Rh, Pd-Pt and Rh-Ir) clusters have been homogeneously dispersed within the pores of MIL-101(Cr). The insertion of the nanoparticles was carried out by double solvent impregnation technique followed by a reduction under H_2/Ar flow. The obtained composites were characterized by X-ray diffraction, transmission electron microscopy, N_2 adsorption to determine physicochemical properties, and by in-situ X-ray absorption, thermal desorption spectroscopy and absorption measurements of hydrogen to determine the sorption properties of H_2.

Interestingly, 1 nm Pd clusters form solid solutions with hydrogen at room temperature and atmospheric pressure instead of a hydride phase, as observed for bulk Pd. This can be explained by a decrease in the critical temperature of the bi-phasic region (α-β) in the Pd-H phase diagram. However, under the same conditions, rhodium absorbs hydrogen and forms solid solutions, in contrary to bulk Rh.

These results may open the route to a new material design strategy not only for solid-state hydrogen storage but also for heterogeneous catalysis field, given that Pd and Rh-based catalysts are widely used for many chemical reactions involving hydrogen.

Keywords: Metal-Organic Framework, Metal nanoparticles, Hydrogen storage

---

MATERIAUX MOFs DOPES PAR DES METAUX POUR LE STOCKAGE D'HYDROGENE

Grâce à leur très grande surface spécifique et de leur structure cristalline ordonnée, les structures organométalliques (Metal-Organic Framework, MOF) présentent un grand intérêt dans divers domaines, tels que la catalyse, le transport de médicaments et le stockage de l'hydrogène. Les pores des MOFs peuvent jouer un rôle important dans le nanoconfinement des particules métalliques. En effet, la porosité ordonnée assure la monodispersion des nanoparticules et le contrôle de leur taille, leur stabilisation contre la coalescence. Les propriétés cinétiques et thermodynamiques de l'absorption d'hydrogène peuvent également être modifiées par la nanostructuration des métaux.

L'objectif de ce projet de thèse est de déterminer l'effet de la taille des nanoparticules sur les propriétés physicochimiques et d'hydrogénation. En effet, des clusters de 1 nm de palladium, rhodium et bimétalliques (Pd-Rh, Pd-Pt et Rh-Ir) ont été dispersés de manière homogène dans les pores de MIL-101(Cr). L'insertion des nanoparticules a été réalisée par la technique d'imprégnation par double solvant suivie d'une réduction sous flux H_2/Ar. Les composites obtenus ont été caractérisés par diffraction des rayons X, microscopie électronique à transmission, adsorption de N_2 pour déterminer les propriétés physicochimiques, et par absorption in situ des rayons X, spectroscopie de désorption thermique et mesures d'absorption de l'hydrogène afin de déterminer les propriétés de sorption de H_2.

Fait intéressant, les clusters de Pd de 1 nm forment des solutions solides avec de l'hydrogène à température ambiante et à pression atmosphérique au lieu d'une phase hydrure, comme observé pour le Pd massif. Cela peut s'expliquer par une diminution de la température critique de la région biphasique (α-β) dans le diagramme de phase Pd-H en dessous de l'ambiante. Cependant, sous les mêmes conditions, le rhodium nanométrique (~ 3 nm) absorbe l'hydrogène et forme des solutions solides contrairement au Rh massif.

Ces résultats pourraient ouvrir la voie à une nouvelle stratégie de conception de matériaux, non seulement pour le stockage d'hydrogène à l'état solide, mais également pour le domaine de la catalyse hétérogène, étant donné que les catalyseurs à base de Pd et de Rh sont largement utilisés pour de nombreuses réactions chimiques impliquant de l'hydrogène.

Mot clés : Hybrides poreux de type MOF, Nanoparticules métalliques, Stockage d'hydrogène